Far-infrared/submillimeter properties of the interstellar medium in nearby galaxies

Ilse De Looze

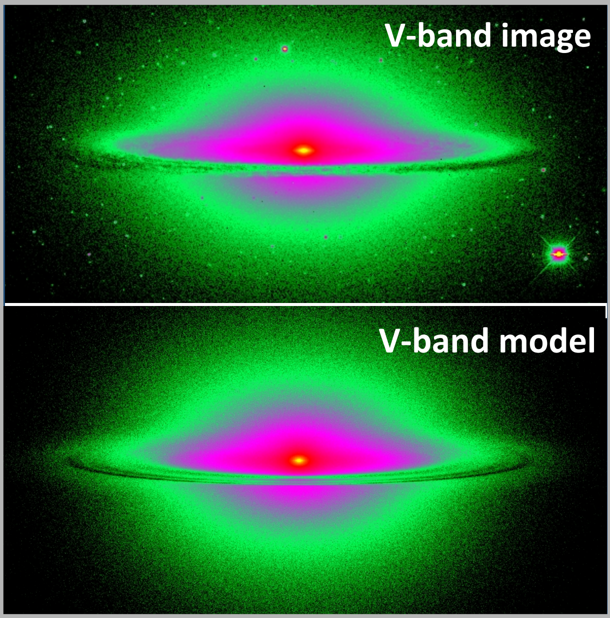

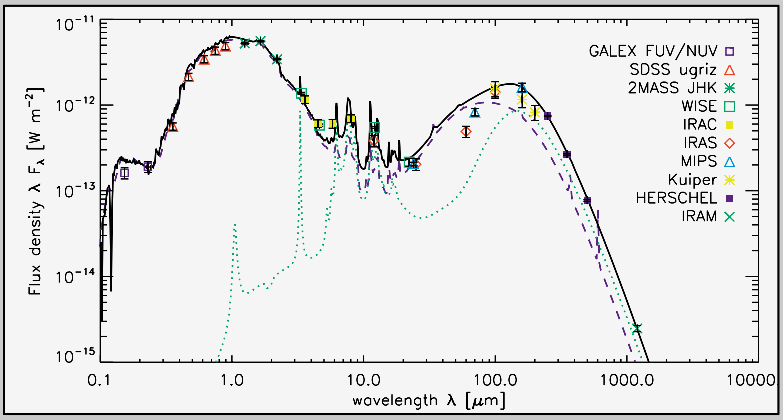

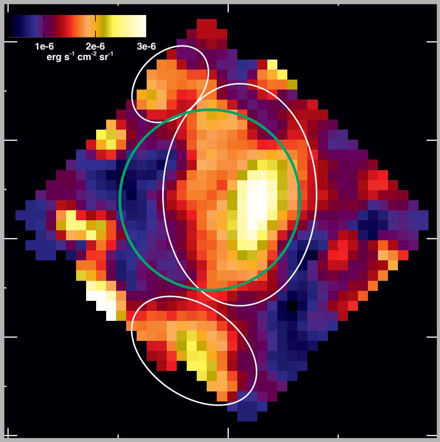

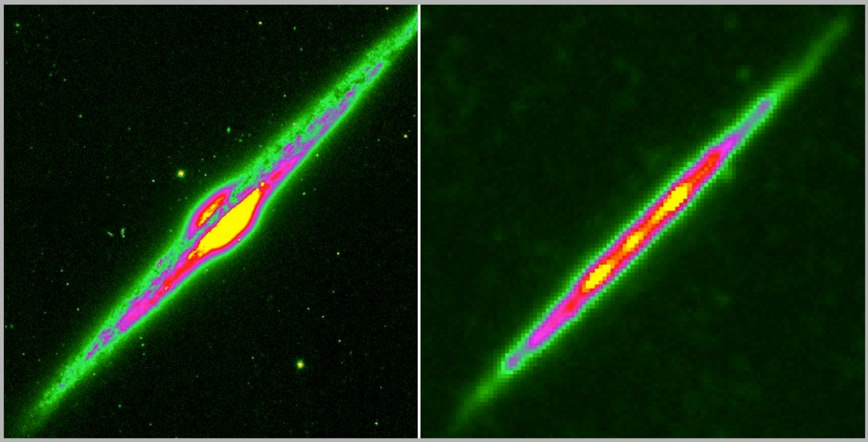

UNIVERSITEIT
GENT

Faculty of Sciences

Department of Physics and Astronomy

Far-infrared/submillimeter properties of the interstellar medium in nearby galaxies.

Dissertation

to obtain the degree of

Doctor in Astronomy,

to be publicly defended on

Thursday the 31st of May 2012, 4:00 pm

by

Ilse De Looze

Cover (from left to right, top to bottom) :
- optical view on NGC 205
- V band images of the Sombrero galaxy: observed (top) and radiative transfer model (bottom)
- observed (symbols) and modelled (black curve) spectral energy distribution for NGC 4565
- SDSS g band (left) and SPIRE 250 μm (right) images of NGC 4565
- [CII] map of the central regions in NGC 205

Promotor:
Prof. Dr. Maarten Baes
Universiteit Gent
Sterrenkundig Observatorium

Reading committee:
Prof. Dr. Frank Israel
Universiteit Leiden
Sterrewacht Leiden

Prof. Dr. Christoffel Waelkens
Katholieke Universiteit Leuven
Instituut voor Sterrenkunde

Prof. Dr. Sven De Rijcke
Universiteit Gent
Sterrenkundig Observatorium

Prof. Dr. Maarten Baes
Universiteit Gent
Sterrenkundig Observatorium

Other members of examination board:
President:
Prof. Dr. Dirk Ryckbosch
Universiteit Gent
Vakgroep Fysica & Sterrenkunde

Prof. Dr. Herwig Dejonghe
Universiteit Gent
Sterrenkundig Observatorium

Prof. Dr. Christophe Detavernier
Universiteit Gent
Vakgroep Vaste-Stofwetenschappen

Dr. Jacopo Fritz
Universiteit Gent
Sterrenkundig Observatorium

Dr. Mina Koleva
Universiteit Gent
Sterrenkundig Observatorium

Acknowledgements

Since I will definitely forget to thank a lot of people on this small page of text, I want to start by thanking everybody who helped me over the last three years and has contributed (directly or indirectly) to the writing of this PhD thesis.

First of all, I want to thank my supervisor, Maarten Baes, for giving me the opportunity to start a career in astronomy. Besides the interesting science topics I was allowed to work on, I'm grateful for the many conferences and workshops I could attend and observing sites I could visit. Furthermore, I would like to thank all people working at the astronomy department in Ghent for the pleasant collaboration. In particular, I would like to thank Jacopo Fritz for learning me the skills to work with a lot of astronomical software and for the interesting science discussions. Furthermore, I'm grateful to Gianfranco Gentile and Maarten Baes for reading the long list of proposals I have produced over the last three years and for providing useful feedback on them. I also cared a lot about the enjoyable talks and coffee-breaks with all the people in the department whenever science was making our heads explode. And of course, I can not forget to thank Gerbrand and Inge, who have made the technical and administrative life at the University here a lot more comfortable.

Thanks to the international character of most projects related to this PhD research, I was given the opportunity to collaborate with a lot of interesting astronomers and learn from their expertise in the field. Some special words of thanks are reserved for George Bendo, Luca Cortese, Suzanne Madden, Jon Davies, Marco Grossi, Christine Wilson and many others for interesting discussions and their contribution to many of my science projects. Although all conferences and workshops I have attended were interesting on their own, I especially always looked forward to the half-yearly meetings of the Herschel Virgo Cluster Survey consortium. Those meetings were memorable for their carefully selected venues (Ghent, Cardiff, Lisbon, Athens, Paris), the exploration of the local cuisine and the pleasant reunion with a bunch of friends, rather than astronomy colleagues.

With the last three years often having been hectic and stressful, especially during the last few busy months, I want to thank my family and friends for their patience. I'm also grateful for their support and understanding for this passion in astronomy, even though the exact contents of my research was not always comprehensible to them. I especially want to thank my boyfriend Bart for his patience whenever I had to work long hours or go abroad for observations and conferences and just for being there for me during the last years. I also want to give a special thanks to my parents, who are always there for me to help, support and encourage me. I still love to go home and spend some time at my parents place for some chatting with my mother or a jogging/biking trip with my father. I also want to thank my grandfather for the pleasant trips to watch my favorite local football team and nice talks on sports in general.

I want to thank my friends in Hamme and surroundings for the regular reunions during the week-ends for entertaining talks. Also the weekly lunches with my former colleagues in mathematics are always inspiring and pleasant. In particular, the birthday lunches with delicious home-made pies and cakes are very much appreciated.

Contents

List of Figures **iv**

List of Tables **vi**

1 Introduction: the interstellar medium **1**

1.1 Constituents of the ISM 2

1.1.1 Introduction 2

1.1.2 The gas component 3

1.1.3 The dust component 6

1.1.4 Cosmic rays 8

1.2 The interplay between stars, gas and dust in the ISM 10

1.2.1 Heating and cooling mechanisms of dust 10

1.2.2 Heating and cooling mechanisms of gas 12

1.3 Study of the ISM properties from infrared observations. 16

1.3.1 The Herschel Space Observatory 16

1.3.2 The Herschel Virgo Cluster Survey 19

1.3.3 The Herschel Reference Survey 20

1.3.4 The Very Nearby Galaxy Survey 22

1.4 Goals of this PhD thesis 24

1.4.1 The [CII] line as a star formation rate diagnostic 24

1.4.2 Interstellar dust in cluster dwarf elliptical galaxies 25

1.4.3 NGC 205 and its missing ISM mass problem 26

1.4.4 The dust energy balance in M104 and NGC 4565 27

2 The [CII] spectral line: a SFR diagnostic **31**

2.1 Ambiguity about origin of [CII] emission in a galaxy 32

2.1.1 Diffuse ISM 33

2.1.2 PDR 34

2.1.3 HII regions 34

2.2 Investigating the reliability of [CII] as a SFR tracer 35

2.2.1 Sample selection 35

2.2.2 Reference SFR tracer 43
2.2.3 [CII]-SFR correlation 49
2.2.4 Applicability of the relation 51
2.2.5 Nature of the [CII] emission in galaxies 53

3 Dust in cluster dwarf elliptical galaxies 60
3.1 First detection of dust in cluster dwarf ellipticals 61
3.1.1 Virgo Cluster 61
3.1.2 Sample selection 61
3.1.3 First detection of dust in cluster dEs 62
3.1.4 Credibility of detection 63
3.1.5 Properties of detected dEs 64
3.1.6 Stacking analysis of non-detections 65
3.1.7 Detection rate 67
3.2 Transition-type dwarf galaxies in Virgo 69
3.2.1 Transition-type galaxies: definition and selection 69
3.2.2 Herschel detections 74
3.2.3 Properties of Herschel-detected transition-type galaxies. 80

4 NGC 205: missing ISM mass problem 86
4.1 Theoretical gas mass predictions 87
4.2 Observations of the ISM content 89
4.3 Herschel dust continuum observations 91
4.3.1 Data reduction 91
4.3.2 Structure of the ISM in NGC 205 93
4.3.3 Consistency of Herschel fluxes with previous observations 95
4.3.4 Dust masses 97
4.3.5 Cold dust component? 99
4.4 Molecular gas mass: new results 103
4.4.1 JCMT CO(3-2) 103
4.4.2 PACS spectroscopy: [CII], [OI], [OIII] 104
4.5 Missing ISM mass problem: revisited 109
4.6 Inaccurate theoretical models or gas removal? 111
4.6.1 Non-standard conditions 111
4.6.2 Gas removal 111
4.7 Other dwarf galaxies with missing ISM problem 115

5 Sombrero Galaxy (M104, NGC 4594) 116
5.1 Worth knowing about Sombrero 117

5.2 Multi-wavelength dataset 119
5.2.1 Optical data 119
5.2.2 Infrared+submm data 119
5.3 Dust energy balance study 121
5.3.1 Model I: standard model 121
5.3.2 Model II: model with embedded star formation 125
5.3.3 Model III: model with embedded star formation + clumpy dust component 128
5.4 Comparison to other dust energy balance studies 130

6 Needle Galaxy (NGC4565) 137
6.1 Worth knowing about the Needle galaxy 138
6.2 Multi-wavelength dataset 142
6.2.1 Herschel data (250-500 micron) 142
6.2.2 Spitzer data (3.6-160 micron) 145
6.2.3 Other infrared/(sub)millimeter data 149
6.2.4 GALEX and optical data (0.15-0.89 micron) 150
6.3 Dust energy balance study 152
6.3.1 Model I: standard model 152
6.3.2 Model II: standard model with star formation 154
6.3.3 Model III: standard model with star formation and clumpy dust component 158
6.4 Comparison to other dust energy balance studies 162

7 Conclusions and future work 164

8 Nederlandse samenvatting 167

Bibliography 178

List of Figures

1.1 Schematic overview of the different ISM components and interactions . 3
1.2 Schematic overview of the PDR structure and chemistry 6
1.3 Schematic overview of the XDR structure and chemistry 7
1.4 Schematic overview of different PAH molecules 9
1.5 Schematic overview of the photoelectric heating mechanism 13
1.6 Schematic overview of the far-ultraviolet pumping mechanism 14
1.7 The Herschel Space Observatory 17
1.8 Maps of the Virgo Cluster with X-ray contours – with optically selected VCC galaxies – at SPIRE 250 micron 20
1.9 HRS sample of galaxies 21
1.10 VNGS sample of galaxies 23
1.11 The famous edge-on spiral galaxy NGC 891 28

2.1 Plot of $L_{24\mu m}$ versus $L_{[CII]}$ for the complete and reduced galaxy sample . 41
2.2 Plot of L_{TIR} versus $L_{[CII]}$ for the complete and reduced galaxy sample . 42
2.3 Plot of f_ν(60μm)-to-f_ν(100μm) versus $L_{\rm TIR}$ 43
2.4 Plot of $L_{\rm FUV,\,obs}$ / 6.31 $L_{24\mu\rm m}$ versus SFR 44
2.5 Threefold analysis of the SFR (24 μm) - C$^+$ correlation 56
2.6 Threefold analysis of the SFR (FUV+24 μm) - C$^+$ correlation 57
2.7 Plot of $L_{[CII]}$ versus SFR for different subsamples 58
2.8 Comparison of different SFR - $L_{[CII]}$ calibrations 58
2.9 Plot of $L_{\rm [CII]}$-to-$L_{\rm FIR}$ versus f_ν(60μm)-to-f_ν(100μm) ratio 59

3.1 VCC 781 and VCC 951: g, g-i colour, MIPS 24 μm and SPIRE 250 μm images 63
3.2 Grey body fit for VCC 781 66
3.3 Plot of the FUV-H colour versus L_H 70
3.4 Transition-type galaxies: position within the Virgo cluster 75
3.5 Transition-type galaxies: overview of data 80
3.6 Transition-type galaxies: plot of M_d versus L_H 84
3.7 Transition-type galaxies: histogram of heliocentric velocities 85

4.1 Herschel dust continuum maps of NGC 205 94
4.2 Gas and dust observations of NGC 205 95
4.3 Pixel-by-pixel maps of the dust temperature and mass in NGC 205 . . . 98
4.4 Fit of the global spectral energy distribution (SED) in NGC 205 101
4.5 Optical and far-infrared view of NGC 205 with PACS AOR overlays . . . 104
4.6 PACS spectroscopic C^+ line map of NGC 205. 106
4.7 PACS spectroscopic C^+ and OI line plots in NGC 205 107

5.1 HST image of the Sombrero galaxy 118
5.2 Model 1: observed and modelled SED + minor-axis extinction profiles . 131
5.3 Model 1: observed and modelled optical and infrared data 132
5.4 Model 2: observed and modelled SED + minor-axis extinction profiles . 133
5.5 Model 2: observed and modelled NUV and 24 μm major-axis profiles . . 134
5.6 Model 2: observed and modelled optical and infrared data 135
5.7 Spectral energy distribution for a Sombrero model with quiescent dust clumps 136

6.1 Optical image of the Needle galaxy 139
6.2 The observed stellar and dust emission from NGC 4565 146
6.3 Major-axis profiles of the dust emission and gas column density 147
6.4 Model 1: the observed and modelled g band image 154
6.5 Model 1: the observed and modelled SED 155
6.6 Model 2: observed and modelled NUV/MIPS 24 μm major axis profiles 159
6.7 Model 2: observed and modelled UV/optical constraints 160
6.8 Model 2: the observed and modelled SED 161

8.1 Elektromagnetisch spectrum 169
8.2 Straling doorheen het elektromagnetische spectrum 170
8.3 Hubble Space Telescope: impressionante beelden 171
8.4 Correlatie tussen de stervorming en [CII] emissie 172
8.5 Optische en Herschel waarnemingen van VCC 781 en VCC 951 173
8.6 Herschel waarnemingen van NGC 205 174
8.7 M104 en NGC 4565 176

List of Tables

1.1 Ten most abundant elements in the Milky Way Galaxy 4
1.2 Herschel programs with UGent involvement 19

2.1 Properties for galaxies in our sample 38
2.2 Flux measurements for galaxies in our sample 39
2.3 Star formation rates for galaxies in our sample 49
2.4 SFR - $L_{[CII]}$ relation: slope and intercept of best-fitting line 50

3.1 Transition-type galaxies: general properties 71
3.2 Transition-type galaxies: gas and dust properties 77

4.1 Far-infrared/submm photometry for NGC 205. 96
4.2 Spectral energy distribution: results of fitting procedures 100
4.3 Herschel/PACS spectroscopy observations for NGC 205: 1σ noise levels 105
4.4 C^+ line measurements within different elliptical apertures 106

5.1 Overview of photometry measurements for the Sombrero galaxy 120
5.2 Stellar component in M104: details of the V band MGE fit 121
5.3 Stellar component in M104: details of the R_C band MGE fit 122
5.4 Dust component in M104: details of the Gaussian dust ring 124
5.5 Star formation rates estimates for M104 127

6.1 Overview of photometry rmeasurements for the Needle galaxy 143
6.2 Best fitting model parameters for NGC 4565 162

1

Introduction: the interstellar medium

1.1.1 Introduction

A galaxy is a collection of millions of stars, held together by a mutual gravitational interaction. Although stars dominate a galaxy's appearance at visual wavelengths, the majority of mass in a galaxy is attributed to dark matter, a component that does not interact with photons and therefore remains unseen in astronomical observations. Its composition, distribution and nature remain largely unknown and can only be analyzed indirectly (for example through the study of a galaxy's rotation curve).

In between the stars, the large volume in a galaxy is filled with the interstellar medium (ISM), which is composed of gas, dust and cosmic rays. The ISM provides the reservoir of gas and dust from which new stars are born and at the same time is the storage for leftovers from stars whose lives might have ended in violent supernova explosions. Depending on the temperature, density and state of ionization of matter, different phases of the ISM can be distinguished as a consequence of the complex interplay between the stars and the surrounding medium of gas and dust (see Tielens 2005, Kwok 2007 and Hollenbach & Tielens 1999 for more information on the physics and chemistry of the ISM).

Originally, the ISM was considered to be composed of two phases. Based on calculations for the thermal stability of the ISM taking into consideration cosmic ray heating and cooling through excitation of H, He and C^+, Field, Goldsmith & Habing (1969) could identify a cold ($T < 100\,\mathrm{K}$) and dense ($n \sim 30\,\mathrm{cm}^{-3}$) ISM component and a warm ($T \sim 10^4$ K) and diffuse ($n \sim 0.3$ cm^{-3}) ISM phase. The latter component is composed of the warm neutral medium (WNM) and warm ionized region (WIM), while the cold phase only consists of the cold neutral medium (CNM). Through studies of the outcome of supernova explosions on the ISM, McKee & Ostriker (1977) could soon identify a third phase: a low-density ($\sim 10^{-2.5}$ cm^{-3}), hot ($T \sim 10^6$ K) intercloud medium (HIM). With this hot, diffuse ISM phase dominating the ISM in volume, McKee & Ostriker (1977) furthermore showed that the shock waves from supernovae propagating through the HIM also shape the overall morphology of the ISM and induce the turbulent nature of the ISM. Within each of these phases a thermal pressure equilibrium is established. But the ISM also consists of small cores, where the thermal pressure exceeds the average value in the ISM (e.g. HII regions, gravitationally bound molecular clouds). The pressure in those cores typically rises to overcome gravity, which makes the cores no longer in equilibrium and eventually collapse to form stars.

In order to gain insight into the different phases of the ISM, one needs to understand

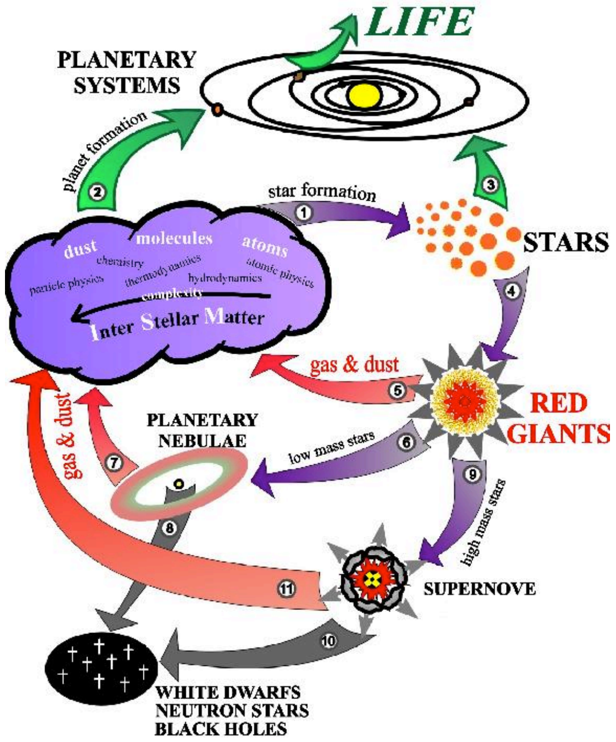

Figure 1.1: Schematic overview of the different ISM components and how each one of them interacts with the stars in galaxies and the other ISM constituents (adopted from Cycle Of Matter).

the properties of its components (gas, dust and cosmic rays) (see Sections 1.1.2, 1.1.3 and 1.1.4) and the influence of interactions between those different components on the structure, chemistry and thermal balance of the ISM (see Section 1.2). Figure 1.1 gives a schematic overview of those different ISM components and interactions.

1.1.2 The gas component

The most abundant element in the Universe is hydrogen with a mass contribution of about 74%. Hydrogen can be found either in the atomic (H I), molecular (H_2) or ionized (H II) phase. Helium (He) is the second most abundant element, accounting for roughly 24% of the total baryonic mass in the Universe. The remaining fraction of the baryonic matter, some 2%, consists of heavier elements, of which oxygen and carbon are the most important contributors (with abundances of only $\sim 3 \times 10^{-4}$ and $\sim 1.4 \times 10^{-4}$ relative to hydrogen). Whereas hydrogen, helium, and small traces of lithium, beryllium and boron formed in the earliest phases of the Universe, all heavier elements are produced as a result of stellar nucleosynthesis. Due to this dependence on stellar evolution, the abundance of elements roughly decreases with increasing atomic number (see Table 1.1).

Z	Element	Mass fraction (per million particles)
1	Hydrogen	739,000
2	Helium	240,000
8	Oxygen	10,400
6	Carbon	4,600
10	Neon	1,340
26	Iron	1,090
7	Nitrogen	960
14	Silicon	650
12	Magnesium	580
16	Sulfur	440

Table 1.1: Ten most abundant elements in the Milky Way Galaxy obtained from spectroscopic measurements. For each element, the atomic number and mass fraction per million particles are presented.

Atomic hydrogen is the dominant cold gas component in most late-type galaxies and therefore often used to trace the overall gas content. In early-type galaxies, a significant fraction of the gaseous component might be locked in hot X-ray emitting gas halos. Due to a small difference in energy between hydrogen atoms with a parallel or anti-parallel spin, the HI content in a galaxy can be easily quantified by looking at the hydrogen 21 cm hyperfine transition. Although the decay half-life for this transition is about 1.1×10^7 years, the vast amount of HI gas in galaxies makes this emission feature observable at a quantified wavelength of 21 cm.

Molecular hydrogen (H_2) is formed in the ISM on the surfaces of interstellar dust grains (Hollenbach & Salpeter, 1971a; Hollenbach, Werner & Salpeter, 1971b). The molecular gas component is an important ISM constituent in galaxies since it provides the building material for the formation of new stars. Since molecular hydrogen molecules do not have a dipole moment, the emission from H_2 molecules can only be recorded through transitions in their vibrational state in near- and mid-infrared wavebands or from heavily obscured absorption features in the ultraviolet. The lack of rotational transitions for H_2 molecules hamper probing the cold molecular gas component in galaxies. Alternatively, the cold molecular gas phase is often traced through CO emission, which is produced through collisional excitation by H_2 molecules. Typically the first rotational transition CO(1-0) is used, but also higher order rotational transitions are helpful tracers. From CO observations, the molecular gas component is found to be predominantly clumped together in clouds of varying size (diameter $\sim$ 10-100 pc) and masses ($M_{H_2} \sim 10\text{-}10^6\ M_\odot$).

The uncertainty in the CO-to-H_2 conversion (the so-called X_{CO} factor) complicates the determination of the molecular gas mass in a galaxy. Indeed, the value of the X_{CO} factor has been shown to depend on the metallicity (e.g. Wilson 1995; Bolatto et al. 2008) and the density (e.g. Shetty et al. 2011) of gas and might be affected by the optical thickness of CO. Therefore, CO line measurements are often complemented or superseded by observations of other molecular and ionic line transitions (emitted predominantly in far-infrared, submillimeter and millimeter wavebands). Studying the molecular gas component in a galaxy through line emission from such molecules and ions provides valuable information on the physical properties of the ISM. With the youngest stars in galaxies and most active galactic nuclei often enshrouded by compact clouds of gas and dust, line diagnostics offer valuable insight into those heavily-obscured star formation regions and AGNs. Modelling the multi-wavelength line emission spectrum enables furthermore to gain information on the complex ISM chemistry, density and temperature of gas, dust temperature, cosmic-ray ionization as well as shape and strength of the radiation field in a galaxy.

Besides neutral atomic and molecular hydrogen components, part of the hydrogen atoms are ionized by the hard radiation of far-ultraviolet sources ($h\nu > 13.6$ eV). When those free electrons recombine with protons, the absorbed energy is re-emitted in hydrogen recombination lines. Since only hot, luminous and short-lived O and B-type stars provide photons strong enough for the ionization of hydrogen atoms, H II regions are interesting sites to study recent star formation in galaxies.

On the boundary of those H II regions, we find neutral regions where the chemistry and structure is dominated by ultraviolet radiation from young stars residing in the H II regions. In those photo-dissociation regions (PDRs, often also called Photon Dominated Regions, e.g. Crawford et al. 1985; Tielens & Hollenbach 1985; Wolfire, Tielens & Hollenbach 1989; Hollenbach, Takahashi & Tielens 1991; Stacey et al. 1991; Bakes & Tielens 1998), the UV radiation from young stars (6-13.6 eV) is sufficient to photo-dissociate H_2, but the ionization fraction too low to globally overcome the recombination rate of hydrogen atoms. For increasing distance from the surface of those H II regions, the incident UV flux decreases due to multiple attenuation processes, implying that most hydrogen atoms are bound in H_2. PDRs form the interface between the ionized H II regions and the molecular clouds in galaxies. The part of the PDR closer to the H II region is often referred to as the ionization front, with the dissociation front defining the area adjacent to the molecular clouds. Figure 1.2 gives a schematic overview of the PDR structure, and the different chemical species emerging in different areas of the PDR depending on the intensity of the incident UV flux.

With UV radiation (6-13.6 eV) from young stars regulating the chemistry in PDRs, X-ray dissociation regions (XDRs, e.g. Lepp & Dalgarno 1996; Maloney, Hollenbach & Tielens 1996) can be thought of as the analogues of neutral PDRs, but dominated by

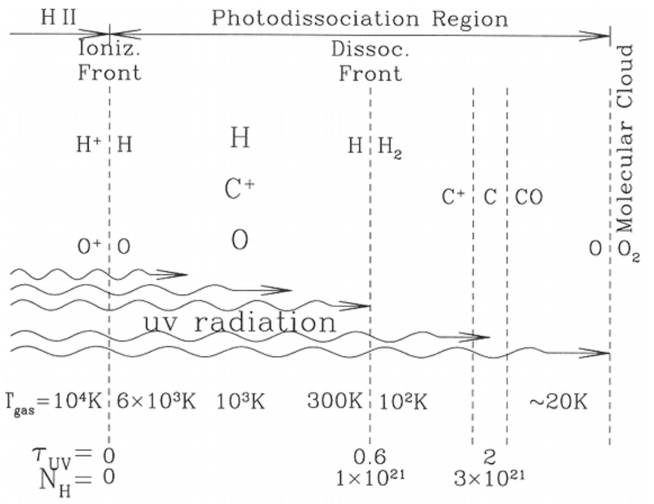

Figure 1.2: Schematic overview of the PDR structure with the gas temperatures and chemical species emerging at increasing distance from the HII regions (adopted from Draine 2011).

incident X-ray radiation. Most of the XDRs are found in the X-ray emitting regions in the surroundings of gas accreting massive black holes. However, X-ray emission in galaxies is also known to originate from supernova remnants, hot and massive stars, X-ray active chromospheres, X-ray binaries, etc. The X-ray chemistry in XDRs after the absorption of a X-ray photon involves different levels of energy flows and heating, which are summarized in the schematic overview of Figure 1.3.

1.1.3 The dust component

Dust particles in a galaxy are thought to represent only 1% of the ISM mass. Although those dust grains only make up a small part of the ISM, they play an important role in several astrophysical processes in a galaxy. They regulate the heating of gas in the ISM through photoelectric heating and inelastic interactions with gas particles. Dust particles furthermore act as a catalyst in the formation of molecular hydrogen, the birth material for the production of young stars. Due to the formation of molecular hydrogen on the surfaces of dust particles, dust is abundantly present in molecular clouds. Those dust grains provide the shelter for the formation of a variety of molecules, which would otherwise be dissociated through the strong emission from energetic photons. The often irregular shape and large size of dust grains compared to hydrogen atoms offer an extra shield for atoms to congregate and combine. Due to shielding of molecules and ions from the hard radiation from young stars by dust, the gas is able to cool through the emission of far-infrared fine-structure and molecular rotational lines. This process of cooling allows the gas in a galaxy to eventually condense into stars. Dust particles also distort our view on the stars populating a galaxy due to the extinction

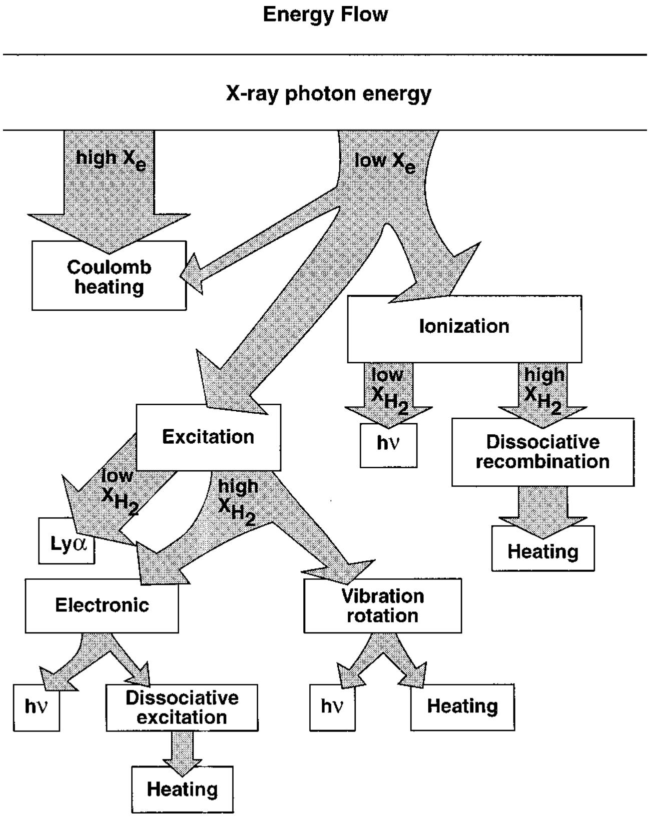

Figure 1.3: Schematic overview of the XDR structure with the different energy flows and heating mechanisms (adopted from Maloney, Hollenbach & Tielens 1996).

of stellar photons. A profound knowledge of the dust properties in a galaxy is thus important to understand galaxy evolution processes such as star formation and determine the specific amount of stellar photons reprocessed by dust particles.

The formation of dust grains is thought to occur predominantly in the stellar atmospheres of oxygen and carbon-rich AGB stars. Through the radiation pressure of those stars, they are ejected into the ISM. Dust grains have been shown to also form in the circumstellar envelopes of novae, supernovae and Wolf-Rayet stars. The solid grains produced in those circumstellar environments are affected by interstellar UV radiation, cosmic rays and shocks once they are injected into the ISM. The outcome of those ISM interactions is still poorly known, with interstellar UV radiation, cosmic rays and shocks considered capable of destroying a fraction of the newly formed dust grains.

The dust component in galaxies is in general composed of amorphous/graphitic carbonaceous grains, amorphous silicates and polycyclic aromatic hydrocarbons (PAHs). Silicates are thought to form predominantly in O-rich stars, whereas carbonaceous matter grows in more C-rich environments. The formation of those dust grains occurs in different steps. In a first step, a seed for condensation needs to be formed (e.g. Al_2O_3, TiO_2). During a second step, the accretion of atoms and molecules (e.g. O, Mg, Al, Si, Fe, OH, H_2O, O_2, etc.) results in the formation of composite grain mantles such as SiO_2, Al_2O_3, etc. Those grain mantles form the basis for the further grain growth and development of molecular species with diverse compositions and complexities. Besides the three major components (carbonaceous grains, amorphous silicates and PAHs), other forms of dust (e.g. SiC, Treffers & Cohen 1974) and ices (in particular water ice) are suggested to be present in particular ISM environments (e.g. ices are found typically in the cold cores deep inside molecular clouds).

Polycyclic aromatic hydrocarbons (PAHs) are considered to be the tiniest dust grains and form some intermediate state between dust grains and large molecules. They consist of planar benzene rings of linked sp^2-hybridized C atoms, with H atoms or other groups saturating the outer bonds of peripheral C atoms (see Figure 1.4). Depending on whether some C atoms belong to three rings or at most two rings, the PAH molecules are subdivided in compact and non-compact PAH classes, respectively. As a result of bending and stretching modes of these large aromatic molecules (Bauschlicher, Peeters & Allamandola, 2009), strong PAH emission features characterize mid-infrared wavebands. The PAH emission in those mid-infrared wavebands is complex due to the particular shape, size and ionization-charge of the large molecular species and difficult to realistically incorporate into dust models. Therefore, either PAH templates (e.g. Desert, Boulanger & Puget 1990) or the modelling of physical processes in a similar way as done for small dust grains (e.g. Weingartner & Draine 2001; Draine & Li 2007) are commonly used in dust models. Whereas large dust grains are assumed to attain a certain common equilibrium temperature, small grains ($a \leqslant 100$ Å) are stochastically heated, i.e. the heating of small dust grains is characterized by a temperature distribution function rather than a simple equilibrium temperature. Due to the smaller grain sizes, absorption processes indeed occur less frequently, which allows significant cooling in between photon impacts.

1.1.4 Cosmic rays

Cosmic rays (CRs) are energetic charged particles, which are composed of subatomic particles, such as protons (90%), helium nuclei (9%, also called alpha particles) and electrons or other elements (1%). Most of the elements are present in cosmic rays, with roughly the same mass abundance as in the solar neighborhood. Studying differences in elemental abundances in cosmic rays as well as the occurrence of very rare elements and isotopes provides insight into the origin of cosmic rays. Most of the cosmic rays originate from supernova remnants, where they are accelerated in the blast waves of

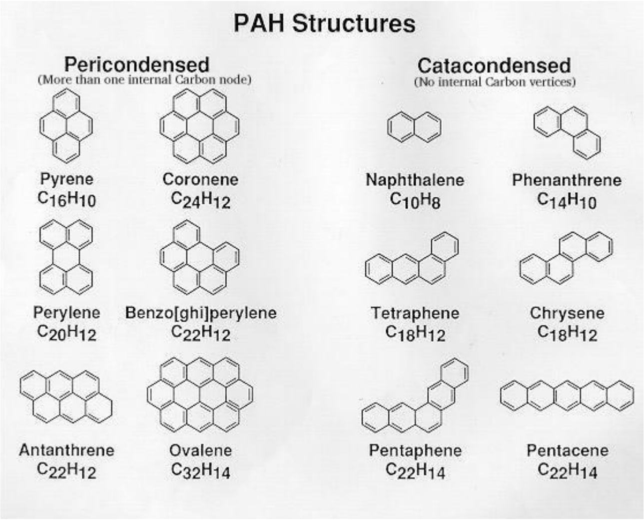

Figure 1.4: Schematic overview of different PAH molecules (adopted from Salama 1999).

expelled material after the explosion. With the remnants of violent supernovae lasting several thousands of years, the expanding shell of material provides the excellent environment for the acceleration of cosmic rays in the associated magnetic fields. With energies of $\sim 10^{20}$ eV, cosmic rays are often the onset for chemical reactions and the formation of unstable isophotes in the ISM. Owing to their high energies, cosmic rays also contribute to the heating of gas in galaxies (see Section 1.2.2). When cosmic rays have gained enough energy to overcome the gravitational potential of the galaxy, the particles can escape into the intergalactic medium. Since cosmic rays eventually escape from supernova remnants in galaxies, the particles can only attain a certain maximum energy level, depending on the strength and size of the magnetic field. Nevertheless, cosmic rays have been observed with velocities higher than capable of generating in supernova remnants. The origin of those high-energy cosmic rays is still unclear and remains difficult to comprehend as a consequence of the magnetic fields in our own Milky Way and other galaxies, bending the CR trajectory and, thus, erasing all information on the direction of the incoming cosmic rays.

1.2 The interplay between stars, gas and dust in the ISM

Most physical processes in the ISM of galaxies are connected to interactions with far-ultraviolet photons, originating mainly from young, massive stars in galaxies. In the following paragraphs, we discuss the importance of those ISM interactions in reprocessing stellar light through radiative transfer processes and in regulating the thermal balance through the heating and cooling of gas in galaxies (see also Hollenbach & Tielens 1999).

1.2.1 Heating and cooling mechanisms of dust

Dust grains are primarily heated through the absorption of stellar photons. To remain in thermal equilibrium with the surrounding medium, dust grains re-emit the absorbed energy at infrared and (sub)millimeter wavelengths.

The radiative transfer equation describes the interaction between stellar photons and material in the interstellar medium. In the most simple form, the change of the stellar intensity through interaction with atoms and/or molecules in the ISM can be calculated using the radiative transfer equation, of which the general form reads

$$\frac{\mathrm{d}I_\lambda}{\mathrm{d}s} = -\kappa_\lambda\,\rho\,I_\lambda + j_\lambda \tag{1.1}$$

In this equation j_λ is the emission coefficient, κ_λ is the absorption coefficient, ρ is the density of the ISM material and I_λ is the specific intensity of the radiation field. Written in this general form, the radiative transfer equation seems a simple first-order differential equation that can be solved immediately. This form is somewhat misleading though, as the source and sink terms can depend in a non-linear way on the intensity.

When we consider specifically the transfer of radiation through a dusty ISM, the radiative transfer equation becomes a complicated partial integro-differential equation where all directions and wavelengths are coupled. The primary source term in the ISM of a galaxy is the emission j_λ that arises from stellar radiation. Two physical processes will act as sinks in dust radiative transfer, in such a way that cosmic dust prevents the photons from continuing their journey through the interstellar medium along the same path. As a first obstacle, photons can be absorbed by a dust grain, which converts the absorbed energy into internal energy that finally heats the dust grain. The stellar radiation that is absorbed by dust grains will be re-emitted at infrared wavelengths. Rather than absorbing the incoming radiation, photons can be scattered by dust grains as well, i.e. the direction of propagation of a photon is changed through the interaction with a dust particle. Scattering of light by dust grains is nothing more than the redirection of a propagating photon from one direction into another. Although scattering of stellar photons by dust grains will take away stellar light on its path to the observer along the line-of-sight, a fraction of photons will be redirected in the direction towards the observer.

Taking into account all these different source and sink terms, the radiative transfer equation becomes

$$\begin{aligned}\frac{\mathrm{d}I_\lambda}{\mathrm{d}s}(\boldsymbol{x},\boldsymbol{n}) &= j_\lambda(\boldsymbol{x}) - (\kappa_\lambda^{\text{abs}} + \kappa_\lambda^{\text{sca}})\,\rho(\boldsymbol{x})\,I_\lambda(\boldsymbol{x},\boldsymbol{n}) \\ &\quad + \kappa_\lambda^{\text{sca}}\,\rho(\boldsymbol{x})\int_{4\pi} I_\lambda(\boldsymbol{x},\boldsymbol{n}')\,\Phi_\lambda(\boldsymbol{n},\boldsymbol{n}')\,\mathrm{d}\Omega' + \kappa_\lambda^{\text{abs}}\,\rho(\boldsymbol{x})\,B_\lambda(T(\boldsymbol{x}))\end{aligned} \tag{1.2}$$

In this equation, $\kappa_\lambda^{\text{abs}}$ and $\kappa_\lambda^{\text{sca}}$ represent the absorption and scattering coefficients, respectively. The phase function $\Phi_\lambda(\boldsymbol{n},\boldsymbol{n}')$ describes the probability that a photon incident from a direction $\boldsymbol{n}'$ will be scattered into a unit solid angle about the direction $\boldsymbol{n}$ and is normalized such that

$$\int_{4\pi} \Phi(\boldsymbol{n},\boldsymbol{n}')\mathrm{d}\Omega' = 1 \tag{1.3}$$

In radiative transfer calculations, the Henyey-Greenstein phase function is often used to describe the directivity of the scattered photons

$$\Phi_\lambda(\cos\alpha) = \frac{1-g_\lambda^2}{4\pi}\,\frac{1}{(1+g_\lambda^2-g_\lambda\cos\alpha)^{3/2}} \tag{1.4}$$

where α is the scattering angle between the incoming and outgoing propagation directions and g_λ is the anisotropy parameter of the phase function,

$$g_\lambda = \frac{1}{4\pi}\int_{4\pi} \Phi_\lambda(\cos\alpha)\cos\alpha\,\mathrm{d}\Omega \tag{1.5}$$

To have a complete description of scattering, one requires a value for g_λ at all wavelengths, depending on the chemical composition, size and shape of the dust grains. Interestingly, the phase function does not have a theoretical physical background, but was derived empirically from a study of the scattering of light in reflection nebulae in the Galaxy.

The last term in expression (1.2) represents the thermal re-emission of dust grains, with $B_\lambda(T)$ describing the Planck function at a temperature T. When a photon is absorbed by a dust grain, the photon energy is used to enhance the internal energy of the dust particle and increase its dust temperature. For large grains, the assumption of local thermal equilibrium is typically valid, i.e. dust grains will tend to emit the absorbed energy to remain in balance with the heating provided by the ambient radiation field. Dust particles will attain an equilibrium temperature T which is determined from the assumption that the dust grain absorbs and re-emits an equal amount of photon energy. Since the equilibrium temperature differs for a grain type with a particular composition, size and shape and depends on the absorbed energy from all directions and at all wavelengths, the equilibrium temperature is determined by solving the balance equation

$$\int_0^\infty \mathrm{d}\lambda \int_{4\pi} \kappa_\lambda^{\mathrm{abs}} \rho(\boldsymbol{x})\, I_\lambda(\boldsymbol{x}, \boldsymbol{n})\, \mathrm{d}\Omega = \int_0^\infty \mathrm{d}\lambda \int_{4\pi} \kappa_\lambda^{\mathrm{abs}} \rho(\boldsymbol{x})\, B_\lambda(T(\boldsymbol{x}))\, \mathrm{d}\Omega \tag{1.6}$$

or

$$\int_0^\infty \kappa_\lambda^{\mathrm{abs}} J_\lambda(\boldsymbol{x})\, \mathrm{d}\lambda = \int_0^\infty \kappa_\lambda^{\mathrm{abs}} B_\lambda(T(\boldsymbol{x}))\, \mathrm{d}\lambda \tag{1.7}$$

with J_λ the mean radiation field. For typical values of the optical properties of dust grains and the strength of the radiation field in the ISM of galaxies, solving this equation yield dust equilibrium temperatures of the order of 15 to 30 K. Dust hence clearly transforms UV/optical radiation to FIR/submm radiation.

The approximation of local thermal equilibrium is typically only valid for large dust grains, whereas smaller dust particles and PAHs are transiently heated to temperatures deviating from this equilibrium temperature (see Section 1.1.3). Indeed, the balance between heating and self-cooling requires that the absorbed photon energy is distributed efficiently throughout the dust grain. This assumption is not valid for small dust grains for which the energy of absorbed photons exceed the internal heat energy due to lattice vibrations. Therefore, the grain temperature is capable of rising sharply when absorbing a single photon, after which the grain temperature falls back to a smaller value. This large variation in temperature on short time scales characterizes a fluctuating grain temperature of very small grains in time, rather than the constant equilibrium temperature approximation for large dust particles. Very small grains are capable of radiating intensely at mid-infrared temperatures when attaining high enough temperatures.

1.2.2 Heating and cooling mechanisms of gas

In general, the heating of gas in a galaxy is dominated by two processes, both indirectly related to the far-ultraviolet emission of young stars.

A first important gas heating mechanism is the photoelectric effect on large molecules and small dust grains. This photoelectric effect refers to a photo-ionization process from photons on dust grains, for which the excess kinetic energy of the ejected photoelectron is used to collisionally excite and, thus, thermally heat the gas. This pho-

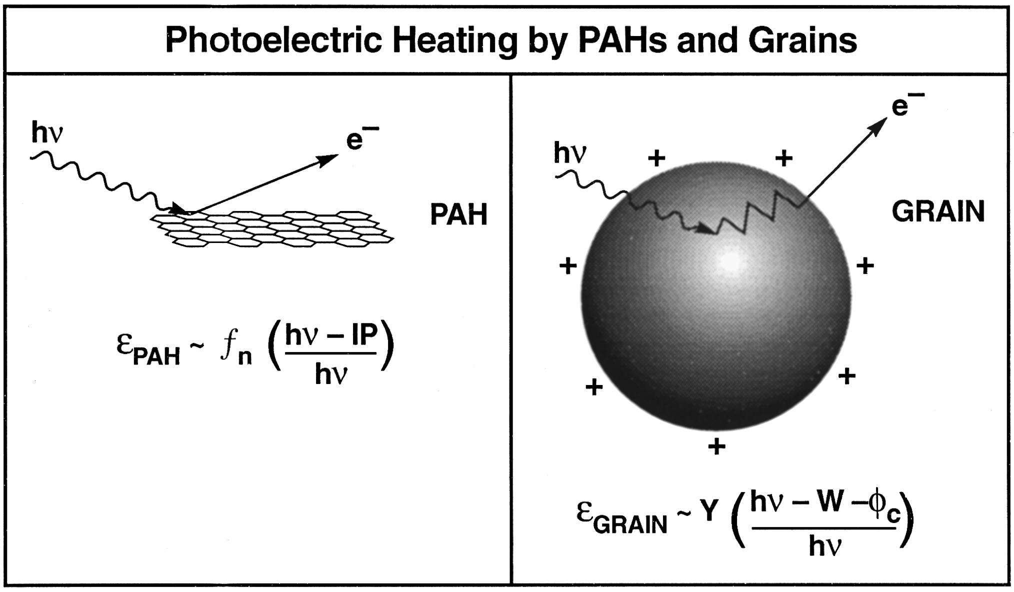

Figure 1.5: Schematic overview of the photoelectric heating mechanism (adopted from Figure 13 in Hollenbach & Tielens 1999).

toelectric heating process is dominated by very small grains and PAHs (Verstraete et al., 1990; Bakes & Tielens, 1994). When those interstellar grains absorb a far-ultraviolet photon, energetic electrons are created and diffused in the grain. When reaching the grain surface, those electrons may overcome the binding energy of the grain, i.e. the work function W of the grain and a possible Coulomb potential ϕ_C when the grain is charged. Successful electrons are then released into the gas component of the ISM with an excess kinetic energy (see Figure 1.5 for a schematic overview of the process of photoelectric heating). The efficiency $\epsilon_{\mathrm{grain}}$ of this photoelectric effect is given by the ratio of the gas heating rate to the far-ultraviolet absorption rate of the grain and expressed as

$$\epsilon_{\mathrm{grain}} \simeq Y \left(\frac{h\nu - W - \phi_C}{h\nu} \right) \tag{1.8}$$

where Y is the electron escape probability (also called yield) and the term between brackets represents the fraction of the photon energy carried away as kinetic energy by the electron. The large uncertainty factor is the yield factor, which is a complex function of the grain size a, the photon energy $h\nu$, the collision scale length l_e ($\simeq 10$ Å) for low-energy electrons in solids, and the far-ultraviolet absorption scale length l_a ($\simeq$ 100 Å) inside a grain (Watson, 1972; Draine, 1978; Bakes & Tielens, 1994).

Another indirect thermal coupling of gas and penetrating far-ultraviolet photons occurs through pumping of H_2 molecules to a bound excited electronic state. While at low densities, vibrationally excited H_2 molecules decay to the ground level through the emission of infrared photons, collisions with atomic H can become an important

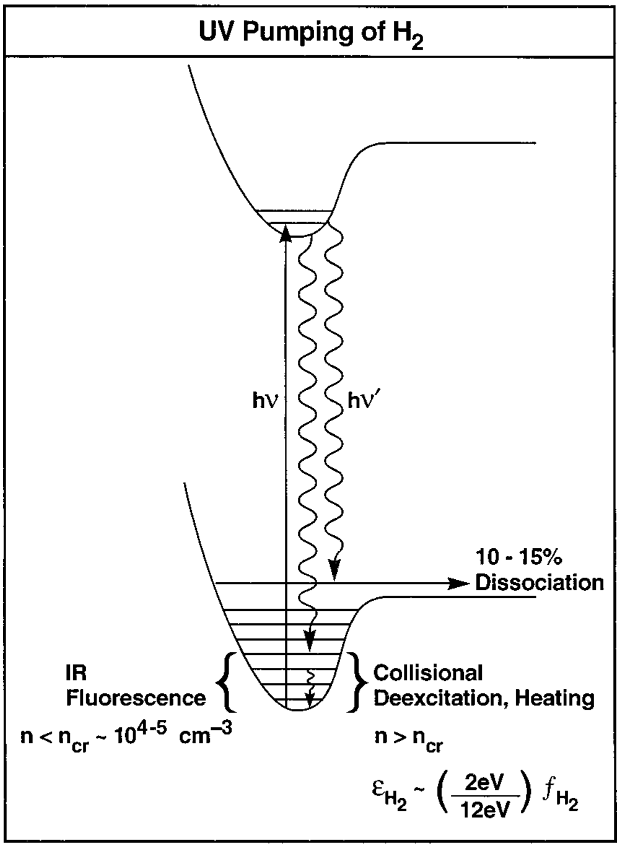

Figure 1.6: Schematic overview of the far-ultraviolet pumping of H_2 mechanism, subsequent collisional de-excitation of H_2 and gas heating processes (adopted from Figure 8 in Hollenbach & Tielens 1999).

excitation mechanism at high densities (n $\geqslant 10^{4-5}$ cm^{-3}). The efficiency of this heating process depends on the fraction of far-ultraviolet photons flux pumping H_2, f_{H_2}, rather than being absorbed by dust grains, and the temperature of the gas (Martin & Mandy, 1995; Martin, Schwarz & Mandy, 1996). For $G_0/n \leqslant 4 \times 10^{-2}$ cm^3 (G_0 represents the incident far-ultraviolet flux between 6 eV $\leqslant h\nu \leqslant$ 13.6 eV in units of 1.6×10^{-3} erg cm^{-2} s^{-1}, Habing 1968) and $f_{H_2} \sim 0.25$, the dust opacity decreases, implying that the gas heating through far-ultraviolet pumping of H_2 molecules becomes an efficient mechanism (see also Sternberg & Dalgarno 1989 and Burton, Hollenbach & Tielens 1990).

Besides these main heating mechanisms related to the far-ultraviolet emission originating from young stars, low-energy cosmic rays also contribute to the gas heating, through ionization and excitation processes. Owing to the high energy of cosmic rays, they are capable of penetrating deep into the molecular clouds, where they also charge particles through Coulomb interactions with free electrons. In the warm, diffuse medium or in the immediate surroundings of a supernova remnant, X-rays are responsible for the removal of electrons from atoms and ions. Those photoelectrons can in turn induce a secondary ionization and, in this manner, heat the gas. In the inner cores of giant molecular clouds and in supernova remnants, the temperature and density is sufficient to also heat the gas through collisions of gas atoms and molecules with dust grains. These three heating mechanisms (grain-gas collisions, cosmic ray and X-ray heating) are, however, negligible in most ISM environments, where the UV radiation is the dominant factor driving the gas heating.

With gas heated mainly through the photoelectric effect on PAHs and small dust grains and the pumping of H_2 molecules by far-ultraviolet photons, the gas needs to be cooled to balance the thermal equilibrium of the ISM. Gas cooling happens predominantly through the emission of far-infrared fine-structure and molecular rotational lines. The molecular line emission is dominated by rotational line transitions of CO. At the boundary of PDRs, the gas cooling occurs through the emission of far-infrared fine-structure lines. The cooling efficiency in particular regions of the ISM depends on the specific conditions of the ISM (i.e. the gas density and the incident far-ultraviolet radiation field). In most star-forming galaxies, the cooling is dominated by the [CII] and [OI] fine-structure lines. As soon as the gas temperature increases to about 5000 K, [FeII] (1.26, 1.64 μm), [OIII] (88 μm) and [SII] (67.3 μm) account for a significant fraction of the gas cooling (Burton, Hollenbach & Tielens, 1990). For high enough densities, cooling through collisions with cool dust grains might have an important share in gas cooling as well (Burke & Hollenbach, 1983). To relate the emission from far-infrared fine-structure lines and molecular rotational lines to the cooling efficiency in a galaxy, full radiative transfer calculations are needed to model the distribution and characteristics of different ISM phases.

1.3 Study of the ISM properties from infrared observations.

In the previous sections, the different ISM components were introduced and the interactions of the gaseous and dust components with stellar radiation discussed. In this PhD thesis, we aim to characterize specific properties of those ISM components and understand the physics behind their interaction processes. With the characteristic emission associated to the cold ISM material predominantly emerging at infrared, submillimeter and millimeter wavelengths, we analyze the properties of the ISM in galaxies through observations in those wavebands.

1.3.1 The Herschel Space Observatory

Until recently, observations of the ISM in galaxies were hampered by the poor resolution and limited wavelength coverage of infrared instrumentation. Previous generation far-infrared space satellites such as the Infrared Astronomical Satellite (IRAS, Neugebauer et al. 1984), the Infrared Space Observatory (ISO, Kessler et al. 1996, 2003), the Spitzer Space Telescope (Werner et al., 2004) and Akari (Murakami et al., 2007) only covered mid- and far-infrared wavelengths up to 200 μm. Ground-based submillimeter telescopes suffer severely from the opacity of the earth's atmosphere at the highest frequencies and are mainly operational from 850 μm onwards. Both restrictions imply that the spectral energy distribution of galaxies between 200 and 800 μm, where the emission from cold gas and dust dominates, is largely unexplored.

Recently, this large gap in wavelength coverage was bridged due to the launch of the Herschel Space Observatory (Pilbratt et al., 2010). Herschel, the fourth cornerstone of ESA's Cosmic Vision 2005-2015 program, was launched on the 14th of May 2009 on board an Ariane 5 ECA, together with the Planck satellite. After the launch of the Ariane 5 the telescopes detached and continued their own journey in space. Both the Herschel and Planck satellites travelled towards the second Lagrange point of the Sun-Earth system (L2) around which it orbits on a Lissajous trajectory. Since the L2 point is a relatively stable point, only little energy pulses are required to keep the telescopes in position. With a Cassegrain telescope of size 3.5m, the Herschel Space Observatory is the largest telescope ever launched into space (see Figure 1.7). With a wavelength coverage from 51 to 670 μm, Herschel is the first space mission covering a spectral range from the far-infrared to the submillimeter wavelength domain.

On board the Herschel satellite three instruments collect the radiation originating from the coldest material in the Universe. The Heterodyne Instrument for the Far-Infrared (HIFI, 480-1910 GHz, de Graauw et al. 2010) is a high-resolution heterodyne spectrometer performing spectral line observations with an unprecedented spectral resolu-

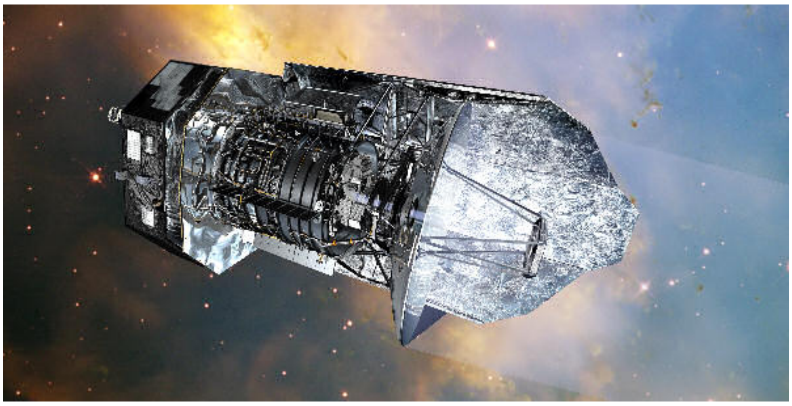

Figure 1.7: The Herschel Space Observatory.

tion (0.3-300 km/s) and an instantaneous bandwidth of 4 GHz. The Photometer Array Camera (PACS, 51-220 μm, Poglitsch et al. 2010) has a FIR imaging photometer composed of two filled bolometer arrays (64 × 32 for the blue channel and 32 × 16 for the red channel) and an integral field (grating) spectrometer. Also the Spectral and Photometer Imaging Receiver (SPIRE, 200-670 μm, Griffin et al. 2010) is optimized for both photometry and spectroscopy observations with a submillimeter imaging photometer and a Fourier Transform Spectrometer (FTS). Continuum observations with SPIRE photometers simultaneously probe the signal in three wavebands (250, 350 and 500 μm), whereas the PACS bolometers can observe simultaneously at 160 μm and at 70 or 100 μm.

Considering that the wavelength range covered by Herschel is dominated by emission from very cold objects, the instruments on board the satellite are very sensitive to radiation from the instrumental equipment. To keep the contaminating emission from the instrumentation to an absolute minimum the instruments are continuously cooled with superfluid helium to a temperature of about 2 K. Since the amount of cooling liquid on board Herschel that could be launched into space was limited and refilling of the helium tank is not an option, Herschel is condemned to have a limited lifetime of operation. Before launch an estimated lifetime of 3.5 years was predicted. The present best estimate of the remaining cryogen lifetime predicts that Herschel will be performing science observations until approximately February 2013.

Herschel is providing the astronomical community with a large inventory of observations at far-infrared and submm wavelengths. Many observing programs, both large-scale key programs and smaller-scale focused projects, are targeting different aspects of the cold ISM in galaxies. A complete list of the approved Herschel programs can be found on the website of the Herschel Science Centre (http://herschel.esac.esa.int). The UGent astronomy group is involved in several of these projects. The participation in many of those Guaranteed Time projects is thanks to the involvement of Belgium in the development of the spectrometer (IMEC, C.S. Liège) and the responsibility of operation and calibration of the instrument during the flight mission (K.U. Leuven). Owing to the large contribution of Belgian institutes (20 %) and Prof Dr. Christoffel Waelkens (K.U. Leuven) being the co-Principle Investigator of the PACS instrument, they were awarded with $\sim$ 400 hours of guaranteed time which was generously distributed among the different astronomical institutes in Belgium. The majority of the projects in which the University of Ghent is involved mainly aim to study the characteristics of the ISM in nearby galaxies. These projects can be broadly subdivided in three groups. The first set of project consists of large-scale "blind" surveys of regions of the sky. In this category, the Herschel Astrophysical Terahertz Large Area Survey (H-ATLAS), the largest open time key program done with Herschel, has surveyed 550 deg^2 of extragalactic sky with PACS and SPIRE. Smaller but deeper survey areas pointing towards the Virgo Cluster and Fornax Cluster have been observed as part of the Herschel Virgo Cluster Survey (HeViCS) and the Herschel Fornax Cluster Survey (HeFoCS), respectively. The second class of projects were the UGent group is involved in are studies of samples of galaxies aiming at a systematic study of the dust and gas distribution in different classes of nearby galaxies. The Herschel Reference Survey (HRS) and the Dwarf Galaxy Survey (DGS) are guaranteed time projects focusing on large samples of normal and dwarf galaxies, respectively. A sample of dust-lane galaxies are targeted in three linked smaller projects, i.e. the Herschel Observations of Edge-on Spirals (HEROES), the New HErschel Multi-wavelength Extragalactic Survey of Edge-on Spirals (NHEMESES) and the Far-infraRed Investigation of Early-type galaxies with Dust Lanes (FRIEDL). Finally, a number of projects target individual interesting objects which deserve a detailed investigation of their ISM. The largest of these project is the Very Nearby Galaxies Survey (VNGS) where 13 prototypical galaxies are studied in detail with PACS and SPIRE. Smaller projects target the massive elliptical M87, the Andromeda Galaxy (Herschel Exploitation of Local Galaxy Andromeda, HELGA), the Local Group dwarf ellipticals NGC 185 and NGC 147, and the region of the Large Magellanic Cloud around SN 1987A. Table 1.2 presents an overview of all Herschel projects that the UGent is involved in.

Most of the scientific research presented in this PhD thesis was performed in the frame of the HeViCS, HRS and VNGS projects (see Section 1.4). Therefore, these Herschel programs are presented in the following subsections giving an overview of their observing strategy and main science goals and highlighting some of their first scientific results.

Project name	PI	Type	Instruments	Time
HeViCS	Jon Davies	OTKP	PACS, SPIRE	286.0
HRS	Stephen Eales	GTKP	SPIRE	112.6
HRS-PACS	Luca Cortese	OT1	PACS	50.8
DGS	Suzanne Madden	GTKP	PACS, SPIRE	104.9
VNGS	Christine Wilson	GTKP	PACS, SPIRE	143.9
H-ATLAS	Stephen Eales	OTKP	PACS, SPIRE	600.0
HELGA	Jacopo Fritz	GT1	PACS, SPIRE	18.1
HEROES	Maarten Baes	GT1	PACS, SPIRE	6.0
NHEMESES	Benne Holwerda	OT2	PACS, SPIRE	10.3
FRIEDL	Maarten Baes	GT2	PACS, SPIRE	3.4
M87	Jacopo Fritz	GT2	PACS	2.0
Local Group dEs	Ilse De Looze	OT2	PACS	4.5
SN 1987A	Maarten Baes	GT2	PACS, SPIRE	2.9
HeFoCS	Jon Davies	OT2	PACS, SPIRE	31.1

Table 1.2: An overview of the Herschel projects with UGent involvement.

1.3.2 The Herschel Virgo Cluster Survey

The Herschel Virgo Cluster Survey (HeViCS[1], see also Davies et al. 2010a) is an Open Time Key Project that was awarded 286 hours of observing time to cover the most nearby cluster, Virgo, with the PACS (100, 160 μm) and SPIRE (250, 350, 500 μm) photometers. The cluster was mapped in four 4×4 deg^2 areas (see Figure 1.8). Upon completion of the complete survey, the Herschel telescope has observed 84 deg^2 of the Virgo cluster, of which 55 deg^2 were covered at full depth in each of the 5 photometric bands. The observations were performed in parallel scan map mode, which means that PACS and SPIRE observations were collected simultaneously. Auld et al. (subm.) detected 254 (36%) of the 708 optically selected Virgo Cluster Catalogue galaxies within the survey boundary in at least one band, among which 164 galaxies were detected in all five bands. The primary science goals of the Herschel Virgo Cluster Survey include the detection of dust in the extreme outskirts of galaxies and in the intergalactic medium, a study of the FIR/submm SED and luminosity functions and an analysis of the dust properties in dwarf elliptical, irregular and early-type galaxies. This survey also provides an ideal local benchmark for environmental studies in clusters to compare with similar field surveys of distant clusters.

The first phase of the HeViCS science exploitation was based on the Science Demonstration Phase data, covering the central $4^\circ \times 4^\circ$ region of the Virgo cluster. Based

---

[1] More details on HeViCS can be found on http://www.hevics.org.

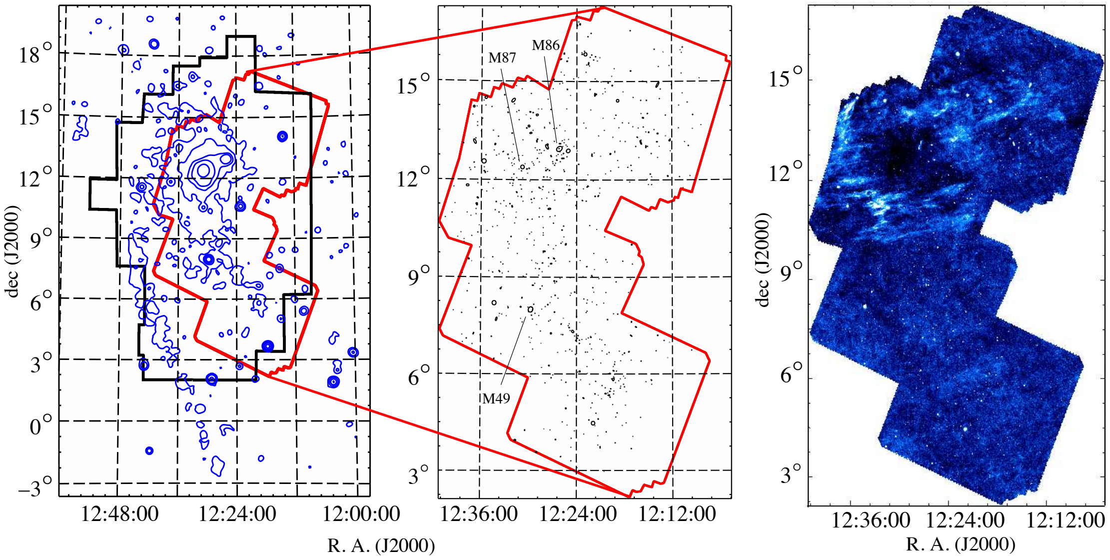

Figure 1.8: Map of the Virgo Cluster where the X-ray contours from Böhringer et al. (1994) are shown in blue, the VCC survey region is outlined in solid black and the full extent of HeViCS is outlined in red (left panel). The middle panel represents the optically selected VCC galaxies with black ellipses representing their optical discs measured to D_{25}. Dominant cluster galaxies have been labelled as well. The right panel shows the Herschel/SPIRE 250 μm image of the complete survey. These figures were adopted from Auld et al. (subm.).

on this limited data set, we have analyzed the FIR luminosity function (Davies et al., 2010a), the truncation of dust disks in HI deficient spirals (Cortese et al., 2010a), the upper limits on the dust lifetime in early-type galaxies (Clemens et al., 2010), the distribution of dust mass and temperature in cluster spirals (Smith et al., 2010) and have probed the dust content in metal-poor, star-forming dwarfs (Grossi et al., 2010), the dominant cluster elliptical galaxy M87 (Baes et al., 2010) and cluster dwarf elliptical galaxies (De Looze et al., 2010). More recently, Davies et al. (2012) have analyzed the global far-infrared properties of 78 optically bright galaxies based on Herschel observations of the full survey area at a limited depth (one single cross-scan coverage). From the same dataset of observations, Magrini et al. (2011) investigated the dependence of the molecular gas conversion factor, X_{CO}, on metallicity. A series of papers exploiting the entire dataset covering the complete survey area at full depth are currently in preparation.

1.3.3 The Herschel Reference Survey

The Herschel Reference Survey (HRS, Boselli et al. 2010a) is a guaranteed time key project which is led by the SAG-2 consortium. It has observed a volume-limited, K-band selected sample of 323 galaxies in the nearby Universe with the SPIRE instrument (a complementary project to observe the same galaxies with PACS is being executed as

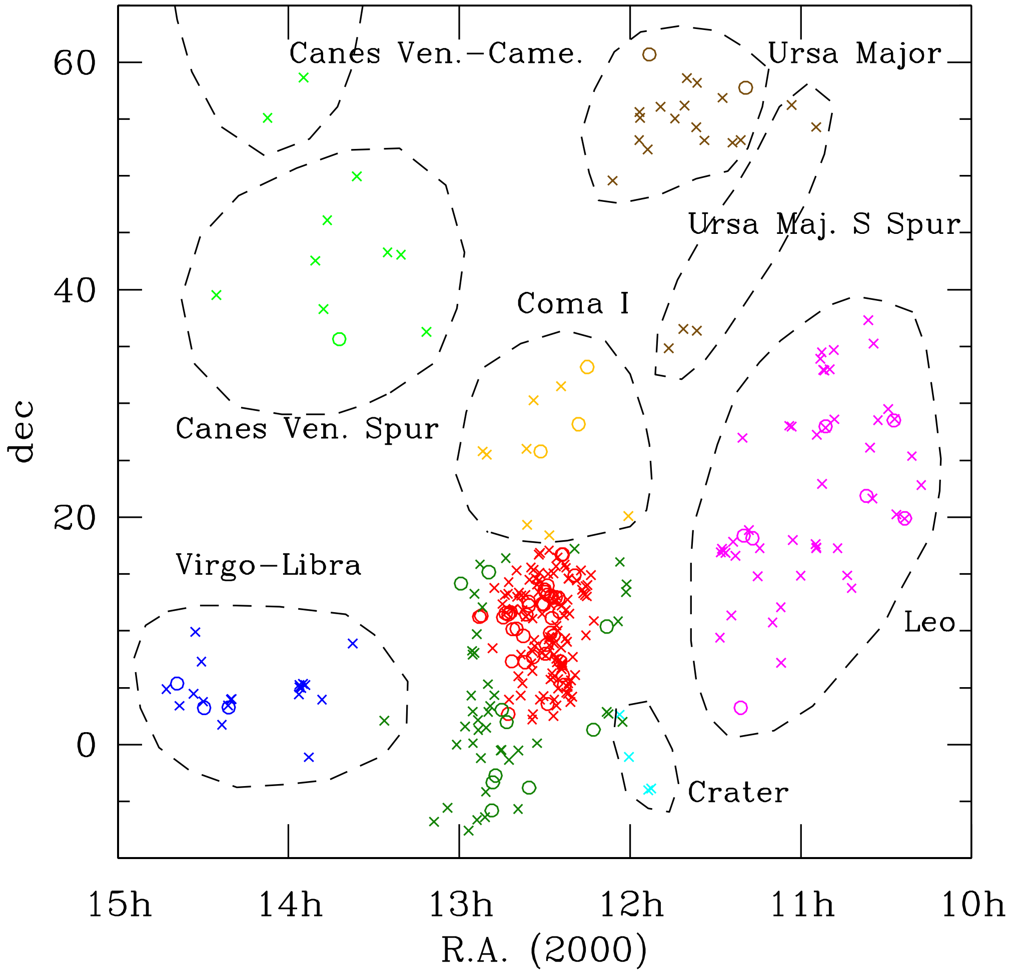

Figure 1.9: The sample of HRS galaxies indicating for each individual object its sky distribution (Virgo cluster: red; Virgo outskirts: green; Coma I Cloud: orange; Leo Cloud: magenta; Ursa Major Southern Spur and Cloud: brown; Crater Cloud: cyan; Canes Venatici Spur and Camelopardalis: light green and Virgo-Lybra Cloud: blue) and morphological classification (E-S0-S0a: circles and Sa-Sd-Im-BCD: crosses).

well). The galaxies are located at a distance between 15 and 25 Mpc, and span the whole range of morphological types (from elliptical to late-type spirals) and environments (from isolated field galaxies to members of the central, dense regions of the Virgo cluster). To prevent any duplication of Herschel observations, 79 objects of the 323 galaxies were observed as part of the Herschel Virgo Cluster Survey. Owing to the large sample size, diversity in galactic properties and availability of a large ancillary dataset, a detailed analysis of the statistical properties of this sample is possible and provides a benchmark study of dust in the nearby Universe (see Figure 1.9 for an overview of the HRS galaxy sample indicating their position and morphological classification). The main scientific goals of this program include the investigation of (i) the dust content of galaxies as a function of Hubble type, stellar mass and environment,

(ii) the connection between the dust content and composition and the other phases of the interstellar medium, and (iii) the origin and evolution of dust in galaxies.

The first scientific results obtained from the dataset of Science Demonstration Phase (SDP) observations analyze the far-infrared colours of late-type HRS galaxies (Boselli et al., 2010b). A more thorough analysis of the far-infrared colours exploiting the full dataset of the HRS survey is reported in Boselli et al. (2012). Based on this complete dataset, Cortese et al. (2012a) explore the dust scaling relations for wide ranges of environmental conditions and galaxy types, with Smith et al. (2012) investigating the dust properties in early-type HRS galaxies. Besides those global studies on statistically significant subsamples of HRS galaxies, spatially resolved studies on individual objects have also been presented, including the massive elliptical M86 (Gomez et al., 2010), the disturbed galaxy NGC 4438 (Cortese et al., 2010b) and the face-on spiral galaxies M99 and M100 (Sauvage et al., 2010; Pohlen et al., 2010; Eales et al., 2010b). Boquien et al. (2012) study the IRX-β relation on subgalactic scales in star-forming galaxies. The analysis of the dust energy balance study in the edge-on spiral galaxy NGC 4565 exploits the HRS observations for this galaxy and the large dataset of ancillary observations (see Chapter 6, De Looze et al., in prep.). A complete overview of the Herschel photometry of all galaxies in the HRS sample is presented in Ciesla et al. (2012).

1.3.4 The Very Nearby Galaxy Survey

The Very Nearby Galaxy Survey (VNGS) is another guaranteed time key project led by the SAG-2 consortium. VNGS has observed 13 nearby galaxies covering a wide galaxy parameter space. The Herschel observations, providing PACS (70, 160μm) and SPIRE (250, 350, 500μm) maps are crucial for understanding the ISM properties in galaxies, including the processes that govern galaxy formation. For several of the target galaxies, deep PACS spectroscopy maps and SPIRE FTS spectroscopic data are available as well. Because of the wide variety of sample galaxies, the survey will also be able to address the influence of environment on galaxy evolution. Besides very famous and bright nearby galaxies such as the Whirlpool galaxy (M51), the Antennae (NGC 4038/4039), Cen A, Arp 220 and many others, NGC 205, a bright dwarf satellite of the Andromeda galaxy, was covered by VNGS as well. Figure 1.10 displays GALEX UV images of all nearby galaxies observed in the frame of the Very Nearby Galaxy Survey.

The first results of the VNGS present detailed photometric and/or spectroscopic studies of individual galaxies from this sample. Based on the SPIRE FTS spectroscopy, Panuzzo et al. (2010) and Rangwala et al. (2011) discuss the specific excitation conditions in the ISM of M82 and Arp 220, respectively. Roussel et al. (2010) probe the far-infrared colours and physical properties of dust in the wind and tidal streams of

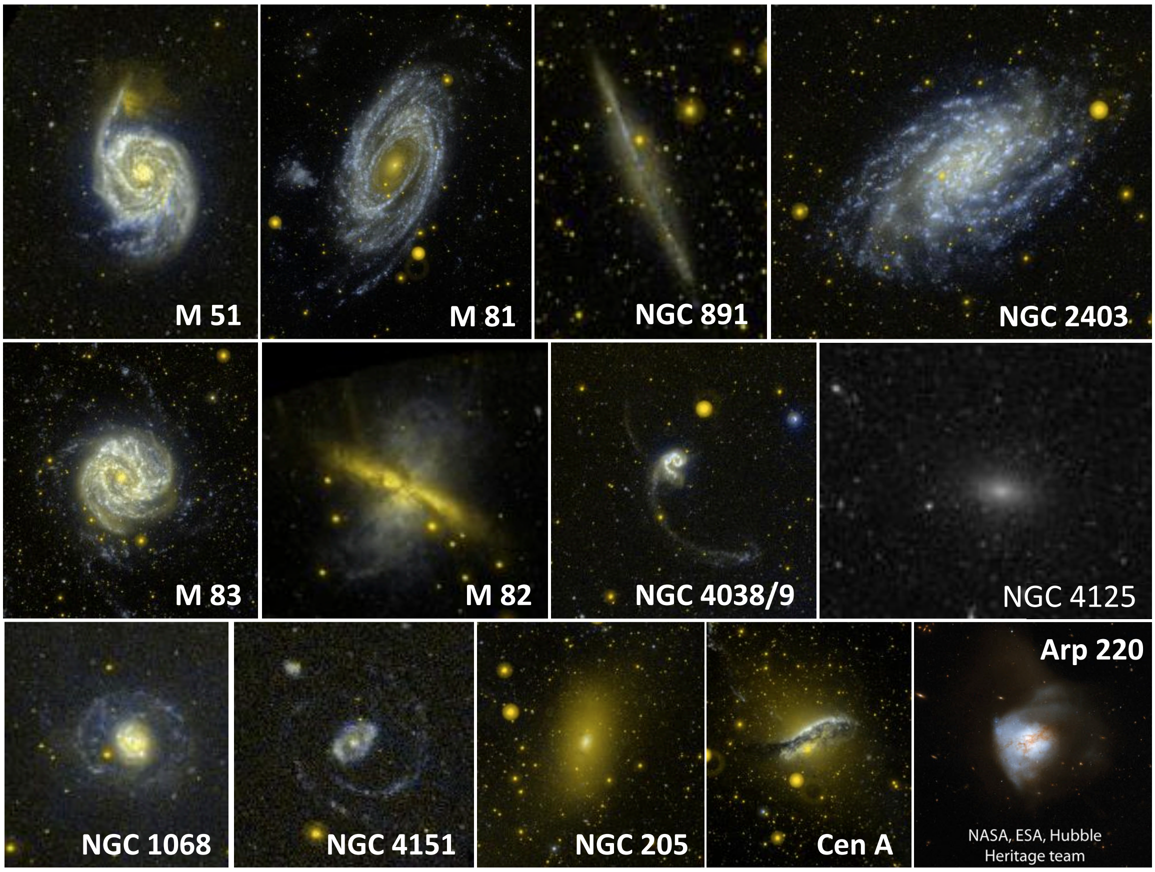

Figure 1.10: GALEX images of the galaxies in the sample of the Very Nearby Galaxy Survey.

M82. The origin of the diffuse far-infrared emission in the M81 group was the subject of Davies et al. (2010b). The heating mechanisms and gas-to-dust ratio in Cen A was the main topic of the papers Auld et al. (2012) and Parkin et al. (2012), respectively. Bendo et al. (2010, 2012) investigate the dust heating mechanisms from the photometry data of three nearby, face-on spiral galaxies, M81, M83 and NGC 2403. The properties of the dust and gas in the nearby, barred galaxy M83 were discussed in Foyle et al. (2012). The stars, dust and gas in the Whirlpool galaxy (M51) are investigated from a spatially resolved SED fitting procedure in Mentuch et al. (subm.). Exploring the photometry data as well as PACS spectroscopy maps for the early-type dwarf galaxy, NGC 205, the missing ISM mass problem in this object could be reanalyzed (see Chapter 4, De Looze et al. 2012b).

1.4 Goals of this PhD thesis

In the previous sections, the unique possibilities of the Herschel Space Observatory to study the cold dust and gas components have been demonstrated. Section 1.3 also briefly mentions the goals of a number of Herschel programs in which the UGent group is involved and which are related to this PhD thesis. In this section, the concrete research topics and the main scientific goals of this PhD thesis are presented.

1.4.1 The [CII] line as a star formation rate diagnostic

In the first part of this PhD thesis, we aim to characterize the [CII] cooling efficiency and relate the [CII] line flux to the star formation activity in galaxies. It is reasonable to expect a correlation between the emission from far-infrared fine-structure and molecular rotational lines and the star formation activity in a galaxy. Among those cooling lines, the far-infrared fine-structure [CII] line (λ = 157.714 μm) is typically one of the brightest spectral lines in star-forming galaxies ($L_{\rm [CII]}$ / $L_{\rm FIR} \sim$ 0.1-1%) and, therefore, an excellent candidate to probe the star-forming activity in those objects.

Carbon is the fourth most abundant element and has a lower ionization potential (11.26 eV) than hydrogen, implying that carbon will be ionized to C^+ in the surface layers of neutral gas clouds illuminated by far-ultraviolet photons. Because the [CII] line is relatively easy to excite ($\Delta E/k \simeq$ 91 K), it is capable of cooling warm neutral gas (30 K $< T <$ 10^4 K), where the most abundant atoms H and He provide inefficient cooling mechanisms (Tielens & Hollenbach, 1985; Wolfire, Tielens & Hollenbach, 1989). Owing to the brightness of the [CII] line in star-forming galaxies and its cooling efficiency in neutral gas, the [CII] line is thought to be an alternative probe for the star formation rate as well as the molecular gas content in galaxies (in particular in low-metallicity objects, e.g. Madden 2000; Cormier et al. 2010).

A direct relation between the [CII] luminosity and the star formation activity in galaxies is, however, contaminated by several factors. Indeed, the [CII] emission in galaxies is often not restricted to the neutral layers of photo-dissociated gas surrounding the active star formation regions, but might have an important contribution from ionized gas regions and diffuse HI clouds. Moreover, the efficiency of gas cooling through [CII] line emission depends on the specific conditions of the gas (i.e. density, temperature, metallicity, etc.). The different contributors to the [CII] line emission in galaxies and deviation from the linear trend for more relaxed and/or extreme star formation conditions are discussed into more detail in Section 2.1. Despite those bottlenecks, we analyze in this PhD thesis whether the [CII] line emission from galaxies can be used to probe its star formation activity. As an extension of the work done by Boselli et al.

(2002b), we recalibrate the relation of the [CII] line flux with the SFR for a sample of galaxies with a broader range in far-infrared luminosity (up to $L_{\rm FIR} \sim 10^{11.6}$ $L_{\odot}$) (see Chapter 2). The selection of our galaxy sample was performed in the pre-Herschel epoch and, therefore, obtained from a catalog consisting of all galaxies with ISO observations of the [CII] line emission. For the calibration of the SFR, we compare several star formation indicators and select the most reliable tracer. The empirical calibration of this correlation in the local Universe will prove its utility to trace the star formation productivity in galaxies at high redshift, in which the emission of young stellar objects is heavily obscured and for which the bright [CII] cooling line can offer an interesting alternative measure of the star formation rate.

1.4.2 Interstellar dust in cluster dwarf elliptical galaxies

Early-type dwarf galaxies (dEs) are the dominant morphological type in galaxy clusters. They were originally seen as a rather homogeneous population of dwarf galaxies with an old stellar age, no features resembling any recent or ongoing star formation, and no indications of a significant interstellar medium (ISM). This viewpoint has changed radically in the past few years. Deep imaging observations of dEs have revealed their heterogeneous morphology. In particular, the population of dEs can be subdivided into nucleated and non-nucleated subclasses and several papers report evidence for the presence of disks, spiral structure, bars or star formation (e.g., Jerjen, Kalnajs & Binggeli 2000; Barazza, Binggeli & Jerjen 2002; Geha, Guhathakurta & van der Marel 2003; Graham & Guzmán 2003a; Graham et al. 2003b; De Rijcke et al. 2003; Lisker, Grebel & Binggeli 2006a; Lisker et al. 2006b). Kinematical studies demonstrate that dEs are not simple pressure-supported systems: some dEs seem to be rotationally supported (Simien & Prugniel, 2002; Pedraz et al., 2002; Geha, Guhathakurta & van der Marel, 2003; De Rijcke et al., 2003; van Zee, Skillman & Haynes, 2004; Toloba et al., 2009), whereas others show evidence of kinematically decoupled cores (De Rijcke et al., 2004; Thomas et al., 2006).

Adding to this morphological and kinematical inhomogeneity is the detection of a significant interstellar medium in various dEs. Atomic and molecular gas was discovered for the first time in the Local Group dEs NGC 185 and NGC 205 using deep VLA and BIMA observations (Young & Lo, 1997). In the Virgo cluster, Conselice et al. (2003) estimate a HI detection rate of 15% for dEs down to a 3σ limit of 8×10^{6} $M_{\odot}$, while di Serego Alighieri et al. (2007) report a 1.7% HI detection rate with a 3σ detection limit of 3.5×10^{7} $M_{\odot}$. Large amounts of cold interstellar matter are unexpected in dEs, as both internal (supernova explosions) and external effects (ram-pressure stripping, galaxy interactions, tidal effects) are thought to be able to expel the gas from the shallow potential on short timescales (Michielsen, De Rijcke & Dejonghe, 2004; van Zee, Skillman & Haynes, 2004; Roediger & Hensler, 2005; Boselli et al., 2008a,b; Valcke, De Rijcke & Dejonghe, 2008). That the HI detected dEs are found preferentially near the edge of the cluster supports the idea that understanding environmental effects is crucial to constrain the evolutionary history of dEs. Buyle et al. (2005) and Bouchard et al. (2005) performed HI observations in the outskirts of the Fornax cluster and the Sculptor group, respectively, and confirmed the tendency of gas-deficient galaxies to be located near the center of the cluster.

Continuum emission from interstellar dust is a promising alternative way to determine the ISM content of dEs. In particular, the ISM in the immediate surroundings of M87 can be traced by dust emission, as strong radio continuum emission considerably reduces the HI detection sensitivity within 1° of M87 (Giovanelli et al., 2007). Until recently, the Andromeda satellites NGC 205 and NGC 185 were the only dEs that have been detected in the far-infrared (Haas 1998; Marleau et al. 2006, 2010). In particular, no dust emission had been detected from cluster dEs. While extinction features in optical images are indicative of dust in at least some cluster dEs (Ferrarese et al., 2006; Lisker, Grebel & Binggeli, 2006a; Lisker et al., 2006b), the direct detection of dust emission has been hampered by the limited sensitivity and wavelength coverage of the previous generation of far-infrared instrumentation. The advent of the *Herschel* Space Observatory offers new possibilities for mapping the ISM in dEs. With the Herschel observations of the Virgo cluster in the frame of the HeViCS and HRS programs covering the central, dense and outer, diffuse regions of the Virgo cluster, respectively, we search in this PhD thesis for the first detection of far-infrared dust continuum emission from cluster dwarf elliptical galaxies (Chapter 3).

1.4.3 NGC 205 and its missing ISM mass problem

NGC 205 is one of the three early-type dwarf satellite galaxies of the Andromeda galaxy. At its distance of only 824 kpc (McConnachie et al., 2005), it possible to study such low surface brightness galaxies, whereas galaxies at the low luminosity end often remain undetected at larger distances. Moreover, the Local Group allows probing the interstellar medium (ISM) of its residents at high resolution and, at the same time, offers a wealth of ancillary data. Studying the properties of the ISM and metal-enrichment in metal-poor dwarf galaxies offers a promising way to learn more about the conditions in the early Universe and the evolution of dwarf galaxies throughout the history of the universe.

NGC 205 is of particular importance due to its relatively low metal abundance ($Z \sim 0.13\ Z_\odot$, Richer & McCall 2008), interesting star formation history and indications of a tidal encounter with its massive companion M31. The star formation history in NGC 205 has been studied extensively (Baade, 1951; Hodge, 1973; Bertola et al., 1995; Davidge, 2003). An old stellar population (10 Gyr, Bica, Alloin & Schmidt 1990) dominates the overall stellar content of the dwarf galaxy and a plume of bright blue star clusters in the central region of NGC 205 was already identified approximately 60 years ago (Baade, 1951; Hodge, 1973). Based on observations of this young stellar population in combination with adequate model assumptions has provided several independent theoretical predictions of the current gas content in NGC 205 (see Section 4.1). Upon comparison of this theoretical gas content with observations (see Section 4.2), a large reservoir of gas has been found missing in NGC 205. This deficiency in ISM content is often referred to as the *missing ISM mass problem*.

In this PhD thesis, we present Herschel observations of NGC 205 observed as part of the VNGS and HELGA projects, with the aim of making an inventory of all the dust in NGC 205. Furthermore, we report new gas mass measurements from James Clerk Maxwell Telescope (JCMT) CO(3-2) observations and Herschel [CII] 158 μm and [OI] 63 μm line spectroscopy mapping. From those new dust and gas mass estimates, we are able to revise the “missing ISM” problem in NGC 205.

1.4.4 The dust energy balance in M104 and NGC 4565

Dust energy balance studies involve a complementary study of the dust component in galaxies, based on the extinction features of dust as seen in UV/optical images as well as the thermal emission of dust at FIR/submm wavelengths. The general approach in those dust energy balance studies initiates with the construction of a radiative transfer model for the stars and dust in a galaxy based on optical observations, revealing the extinguishing effect of dust grains on stellar light at different wavelengths. In a second step, the radiative transfer equation is solved for the specific parameters in the radiative transfer model and the dust emission is calculated. The predictions for the dust emission from the model allow an independent comparison with observations at infrared/submm wavelengths. We expect that the reprocessed stellar light at FIR/submm wavelengths, i.e. the thermal re-emission of dust, exactly compensates for the amount of photon energy absorbed at UV/optical wavelengths. In case of discrepancies, the radiative transfer model contains flaws and requires further refinement until all inaccuracies have been removed from the model and the observed dust emission is in balance with the absorption of stellar light by dust grains.

Edge-on spiral galaxies are considered ideal case studies for detailed dust energy balance studies (e.g. Popescu et al. 2000; Popescu &Tuffs 2002; Popescu et al. 2011; Misiriotis et al. 2001; Alton et al. 2004; Dasyra et al. 2005; Baes et al. 2010). To enable a com-

Figure 1.11: The famous edge-on spiral galaxy NGC 891.

plementary study of the dust component, dust energy balance studies require observations of the dust emissivity at FIR/submm wavelengths and the extinction of dust grains in optical/UV wavebands. Since the vertical extent of dust in galaxies is typically more confined than the stellar distribution (e.g.: Kylafis & Bahcall 1987; Xilouris et al. 1997, 1998, 1999; Alton et al. 2004; Bianchi 2007), only objects with a huge amount of dust along the line-of-sight will reveal the obscuring effect of dust at optical wavelengths. This implies that only extremely dusty systems or objects seen under an inclination angle close to 90° qualify for a panchromatic study of the dust energy balance. Due to their edge-on view, these objects are also the only systems for which the dust can be resolved vertically. Unfortunately, the high inclination of the disk also implies that most of the details of the spiral arms in the stellar disk are smeared out and most details of the dust distribution vanish when integrating along the line-of-sight.

Several edge-on spirals have been the target of detailed analyses of their dust energy balance, among which NGC 891 stands out as the most extensively studied object (see Figure 1.11). In general, those studies indicate that 30% of the bolometric luminosity of the galaxy is emitted by interstellar dust in the infrared, whereas the optical radiative transfer models suggest an absorption of only 10% of the stellar radiation (Popescu et al., 2000; Misiriotis et al., 2001; Popescu &Tuffs, 2002; Alton et al., 2004; Dasyra et al., 2005; Baes et al., 2010; Popescu et al., 2011). This inconsistency is referred to as the 'dust energy balance problem'. Different scenarios have been suggested to explain this problem.

Popescu et al. (2000, 2011) and Misiriotis et al. (2001) tried to explain the discrepancy in the dust energy budget by including a second thin diffuse dust disk, associated with a young stellar population. Although this additional dust is able to account for the missing observed FIR/submm emission, Dasyra et al. (2005) and Bianchi (2007) show that this second disk scenario contradicts with K band observations. Alternatively, a secondary dust component can be added in optically thick clumps distributed throughout the dust disk. Neglecting a clumpy dust structure can result in an underestimate of the optical dust mass by 40-50% (Witt & Gordon, 1999; Alton et al., 2000; Misiriotis & Bianchi, 2002). These clumps can either have embedded star-forming regions or have no associated sources. The latter clumps are referred to as 'quiescent'. Bianchi (2008) shows that a clumpy dust structure, associated to localized embedded sources and encompassing half of the dust mass (compared to the diffuse dust component), is able to solve the dust energy balance problem in NGC 891. Also the results in Baes et al. (2010) support the presence of heavily obscured star formation in clumpy dust clouds, to account for the missing infrared radiation in UGC 4754.

An alternative explanation that does not require the assumption of an additional dust component was explored in Alton et al. (2000, 2004) and Dasyra et al. (2005). They argue that an increase in dust emissivity compared to Galactic values in the submm wavelength range (in the diffuse component as well as the denser dust environments) also offers a possible solution to the dust energy balance problem. Assuming an increased emissivity by a factor of 4 and 1.5 at 850 μm and 1.2 mm, respectively, compared to the model prediction from Draine & Lee (1984), Alton et al. (2004) is capable of explaining the discrepancy in the dust energy balance of three edge-on spirals (NGC 4013, NGC 4565, NGC 5907).

The poor wavelength coverage of the previous generation of FIR/submm instruments, and the limited number of objects for which an energy balance study was possible in the past have hampered the interpretation of dust energy balance studies. Thanks to the increasing number of far-infrared and (sub)millimeter observations and the ongoing development of powerful radiative transfer codes, the pathway is now open for dust energy balance studies on larger galaxy samples. However, if we want to understand the subtle interplay of the star-dust geometry on observed galaxy properties, spatially resolved studies of well-resolved, individual galaxies are an absolute necessity. The valuable information obtained from those spatially resolved studies enable a thorough investigation of the dust energy balance in a galaxy. Unfortunately, only a handful of objects are suited for a dust analysis at high resolution.

In this PhD thesis, we analyze the dust energy balance on spatially resolved scales in two nearby spiral galaxies: the Sombrero Galaxy M104 (see Chapter 5) and the Needle Galaxy NGC 4565 (see Chapter 6).

2

The [CII] spectral line: a SFR diagnostic

The [CII] line is one of the most important coolants of the interstellar gas, that is heated mainly through the photoelectric effect on very small dust grains and PAHs, exposed to ultraviolet radiation from young stars. The photo-ionization of dust particles is particularly efficient for radiation with energies in the range $6 \leqslant h\nu \leqslant 13.6$ eV. Those photons typically originate from B3 to B0 stars with stellar masses $5 \leqslant M \leqslant 20$ $M_{\odot}$ (Xu & Buat, 1995), while locally a fraction might also reside from more massive stars. Based on this argumentation, the [CII] line emission is thought to be a reliable tracer of the star formation activity in a galaxy. In the past, the [CII] line was already exploited to detect star formation in nearby galaxies (Genzel & Cesarsky, 2000; Malhotra et al., 2001; Boselli et al., 2002b; Luhman et al., 2003; Pierini, Leech & Völk, 2003). Stacey et al. (1991) and Pierini et al. (1999) even suggested the use of [CII] as a SFR diagnostic in non-starburst galaxies. Similarly, Leech et al. (1999) found an indirect correlation between the [CII] emission and star formation activity in galaxies, from correlations of the [CII]-to-FIR and [CII]-to-K′ flux ratios with galaxy lateness, which is in its turn related to massive star formation activity in a galaxy. Boselli et al. (2002b) was the first to calibrate the [CII] line flux as a star formation tracer based on Hα + [NII] line fluxes. For a sample of 22 nearby late-type galaxies, spanning a far-IR luminosity range of $10^{8} \leqslant L_{FIR} \leqslant 10^{10.5}$ $L_{\odot}$, Boselli et al. (2002b) only found a weak trend in the relation between the [CII] line intensity and the star formation rate. The scatter in their SFR calibration is however significant, with an uncertainty factor of ~ 10 when estimating the SFR from the [CII] line emission. In view of the progress in techniques dealing with [NII] contamination (Decarli et al., 2007) and the recent improvement in accuracy of attenuation corrections for Hα data (Boselli et al., 2009a), we argue that part of the scatter in their SFR calibration might be owing to uncertainties related to data analysis of the Hα + [NII] line fluxes.

However, several issues regarding the origin of the [CII] emission in a galaxy hamper a simple proportionality of the line emission with the SFR. Since the UV emission responsible for the photoelectric heating of the gas might originate from different locations within a galaxy with diverging physical conditions, the origin of [CII] emission in a galaxy is difficult to interpret.

Aside from the ambiguity about the dominant source of [CII] emission in a galaxy, the excitation of [CII] might saturate at high temperatures and densities (Kaufman et al., 1999), implying that a direct conversion from [CII] line emission to a degree of star formation activity might fail to detect more extreme star formation events in a galaxy. However, the use of the [CII] line flux in probing the SFR in a galaxy does benefit from the fact that it is unaffected by extinction in most cases. Exceptions might be extreme starbursts (Luhman et al., 1998; Helou, 2000) or edge-on galaxies (Heiles, 1994). Papadopoulos, Isaak & van der Werf (2010) even argue that the [CII] deficiency in local starburst galaxy Arp 220 is due to a higher dust optical depth at FIR/submillimeter wavelengths rather than being caused by saturation of the [CII] excitation in higher density PDRs. A similar explanation is given in Rangwala et al. (2011) for Arp 220 and in Graciá-Carpio et al. (2011) for a sample of 44 local starburst, Seyfert or ultraluminous infrared galaxies (ULIRGS). Graciá-Carpio et al. (2011) argue that the line deficit is not restricted to the [CII] line, but similar deficits are being observed for other FIR fine-structure lines such as [NII] and [OI]. They attribute the line deficiencies to a higher ionization parameter in ULIRGS, implying an increase in the dust absorption of UV photons and, thus, a decrease in available ionizing photons to excite the FIR fine-structure lines. The separation between normal galaxies and more extreme starbursts ($L_{FIR}/M_{H_2} \geqslant 80$ $L_{\odot}/M_{\odot}$) coincides with the distinction between two different modes of star formation.

While the galaxies in our sample are neither extreme starburst nor edge-on galaxies, we only have to take the variable contribution from different phases of the ISM to the [CII] emission in a galaxy into consideration. In the next paragraphs, we briefly summarize the different contributors in the ISM of a galaxy to the [CII] line emission and their relative importance to the global [CII] line flux. The overview of the [CII] contributions from the different phases in the ISM is based on the discussions in Hollenbach & Tielens (1999) and Boselli et al. (2002b). However, the contributions from each of those ISM components is highly uncertain and varies among galaxies. In the near future, spatially resolved observations of multiple fine-structure lines (in particular [CII], CO, [NII] and [OI]) will allow to gain better insight in the origin of [CII] emission in a galaxy. Currently, the most important contributions to the [CII] emission in a galaxy are thought to arise from the following ISM components:

2.1.1 Diffuse ISM

The diffuse ISM includes both the neutral diffuse medium (HI clouds) and the warm ionized medium (WIM). In view of their temperatures and densities, diffuse HI clouds are predominantly cooled through the [CII] line (Dalgarno & McCray, 1972; Black, 1994; Hollenbach & Tielens, 1999). Also the contribution from warm neutral media is often non-negligible in galaxies. From observations of the local diffuse medium in the Solar neighborhood as observed by COBE at high galactic latitudes (Bennett et al., 1994), two-thirds of the [CII] emission is thought to arise from the neutral diffuse medium while the remaining one-third is associated to the WIM (Boselli et al., 2002b).

On global galaxy scales, the contribution from the diffuse ionized gas in nearby starburst galaxies (e.g. M82, Lord et al. 1996; Colbert et al. 1999, and NGC 253, Carral et al. 1994) has been show to be at most $\sim 30\%$, based on studies of the ionized and photodissociated gas from bright FIR fine-structure lines and FIR continuum emission.

2.1.2 PDR

Photo-Dissociation Regions or PDRs are neutral regions in the interstellar medium at the interface between molecular clouds and HII regions, where the heating and chemistry is governed by far ultraviolet (FUV) photons. While most of the [OI] emission in a galaxy originates from PDR regions, also a significant portion of the [CII] emission in a galaxy is thought to reside from PDRs. The importance of PDRs in the [CII] budget of a galaxy was first revealed from the good correlation between the [CII] and CO emission in a galaxy rather than with the HI emitting regions (Stacey et al., 1985; Shibai et al., 1991). This suggested that –at least part of– the [CII] emission in a galaxy is associated with PDRs, i.e. neutral regions on molecular cloud surfaces created by nearby OB associations and/or the ambient interstellar radiation field (HI halos). In particular the weaker PDRs contribute to the [CII] emission in a galaxy, because in strong, dense PDRs the high densities and hard radiation field saturate the upper level of the [CII] transition (e.g. Stacey et al. 1993). In low-metallicity environments, the contribution from those strong PDRs might however be substantial (e.g. Magellanic Clouds, Israel et al. 1996). The low metal abundance results in less absorption of far-ultraviolet photons by dust grains and thus less far-infrared dust emission. At the same time, the low metal abundance allows a deeper penetration of UV light inside the molecular clouds (Pak et al., 1998). The contribution from PDRs to the global [CII] line emission in a galaxy is considered to be around 70 %, based on direct measurements of the [CII]-to-[NII]$_{205\mu m}$ ratio in the Carina nebula and appropriate assumptions on the gas phase C/N abundance ratio (Oberst et al., 2006).

2.1.3 HII regions

In normal galaxies, the contribution from both low-density, extended and warm, ionized HII regions is thought to be negligible on galactic scales. This is demonstrated from the relation between the observed [NII] emission with the [CII] intensity. With an ionization potential for neutral N (14.53 eV) a bit higher than for H (13.6 eV), the [NII] emission in a galaxy is particularly found in ionized HII regions. Because of the nonlinearity in this relation, the warm ionized HII regions are only considered important at high [CII] intensities.

2.2.1 Sample selection

The selection is based on the galaxy sample in Brauher, Dale & Helou (2008), who assembled all galaxies with available [CII] data from the ISO archive. More specifically, we restrict our sample to those galaxies for which the [CII] line fluxes do not correspond to upper limits (i.e. non-detections) and which are classified in this analysis as unresolved in the far-IR with respect to the $\sim 75''$ ISO LWS beam. This latter criterion implies that an aperture correction is not required for the [CII] line flux. Although a substantial fraction of the flux from an on-axis point source is diffracted out of the aperture beyond the diffraction limit at about 110 μm for all LWS detectors, these losses will be cancelled out in the calibration process, provided it is applied to point sources observed on-axis (Gry et al., 2003).

From this sample of 153 unresolved galaxies, we retain all galaxies that have been observed in both GALEX *FUV* and MIPS 24 μm bands, which gives us a final sample of 39 unresolved galaxies.

Some galaxies have multiple [CII] data, corresponding to apertures taken at different positions. For every galaxy, we only include one data point, preventing the introduction of any bias in our sample. If the different apertures show some overlap in area, we choose the aperture corresponding to the [CII] flux with the smallest uncertainty. If the overlap is insignificantly small, we add all fluxes from the apertures taken at different positions. The fluxes from the different apertures for the GALEX *FUV* and MIPS 24 μm are summed accordingly. This kind of flux summation has only been applied for two galaxies in our sample: NGC 4651 and NGC 7217.

Since *FUV* data are affected by galactic extinction, we have to apply appropriate corrections. At a galactic latitude $b = 11.^{\circ}2$ (Clements, 1983), NGC 1569 suffers from a large amount of Galactic extinction. Inconsistencies among the different reported estimates for the V-band extinction (e.g. $A_{\rm V} = 1.79$, Israel 1988; $A_{\rm V} = 1.61$, Devost, Roy & Drissen 1997; $A_{\rm V} = 2.32$, Schlegel, Finkbeiner & Davis 1998), made us decide to remove NGC 1569 from our sample, considering we want to avoid the introduction of any bias. This reduces our sample to 38 galaxies.

Table 2.1 gives an overview of all relevant information for our sample galaxies. We arranged their properties as follow:

- Column 1: galaxy name, NGC, IC, CGCG, UGC or IRAS, for the sample galaxies.
- Column 2: distance [Mpc], derived from the Nearby Galaxies Catalogue (Tully,

1988) and for other galaxies, from their recession velocity (from NED) assuming $H_0 = 70$ km s^{-1} Mpc^{-1}.

- Column 3: morphological type, adopted from de Vaucouleurs (1991).
- Column 4, 5: classification of the nuclear spectrum: HII or starburst, LINER, Seyfert (1 or 2), and the corresponding references for this classification.
- Column 6: $f_\nu(60\mu\text{m})$-to-$f_\nu(100\mu\text{m})$ ratio of the IRAS fluxes, a proxy for the effective dust temperature.
- Column 7: Total-IR luminosity [erg/s], as calculated from equation (5) in Dale & Helou (2002).

Data processing

Far-ultraviolet (FUV, λ=1539Å, $\Delta\lambda$=442Å) observations of galaxies in our sample have been obtained from the GALEX GR4/5 public release. In order to derive accurate FUV photometry we only used fields with integration times greater then 800 sec, obtained as part of the Nearby Galaxy Survey, the Medium Imaging Survey or Guest Investigator programs (70 galaxies from our unresolved sample of 153 galaxies have been observed by GALEX). We performed aperture photometry on the intensity maps produced by the standard GALEX pipeline. Details about the GALEX pipeline can be found in Morrissey et al. (2007). The GALEX FUV data have been corrected for galactic extinction according to Schlegel, Finkbeiner & Davis (1998), using the extinction relation obtained from Cardelli, Clayton & Mathis (1989).

The 24 micron images were created from raw data produced by the Multiband Imaging Photometer for Spitzer (MIPS; Rieke et al. 2004) on the Spitzer Space Telescope (Werner et al., 2004). The raw data were taken by a variety of programs using either the photometry mode (which produces 5 times 5 arcmin maps) or the scan map mode (which produces images that are typically 1 degree in length). We used the MIPS Data Analysis Tools (Gordon et al., 2005) along with additional processing steps to produce the final images. The individual data frames were processed through droop correction (to remove excess signal in each pixel proportional to the signal in the entire array), non-linearity correction, dark current subtraction, scan mirror position-dependent and position-independent flatfielding, and latent image removal steps. Background emission from the zodiacal light and additional scattered light that is related to the scan mirror position is then subtracted out. For objects observed in the scan map mode, the data from separate astronomical observation requests were used to make mosaics taken at individual epochs. These images were then subtracted from each other to identify asteroids, and the regions with asteroids were then masked out. Preliminary mosaics of each object were made using all data for each object to identify pixels in individual frames with values that are statistical outliers compared to other co-spatial pixels in other frames. These pixels were masked out, and then final mosaics were made using an image scale of 1.5 arcsec pixel^{-1}. Any residual background in the images was measured in multiple regions surrounding the optical disc and was then subtracted from the image. The final images are then calibrated using the conversion factor given by Engelbracht et al. (2007), which has an uncertainty of 4%. The FWHM of the PSF is 6 arcsec (Spitzer Science Center 2007).

Flux determination

We determine GALEX *FUV* and MIPS 24 μm fluxes within the same aperture as the $\sim 75''$ ISO LWS beam. Variation in the shape of the point spread function used by the different instruments should not be an issue, as the necessary corrections have been applied through the calibration on a point source.

The GALEX *FUV* and MIPS 24 μm fluxes were determined using the source-extracting code SExtractor (Bertin & Arnouts, 1996). To align the apertures with the exact same position at which the [CII] fluxes were determined, we have created a fake object in IRAF (using the task mkobjects) at the same position coordinates of the actual pointing of the [CII] observation. Feeding SExtractor with this artificially created map and the *FUV* or 24 μm image, assures us that the *FUV* and 24 μm fluxes are extracted within the same area on the sky as the [CII] fluxes.

Table 2 summarizes all relevant published data and measured fluxes within the $\sim 75''$ ISO LWS beam for the analysis in this thesis. Summing up:

- Column 1: galaxy name, NGC, IC, CGCG, UGC or IRAS, for the sample galaxies.
- Column 2, 3: Actual pointing position: right ascension (RA) and declination (DEC) from the [CII] observation, both in decimal degrees (from Brauher, Dale & Helou 2008).
- Column 4: [CII] line flux, in [fW/m^2], and the uncertainty on this flux measurement (from Brauher, Dale & Helou 2008).
- Column 5: GALEX *FUV* flux, [mJy], and the corresponding uncertainty. Both values have been corrected for galactic extinction, according to Schlegel, Finkbeiner & Davis (1998) and Cardelli, Clayton & Mathis (1989).
- Column 6: Spitzer MIPS 24 μm flux, [mJy], and the corresponding uncertainty, including both uncertainties in the flux extraction ($< 2\%$) and the calibration (4%, Engelbracht et al. 2007).

Spectral classification

Considering we will calibrate the [CII] luminosity against the SFR, derived from either the corrected *FUV* flux (for which the attenuation correction is based on IR data), 24 μm data or TIR luminosities, we have to make sure that the star-forming regions are

Name (1)	Distance (Mpc) (2)	Type[1] (3)	Spectral type (4)	Ref[2] (5)	IRAS 60 / IRAS 100 (6)	log $L_{\rm TIR}$ log (erg/s) (7)
Cartwheel	129.3	RING	HII/sb	no[3]	0.46	44.30
NGC 0520	27.8	Pec	HII/sb	3	0.66	44.41
NGC 0625	3.9	SB(s)m? edge-on	HII/sb	1	0.56	42.08
NGC 0660	11.8	SB(s)a pec	LINER	1, 2, 3	0.64	44.03
NGC 0695	139.1	S0? pec	HII/sb	2	0.58	45.28
NGC 0986	23.2	SB(rs ab	HII/sb	4	0.49	44.32
UGC 02238	92.3	Im?	LINER	2	0.54	44.92
NGC 1156	6.4	IB(s)m	HII/sb	3	0.50	42.48
NGC 1266	31.3	(R′) SB(rs) 0∧0 pec:	LINER	1, 2	0.81	44.07
NGC 1275	75.2	Pec	Seyfert	1, 3	1.02	44.49
NGC 1317	16.9	SAB(r)a	HII/sb	no	0.34	43.28
NGC 1569	1.6	IBm	HII/sb	3	0.98	42.15
IRAS 05189-2524	182.3		Seyfert	1, 2	1.20	45.74
UGC 03426	57.9	S0:	Seyfert	1	1.12	44.58
NGC 2388	59.1	S?	HII/sb	2	0.67	44.83
NGC 4041	22.7	SA(rs)bc:	HII/sb	3	0.41	44.06
NGC 4189	16.8	SAB(rs) cd?	HII/sb	no	0.34	43.24
NGC 4278	9.7	E1-2	LINER	3	0.36	42.09
NGC 4293	17.0	(R) SB(s) 0/a	LINER	3	0.44	43.32
NGC 4299	16.8	SAB(s)dm:	HII/sb	no	0.33	43.17
NGC 4490	7.8	SB(s)d pec	HII/sb	3	0.60	43.51
NGC 4651	16.8	SA(rs)c	LINER	3	0.35	43.44
NGC 4698	16.8	SA(s)ab	Seyfert	1, 3	0.31	42.65
IC 4329A	68.8	SA0∧+: edge-on	Seyfert	1	1.22	44.59
NGC 5713	30.4	SAB(rs)bc pec	HII/sb	4	0.57	44.43
CGCG 1510.8+0725	55.7		Seyfert	6	0.66	44.76
NGC 6221	19.4	SB(s)c	Seyfert	1	0.50	44.37
NGC 6240	104.8	I0: pec	LINER	1, 2	0.82	45.43
IRAS 19254-7245	264.3		Seyfert	1, 5	0.95	45.68
NGC 6810	25.3	SA(s)ab:	Seyfert	4	0.52	44.28
IRAS 20551-4250	184.1		Seyfert	1, 5[4]	1.29	45.55
NGC 7217	16.0	(R)SA(r)ab	LINER	1, 3	0.27	43.46
NGC 7469	69.9	(R′)SAB(rs)a	Seyfert	1, 2	0.74	45.25
IRAS 23128-5919	191.0		Seyfert	1, 5[5]	0.98	45.58
NGC 7552	19.5	(R′)SB(s)ab	HII/sb	1	0.71	44.54
NGC 7582	17.6	(R′)SB(s)ab	Seyfert	1	0.67	44.25
NGC 7714	36.9	SB(s)b: pec	HII/sb	1, 2	0.90	44.31
IRASF23365+3604	276.2		Seyfert	1	0.84	45.74
NGC 7771	61.1	SB(s)b: pec	HII/sb	2	0.49	45.00

9

Table 2.1: Properties for the galaxies in our sample.

[1] The galaxy type has been adopted from de Vaucouleurs (1991). If no galaxy type is mentioned, there was no classification available in the literature.

[2] The references of the spectral type: 1: Véron-Cetty & Véron (2010); 2: Veilleux et al. (1995); 3: Ho, Filippenko & Sargent (1997a); 4: Véron-Cetty & Véron (1986); 5: Risaliti (2004) 6: Baan & Klöckner (2006)

[3] ″no″ indicates that no classification was found in the literature. These objects were classified in the HII/starburst group based on detected HII regions in their nuclei. The paragraph on spectral classification discusses the classification for these galaxies more into detail.

[4] Based on optical spectra IRAS 20551-4250 was classified as a starburst galaxy (Véron-Cetty & Véron, 2010), but according to L-band diagnostics a significant AGN contribution is present (Risaliti, 2004).

[5] This galaxy has a pair of optical nuclei, which is probably a remnant of a merging process. Véron-Cetty & Véron (2010) identified this galaxy as HII region, while Risaliti (2004) reported that one nucleus shows AGN features and the other nucleus resembles a HII region. Since both nuclei fall within the ISO LWS beam, we have classified this object as a Seyfert galaxy, based on the AGN-contribution from at least one nucleus.

Name (1)	RA (deg) (2)	DEC (deg) (3)	[CII] (fW/m^2) (4)	GALEX FUV (mJy) (5)	MIPS 24 (mJy) (6)
Cartwheel	9.4171	-33.7239	0.15 ± 0.02	1.980 ± 0.009	63.7 ± 2.7
NGC 0520	21.1458	+3.7950	2.83 ± 0.07	0.787 ± 0.009	2139.3 ± 85.7
NGC 0625	23.7799	-41.4357	1.00 ± 0.08	8.239 ± 0.016	776.0 ± 31.2
NGC 0660	25.7595	+13.6458	7.67 ± 0.19	0.386 ± 0.007	2889.9 ± 115.7
NGC 0695	27.8091	+22.5825	2.04 ± 0.08	3.869 ± 0.003	672.4 ± 27.0
NGC 0986	38.3922	-39.0462	3.04 ± 0.11	0.964 ± 0.011	2355.9 ± 94.4
UGC 02238	41.5726	+13.0958	2.35 ± 0.09	0.448 ± 0.012	496.2 ± 20.0
NGC 1156	44.9271	+25.2375	1.56 ± 0.14	23.307 ± 0.115	447.1 ± 18.0
NGC 1266	49.0032	-2.4271	0.50 ± 0.10	0.216 ± 0.009	804.1 ± 32.3
NGC 1275	49.9525	+41.5105	1.16 ± 0.07	4.766 ± 0.014	2814.7 ± 112.7
NGC 1317	50.6862	-37.1027	0.91 ± 0.05	1.974 ± 0.013	207.2 ± 8.4
NGC 1569	67.7046	+64.8478	5.99 ± 0.16	105.217 ± 0.314	6495.8 ± 260.0
IRAS 05189-2524	80.2558	-25.3624	0.14 ± 0.02	0.126 ± 0.004	2786.6 ± 111.6
UGC 03426	93.9016	+71.0376	0.41 ± 0.02	0.662 ± 0.020	2238.1 ± 89.7
NGC 2388	112.2229	+33.8182	1.74 ± 0.08	0.135 ± 0.005	1585.2 ± 63.5
NGC 4041	180.5501	+62.1363	3.48 ± 0.05	1.880 ± 0.001	1159.7 ± 46.5
NGC 4189	183.4465	+13.4240	0.94 ± 0.06	2.243 ± 0.001	295.7 ± 12.0
NGC 4278	185.0276	+29.2824	0.25 ± 0.03	0.883 ± 0.010	49.1 ± 2.1
NGC 4293	185.3050	+18.3844	0.28 ± 0.02	0.111 ± 0.003	520.1 ± 20.9
NGC 4299	185.4189	+11.5012	0.93 ± 0.09	8.996 ± 0.030	210.4 ± 8.5
NGC 4490	187.6536	+41.6398	4.32 ± 0.11	10.248 ± 0.022	1394.8 ± 55.9
NGC 4651	190.9271	+16.3942	2.03 ± 0.08	4.048 ± 0.015	383.1 ± 15.5
NGC 4651	190.9442	+16.3972	0.50 ± 0.06	1.533 ± 0.010	79.6 ± 3.3
NGC 4651	190.91	+16.3914	0.76 ± 0.09	1.732 ± 0.010	88.0 ± 3.6
NGC 4651	total from all positions		3.29 ± 0.13	7.314 ± 0.021	550.7 ± 22.2
NGC 4698	192.0969	+8.4875	0.13 ± 0.02	0.289 ± 0.004	34.9 ± 1.5
IC 4329A	207.3304	-30.3095	0.15 ± 0.02	0.073 ± 0.003	1945.3 ± 77.9
NGC 5713	220.0478	-0.2905	4.68 ± 0.13	4.061 ± 0.020	2144.6 ± 85.9
CGCG 1510.8+0725	228.3053	+7.2265	0.33 ± 0.05	0.086 ± 0.004	514.3 ± 20.7
NGC 6221	253.1913	-59.2167	6.64 ± 0.25	4.527 ± 0.063	4528.1 ± 181.3
NGC 6240	253.2450	+2.4013	2.72 ± 0.06	0.637 ± 0.004	2735.4 ± 109.5
IRAS 19254-7245	292.8400	-72.6319	0.26 ± 0.07	0.162 ± 0.005	1059.0 ± 42.5
NGC 6810	295.8915	-58.6556	3.83 ± 0.13	0.553 ± 0.010	2882.1 ± 115.4
IRAS 20551-4250	314.6116	-42.6518	0.41 ± 0.03	0.600 ± 0.006	1450.9 ± 58.2
NGC 7217	331.9775	+31.35833	0.66 ± 0.06	1.557 ± 0.008	197.9 ± 8.0
NGC 7217	331.95833	+31.35972	0.62 ± 0.07	1.331 ± 0.008	185.2 ± 7.5
NGC 7217	total from all positions		1.28 ± 0.09	2.888 ± 0.012	383.1 ± 15.5
NGC 7469	345.81417	+8.87361	2.27 ± 0.03	6.963 ± 0.020	4421.9 ± 177.0
IRAS 23128-5919	348.9454	-59.0544	0.58 ± 0.05	0.557 ± 0.005	1242.2 ± 49.8
NGC 7552	349.045	-42.5844	6.37 ± 0.15	3.746 ± 0.011	9443.8 ± 377.9
NGC 7582	349.5988	-42.3703	4.12 ± 0.13	0.900 ± 0.006	5516.4 ± 220.8
NGC 7714	354.0612	+2.1550	1.83 ± 0.10	7.893 ± 0.018	2131.7 ± 85.4
IRASF23365+3604	354.7554	+36.3528	0.16 ± 0.02	0.197 ± 0.006	585.2 ± 23.5
NGC 7771	357.8534	+20.1119	2.98 ± 0.09	0.906 ± 0.012	1216.5 ± 48.8

Table 2.2: Sample galaxies: data

the dominant contributor to this IR emission. Therefore, we will classify our sample according to their nuclear spectral classification (see Table 2.1). We have made three different subdivisions. The first subgroup encompasses all objects resembling features typical of HII regions or starbursts. The second and third subset will include LINER and Seyfert galaxies, respectively. For this spectroscopic classification, we mainly rely on Véron-Cetty & Véron (2010), who have composed a compilation of AGN host galaxies. For the identification of the remaining sources and the objects with an uncertain classification in Véron-Cetty & Véron (2010), we have adopted the classification based on the optical spectra in Veilleux et al. (1995) and Ho, Filippenko & Sargent (1997a), who both use similar selection criteria in their classification procedure. Additionally, for some sources we used the classification from Véron-Cetty & Véron (1986). Considering that the optical spectroscopic classification for FIR-luminous objects not always offers a clear distinction between starburst- or AGN-dominated nuclear activity, we additionally examine spectroscopic L-band data (Risaliti, 2004) and radio properties (Baan & Klöckner, 2006), if available for those objects. Based on several L-band diagnostics, Risaliti (2004) found a dominant AGN-contribution to the energy output in the infrared for IRAS 19254-7245, IRAS 20551-4250 and one of the two optical nuclei in IRAS 23128-5919. Baan & Klöckner (2006) found from their radio observations that an AGN is the dominant power source in the nucleus of CGCG1510.8+0725. Four sources remain unclassified, but since they all host HII regions (Cartwheel: Gao et al. 2003, NGC1317: Crocker, Baugus & Buta 1996, NGC 4189 and NGC 4299: Hodge & Kennicutt 1983), we assign them to the HII/starburst group.

Our sample of 38 galaxies contains 16 galaxies for which HII regions or starbursts dominate their central regions, while the remaining sources in our sample are host galaxies of an AGN (14 galaxies) or LINER (8 galaxies). For these different nuclear regimes, we will examine the power sources that mainly contribute to the 24 μm and TIR emission. Plotting $L_{[\mathrm{CII}]}$ as a function of the MIPS 24 μm and TIR luminosities for the three different subsets, we immediately deduce a significant contribution from the AGN in Seyfert galaxies to the 24 μm and TIR emission (see the upper panels in Figures 2.1 and 2.2, respectively). The dispersion around the mean trend for the complete sample of galaxies is 0.51 dex and 0.35 dex in Figure 2.1 and 2.2, respectively. For galaxies classified as a LINER, starbursts appear to be the main power supply for the MIPS 24 μm and TIR emission. Although the spectral line emission in some LINERs might also be generated by a quiescent AGN, this contribution does not appear to be significant for the LINER galaxies in our sample. Because of the insignificant AGN contribution to the IR emission in LINERs, we perform our calibration analysis on a reduced sample that combines the two subsets (HII regions, starbursts and LINERs), which all have a dominant contribution from star formation related radiation to the IR emission. This final sample consists of 24 galaxies of which 16 show features of HII regions and 8 other galaxies are classified as a LINER. Plotting again the same correlations for this

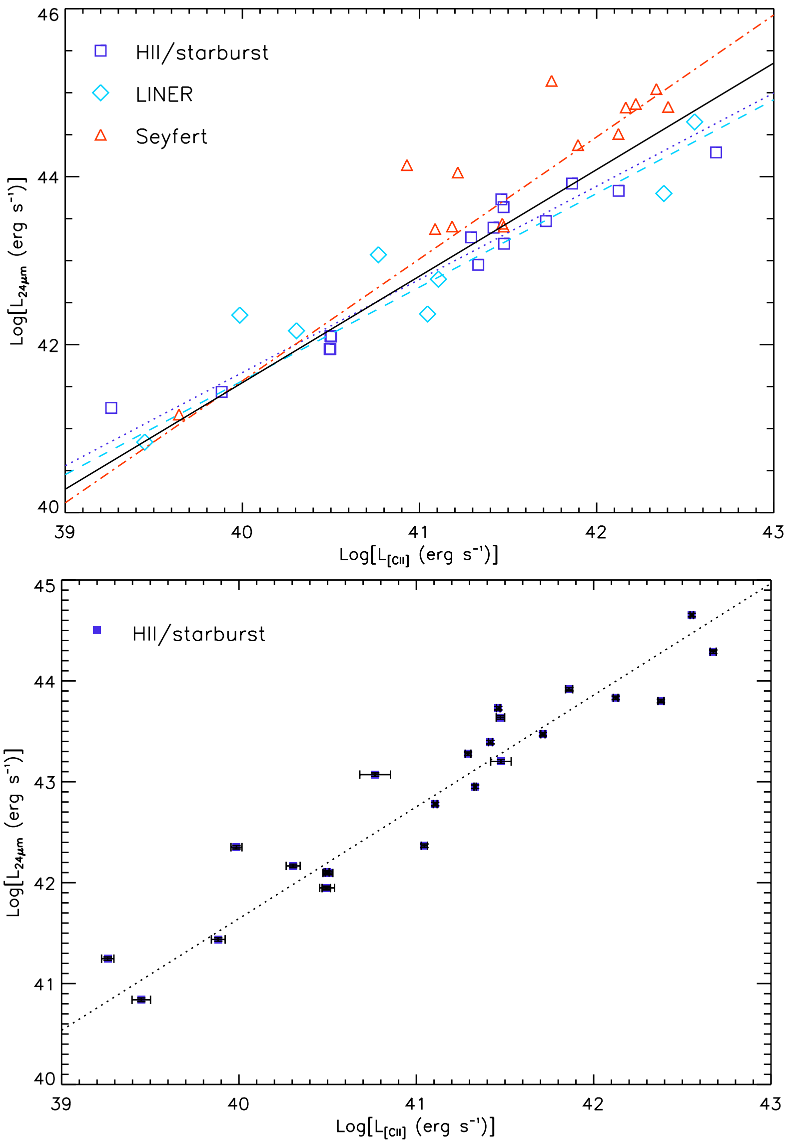

Figure 2.1: $L_{[\mathrm{CII}]}$ as a function of $L_{24\mu\mathrm{m}}$. Top panel: the three subsamples are represented (blue squares = HII/starburst, cyan diamond = LINER, red triangle = Sy1/Sy2). For reasons of clarity, we have omitted the errorbars from this plot. The best fitting line through the data points are indicated with a blue dotted, cyan dashed and red dashed-dotted line for the HII/starburst, LINER and Seyfert subsample, respectively. The mean trend for the complete sample is represented by a black solid line. The data points have a dispersion of 0.51 dex around this mean trend. Bottom panel: the reduced sample, combining HII, starburst and LINER galaxies. The dotted line represents the best fitting line through the data points with a dispersion of 0.31 dex.

final sample (see Figures 2.1 and 2.2, bottom panels), we can quantify that most of the scatter in previous plots was due to the contribution of an AGN to the IR emission (MIPS 24 μm and TIR). Indeed, the dispersion around the mean trend reduces to 0.31 dex in Figure 2.1 and 0.22 dex in Figure 2.2.

The galaxies in our final sample span a range of almost 4 orders of magnitude in total

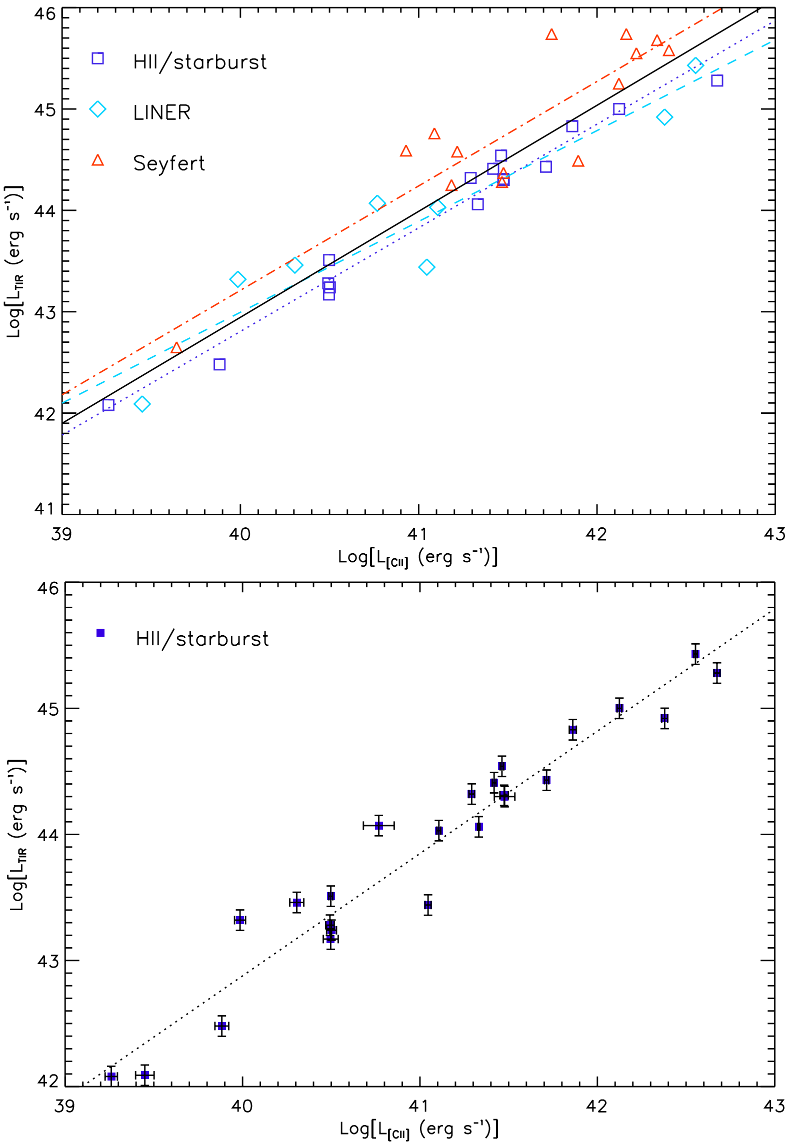

Figure 2.2: $L_{[\mathrm{CII}]}$ as a function of L_{TIR}, as calculated from Dale & Helou (2002) and the IRAS fluxes for the sample galaxies. Top panel: the three subsamples are represented. The legend for the data points and mean trends is identical to Figure 2.1. For reasons of clarity, we have omitted the errorbars from this plot. The data points have a dispersion of 0.35 dex around the mean trend for the complete sample. Bottom panel: the reduced sample, combining HII, starburst and LINER galaxies. The dotted line represents the best fitting line through the data points with a dispersion of 0.22 dex.

infrared luminosity (L_{TIR}), from $\sim 1.2 \times 10^{42}$ to $\sim 2.7 \times 10^{45}$ erg s^{-1} (L_{TIR} was calculated based on equation (5) in Dale & Helou (2002), relying on IRAS 25, 60 and 100 μm fluxes). In this final sample of 24 galaxies (HII regions, starbursts and LINERs), five galaxies are classified as LIRG ($L_{\mathrm{TIR}} > 10^{11}\ L_{\odot}$). Figure 2.3 demonstrates this wide range in L_{TIR} and shows its dependence on the $f_{\nu}(60\mu\mathrm{m})$-to-$f_{\nu}(100\mu\mathrm{m})$ ratio, which is a proxy for the effective dust temperature. As most galaxies in our sample have high

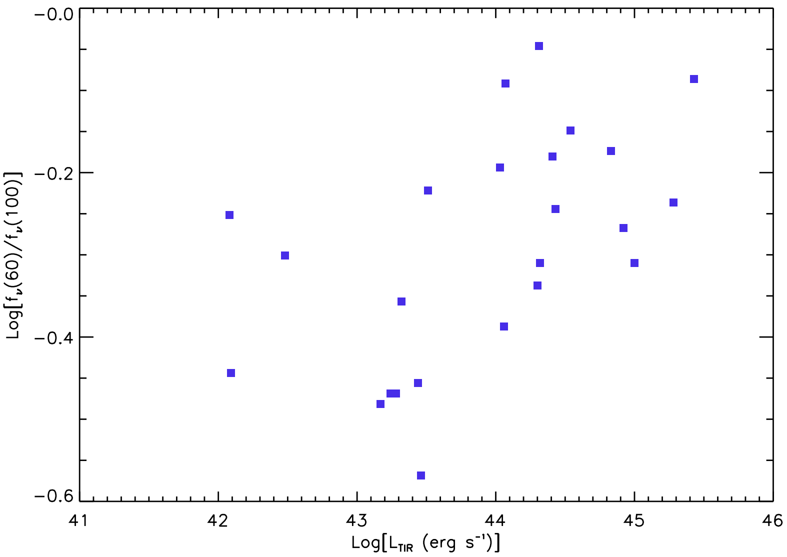

Figure 2.3: Plot of the ratio $f_\nu(60\mu\text{m})$-to-$f_\nu(100\mu\text{m})$, which is a proxy for the effective dust temperature, as a function of the total infrared luminosity $L_{\rm TIR}$ for the final galaxy sample.

effective temperatures, the IRAS 100 μm flux samples the SED peak of dust emission rather well. This was also confirmed by Kennicutt et al. (2009), as they found that the IRAS fluxes give a reliable representation of the total infrared luminosity for galaxies obeying $f_\nu(60\mu\text{m})/f_\nu(100\mu\text{m}) > 0.4$. Only six galaxies in our sample have a $f_\nu(60\mu\text{m})$-to-$f_\nu(100\mu\text{m})$ ratio below this value. Our sample covers a large range in distance, going from 3.9 to 139.1 Mpc. Four galaxies (NGC 4189, NGC 4293, NGC 4299 and NGC 7714) are in common with the sample that was used in Boselli et al. (2002b).

Although this final sample of 24 galaxies, gathering objects classified as HII region, starburst or LINER, is neither statistically significant nor representative for the whole of galaxies with diverging properties, this sample enables us to make a first preliminary analysis of the diagnostic capabilities of [CII] in tracing the star formation activity in galaxies. For a thorough analysis based on a more extensive sample of galaxies, we will have to wait until the completion of all [CII] surveys with the Herschel Space Observatory. Nevertheless, the broad range of optical and infrared luminosities covered in our sample enables us to infer the reliability of [CII] as a star formation indicator in star-forming galaxies spanning almost 4 orders of magnitude.

2.2.2 Reference SFR tracer

Having a complete picture of the star formation activity in a galaxy requires a combination of indicators that trace the dust-enshrouded and unobscured star formation. Since UV radiation is mainly originating from massive young stars, it is an ideal tracer for the unobscured star formation. Solely relying on this unobscured fraction will un-

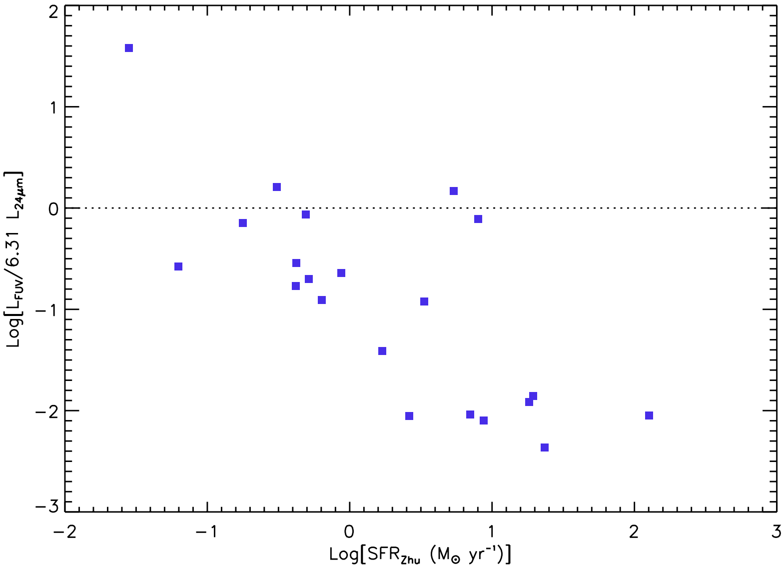

Figure 2.4: The ratio $L_{\mathrm{FUV,\,obs}}$ / 6.31 $L_{24\mu\mathrm{m}}$ as a function of the the total SFR, as derived from formula 2.4 and 2.5. This ratio of luminosities represents the fraction of unobscured star formation. The factor α in the denominator is the proportionality factor adopted from Zhu et al. (2008). For α = 6.31, they found that the sum $L_{\mathrm{FUV,obs}}$ + 6.31 $L_{24\mu\mathrm{m}}$ is a good approximation of the attenuation corrected *FUV* flux.

derestimate the true star formation activity, as starburst regions are often affected by strong attenuation from surrounding interstellar dust clouds. To acquire a complete picture of the rate at which stars are formed, the dust-enshrouded star formation must be traced as well. The total amount of enshrouded star formation can be traced by the total IR-luminosity. But also several monochromatic SFR indicators have proven to be reliable estimators for the star formation activity. In particular, the mid-IR emission at 24 μm shows a general correlation with the star formation rate (Boselli, Lequeux & Gavazzi, 2004; Calzetti et al., 2005; Wu et al., 2005; Alonso-Herrero et al., 2006; Pérez-González et al., 2006; Calzetti et al., 2007; Relaño et al., 2007; Bavouzet et al., 2008; Zhu et al., 2008; Rieke et al., 2009; Salim et al., 2009; Kennicutt et al., 2009)

Since the galaxies in our sample are dominated by dust-enshrouded star formation (see Figure 2.4, which shows the ratio of unobscured and dust-enshrouded star formation as a function of the SFR), the MIPS 24 μm and TIR luminosities, whether or not in combination with GALEX *FUV* fluxes, are considered a more reliable SFR indicator for the galaxies in our sample. One exception is NGC 4278, for which the unobscured fraction of star formation dominates dust-enshrouded 24 μm emission of young stellar objects. Furthermore, Figure 2.4 shows a hint for a decreasing trend in the unobscured fraction of star formation towards higher SFR. This trend can be accounted for by an increasing opacity for galaxies which form stars at a higher rate.

Comparison of different SFR indicators

In order to compare the different star formation relations, it is important that they are calibrated in the same way. Therefore we will relate all relations to the same initial mass function (IMF). This reference IMF will be the Kroupa (2001) IMF, characterized by a power law $\xi(\mathrm{m}) \propto \mathrm{m}^{-\alpha}$ with slope α = 2.3 for 0.5-100 $\mathrm{M}_{\odot}$ and α = 1.3 for 0.1-0.5 $\mathrm{M}_{\odot}$. We prefer the Kroupa (2001) IMF rather than the more commonly used Salpeter (1955) IMF (with a single slope α = 2.35 for 0.1-100 $\mathrm{M}_{\odot}$), since the former better correlates with IMF observations in the Galactic field (Chabrier, 2003; Kroupa & Weidner, 2003).

Analyzing all SFR relations and comparing them, requires a complete threefold approach:

- We first analyze the simple relation of the SFR as a function of the [CII] luminosity. Although this approach is most straightforward, the data might be biased towards larger distances. Since the distances to the galaxies in our sample range from 3.9 to 139.1 Mpc, we have to eliminate the distance bias in this luminosity versus luminosity relation.
- Plotting SFR/$4\pi D^2$ as a function of the [CII] flux, the distance bias is removed. If a true [CII]-SFR correlation is present, it will be confirmed in this plot.
- The dispersion around the mean trend is best quantified in a plot of the [CII] luminosity versus the residual of the best fitting relation between $L_{[\mathrm{CII}]}$ and the SFR. The SFR relation showing the tightest correlation with the [CII] luminosity will be characterized by the lowest dispersion in the residual plots. Thus, these plots will be useful to finally select the best SFR tracer suitable for calibrating the SFR against the [CII] luminosity.

1. **SFR calibration based on L_{TIR}**
   Taking into account that the 24 μm emission from a galaxy better correlates with the SFR as opposed to monochromatic FIR measurements at longer wavelengths (70 and 160μm) (Calzetti et al., 2010), we have only estimated the SFR, which is used for the final calibration of the SFR-[CII] relation, from 24 μm data (or FUV luminosities which have been corrected for attenuation based on 24 μm data) in this work. To obtain a second independent SFR diagnostic, we have investigated whether TIR luminosities for these galaxies could be used as a calibrator. Since we only have IRAS fluxes covering the whole galaxy for all sample objects to estimate the TIR luminosity, we checked whether an aperture correction was required. Although the galaxies in our sample were selected based on the criterion that they are unresolved in the FIR with respect to the ISO LWS beam, many of them are resolved within the ISO beam in optical data. Therefore, we visually inspected the MIPS 24 μm images and could indeed quantify that also

in the MIR a significant fraction of the total flux for several galaxies fell outside the aperture of the ISO beam. Subsequently, we verified the availability of MIPS 70 and 160 μm data in the Spitzer archive, to determine the correct TIR luminosities which correspond to the portion of the flux that falls within the same ISO beam. Considering that only 28 of the 38 sample galaxies have full coverage in all Spitzer bands, and some of those galaxies were only observed in small fields which does not allow proper convolution with the appropriate kernel to match the PSF's in all Spitzer bands, we decided not to use these Spitzer data. Moreover, the varying sizes of the sample galaxies would imply a different aperture correction (some are point sources and others are clearly more extended), introducing an additional bias to the TIR luminosity derived from these Spitzer data. While the MIPS 24 μm clearly demonstrate that the majority of our sample galaxies requires some kind of aperture correction, we have verified that the data currently at hand are not able to properly correct for these aperture issues. Any empirical correction can significantly bias the correlations between the [CII] luminosity and the SFR derived from this aperture-corrected TIR luminosity and does not allow us to draw any firm conclusion. Therefore, this analysis only investigates the correlation between [CII] and the SFR, when estimated from the 24 μm or attenuation-corrected FUV flux.

2. **SFR calibration based on $L_{24\mu m}$**
   Several SFR relations based on 24 μm emission have been published. Some authors claim a linear relation between the SFR and $L_{24\mu\text{m}}$ (Wu et al., 2005; Zhu et al., 2008), while others argue that only a non-linear relation can account for the increasing 24 μm emission in more IR-luminous galaxies which form stars at a higher rate (Wu et al., 2005; Pérez-González et al., 2006; Alonso-Herrero et al., 2006; Calzetti et al., 2007; Relaño et al., 2007; Zhu et al., 2008; Rieke et al., 2009; Boquien et al., 2010). As some galaxies in our sample are situated at the high luminosity end, we should be aware that this non-linear effect might affect our results. We choose to estimate the SFR from the relation in Rieke et al. (2009).

   Rieke et al. (2009) use a combination of a linear trend at lower TIR-luminosities and a non-linear relation above a threshold of $L_{\text{TIR}} > 10^{11}$ $L_{\odot}$ or $L_{24\mu\text{m}} > 1.3 \times 10^{10}$ $L_{\odot}$. Both relations were derived from a sample of dusty, luminous star-forming galaxies and hold up to $L_{\text{TIR}} = 2 \times 10^{12}$ $L_{\odot}$, which is higher than the most luminous galaxy in our sample (NGC 6240; 7.0×10^{11} $L_{\odot}$). The overlap between our range in TIR luminosities and the similar characteristics of both samples make us confident that this relation gives a good indication of the true star formation rate in our sample galaxies. The two relations from Rieke et al. (2009) are adjusted to our reference Kroupa (2001) IMF, as was done in Calzetti et al.

(2010):

$$\mathrm{SFR} = 2.04 \times 10^{-43} L_{24\mu m} \quad (2.1)$$

for $4 \times 10^{42} \leqslant L_{24\mu\mathrm{m}} \leqslant 5 \times 10^{43}$ erg s^{-1} and

$$\mathrm{SFR} = 2.04 \times 10^{-43} \times L_{24\mu m}(2.03 \times 10^{-44} L_{24\mu m})^{0.048} \quad (2.2)$$

for $L_{24\mu\mathrm{m}} > 5 \times 10^{43}$ erg s^{-1}, where SFR and $L_{24\mu\mathrm{m}}$ have units M$_\odot$ yr^{-1} and erg s^{-1}, respectively.

After estimating the SFR from these relations, we verify the strength of the correlation between $L_{[\mathrm{C\,II}]}$ and the SFR through a three-pronged approach. First, we plot the derived SFR as a function of $L_{[\mathrm{C\,II}]}$ (see Figure 2.5, upper panel). The best fitting line through the data points corresponds to:

$$\log \mathrm{SFR}_{24\mu m} = 1.040 \log L_{[\mathrm{C\,II}]} - 42.535 \quad (2.3)$$

where the units of $\mathrm{SFR}_{24\mu\mathrm{m}}$ and $L_{[\mathrm{C\,II}]}$ are in M$_\odot$ yr^{-1} and erg s^{-1}, respectively. The 1σ dispersion of the individual galaxies around the best fitting line is 0.30 dex. This 1σ dispersion has been calculated as the standard deviation of the logarithmic distance from the data points to the best fitting line weighted by the error on the individual quantities. Since the observed trend in this plot of luminosity versus SFR (and thus indirectly luminosity) might be biased by the range in distances among our sample galaxies, we remove this distance bias in the central panel of Figure 2.5. In this figure, we plot the SFR-to-4πD^2 ratio as a function of the [CII] flux. Since this distance-independent plot still shows a similar correlation between [CII] and the SFR and the dispersion 0.30 dex is of the same order as in the first panel, we safely conclude that the observed correlation in the upper panel of Figure 2.5 is not due to a distance bias in the data set. The dispersion around the mean trend (see Equation 2.3) is better represented in the bottom panel of Figure 2.5, which shows the residual plot. This residual plot will be of particular importance to quantify the dispersion of the data points and finally select the SFR relation with the tightest correlation (and thus smallest dispersion) to calibrate the SFR-$L_{[\mathrm{C\,II}]}$ relation.

3. **SFR calibration based on L_{FUV} + $L_{24\mu m}$**
   Before the GALEX *FUV* flux can be used as a direct quantifier of the star formation activity in a galaxy, a correction for internal dust attenuation has to be applied. The specific amount of extinction that is affecting the UV light is difficult to quantify, because different galaxies will be characterized by different extinction laws and a variation of stellar and dust distributions. In this section, we will

rely on SFR relations that use a combination of the GALEX *FUV* flux and the monochromatic MIR emission at 24 μm to obtain a complete picture of the star formation activity.

Two SFR relations have been reported, making use of both photometric data. First, Zhu et al. (2008)) derived a linear relation to estimate the attenuation-corrected *FUV*-flux based on the observed *FUV* and 24 μm data:

$$L_{\mathrm{FUV,corr}}[L_{\odot}] = L_{\mathrm{FUV,obs}}[L_{\odot}] + 6.31 L_{24\mu\mathrm{m}}[L_{\odot}]. \tag{2.4}$$

For the derivation of this relation, Zhu et al. (2008) relied on a sample of 187 star-forming (non-AGN) galaxies.

Another relation, reported in Leroy et al. (2008), also computes the SFR from both *FUV* and 24 μm data. Since a large fraction of our sample galaxies are characterized by a much higher star formation activity with respect to the sample in Leroy et al. (2008), we will apply the attenuation correction as reported in Zhu et al. (2008) and rely on the SFR relation in Kennicutt et al. (2009):

$$\mathrm{SFR} = 0.88 \times 10^{-28} L_{\mathrm{FUV,corr}}, \tag{2.5}$$

where the units of $L_{\mathrm{FUV,corr}}$ are in erg s^{-1} Hz^{-1}, to derive a star formation rate from the extinction-corrected *FUV* data. This relation was derived for a sample of normal galaxies in the Local Universe and most star-forming galaxies out to redshifts z $\sim$ 1. With an upper limit of log $L_{\mathrm{TIR}}[L_{\odot}] \sim 11.9$, the relation is not immediately representative for the most dust-obscured LIRGs or ULIRGs found in the present-day Universe (but this is not applicable for galaxies in our non AGN-dominated sample).

Figure 2.6 shows the correlation between $L_{[\mathrm{CII}]}$ and the $\mathrm{SFR}_{\mathrm{FUV+24}\mu\mathrm{m}}$ derived in this way. The best fitting line through all data points is given by:

$$\log \mathrm{SFR}_{\mathrm{FUV+24}\mu\mathrm{m}} = 0.983 \log L_{[\mathrm{CII}]} - 40.012 \tag{2.6}$$

where the units of $\mathrm{SFR}_{\mathrm{FUV+24}\mu\mathrm{m}}$ and $L_{[\mathrm{CII}]}$ are in M$_{\odot}$ yr^{-1} and erg s^{-1}, respectively. The spread around the mean trend is represented in the bottom panel of Figure 2.6 and can be quantified by a 1σ dispersion of 0.27 dex. The central panel of Figure 2.6 again confirms that the observed trend is not due to a distance bias in our sample, since the 1σ spread around the mean trend (0.26 dex) hardly differs in this distance independent relation.

Name (1)	Rieke+ 2009 ($M_\odot$ yr^{-1}) (2)	Zhu+ 2008+Kennicutt+ 2009 ($M_\odot$ yr^{-1}) (3)
Cartwheel	3.25 ± 1.14	7.97 ± 1.63
NGC 0520	5.04 ± 1.77	7.02 ± 1.43
NGC 0625	0.04 ± 0.01	0.06 ± 0.01
NGC 0660	1.23 ± 0.43	1.70 ± 0.35
NGC 0695	42.37 ± 14.88	62.63 ± 12.78
NGC 0986	3.87 ± 1.36	5.39 ± 1.10
UGC 02238	13.04 ± 4.58	18.19 ± 3.72
NGC 1156	0.06 ± 0.02	0.18 ± 0.04
NGC 1266	2.40 ± 0.84	3.34 ± 0.68
NGC 1317	0.18 ± 0.06	0.31 ± 0.06
NGC 2388	17.31 ± 6.08	23.35 ± 4.79
NGC 4041	1.82 ± 0.64	2.62 ± 0.53
NGC 4189	0.25 ± 0.09	0.42 ± 0.09
NGC 4278	0.014 ± 0.005	0.03 ± 0.01
NGC 4293	0.46 ± 0.16	0.64 ± 0.13
NGC 4299	0.18 ± 0.06	0.52 ± 0.11
NGC 4490	0.26 ± 0.09	0.42 ± 0.08
NGC 4651	0.47 ± 0.17	0.87 ± 0.18
NGC 5713	6.04 ± 2.12	8.73 ± 1.78
NGC 6240	101.85 ± 35.78	127.15 ± 25.94
NGC 7217	0.30 ± 0.11	0.49 ± 0.10
NGC 7552	10.99 ± 3.86	15.26 ± 3.11
NGC 7714	8.85 ± 3.11	13.34 ± 2.72
NGC 7771	14.06 ± 4.94	19.47 ± 3.97

Table 2.3: Star formation rates for the galaxies in our sample, derived from different SFR relations based on MIPS 24 μm data, or a combination of GALEX *FUV* and MIPS 24 μm data.

2.2.3 [CII]-SFR correlation

In the previous section, we found that the star formation rate correlates well with the [CII] luminosity. Table 2.3 summarizes the star formation rates obtained from the two different star formation relations for all galaxies in our reduced sample. Table 2.4 summarizes the coefficients a and b for the best fitting line $y = ax + b$ for each star formation tracer, the uncertainty on the slope a and intercept b and the 1σ dispersion of the individual galaxies around this mean trend. For both star formation relations, the

Variable	Slope	Intercept	1σ dispersion (dex)
$\mathrm{SFR}_{24\mu m,Rieke+2009}$	1.040±0.035	-42.535±1.441	0.30
$\mathrm{SFR}_{FUV+24\mu m,Zhu+2008+Kennicutt+2009}$	0.983±0.021	-40.012±0.858	0.27

Table 2.4: Coefficients and uncertainties of the best fitting line for the relation between $L_{[\mathrm{CII}]}$ and the two different SFR estimates.

uncertainties on the slope and intercept of the best fitting line are small and the spread around the mean trend is narrow. The dispersion around the correlation is smaller for the SFR derived from a combination of GALEX *FUV* and 24 μm data (0.27 dex), than when estimating the SFR from the single 24 μm luminosities (0.30 dex) (see also the bottom panels of Figures 2.5 and 2.6). Considering that a combination of *FUV* and 24 μm data traces the complete star formation activity, as opposed to the single 24 μm data, which only traces the obscured fraction of star formation, we will use the SFR probing both the dust-enshrouded and unobscured activity to calibrate the SFR relation.

From Eq. 2.6 we derive the SFR calibration:

$$\mathrm{SFR} = \frac{(L_{[\mathrm{CII}]})^{0.983}}{1.028 \times 10^{40}} \tag{2.7}$$

where the SFR and $L_{[\mathrm{CII}]}$ are in units of $\mathrm{M}_{\odot}$ yr^{-1} and erg s^{-1}, respectively. The SFR calibration factors are derived assuming a Kroupa (2001) IMF. This relation is valid for star-forming, late-type galaxies with a star formation activity in the range 0.03 - 127 $\mathrm{M}_{\odot}$ yr^{-1} and objects with a [CII] luminosity between $39.3 \leqslant \log L_{[\mathrm{CII}]}[\mathrm{erg\ s}^{-1}] \leqslant 42.7$ and a TIR luminosity between $42.1 \leqslant \log L_{\mathrm{TIR}}[\mathrm{erg\ s}^{-1}] \leqslant 45.4$.

Since the residual plot of this SFR relation (see Figure 2.6, bottom) indicates that the LINER galaxies in our sample contribute most to the observed scatter, we investigate whether a possible AGN contribution to the LINER galaxies introduces a bias to the derived SFR relation. If we calibrate the SFR relation for the 16 HII and starburst galaxies in our sample, we should see a significant difference if the LINER sample indeed introduces a bias, possibly due to a small AGN contribution to the 24 μm luminosities. From Figure 2.7 we can deduce that the best fitting line in our sample does not change substantially if we neglect the LINER galaxies for the SFR calibration. This already shows that the LINER sample does not introduce any bias due to a small AGN contribution. Moreover, half of the LINER galaxies are situated below the best fitting line.

From this tight correlation between the star formation rate and the [CII] luminosity, we conclude that the [CII] luminosity is a good star formation rate indicator. The applicability of [CII] as a star formation rate diagnostic had already been hinted by several authors (Stacey et al., 1991; Pierini et al., 1999; Leech et al., 1999; Boselli et al., 2002b; Stacey et al., 2010), but we were able to quantify this correlation in an accurate way. Figure 2.8 compares our SFR relation to the calibration obtained in Boselli et al. (2002b). Since Boselli et al. (2002b) assumed a Salpeter (1955) (α = -2.35) in the mass range between 0.1 and 100 $M_{\odot}$, we have divided their calibration coefficient by 1.51, to convert it to the Kroupa (2001) IMF (see Calzetti et al. 2010 for the derivation of the factor 1.51 difference between the Salpeter 1955 and Kroupa 2001 IMF calibrations). For low [CII] luminosity objects both calibrations are still quite consistent, but for galaxies with an increasing [CII] luminosity the SFR estimate provided by Boselli et al. (2002b) quickly diverges from our estimates up to a factor of $\sim$5 for the highest luminosity objects in our sample. This deviation towards higher [CII] luminosities is probably due to an underestimation of the Hα extinction in more luminous galaxies, since the attenuation relations at that time where calibrated without taking into account heavily obscured star formation and thus underestimating the true Hα emission. The scatter around the mean trend in our SFR relation is smaller than a factor of 2, while the dispersion in the [CII]-H_{α} luminosity relation already reaches a factor of $\sim$4. The final uncertainty on the SFR calibration in Boselli et al. (2002b) is estimated to be as high as a factor of $\sim$ 10. We believe the poorly known characteristics of the [NII] contamination and the attenuation correction at the time Boselli et al. (2002b) performed their SFR calibration explain a significant amount of their reported scatter. Benefiting from the increased database of [CII] observations and exploring other reliable SFR tracers in this analysis, we can revise the SFR calibration in Boselli et al. (2002b) and conclude that the [CII] emission is a reliable SFR indicator in most normal star-forming galaxies.

2.2.4 Applicability of the relation

The extension of this SFR relation to ULIRGS should however be treated with caution, since a decrease of the $L_{[\mathrm{CII}]}$-to-L_{FIR} ratio with increasing warm infrared colour for all galaxy types has been observed in many samples (Crawford et al., 1985; Stacey et al., 1991; Malhotra et al., 1997, 2001; Luhman et al., 2003; Verma et al., 2005; Brauher, Dale & Helou, 2008). More specifically, Luhman et al. (2003) report a [CII] line deficit in a sample of 15 ULIRGS, after they had noticed this trend in a few individual ultra-luminous objects (Luhman et al., 1998). Figure 2.9 hints at a similar, but weaker, trend for the galaxies in our sample. This effect is probably due to a decrease in efficiency of the photoelectric heating of the gas in strong radiation fields (Malhotra et al., 2001). Other possible explanations for this trend were given in Negishi et al. (2001) and Bergvall et al. (2000). Negishi et al. (2001) suggest an increased collisional de-excitation of [CII] due to an enhanced gas density, or a decrease in the ionized component for increasing star formation activity. While Bergvall et al. (2000) invokes the self-absorption of [CII] for galaxies with increasing metallicity. Recently, Papadopoulos, Isaak & van der Werf (2010) and Rangwala et al. (2011) claimed that a high dust optical depth could be the cause of this [CII] line deficit in several galaxies. If this trend in the [CII] line deficit holds for more IR-luminous galaxies, this might have its implications for the reliability of [CII] as a star formation indicator in those objects. Even more recently, Graciá-Carpio et al. (2011) inferred from their Herschel observations a similar line deficit for several other FIR fine-structure lines ([NII], [OI] , [NIII] , [OIII]). They allocate this deficit to a transition between two modes of star formation (in normal disk galaxies and major merger systems) with a different star formation efficiency.

On the other hand, Pierini et al. (1999) also report a decrease in the $L_{[\mathrm{CII}]}$-to-L_{FIR} ratio for decreasing Hα EW. This trend has been observed for more quiescent galaxies with Hα EW ≤ 10 Å and can be explained by an increasing contribution from older, less massive stars that heat dust grains and therefore contribute to the FIR-luminosity. The radiation from these stars is not hard enough to substantially heat the dust grains through the photoelectric effect (Pierini, Leech & Völk, 2003). Since collisions with these photoelectrons are the main heating source for the interstellar gas, this inefficient gas heating will render those galaxies [CII] quiet for an increasing contribution from a more evolved stellar population. This effect makes the extension from the SFR relation to quiescent galaxies not straightforward either. For objects with an extremely low star formation activity, Pierini et al. (1999) also found that the main contribution to the [CII] emission arises from the diffuse neutral interstellar medium. In our current sample, two galaxies (NGC 4293 and NGC 7217) satisfy the criterion Hα EW ≤ 10 Å, characterizing a quiescent galaxy (Kennicutt & Kent, 1983; Kennicutt et al., 2008). Since those galaxies do not deviate from the mean trend in the SFR-$L_{[\mathrm{CII}]}$ plot, a larger sample of quiescent galaxies is necessary to further investigate whether our SFR relation is expandable to objects with a lower SFR compared to the galaxies in the present sample.

Because of systematic variations in the $L_{[\mathrm{CII}]}$-to-L_{FIR} ratio and varying contribution with luminosity from several components (PDRs, diffuse cold neutral and warm ionized gas, HII regions) to the [CII] emission, we should be careful in extending the SFR relation in this analysis to more extreme luminosities, on both ends of the luminosity scale. Although the derived star formation relation might not be valid for more extreme cases of star formation activity (either very quiescent or actively star-forming), this calibration might be useful as an alternative indicator of the star formation rate in objects which lack either UV or IR observations. Since [CII] emission is hardly not affected by attenuation in most cases (currently, Arp 220 is the only object where prominent obscuration effects have been claimed), it might provide an immediate probe of the complete star formation activity.

At high redshift, the behaviour of the $L_{\text{[CII]}}$-to-L_{FIR} ratio is even different. Ultra-luminous objects (ULIRGs; $L_{\text{TIR}} > 10^{12}$ $L_{\odot}$) do not seem te be affected by a [CII] deficit. On the contrary, Maiolino et al. (2009) suggest an enhancement by at least one order of magnitude of the [CII] emission in galaxies at high-redshift compared to local galaxies of the same infrared luminosity. Maiolino et al. (2009) argues that this enhanced [CII] emission could be due to lower metallicities of the ISM in those high-redshift galaxies, which tend to have a lower dust content and therefore a larger [CII] emitting region. Independent of the physical origin of this effect, if confirmed by future observations, the strong [CII] emission from IR luminous high-redshift objects would have great implications for future observations at high redshift. This suggested increase in detectability of the [CII] line at high redshift would also imply an extensive applicability of a SFR relation based on [CII] luminosities.

Recently, Stacey et al. (2010) reported the detection of the [CII] line in 12 galaxies at redshifts ranging from 1 to 2. They concluded that for starburst-powered galaxies the [CII] emission is comparable to values found in local star-forming galaxies with similar FIR luminosities ([CII]/FIR $\sim$ 3×10^{-3}), while AGN-dominated galaxies are characterized by [CII]-to-FIR luminosity ratios similar to local ULIRGs ([CII]/FIR $\sim$ 4×10^{-4}), suggesting that this effect of enhanced [CII] emission only becomes apparent at even higher redshift (z>2). Stacey et al. (2010) also reported that [CII] is a reliable star formation indicator for their heterogeneous sample of starburst- and/or AGN-dominated galaxies in the redshift interval z = [1,2]. At even higher redshifts (z>2), the lower metallicity might influence the temperature and chemical structure of PDRs and, thus, the [CII] emission (e.g. Lequeux et al. 1994; Wolfire et al. 1995; Röllig et al. 2006). Future observations of ULIRGs with Herschel and ALMA will provide insight in the applicability of [CII] as a star formation indicator at high redshift and the validity of the star formation relation derived in this analysis.

2.2.5 Nature of the [CII] emission in galaxies

Besides the first accurate quantitative calibration of the star formation rate against the [CII] luminosity, the tightness of this correlation gives us insight in the origin of the [CII] emission on a global galaxy-scale. In this section, we introduce two possible explanations for the tightness of the SFR-[CII] relation.

Although PDRs are the main contributor to the [CII] emission in most galaxies, a significant fraction also originates in the cold neutral medium (CNM) (i.e. HI clouds, Kulkarni & Heiles 1987; Madden et al. 1993; Bennett et al. 1994; Wolfire et al. 1995; Sauty, Gerin & Casoli 1998; Pierini et al. 1999, 2001; Contursi et al. 2002), the warm ionized medium (WIM) (i.e. diffuse HII regions, Madden et al. 1993; Heiles 1994; Malhotra et al. 1997; Leech et al. 1999; Malhotra et al. 2001; Contursi et al. 2002) and to lesser extent also in HII regions (Stasińska, 1990) (see Section 2.1 for a quantitative analysis of these different contributions). Since the contribution from compact HII regions to the [CII] emission is negligible with respect to other components on galactic scales (e.g. Stasińska 1990; Malhotra et al. 2000), it is difficult to believe that the contribution from these star-forming regions alone causes this good correlation.

This brings us to a first possible explanation for the strong correlation between [CII] and the SFR. Considering that PDRs are neutral regions of warm dense gas at the boundaries between HII regions and molecular clouds, we think that most of the [CII] emission from PDRs arises from the immediate surroundings of star-forming regions. This might not be surprising, since FUV photons from young O and B stars escaping from dense HII regions, impinge on the surface of these neutral PDR regions where they will heat the gas through the photoelectric effect on dust grains. We believe that a more or less constant contribution from PDRs to the [CII] emission and the fact that this [CII] emission from PDRs stems from the outer layers of photon-dominated molecular clumps (i.e. at the boundary of molecular clouds and HII regions) might be a reasonable explanation for the tight correlation between the star formation rate and $L_{[\mathrm{CII}]}$. Also, Malhotra et al. (2001) suggest this tight correlation between PDRs and star-forming regions from their analysis of the FUV flux G_0 and gas density n in PDRs. The high PDR temperature and pressure required to fit their data, imply that most of the line and continuum FIR emission arises from the immediate proximity of expanding HII regions. Moreover, mapping of [CII] in the Milky Way (Bennett et al., 1994) and in spatially resolved nearby galaxies (see Sauvage, Tuffs & Popescu 2005 for an overview) provides further indications for a close association between PDRs and ionized gas in these galaxies.

Alternatively, we consider the likely possibility that this tight correlation is not the reflection of shared photoexcitation processes, taking place at the same position within a galaxy. On the contrary, the [CII] emission might not be directly linked to the star formation, but could instead trace the cold ISM being therefore indirectly related to the star formation through the Schmidt law (Kennicutt, 1998). Evidence confirming this indirect link is the association of [CII] emission with modest densities and softer FUV radiation fields (e.g Pineda et al. 2010).

A similar connection between the [CII] emission in a galaxy and the diffuse ISM is typically present in more quiescent objects (Pierini et al., 1999, 2001; Pierini, Leech & Völk, 2003), while in star-forming galaxies the [CII] line emission is found to mainly arise from PDRs (Crawford et al., 1985; Stacey et al., 1991; Madden et al., 1993). Mapping of [CII] at high resolution is necessary to ascertain the nature of the tight correlation between the SFR and [CII] emission for the normal star-forming galaxies in our sample.

Future observations of spatially resolved objects in the nearby universe and at high redshift of [CII], CO(1-0) and [NII] lines for a sample of galaxies ranging several orders of magnitude in IR-luminosity, will be able to disentangle the different components contributing to the [CII] emission, since the CO(1-0) intensity correlates well with [CII] in PDRs (Hollenbach & Tielens, 1999) and [NII] traces the HII regions and the warm ionized medium (Wright et al., 1991; Bennett et al., 1994). Such analysis will enable us to make a distinction between the different sources that contribute to the [CII] emission and, in particular, examine the tight correlation between the star formation rate and [CII] luminosity. High spatial resolution data will be able to distinguish whether [CII] emission from PDRs is closely related to star-forming regions in galaxies or the global [CII] emission in a galaxy rather traces the gas mass. The latter would imply an indirect link between [CII] and the star formation activity in a galaxy through the Schmidt law.

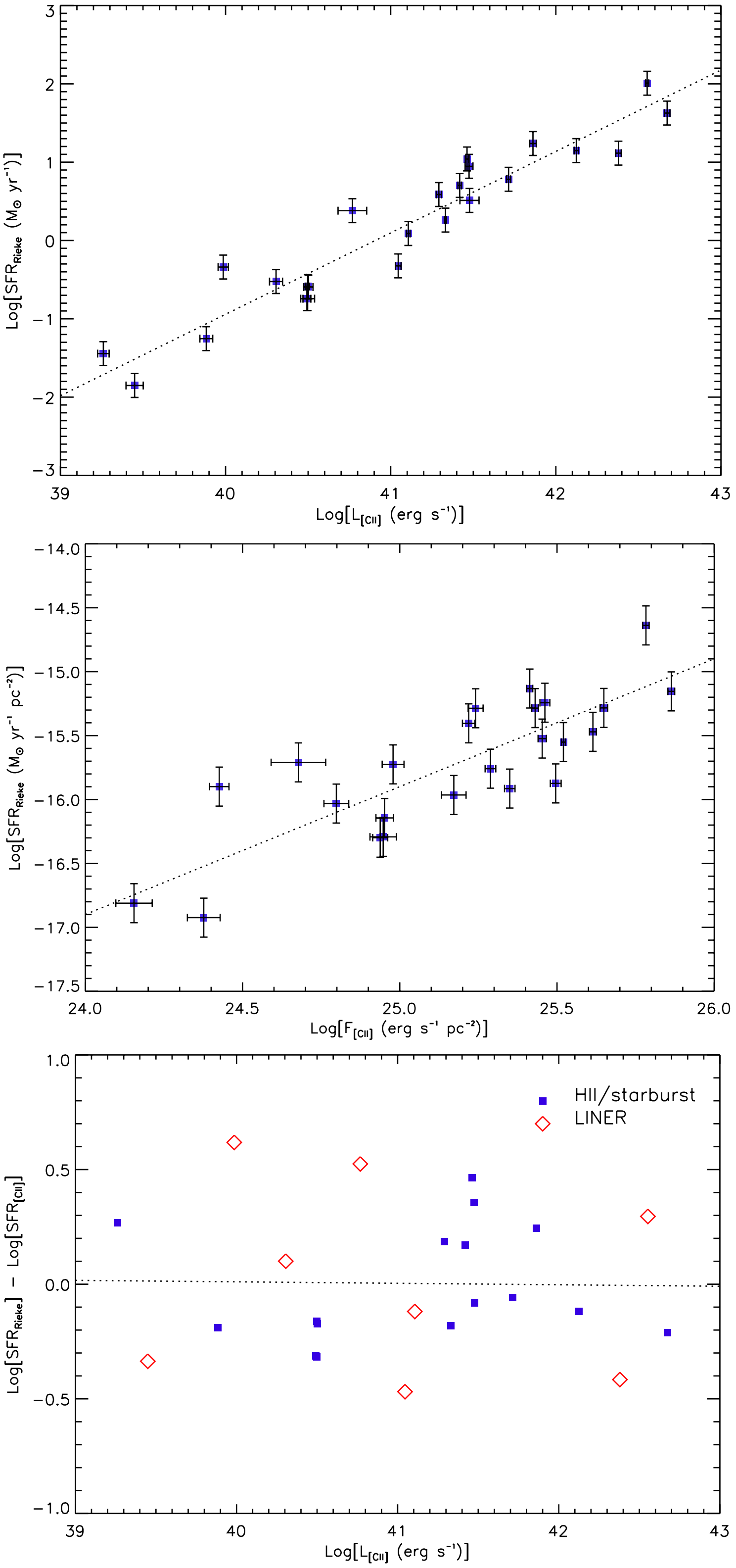

Figure 2.5: Upper panel: SFR$_{24\mu m}$ (SFR relation from Rieke et al. 2009) as a function of $L_{[\text{CII}]}$, central panel: SFR$_{24\mu m}/4\pi D^2$ as a function of [CII] flux, bottom panel: residuals of the SFR$_{24\mu m}$-$L_{[\text{CII}]}$ plot. In this residual plot, HII/starburst and LINER galaxies are indicated as blue filled squares and red diamonds, respectively.

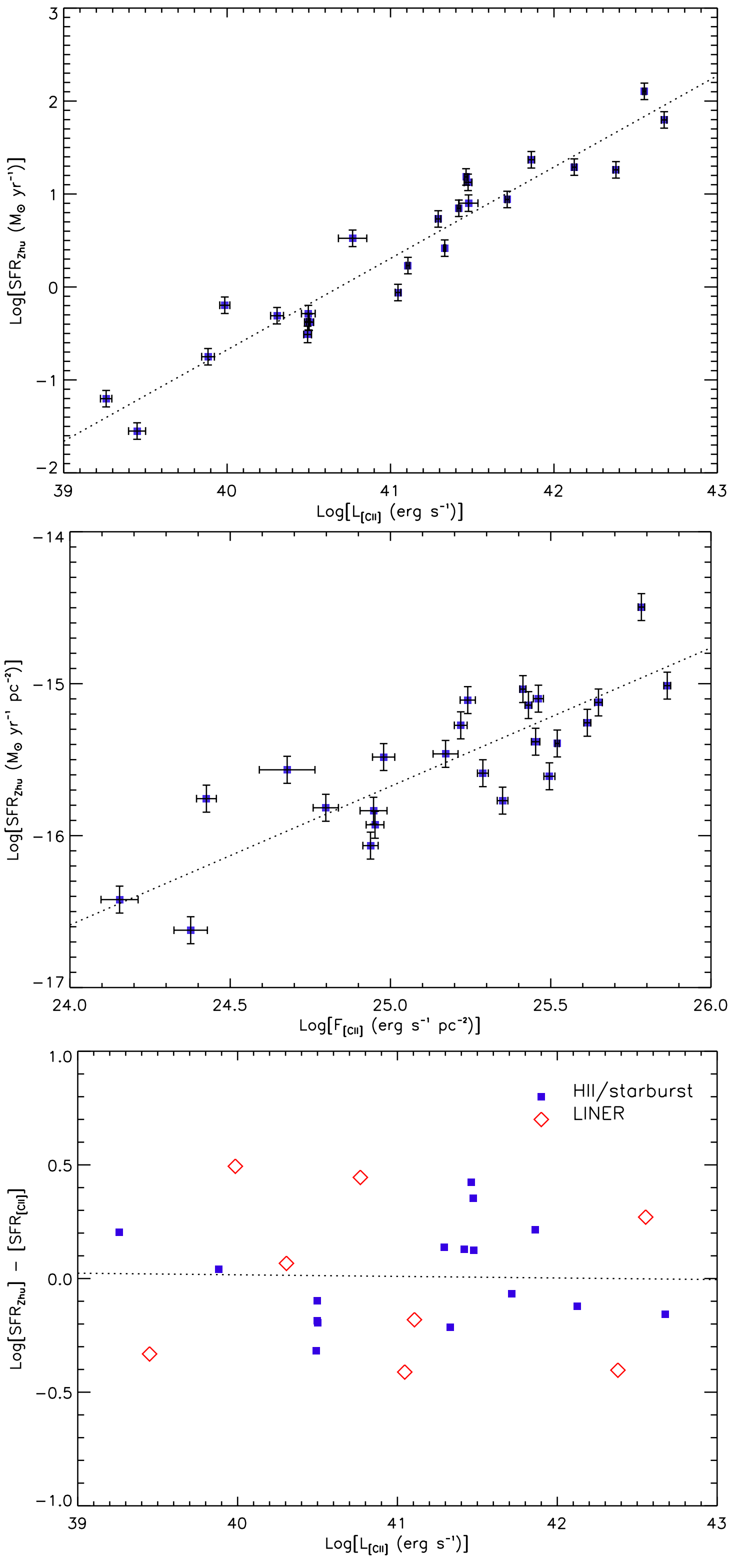

Figure 2.6: SFR$_{FUV+24\mu m}$ (attenuation correction and SFR relation from Zhu et al. (2008) and Kennicutt et al. (2009), respectively) as a function of $L_{[\mathrm{CII}]}$, central panel: SFR$_{FUV+24\mu m}/4\pi D^2$ as a function of [CII] flux, bottom panel: residuals of the SFR$_{FUV+24\mu m}$-$L_{[\mathrm{CII}]}$ plot. In this residual plot, HII/starburst and LINER galaxies are indicated as blue filled squares and red diamonds, respectively.

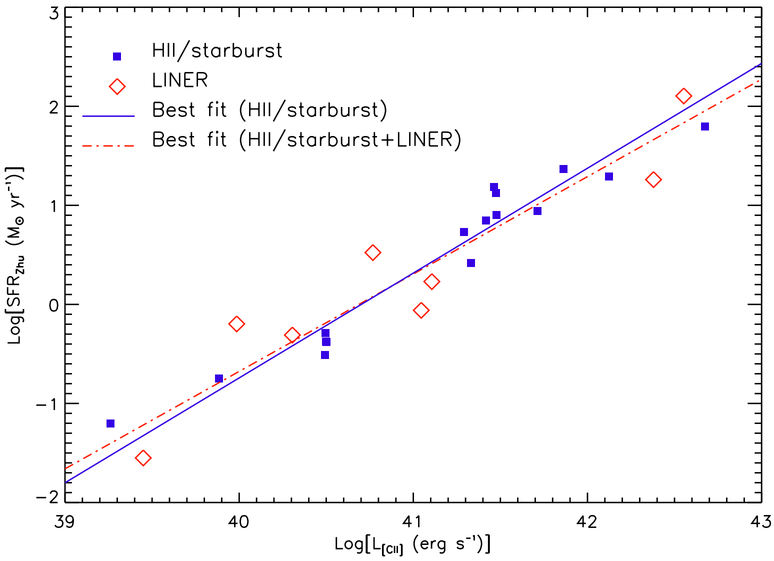

Figure 2.7: SFR$_{FUV+24\mu m}$ (attenuation correction and SFR relation from Zhu et al. (2008) and Kennicutt et al. (2009), respectively) as a function of $L_{[\mathrm{CII}]}$. In this plot, HII/starburst and LINER galaxies are indicated as blue filled squares and red diamonds, respectively. The best fitting line for the HII/starburst sample and the combined HII/starburst+LINER sample are shown as blue plain and red dashed-dotted lines, respectively.

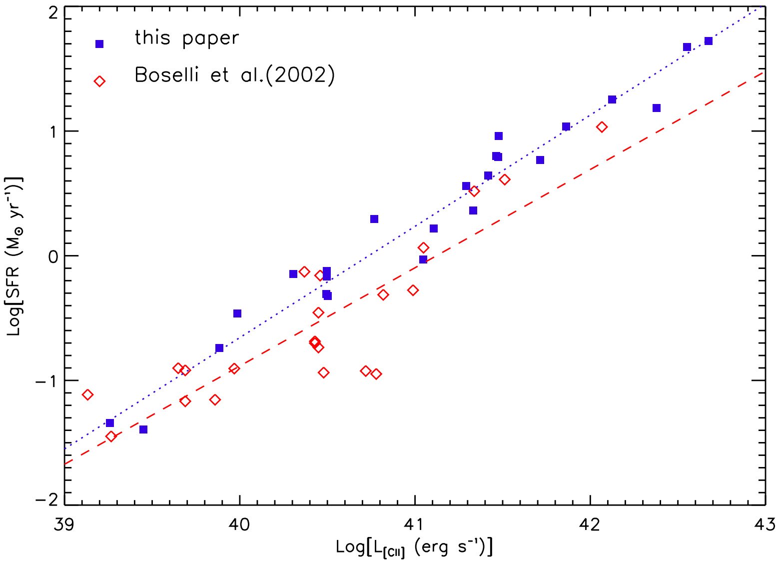

Figure 2.8: The star formation rate as estimated from relation 2.7 in this analysis (blue filled squares) and from the SFR calibration in Boselli et al. (2002b). Since Boselli et al. (2002b) assumed a Salpeter (1955) IMF (α = 2.35) in the mass range between 0.1 and 100 M$_\odot$, we have divided their calibration coefficient by 1.51, to convert it to the Kroupa (2001) IMF we applied. The best fitting lines for our calibration and the one in Boselli et al. (2002b) are indicated as blue dotted and red dashed lines, respectively.

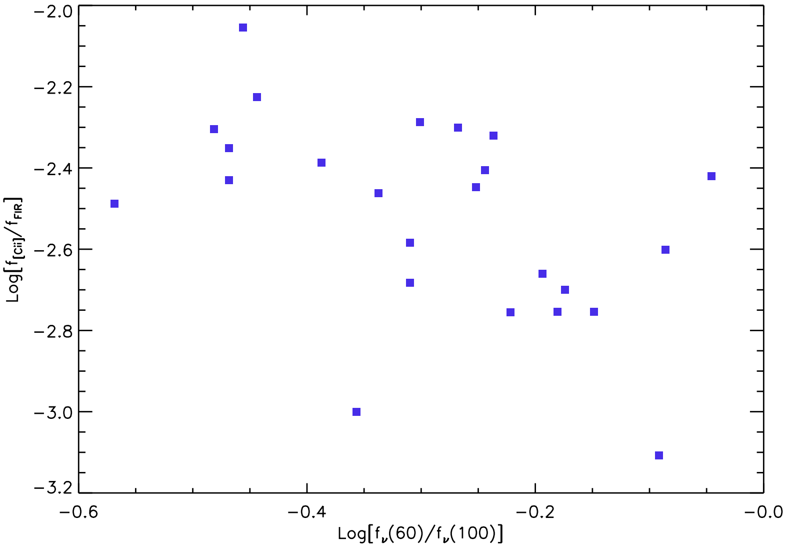

Figure 2.9: The ratio $L_{[\mathrm{C\,II}]}$-to-L_{FIR} as a function of the effective dust temperature, as embodied by the $f_{\nu}(60\mu\mathrm{m})$-to-$f_{\nu}(100\mu\mathrm{m})$ ratio, where the FIR luminosity was derived following Helou, Soifer & Rowan-Robinson (1985). We notice a decrease of the $L_{[\mathrm{C\,II}]}$-to- L_{FIR} ratio with increasing warm dust temperature.

3

Dust in cluster dwarf elliptical galaxies

3.1.1 Virgo Cluster

The Virgo Cluster is at a distance of $\sim$ 16.5 Mpc (Mei et al., 2007) the most nearby cluster and provides the unique opportunity to study galaxies in a cluster environment into large detail. The proximity of the Virgo Cluster also ensures the availability of a multi-wavelength set of ancillary data. In X-rays, Chandra and ROSAT observations are available. The space mission GALEX has also observed most of the Virgo cluster sources in the *NUV* and/or *FUV* bands (Cortese et al. 2004; GuViCS: Boselli et al. 2011). In the optical wavebands, SDSS provides well calibrated photometry in the *ugriz* filters and spectroscopic data covering a wavelength range from 3800 to 9000Å. At near-infrared wavelengths, 2MASS has covered the brightest sources in Virgo while fainter objects can typically be found in the UKIDSS catalog. Some galaxies in the cluster were already observed at far-infrared wavelengths with IRAS, ISO and/or Spitzer. For a large sample of VCC galaxies, Spitzer observations at 24 and 70 μm are at our disposal (Fadda, Biviano & Edwards 2010, Fadda et al. in prep.). Parts of the Virgo cluster were also observed in HI at 21 cm by several teams. With the ALFALFA survey (Giovanelli et al., 2005, 2007) covering the entire cluster, the Arecibo Galaxy Environments Survey (AGES, Auld et al. 2006) only observed some strips within the cluster but with an increased sensitivity.

The Virgo cluster is considered a rich cluster harboring a total mass of $\sim$ 0.15-1.5 $\times$ 10^{15} $M_{\odot}$ (Böhringer et al., 1994; Schindler, Binggeli & Böhringer, 1999) and a population of $\sim$ 2000 cataloged members (Virgo Cluster Catalogue (VCC), Binggeli, Sandage & Tammann 1985). Whereas the Fornax and Coma cluster are virialized clusters, the observed substructure and non-virialized motions in Virgo (e.g. Gavazzi et al. 1999) are indicative for the non-virialized nature of the cluster environment. This allows to study the effect of the cluster environment on individual galaxies and on the evolution of galaxies in general.

3.1.2 Sample selection

In view of testing the capabilities of the instruments on board the Herschel space satellite and arouse people's attention with the first results obtained from Herschel observations, the initial months of the space mission were allocated to Science Demonstration Phase (SDP) observations. In the frame of the Herschel Virgo Cluster Survey (HeViCS), the central 4 $\times$ 4 deg^2 region of the Virgo Cluster was observed by *Herschel* on the 29th of November 2009 as part of the HeViCS SDP observations. For these SDP observations, the central field was only covered once in orthogonal and nominal scan direction, with the complete survey covering this field in four such cross-scans and increasing the observed area by a factor of four. We used the HeViCS SDP observations to search for dust emission from dEs in the central regions of the Virgo Cluster. Selecting the galaxies with morphological type dE and dS0 in the Goldmine catalogue (Gavazzi et al., 2003) resulted in an initial sample of 370 dEs. After the removal of 16 galaxies classified as background sources and the exclusion of 115 sources with an additional optical source within a 6 arcsec radius, our final sample consisted of 239 dEs. Blind aperture photometry was applied to the PACS and SPIRE maps based on the positions of each of these 239 galaxies using Source Extractor (Bertin & Arnouts, 1996).

3.1.3 First detection of dust in cluster dEs

From this sample of 239 sources, 11 dEs were detected above 3σ in the SPIRE 250 μm image. Nevertheless, we only discuss the clear detection of 2 dEs, VCC 781 and VCC 951, excluding all sources raising any kind of doubt. As such, VCC 1502 and VCC 788 were ruled out because their FIR location differs more than FWHM/2 from their optical position. VCC 832 was excluded because SDSS images detect a background source with substructure in the residual image, possibly indicating the presence of dust. Four other objects (VCC 752, VCC 815, VCC 1272, VCC 1512) fall within a crowded field of sources, enhancing the chances of their being background sources. For instance, Binggeli, Sandage & Tammann (1985) report the detection of a blue compact background galaxy, only 4 arcsec to the west of the nucleus of VCC 815. Furthermore, VCC 752 and VCC 1272 appear to have SEDs that do not correspond to a single grey body. This failure in fitting the SED might either be caused by poor flux determination (the error bars are large compared to the low number of counts in the detection) or be a true indication that both detections originate in sources other than dEs. The other two sources VCC 1578 and VCC 767 are clearly detected in the SPIRE 250 μm image at 4.8 and 4σ, respectively, but their high FIR flux relative to their faint optical appearance (both objects are low surface brightness [LSB] galaxies with B-band magnitudes of the order $\sim$21 mag) aroused suspicion. Dust has already been detected in LSBs (Hinz et al., 2007), but mainly in those with large amounts of star formation responsible for dust heating. A lack of evidence of recent star formation in VCC 767 and VCC 1578 strongly argues against the association of the 250 μm emission with the corresponding dEs. Furthermore, we can identify a background source in the immediate surroundings of VCC 1578, which possibly contaminates the SPIRE 250 μm emission.

Although these questionable detections may still be attributable to dust emission from dEs, we restrict our current analysis to the detections with more credibility of being real

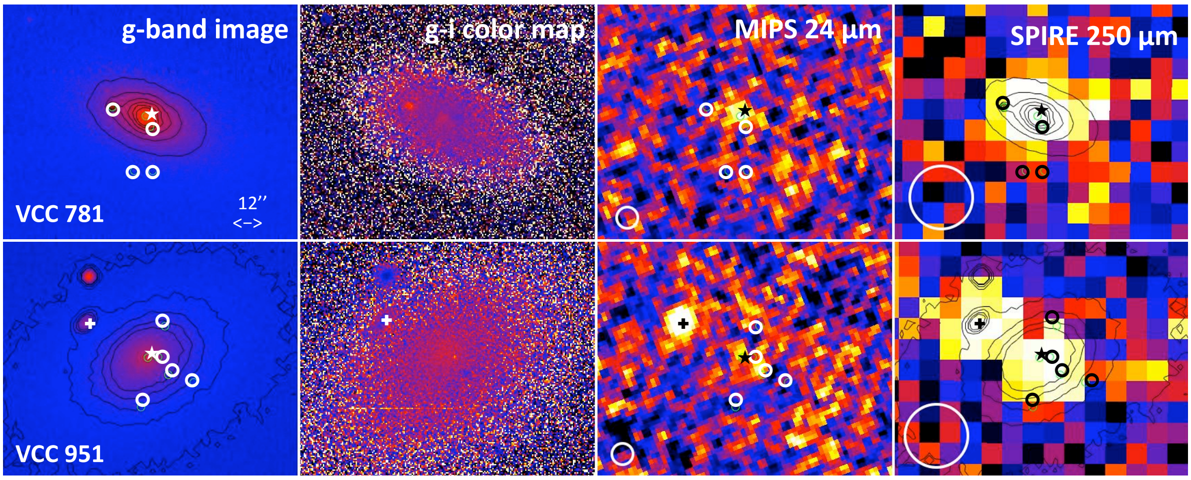

Figure 3.1: From top to bottom, left to right for VCC 781: the g-band image, g-i colour map, MIPS 24 μm image and the detection in the SPIRE 250 μm. All images are on the same scale. The FWHM of the beam is denoted in the MIPS 24 μm and SPIRE 250 μm images. g-band contours are overlaid on the SPIRE 250 μm image. The dwarf's position is indicated as a star, SDSS background sources as open circles, and the neighbouring source of VCC 951 as a cross.

detections. Relying on the complete dataset of Herschel Virgo Cluster observations, we will be able to draw final conclusions about the other sources as well (see Section 3.2). Deeper fields in the future might reveal dust emission in PACS images, where the higher spatial resolution may be able to rule out possible contamination by background sources.

3.1.4 Credibility of detection

VCC 781 and VCC 951 are detected unambiguously in the SPIRE 250 μm image at 9.8 and 11.1σ, respectively (see Fig. 3.1). Adopting a fair 2σ detection cutoff in the other filters, VCC 781 is also detected in the PACS 100 μm, PACS 160 μm, SPIRE 350 μm, and SPIRE 500 μm bands. VCC 951 has additional detections only in both SPIRE 350 μm and 500 μm images. Unfortunately, it is impossible to measure fluxes for VCC 951 at 350 μm and 500 μm because VCC 951 and its neighbouring source, SDSS J122655.56+114000.5, are not resolved at these longer wavelengths.

Since the SPIRE 250 μm image contains a vast number of sources, we need to address the possibility of false detections due to background sources. To perform this check accurately, we search all relevant images/catalogs (SDSS, Goldmine, 2MASS, UKIDSS, *Spitzer*) for sources within 18.1 arcsec (FWHM of SPIRE 250 μm) of the dwarf's positions. For VCC 781, this identifies four SDSS sources within this PSF region that may be contaminating the dust emission from the dwarf galaxy. The superior resolution in the PACS 160 μm image discards three of these optically identified objects, while the remaining source is rejected as a possible background candidate for the IR emission, based on the 24 μm image (data from Fadda et al. in prep.), which has an even higher spatial resolution, and is clearly extended. Hence, the coincidence of the position of detections at various wavelengths makes us confident that the IR emission originates from VCC 781.

The SDSS DR7 catalog provides us with 5 detections within the PSF region of VCC 951, three of which are very likely to be artifacts in the source extraction, since we detected them in neither the SDSS nor the UKIDSS images during our visual inspection. The remaining two, morphologically classified as stellar-like objects, are located at distances of 8″ and 10″, and are also detected in the UKIDSS images. The 24 μm image (see Fig. 3.1) shows some evidence of emission from both VCC 951 and one of the two aforementioned sources, which is spatially resolved at these wavelengths. Based on these data, we cannot definitely conclude that the IR emission detected by SPIRE comes from our dwarf galaxy, but deeper optical and NIR observations may help us to address this issue in the future.

We conclude that, while our analysis is unable to definitely exclude a possible contamination from background sources, the weight of evidence is in favour of a true detection of dust in emission from dEs, and in particular from VCC 781.

3.1.5 Properties of detected dEs

The detected dEs have remarkable morphologies. Binggeli, Sandage & Tammann (1985) classifies VCC 781 as dS0$_3$(5),N and VCC 951 as dS0(2),N or dE2 pec,N. These galaxies are also found to harbor central substructures other than a disk (Lisker, Grebel & Binggeli, 2006a), while Lisker et al. (2006b) identified blue central colours in VCC 781 and VCC 951. Figure 3.1 presents the $g - i$ colour images in which VCC 781 and VCC 951, respectively, exhibit an obvious gradient in their radial $g - i$ colour profiles, strengthening the assumption of recent star formation in the central regions (see also Lisker et al. 2006b).

According to the classification criterion ($3 <$ FUV-H < 6) adopted in Boselli et al. (2008a), VCC 781 and VCC 951 can also be classified as possible transition objects. Although the FUV-H colours of 6.6 and 6.9 mag for VCC 781 and VCC 951, respectively, do not satisfy this relation, both galaxies are clearly located at the blue end of the dE galaxies in Boselli et al. (2008a). That SDSS nuclear spectra of both galaxies exhibit deep Hydrogen absorption lines (EW[Hδ] $>$ 4 Å) indicates that they are in a post-starburst phase. This, and their 24 μm emission, which is indeed centered on the optical nuclei and concentrated ($\sim 6''$ for VCC781 and point-like for VCC951), argues in favour of a connection between dust emission and a recent episode of star-formation.

To estimate dust masses, we determined fluxes in bands where we had detections $> 2\sigma$. Initial apertures were fixed in the SPIRE 250 μm images based on the flattening of the growth curve. These apertures were subsequently adjusted to the pixel scale in other bands such that all apertures cover the same physical area. We first determined a representative dust temperature with the Monte Carlo code SKIRT under the assumption that the dust is in thermal equilibrium with the interstellar radiation field. The stellar body of each galaxy was represented as an exponential profile, with parameters taken from the Goldmine database. The dust was assumed to have the same distribution as the stars. For the intrinsic SED of the model, we used the elliptical galaxy template SED from the PEGASE library (Fioc & Rocca-Volmerange, 1997). Adding these ingredients, we find a representative dust equilibrium temperature of 20.7 K and 19.4 K for VCC 781 and VCC 951, respectively. Relying on these temperatures, we compute the dust masses according to

$$M_{\rm d} = \frac{S_{250}\, D^2}{\kappa_{250}\, B_{250}(T_{\rm d})}, \tag{3.1}$$

where $D = 16.5$ Mpc is the distance to the Virgo Cluster (Mei et al., 2007), $\kappa_{250} = 0.4$ m^2 kg^{-1} is the dust absorption coefficient (Draine & Li, 2001), and $B_{250}(T_{\rm d})$ is the Planck function for the modelled temperature $T_{\rm d}$. We obtain dust masses of 1.85×10^5 M$_\odot$ and 1.28×10^5 M$_\odot$ for VCC 781 and VCC 951, respectively.

As a check for consistency with datapoints other than the SPIRE 250 μm flux, we determine a second estimate of the temperature and dust mass based on grey body fitting. A single grey body fit to the 5 PACS and SPIRE fluxes gives T$_{\rm d}$ = 19.5 K and M$_{\rm d}$ = 2.24×10^5 M$_\odot$ for VCC 781 (see Fig. 3.2). These results are fully consistent with the temperature and dust mass of VCC 781 derived above. The MIPS 70 and 160 μm datapoints also satisfy the fitted greybody curve well (see Fig. 3.2).

Neither of the two dwarf galaxies is detected in HI. An HI mass upper limit was set to 2.3×10^7 $M_\odot$ for VCC 781 (Gavazzi et al., 2003) and 8.0×10^6 $M_\odot$ for VCC 951 (Conselice et al., 2003). Combining the estimated dust masses with these HI upper limits, and neglecting molecular gas, we find HI gas-to-dust upper limits of 124.3 and 62.5, respectively. These values are much lower than the expected canonical gas-to-dust ratio, possibly indicating that there is a dependence on other factors such as metallicity and environment.

3.1.6 Stacking analysis of non-detections

Apart from the two detections described in the previous section, we performed a stacking analysis of non-detected sources. In a first step we masked all bright sources in the surroundings of the dwarf galaxy (we prevented the inner pixel from being

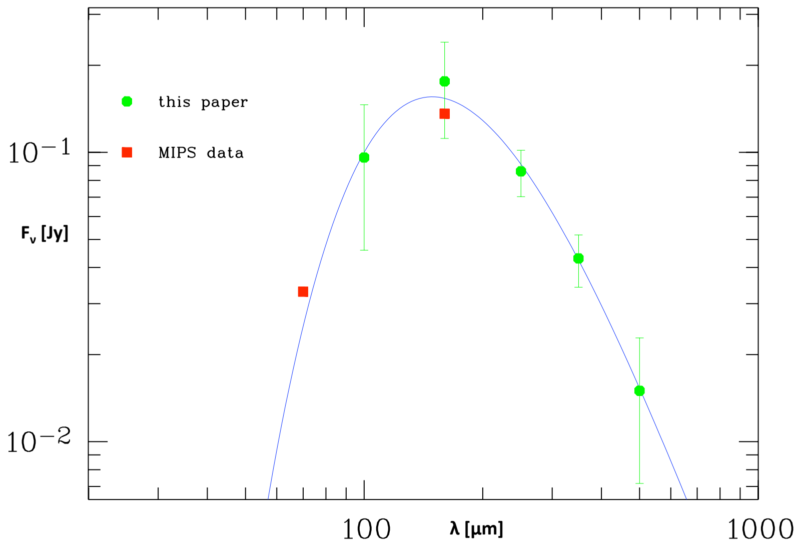

Figure 3.2: The best-fitting grey body for VCC 781 with T_d = 19.5 K and dust mass M_d = 2.24 × 10^5 $M_\odot$.

masked). We enlarged these masks using a boxcar with smoothing kernel of 3 pixels to cover the whole source. The final stacking algorithm weighs the images with the inverse of the background variance to acquire the mean value in each pixel (of all unmasked pixels).

Stacking the SPIRE 250 μm images of all 227 non-detected early-type dwarf galaxies results in no detection. When taking apertures of size equal to the SPIRE 250 μm beam at random positions and calculating the standard deviation in their distribution, we derive an estimated background rms of 0.38 mJy. Assuming an average dust temperature of T_d = 20K, we convert this noise estimate to a 3σ dust mass detection limit of $M_d = 2.44 \times 10^3$ $M_\odot$.

Since the noise measured locally has an average value of rms = 5 mJy/beam, the stacking is not significantly affected by confusion noise (the rms almost scales as Gaussian noise, $5/\sqrt{227} = 0.33 \approx 0.38$). The complete survey of 4 cross-scans will reach a 1σ sensitivity of 4.72 mJy on small spatial scales, considering both instrumental and confusion noise (the latter is determined to be 4 mJy at SPIRE 250 μm). Assuming that the stacking procedure is only marginally affected by confusion noise, this value translates into a 3σ detection limit of $M_d = 2.0 \times 10^3$ $M_\odot$. Comparing both values, we conclude that the stacked image nearly reaches the sensitivity limit, as the detection limit will only improve by a factor of 1.2 after the complete survey.

3.1.7 Detection rate

In our search for far-infrared dust emission in a sample of 239 dEs at the centre of the Virgo Cluster and with a dust detection limit of about 10^4 $M_{\odot}$ in the current SDP data, we have detected two objects at 10σ that have a high probability of being true detections of dEs. These two dwarf galaxies, VCC 781 and VCC 951, are the first detections of dust emission in dEs, apart from the Andromeda satellites NGC 205 and NGC 185. Applying a radiative transfer model to determine the equilibrium dust temperature in their interstellar radiation field, we determined temperatures of the order of 20 K in both galaxies. We estimate dust masses of the order $\mathrm{M_d} = 10^5$ $\mathrm{M_{\odot}}$ in both dEs.

In addition to independent detections of both atomic and molecular gas in dEs, the detection of dust emission here confirms the hypothesis that at least some dEs are transition objects gradually evolving from late-type to early-type, while falling into the cluster.

The detection of an interstellar dust medium in two dEs is rather unexpected, given the efficiency with which the ISM is removed from dwarf galaxies. Boselli et al. (2008a) found that gas removal by ram pressure stripping is extremely efficient in dwarf galaxies, there being a decrease by $\sim$2 orders of magnitude in $\sim$150 Myr of time. In agreement with this rapid morphological transition, only a small number ($10-16\%$) of dwarf galaxies exhibiting properties intermediate between star-forming and spheroidal galaxies are present in the Virgo Cluster.

di Serego Alighieri et al. (2007) find an HI detection rate in the Virgo cluster of only 1.7% to a 3σ mass limit $\mathrm{M_{HI}} = 3.5 \times 10^7$ $\mathrm{M_{\odot}}$. Adopting a canonical gas-to-dust ratio of 1000 (which might still be a conservative lower limit as dEs in Virgo are expected to have metallicities significantly lower than observed in our own Milky Way), we recover a 3σ dust mass limit of 3.5×10^4 $\mathrm{M_{\odot}}$, which is more or less the 3σ dust mass detection limit in the HeViCS SDP field. Our detection rate is also compatible with the 15% found by Conselice et al. (2003). Their HI upper limit corresponds to a 3σ dust mass limit of 8×10^3 $\mathrm{M_{\odot}}$, well above the SDP detection limit. When also taking into account the position in the cluster, we consider our detection rate of less than 1% surprisingly high. Indeed, HI detected dEs are preferentially located in the outskirts of the cluster and may not have been dramatically affected so far by the intracluster medium and interactions with other galaxies (Conselice et al., 2003; Buyle et al., 2005). di Serego Alighieri et al. (2007) also report that the majority of the detected HI-sources are located near the edges of the Virgo cluster. If gas and dust are tightly coupled and dust is as easily removed from the galaxy as gas by ram pressure stripping, harassment, or tidal effects, we expect that the dEs in the central regions of the Virgo Cluster will also be the most dust deficient. Clear evidence of efficient dust stripping in the Virgo

Cluster is seen for the first time in HI-deficient spiral galaxies (Cortese et al., 2010a). A comparison of the far-infrared detection rate with the position in the cluster from the complete HeViCS survey will tell us whether environmental effects have any influence on the detection rate.

3.2.1 Transition-type galaxies: definition and selection

Transition-type galaxies are objects with spectrophotometric properties in between those of late-type spiral galaxies and quiescent early-type galaxies, i.e. they have the optical appearance of elliptical or lens-shaped galaxies, but a number of properties (e.g. starburst- or post-starburst characteristics, significant gas content, bar or spiral subtructure, etc.) hint at their transformation of a late-type spiral galaxy to an early-type object. Upon comparison of a multi-wavelength dataset of observations with predictions of multizone chemospectrophotometric models of galaxy evolution, Boselli et al. (2008a) could identify ram-pressure stripping as the most likely transformation process. They compared the effect of ram-pressure stripping (Gunn & Gott, 1972) and starvation (Larson, Tinsley & Caldwell, 1980) on the gas content, colours, metallicity, etc. of late-type galaxies. On timescales of less than 1 Gyr, ram-pressure stripping was found to be capable of significantly altering the properties of late-type galaxies, whereas starvation would require at least 6 Gyr to achieve such drastic changes in the spectrophotometric properties of galaxies (Boselli et al., 2008a).

With the recent launch of the Herschel telescope, the dust content in those transition-type objects could be probed as well. To identify all transition-type galaxies in the fields covered by the Herschel Virgo Cluster Survey (HeViCS, Davies et al. 2010a) and the Herschel Reference Survey (HRS, Boselli et al. 2010a), we select all early-type galaxies (E, E-E/S0, S0, dE, dE/dS0) from the Goldmine database[1] (Gavazzi et al., 2003). All background sources are excluded from this sample based on the argument that Virgo cluster membership is restricted to galaxies with heliocentric velocities v < 3000 km s^{-1}. Since we are only interested in objects of low mass, which are more easily affected by gravitational and/or environmental processes, we restrict our sample to galaxies with H band luminosities $L_H < 10^{9.6}$ $M_\odot$ (scaled to a distance of D = 17 Mpc). Given our focus on the properties of dust in those objects, we only retain those objects covered in the observed fields of the HeViCS or HRS programs. This selection procedure results in a sample of 886 early-type, low-mass objects observed by Herschel.

From this sample of galaxies, we then select all transition-type galaxies. To identify whether a galaxy is a transition-type object, we look at the FUV-H colour of a galaxy, since this colour has been shown to change most rapidly for galaxies transforming from late-type to early-type objects (Boselli et al., 2008a). Based on the FUV-H colours

---

[1] http://goldmine.mib.infn.it/

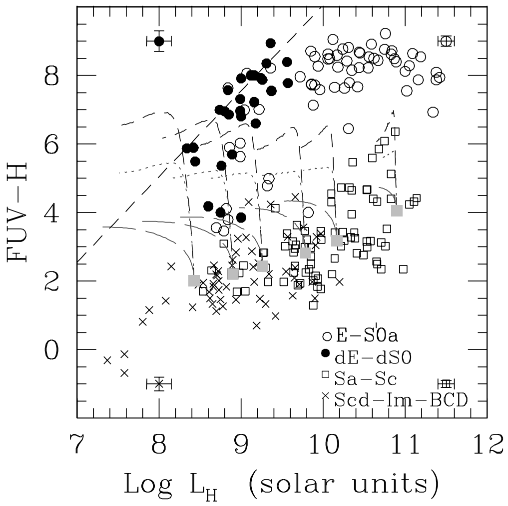

Figure 3.3: FUV - H colour index (in AB magnitudes) as a function of the *H* band luminosity for galaxies in the Virgo cluster. This plot was adopted from Figure 7 in the paper Boselli et al. (2008a). The symbols representing the different galaxy types are indicated in the legend of the image.

of late-type spiral galaxies on the one hand and quiescent early-type galaxies on the other hand (see Figure 3.3), we set up the following colour criterion to select transition-type galaxies:

$$5 < FUV - H\,[AB] < 8, \tag{3.2}$$

where the FUV-H colour is expressed in AB magnitudes. Considering that not all galaxies have *FUV* and/or *H* band measurements, we additionally select galaxies based on their spectral characteristics. All early-type galaxies with available SDSS spectra (i.e. 255 objects) were analyzed with a spectral fitting code (Fritz et al., 2007) to determine Hα, Hβ and Hδ equivalent widths. Both galaxies with spectral properties representative for ongoing star formation, i.e.:

$$H\alpha\ EW_{em} > 2\ \text{Å}, \tag{3.3}$$

as well as galaxies with post-starburst characteristics, fulfilling either

$$H\beta\ EW_{abs} > 2.8\ \text{Å} \tag{3.4}$$

or

$$H\delta\ EW_{abs} > 4.0\ \text{Å} \tag{3.5}$$

are classified as transition-type object. The spectra from galaxies selected based on these criteria were checked by eye, to verify the spectral line measurement. Galaxies with noisy spectra were considered unreliable identifications and, therefore, excluded from the transition-type galaxy sample. Based on the FUV - H colours of 50 galaxies, we retained 17 transition-type galaxies. From the spectral selection criteria, we could identify 11 star-forming and 57 post-starburst galaxies out of 255 objects with available SDSS spectra. Taking into account that some galaxies were selected based on both criteria, the total number of transition-type objects identified in the Virgo cluster sums up to 81 objects. The main properties for those galaxies are summarized in Table 3.1, mentioning the VCC number for each galaxy, its morphological classification, the distance to the galaxy and the sub-cluster or cloud within the Virgo cluster, where the transition-type object is located. The FUV - H colour in AB magnitudes is reported as well as the equivalent widths of Hα emission, Hβ and Hδ absorption lines measured from the SDSS spectrum. Figure 3.4 gives the position within the Virgo cluster of the transition-type galaxies.

Table 3.1: Transition-type galaxies in Virgo with their VCC number, morphological classification, distance D, position within sub-clusters or clouds in Virgo, FUV-H colour, Hα EW, Hβ and Hδ equivalent width.

VCC	**type**	**D [Mpc]**	**Pos**	FUV-H^1 **[AB]**	**Hα EW^1 [Å]**	**Hβ EW^1 [Å]**	**Hδ EW^1 [Å]**
29	dE	32	M	-	2.5	1.18	4.6
46	dE	32	M		-	2.85	5.73
50	dE	32	M	-	2.64	4.25	2.79
93	dE	32	M	-	-0.46	2.94	/
109	dE	32	M	-	2.25	5.44	/
181	dE	17	N	-	-86.34	-14.98	0.47
200	dE	17	N	-	2.51	2.87	2.29
209	dS0	17	N	-	-15.06	-1.51	1.65
216	dE	32	W	-	0.50	3.73	4.38
278	dS0	23	B	-	-9.49	2.84	2.48
304	dE	17	N	-	-19.32	-1.13	/
327	S0	32	W	6.3	-19.57	2.14	4.47
338	dE	32	W	-	/	3.26	2.97
346	dE	23	B	-	/	2.85	5.73
388	dE	23	B	-	3.64	8.68	/
394	dE	32	W	-	/	5.05	/
450	S0	23	B	6.98	-	-	-

Table 3.1 – continued from previous page

VCC	type	D [Mpc]	Pos	FUV-H[1] [AB]	Hα EW[1] [Å]	Hβ EW[1] [Å]	Hδ EW[1] [Å]
501	dE	17	A	-	/	3.77	3.18
525	dE	23	B	-	-10.21	0.94	/
571	S0	23	B	7.44	-	-	-
611	dE	23	B	-	-18.83	-4.41	6.83
636	dE/dS0	17	A	6.86	-	-	-
695	dE	23	B	-	2.77	8.09	4.78
710	dS0	17	S	4.87	-33.66	-4.08	2.68
756	dE	23	B	-	4.19	4.57	
760	dE	17	A	-	/	5.77	1.83
764	S0	17	S	7.11	-	-	-
779	dE	17	A	-	/	-0.59	5.31
781	dS0	17	A	8.29	/	1.49	4.44
788	dE	17	A	8.34	2.54	0.52	5.05
815	dE	17	A	-	/	4.05	/
817	dE	17	A	-	2.33	3.77	3.03
820	dE	23	B	-	2.20	3.08	3.98
861	dE	17	A	-	/	4.15	/
871	dE	17	A	-	/	3.44	5.72
936	dE	17	A	7.69	1.68	-0.05	/
951	dE/dS0	17	A	7.95	1.75	3.16	4.41
953	dE	17	A	8.36	2.70	3.21	4.99
1039	dE	17	A	-	/	8.32	/
1064	dE	17	A	-	/	3.43	5.08
1065	dE	17	A	7.25	2.15	1.99	0.80
1078	dE	23	B	-	-3.72	0.09	3.89
1099	dE	17	A	-	1.45	3.53	/
1104	dE	17	A	-	3.46	0.83	5.07
1129	dE	17	A	-	4.73	7.77	/
1175	E-E/S0	23	B	5.36	-171.99	-35.47	/

Table 3.1 – continued from previous page

VCC	type	D [Mpc]	Pos	FUV-H[1] [AB]	Hα EW[1] [Å]	Hβ EW[1] [Å]	Hδ EW[1] [Å]
1191	dE	17	A	-	/	3.67	5.26
1204	dE	17	S	-	2.35	3.42	/
1209	dE	17	A	-	/	9.30	/
1314	dE	17	A	-	/	6.40	9.20
1323	dE	17	A	-	/	2.87	/
1352	dE	17	A	-	0.08	7.8	4.54
1353	dE	17	A	-	3.46	0.83	5.07
1369	dE	17	A	-	/	2.91	4.93
1389	dE	17	A	6.99	3.26	2.67	3.01
1399	dE	17	A	-	/	3.29	2.13
1407	dE	17	A	8.41	1.91	3.32	1.01
1414	dE	17	A	-	1.19	3.63	/
1420	dE	17	A	-	/	4.42	0.78
1488	E-E/S0	17	S	-	3.25	3.62	4.75
1489	dE	17	A	-	1.85	3.25	2.99
1499	E-E/S0	17	A	5.19	4.85	6.06	6.36
1501	dS0	17	S	5.66	-	-	-
1509	dE	17	S	-	1.22	6.75	/
1512	dS0	17	A	7.03	-	-	-
1539	dE	17	A	7.49	1.20	/	5.0
1606	dE	17	A	-	/	4.18	/
1616	dE	17	A	-	/	7.07	/
1647	dE	17	A	-	3.37	3.53	1.23
1674	dE	17	A	-	/	5.20	/
1682	dE	17	A	-	/	3.31	/
1684	dS0	17	A	6.82	-4.64	1.86	3.13
1695	dS0	17	A	9.39	2.84	3.62	2.84
1704	dE	17	A	-	3.15	4.02	1.45
1710	dE	17	A	-	/	0.50	7.40

Table 3.1 – continued from previous page

VCC	**type**	**D** [Mpc]	**Pos**	*FUV-H*[1] [AB]	**Hα EW**[1] [Å]	**Hβ EW**[1] [Å]	**Hδ EW**[1] [Å]
1711	dE	17	A	-	1.59	1.1	4.12
1715	dE	17	S	5.07	-	-	-
1794	dE	17	E	-	/	7.67	/
1809	S0a-S0/Sa	17	E	6.22	-	-	-
1951	dE	17	E	-	/	2.91	4.93
1989	dE	17	E	-	/	8.01	2.58

[1]'-' means that no data were available for this galaxy,
'/' means no line was detected

3.2.2 Herschel detections

The Herschel observations of the HeViCS and HRS programs are searched for detections of the 81 transition-type galaxies in our sample. From this analysis, we could detect 14 transition-type galaxies with dust reservoirs massive enough to be detectable by Herschel. The fluxes used in this analysis were taken from the paper (Auld et al. subm.), discussing the detectability of galaxies from the VCC catalog in the HeViCS fields. Only one source (VCC 1809) was detected in an observed HRS field, for which we adopted the uncertainty measurements from Ciesla et al. (2012).

From a modified black-body fit for a fixed dust emissivity β = 2 and dust absorption coefficient $\kappa_{250\mu m}$ = 0.4 m^2 kg^{-1} (Draine & Li, 2001) to PACS and SPIRE fluxes, we determine dust masses and temperatures for all detected transition-type galaxies (see Table 3.2). In case fluxes with a signal-to-noise level $> 3\sigma$ are available in less than three wavebands, we estimate the dust mass from the flux measurement in the SPIRE 250 μm waveband. Likewise, dust mass upper limits are calculated from the 3σ upper limit at 250 μm for the non-detections, according to the formula:

$$S_\nu = \frac{\kappa_\nu \, M_d \, B(\nu, T_d)}{D^2}, \tag{3.6}$$

for $\kappa_{250\mu m}$ = 0.4 m^2/kg. For the non-detections, we assume a dust temperature of T_d = 15 K, since this value is close to the average model temperature of the dust in the detected transition-type galaxies. Figure 3.5 (right panels) shows the SED fits for the galaxies with three or more detections in different Herschel bands. The fluxes used

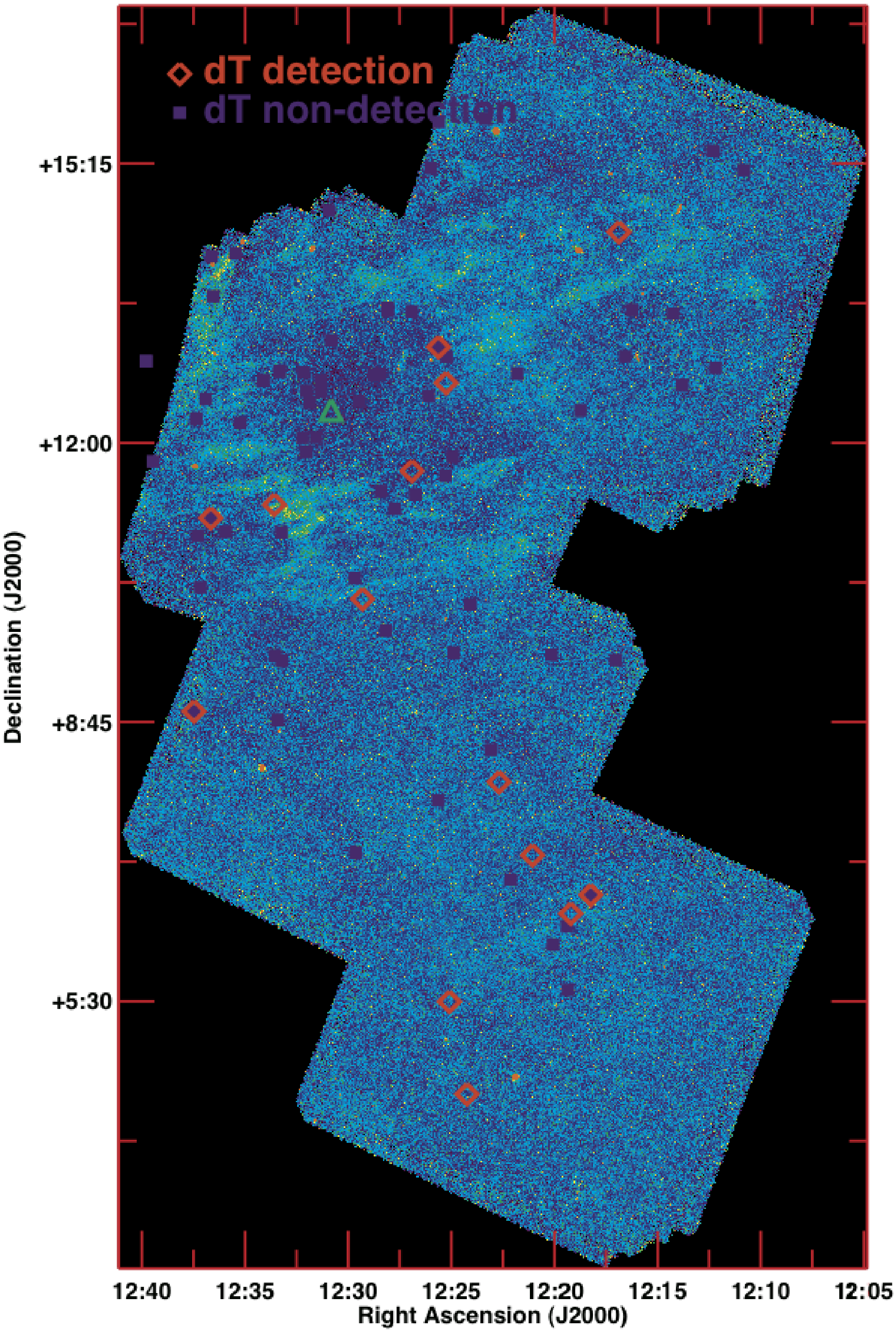

Figure 3.4: Map of the dust emission originating from the Virgo cluster as observed from the SPIRE 250 μm image. The location of all 81 transition-type galaxies are shown on the plot. For better reference, the position of M87 has been indicated by a green triangle.

in the SED fitting procedure are indicated in green. Fluxes that were neglected in the fitting procedure are colour-coded in red. In particular, fluxes at 100 μm were often banned from the SED fit because they showed clear evidence for the presence of a warmer dust component in addition to the colder dust reservoir (e.g. VCC 450) or because the 100 μm flux aroused suspicion (e.g. VCC 209, VCC 571).

Table 3.2: Fitted dust masses and temperatures, HI masses and gas-to-dust ratios for the transition-type galaxies in the Virgo cluster. In case of no detection, 3σ upper limits for the dust mass at an assumed temperature of $T_d \sim 15$ K are provided.

VCC	M_d **[log** $\mathbf{M_\odot}$**]**	T_d **[K]**	$M_{\mathbf{HI}}$[1] **[log** $\mathbf{M_\odot}$**]**	**HI ref**[2]	**G-to-D**[3]
	[log $\mathbf{M_\odot}$**]**	T_d **[K]**	$M_{\mathbf{HI}}$[1] **[log** $\mathbf{M_\odot}$**]**	**HI ref**[2]	**G-to-D**[3]
Herschel detections					
209	6.03	14.8	7.57	1	**35**
278	5.40	15	< 7.63	2	> 170
327	6.11	17.1	< 8.47	2	> 229
450	6.33	15.3	7.66	3	**21**
571	6.03	14.4	< 8.18	2	> 141
710	6.16	12.8	7.87	1	**51**
764	5.29	16.6	8.14	1	**708**
781	5.63	15.3	< 7.37	2	> 55
815	5.30	15	< 7.37	2	> 117
951	5.70	14.1	< 6.9	2	> 16
1175	5.38	15	< 8.18	2	> 631
1512	5.33	15	< 7.37	2	> 110
1684	5.09	15	< 7.37	2	> 191
1715	5.00	15	< 7.37	2	> 234
Herschel non-detections					
29	< 6.27	15	< 7.92	2	-
46	< 5.93	15	< 7.92	2	-
50	< 6.0	15	< 7.92	2	-
93	< 6.0	15	8.11	2	> 129
109	< 5.97	15	< 7.92	2	-
181	< 5.27	15	< 7.37	2	-
200	< 5.39	15	< 7.37	2	-
216	< 5.93	15	< 7.92	2	-
304	< 5.5	15	7.53	3	> 107
338	< 6.02	15	< 7.92	2	-

346	< 5.53	15	< 7.63	2	-
388	< 5.58	15	< 7.63	2	-
394	< 6.05	15	< 7.92	2	-
501	< 5.42	15	< 7.37	2	-
525	< 5.65	15	< 7.63	2	-
611	< 5.61	15	7.12	3	> 32
636	< 5.43	15	< 7.37	2	-
695	< 5.53	15	< 7.63	2	-
756	< 5.58	15	< 7.63	2	-
760	< 5.57	15	< 7.37	2	-
779	< 5.42	15	< 7.37	2	-
788	< 5.55	15	< 7.37	2	-
817	< 5.31	15	< 6.81	2	-
820	< 5.53	15	< 7.63	2	-
861	< 5.93	15	< 7.37	2	-
871	< 5.27	15	< 7.37	2	-
936	< 5.63	15	< 7.37	2	-
953	< 5.42	15	< 6.6	2	-
1039	< 5.53	15	< 7.37	2	-
1064	< 5.45	15	< 7.37	2	-
1065	< 5.47	15	< 7.37	2	-
1078	< 5.79	15	< 7.63	2	-
1099	< 5.42	15	< 7.37	2	-
1104	< 5.39	15	< 7.84	2	-
1129	< 6.27	15	-	-	-
1191	< 5.39	15	-	-	-
1204	< 5.27	15	< 7.37	2	-
1209	< 5.5	15	< 7.37	2	-
1314	< 5.35	15	-	-	-
1323	< 5.57	15	< 7.37	2	-
1352	< 5.5	15	-	-	-
1353	< 5.45	15	-	-	-

1369	<5.27	15	-	-	-
1389	<5.34	15	-	-	-
1399	<5.35	15	-	-	-
1407	<5.35	15	<6.54	2	-
1414	<5.27	15	-	-	-
1420	<5.95	15	-	-	-
1488	<5.76	15	<7.92	2	-
1489	<5.67	15	<7.37	2	-
1499	<5.45	15	-	-	-
1501	<5.49	15	9.05	3	>3631
1509	<5.42	15	<7.37		
1539	<5.39	15	-	-	-
1606	<5.31	15	<7.37	2	-
1616	<5.5	15	<7.37	2	-
1647	<5.5	15	<7.37	2	-
1674	<5.67	15	<7.37	2	-
1682	<5.7	15	<7.37	2	-
1695	<5.35	15	<7.37	2	-
1704	<5.31	15	<7.37	2	-
1710	<5.45	15	<7.37	2	-
1711	<5.42	15	<7.37	2	-
1794	<5.55	15	<7.37	2	-
1809	<6.11	15	<7.25	2	-
1951	<6.55	15	<7.37	2	-
1989	<6.89	15	<7.37	2	-

[1] '-' means that no HI data were available for this galaxy

[2] HI references: (1): Haynes et al. (2011); (2): Goldmine catalog http://goldmine.mib.infn.it/ ; (3): AGES catalog, Taylor et al. (subm.)

[3] Gas-to-dust ratios were only determined for transition-type galaxies with either Herschel or HI detections.

3.2.3 Properties of Herschel-detected transition-type galaxies.

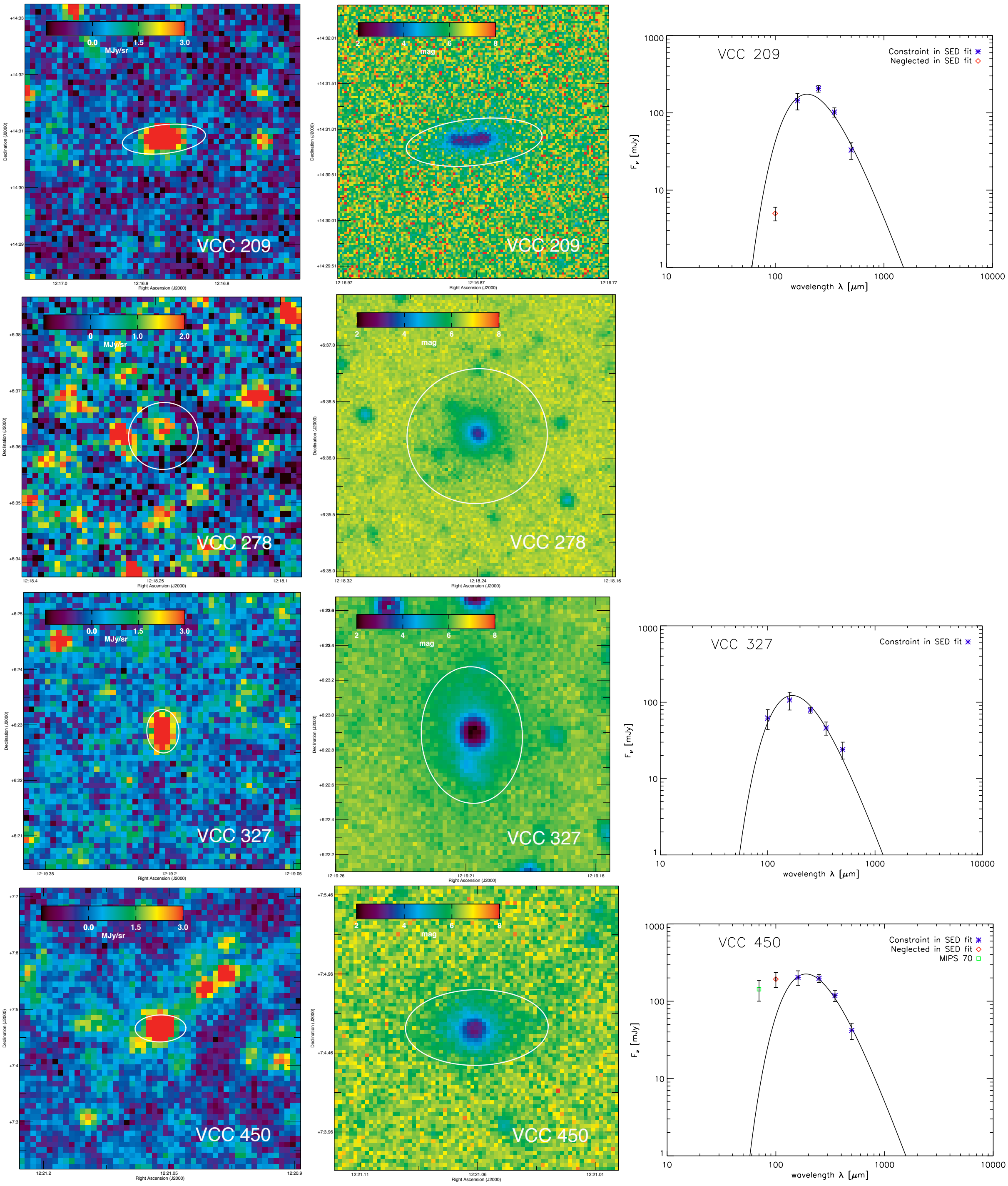

Figure 3.5: Left panel: Herschel detections at 250 μm of the transition-type galaxies. Middle panel: NUV-i colour maps for all transition-type galaxies detected by Herschel. The white ellipses in the last two panels correspond to the optical isophotal diameter (25 mag arcsec^{-2}) as reported by NED. Right panel: SED fits for all transition-type galaxies with $> 3\sigma$ fluxes in more than two wavebands.

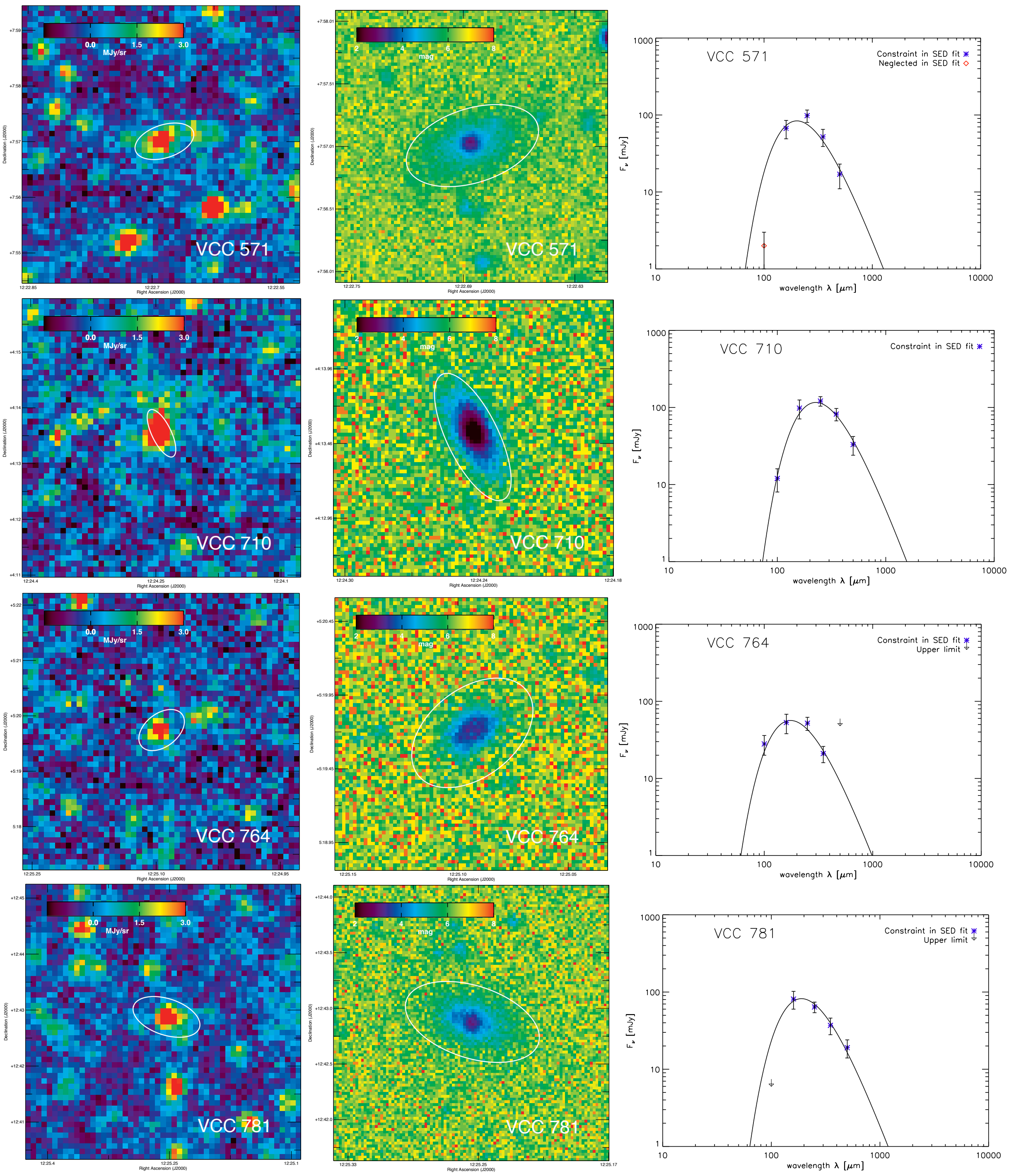

Figure 3.5: Continued from previous page

From our complete sample of transition type galaxies covered by Herschel, the majority of detected objects is classified as lenticular galaxy (12/14). Most genuine elliptical dwarf galaxies (dE) seem to have dust masses which are undetectable due to the sensitivity limits of current infrared instrumentation. The 3σ upper mass limits for these

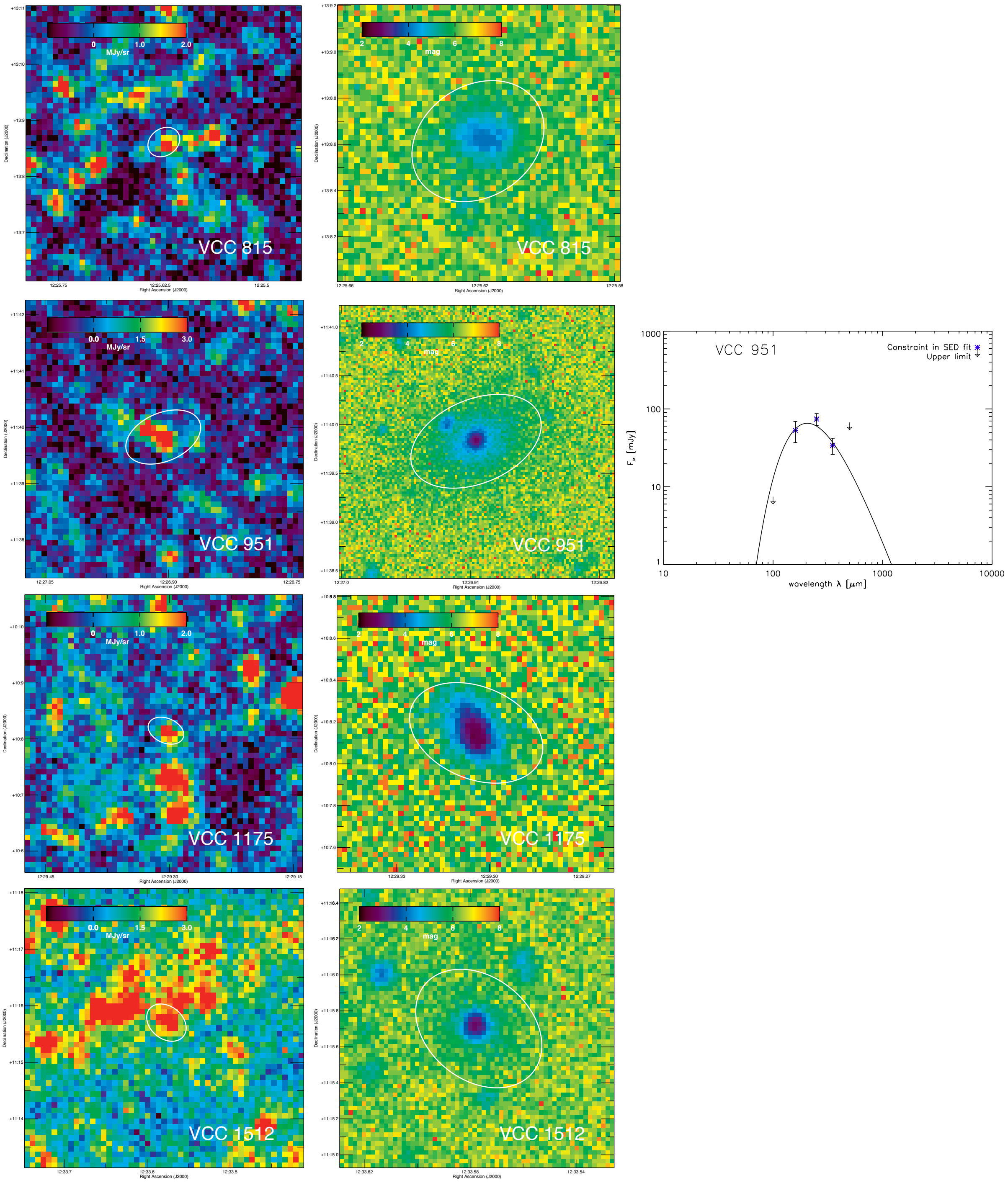

Figure 3.5: Continued from previous page

objects are however often not very different from detected dust reservoirs, not ruling out that also these objects might host a substantial dust content ($\sim 10^{4-5}$ $M_{\odot}$) (see Table 3.2 and Figure 3.6). Figure 3.6 also seems to indicate that merely more massive galaxies (i.e. objects with higher *H* band luminosities) have a detectable dust content. This

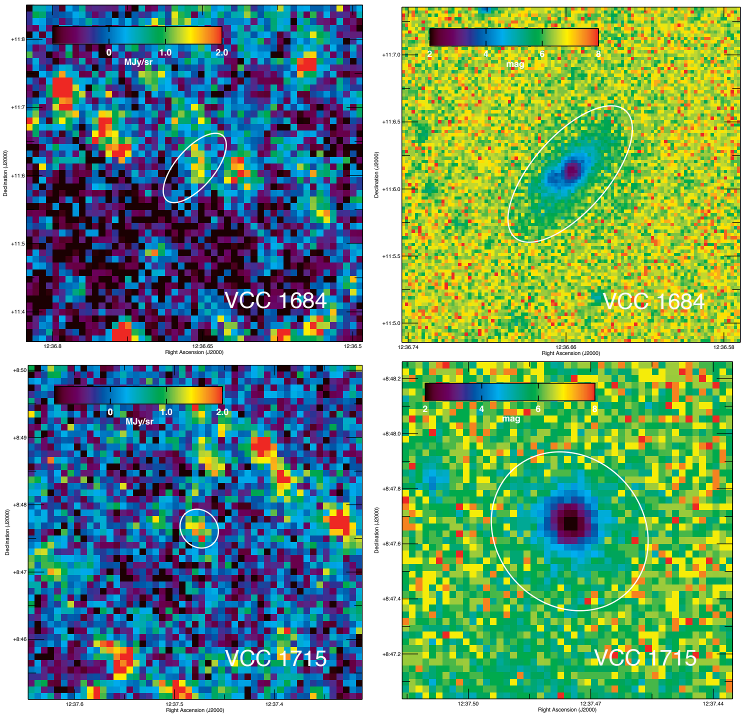

Figure 3.5: Continued from previous page

higher detection rate for S0 galaxies (or any related morphology) compared to dE's is in correspondence with the result for early-type galaxies covering all ranges in galaxy mass in the Herschel Reference Survey (Smith et al., 2012).

A full analysis of the origin of dust in those transition-type objects requires an analysis of their spectrophotometric properties and how these characteristics change under the influence of several transformation processes (e.g. ram-pressure stripping, starvation, etc.). Such a study is beyond the scope of this PhD thesis and will be postponed to future work. However, from studying several characteristics of the transition-type galaxies in our sample , we can already draw some important conclusions:

- The dust content in the Herschel detected transition-type objects is often very compact compared to the optical radius of the galaxies (see Figure 3.5). The size of the dust reservoir is also more compact than in late-type spiral galaxies (i.e. the likely progenitors of these transition-type objects), implying that the dust might be stripped out of the galaxy from the outside to the inside.
- The *NUV*-*i* colour maps of the Herschel detected transition-type galaxies also confirm that material is stripped or exhausted more efficiently on the outskirts of the galaxy, since a clear colour gradient can be identified in all colour maps (see Figure 3.5). This implies that star formation has been prevented in the outer regions either because the required material for star formation has been stripped

or was exhausted. Residual star formation is restricted to the central regions of those transition-type objects.

- The distribution of heliocentric velocities for all transition-type objects, and in particular for the Herschel detections, seems to imply that this population of galaxies is not yet virialized and, therefore, have only recently fallen onto the cluster (see Figure 3.7). This argument is furthermore supported by the position of transition-type galaxies in the Virgo cluster, being more scattered than the centrally concentrated population of quiescent early-type dwarf galaxies (see Figure 3.4).

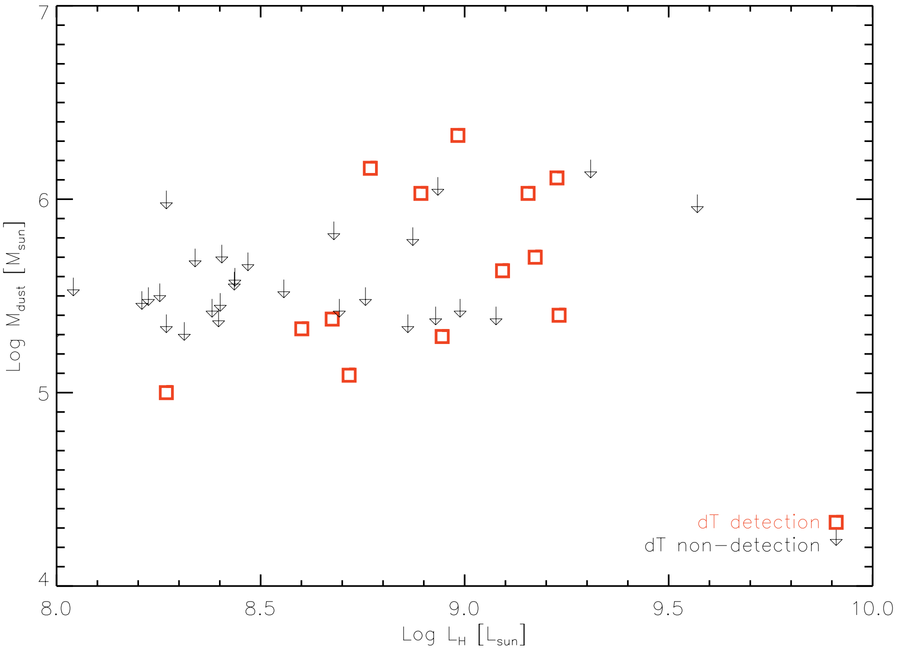

Figure 3.6: Plot of the dust mass (either detected or 3 σ upper limits) as a function of the *H* band luminosity for the transition-type objects in the Virgo cluster.

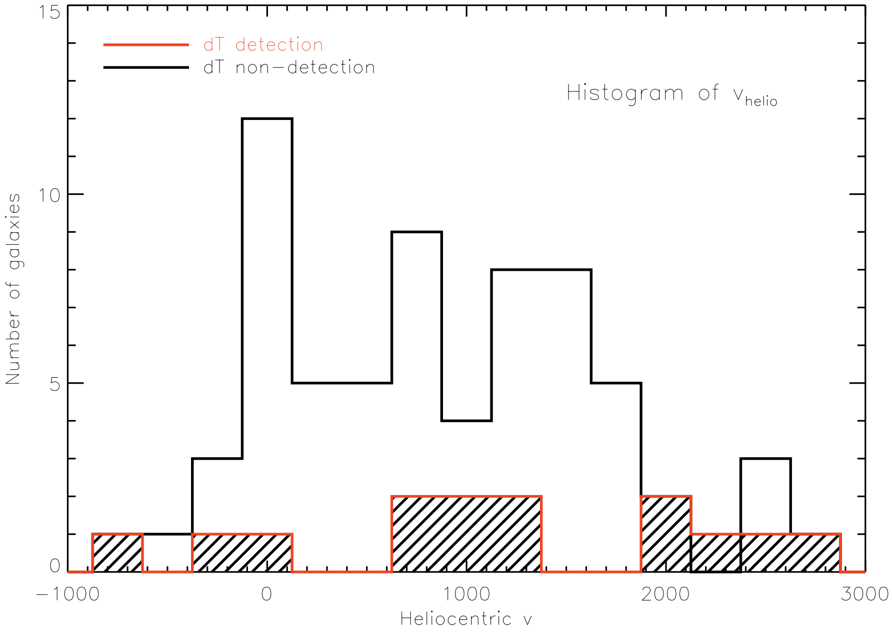

Figure 3.7: Histogram of heliocentric velocities for the Herschel detected (red filled histogram) and non-detected (black empty histogram) transition-type galaxies in velocity bins of 250 km s^{-1}.

4

NGC 205: missing ISM mass problem

Predictions of the current gas content in a galaxy need to account for the left-over gas reservoir after the last epoch of star formation and the build-up of gas returned to the ISM by the evolved stellar population since this last starburst episode. The left-over gas reservoir is predicted from observations of the young stellar population providing an estimate of the total gas mass consumed during the last period of star formation. Usually, it is assumed that a star formation efficiency of 10% is reasonable (e.g. Martín-Manjón et al. 2012; Boylan-Kolchin, Bullock & Kaplinghat 2012. From observations of both the nucleus and a region about 1 arcmin north of the nucleus with the International Ultraviolet Explorer (IUE) within an aperture of 10″ × 20″, Wilcots et al. (1990) report a mass of young ($\sim$ 10 Myr old) stars $M_{\star} \sim 7 \times 10^5$ M$_{\odot}$ in NGC 205, which increases to $M_{\star} \sim 1.4 \times 10^6$ M$_{\odot}$ when extrapolating to the whole galaxy based on the stellar light contribution from OB stars (Wilcots et al., 1990) and also taking stellar masses < 1 M$_{\odot}$ into account (Marleau et al., 2006). According to Bertola et al. (1995) NGC 205 was the host of a starburst starting $\sim$ 500 Myr ago involving a total stellar burst mass of $M_{\star} \sim 5.3 \times 10^7$ M$_{\odot}$, which is considerably higher than the estimate in Wilcots et al. (1990). More recently, Monaco et al. (2009) estimate $M_{\star} \sim 1.9 \times 10^5$ M$_{\odot}$ of stars to be produced between $\sim$ 62 Myr and $\sim$ 335 Myr ago from observations of the nuclear 29″ × 26″ region of NGC 205 with the Advanced Camera for Survey (ACS) on board the Hubble Space Telescope (HST), when assuming a ΛCDM cosmological model. Although the estimated burst mass in Monaco et al. (2009) also includes lower mass stars ($M_{\star} < 1$ M$_{\odot}$), their value should be considered a lower limit of the total burst mass, since only a limited period (from 62 to 335 Myr ago) in the star formation history of NGC 205 is analyzed and the observed area only corresponds to part of the region where the most recent star formation epoch took place. Considering that the estimated burst mass critically depends on the model assumptions and is often biased by the sensitivity and coverage of the observations, we calculate a total burst mass during the last episode of star formation in the range 1.4×10^6 M$_{\odot} \leqslant M_{\star} \leqslant 5.3 \times 10^7$ M$_{\odot}$, where the lower and upper limits correspond to stellar burst mass predictions from Wilcots et al. (1990) and Bertola et al. (1995), respectively. A burst mass of 1.4×10^6 M$_{\odot}$ would predict that the initial gas reservoir before the star formation (SF) episode was $M_g \sim 1.4 \times 10^7$ M$_{\odot}$ for a star formation efficiency (SFE) of $\sim$ 10%. Subtracting the 10% of gas consumed into stars results in the left-over gas reservoir $M_{\mathrm{g}} \sim 1.3 \times 10^7$ M$_{\odot}$ after the star formation epoch.

The total amount of gas returned to the ISM by planetary nebulae is predicted to be $\sim 1.8 \times 10^6$ M$_{\odot}$ (Welch, Sage & Mitchell, 1998), following the prescriptions in Faber & Gallagher (1976) and assuming a time lapse of $\sim$ 500 Myr since the trigger of the last star formation activity. With the lower limit for the stellar burst estimates relying on 10 Myr old stars (Wilcots et al., 1990), the corresponding mass returned to the ISM since the formation of those young stellar objects can be predicted in a similar way ($\sim 3.6 \times 10^4$ M$_\odot$). We only account for the mass loss from planetary nebulae since the mass lost from more massive stars is considered negligible due to their lower mass loss rate and shorter lifetime.

When combining the left-over gas reservoir (i.e. the majority of the ISM mass) and mass loss by planetary nebulae (depending on the assumed time lapse), we estimate a current gas content for NGC 205 ranging between 1.3×10^7 M$_\odot \leqslant M_{\rm g} \leqslant 4.8 \times 10^8$ M$_\odot$.

Up to now, the total gas mass in NGC 205 was estimated from HI, CO(1-0) and dust continuum observations. A total HI mass of 4.0 × 10^5 $M_\odot$, scaled to a distance D = 824 kpc for NGC 205, is reported in Young & Lo (1997) based on VLA observations covering the whole galaxy. Welch, Sage & Mitchell (1998) detect CO(1-0) and CO(2-1) emission above the 3σ level from 3 and 4 positions, respectively, across the plane of NGC 205. Although a partial beam overlap occurs for the CO(1-0) observations (see red circles in Figure 4.2), the covered area in the CO(1-0) observations is 7 times larger than for the second CO(2-1) transition and, thus, provides a better estimate of the molecular gas content in NGC 205. While Welch, Sage & Mitchell (1998) assumed a close to solar metallicity (implying a CO-to-H_2 conversion factor $X_{\mathrm{CO}} = 2.3 \times 10^{20}$ cm^{-2} (K km $\mathrm{s}^{-1})^{-1}$, Strong et al. 1988), we apply a conversion factor of 6.6 × 10^{20} cm^{-2} (K km $\mathrm{s}^{-1})^{-1}$, determined from the expression reported in Boselli et al. (2002a) relating the X_{CO} factor to the oxygen abundance in a galaxy. This value for the X_{CO} factor is based on a metal abundance of $Z \sim 0.3$ $Z_\odot$ in the inner regions of NGC 205. Whereas the earlier reported metallicity value (Z ∼ 0.13 $Z_\odot$) was obtained from averaging the oxygen abundances for 13 planetary nebulae in NGC 205 (Richer & McCall, 2008) and thus refers to the whole galaxy, Sharina, Afanasiev & Puzia (2006) determined a mean metallicity [Z/H] ∼ - 0.5 ± 0.2 for the central regions in NGC 205 from Lick indices. Considering that the last episode of star formation mainly occurred in the inner most regions, this gradient in metallicity and/or age is not surprising. A similar central increase in colour and metallicity has been noticed in several early-type dwarf galaxies in the Fornax cluster (Koleva et al., 2009) and a population of dEs with central blue cores has been observed in the Virgo cluster (Lisker et al., 2006b).

Additional CO(1-0) line emission was detected from a small area (beamsize ∼ 21″) observed in the south of NGC 205 (Young & Lo, 1996) (see green circle in Figure 4.2). Combining those CO(1-0) observations, we obtain an estimate of $M_{\mathrm{H}_2} = 6.9 \times 10^5$ $M_\odot$. This value for the molecular gas mass is however only a lower limit of the total H_2 mass, since the southern part of the galaxy is poorly covered by current CO(1-0) observations. Combining both HI and CO(1-0) observations, which were scaled by a factor of 1.4 to include helium, we derive a total gas mass $M_g \sim 1.5 \times 10^6$ $M_\odot$ for NGC 205, which is about one order of magnitude lower than the more modest theoretical predictions for the gas content. This deficiency in the gas content of NGC 205 is often referred to as the problem of the "missing ISM mass" (Welch, Sage & Mitchell, 1998).

Although gas observations directly probe the ISM component of interest, the dependence of the X_{CO} conversion factor on the metallicity (Wilson, 1995; Bolatto et al., 2008) and density of the gas (Shetty et al., 2011), and the optical thickness of the CO(1-0) line introduces an uncertainty on the estimate of the total gas mass. In particular for metal-poor galaxies the molecular gas phase could be poorly traced by CO (Wilson, 1995; Madden et al., 1997; Leroy et al., 2005, 2007). An alternative and promising method to measure the ISM mass in galaxies is to use observations of the continuum emission from dust (Hildebrand 1983; Guelin et al. 1993, 1995; Boselli et al. 2002a; James et al. 2002; Eales et al. 2010b.

Dust emission from NGC 205 was first detected with IRAS (Rice et al., 1988). NGC 205 was also the first early-type dwarf galaxy detected at millimeter wavelengths (Fich & Hodge, 1991). Based on these IRAS data and 1.1 mm observations for the central 18″ (21 ± 5 mJy) in NGC 205, Fich & Hodge (1991) estimated a dust mass of $M_{\mathrm{d}} \sim 3 \times 10^{3}$ $\mathrm{M}_{\odot}$ at a temperature of $\sim$ 19K. Using ISO observations, Haas (1998) obtained a total dust mass estimate of 4.9×10^{3} $\mathrm{M}_{\odot}$ at a temperature of $\sim$ 20 K. Recently, Marleau et al. (2006) probed the dust emission from NGC 205 with Spitzer and found a dust mass in the range M_{d} = 3.2-6.1 $\times 10^{4}$ $\mathrm{M}_{\odot}$ at a temperature of $\sim$ 18 K. Taking the 1.1 mm observation of the core region into account, Marleau et al. (2006) found a sixteen times more massive dust component in the central region at a temperature $T_d \sim 11.6$ K, suggesting that a substantial amount of cold dust might be overlooked if one only takes IRAS, ISO and Spitzer observations into consideration. Unfortunately only the central region was observed at 1.1 mm, and it could not be investigated whether such a putative cold dust component is present over the entire galaxy. Under the assumption that the colder dust is not only distributed in the central region, but is abundantly present in the entire galaxy, they estimated a total gas mass of 5×10^{7} $\mathrm{M}_{\odot}$ for a gas-to-dust ratio of 100.

To probe a possible cold dust component, we need observations at wavelengths long wards of 160 μm (e.g. Gordon et al. 2010). Longer wavelength data will also allow us to constrain the Rayleigh-Jeans side of the dust SED, from which a more robust temperature estimate for our SED model can be obtained. Therefore, we probed the cold dust component in NGC 205 to make an inventory of all the dust in NGC 205 with the Herschel Space Telescope (Pilbratt et al., 2010), covering a wavelength range from 70 up to 500 μm. Those Herschel observations were taken in the frame of two Herschel Guaranteed Time Projects: the Very Nearby Galaxy Survey (VNGS, PI: C. Wilson) and the Herschel Exploitation of Local Galaxy Andromeda (HELGA, PI: J. Fritz). From the VNGS, we obtained PACS photometry (Poglitsch et al., 2010) at 70 and 160 μm (ObsID 1342188692, 1342188693) and SPIRE photometry (Griffin et al., 2010) at 250, 350 and 500 μm. PACS data were observed on the 29th of December 2009 and cover an area of 1° by 1° centered on NGC 205. This area was observed in nominal and orthogonal scan direction with four repetitions at a medium scan speed (20 arcsec/s). The main scientific objective of HELGA (Fritz et al. subm.) focuses on dust in the extreme outskirts of the Andromeda Galaxy. Thanks to its large survey area, NGC 205 was covered in the field of two overlapping scan observations. HELGA observations were performed in the parallel fast scan mapping mode (60 arcsec/s), obtaining PACS 100, 160 μm and SPIRE 250, 350 and 500 μm photometry (ObsID 1342211294, 1342211309, 1342211319, 1342213207).

4.3.1 Data reduction

PACS photometry

To reduce the PACS data, we used version 13 of the Scanamorphos package (Roussel et al. in prep., [1]) map making technique. Before applying Scanamorphos to the level 1 data, the raw data were pre-processed in Herschel Interactive Processing Environment (HIPE, Ott 2010) version HIPE 6.0.1196. Due to the different observing set-ups, the depth of the PACS observations is inhomogeneous among the different wavebands. For PACS observations at 70 and 100 μm, we only have data available from one survey (either VNGS or HELGA, respectively). This dataset was finally reduced to obtain maps with a pixel size of 2″. The FWHM of the PACS beams are $\sim$ 6″ and $\sim$ 7″ × 13″ at 70 and 100 μm, respectively. Due to the lower level of redundancy and the fast scan speed, the PACS 100 μm waveband was observed in the least favorable conditions, resulting in the largest uncertainty values and interference patterns affec-

---

[1] *http://www2.iap.fr/users/roussel/herschel*

ting the observations (see Figure 4.1, second panel on the top row). In the red filter (PACS 160 μm), NGC 205 was covered by both VNGS and HELGA in medium and fast scan speed, resulting in a FWHM for the PACS beam of $\sim 12''$ and $\sim 12'' \times 16''$, respectively. Our final photometry map combines data from both Herschel projects at this overlapping wavelength with the aim of increasing the signal to noise ratio. The unmatched scan speeds prevent reducing both observations simultaneously, since the drift correction is calculated over a certain stability length which depends on the scan speed of the observation. Therefore, both datasets were reduced individually in Scanamorphos, using the same astrometry for the final maps. Before combining both maps we convolved them to the same resolution of the PSF, to avoid issues with the different beam sizes in both observations. Finally, the separately reduced and convolved VNGS and HELGA maps at 160 μm were combined into one single map in IRAF, with the `imcombine` task. The images were produced with the latest version of the PACS calibration files (version 26) and divided by the appropriate colour correction factors (1.016, 1.034 and 1.075 at 70, 100 and 160 μm, see Müller et al. 2011 for a power-law spectrum with $\beta = 2$). The background was also subtracted from the final PACS images. An estimate for the background was obtained from averaging the background flux within 100 random apertures (diameter $= 4 \times$FWHM). Random apertures were selected within an annulus centered on NGC 205 with inner radius of 5 arcmin and outer radius of 20 arcmin, avoiding regions with bright emission from background sources and M31. Once the random background apertures were selected, those same positions for aperture photometry were applied at all wavelengths.

SPIRE photometry

SPIRE data were observed on the 27th of December 2009 (ObsID 1342188661), obtaining two repetitions of nominal and orthogonal scans at medium scan speed (30 arcsec/s). For all SPIRE bands, datasets from both VNGS and HELGA projects were available and combined into one frame. In the same way as for Scanamorphos, the continuous temperature variations are different for VNGS and HELGA observations. Therefore, the corresponding data are reduced separately before combining them into one map. The SPIRE data were largely reduced according to the standard pipeline (POF5_pipeline.py, dated 8 Jun 2010), provided by the SPIRE Instrument Control Centre (ICC). Divergent from the standard pipeline were the use of the *sigmaKappaDeglitcher* (instead of the ICC-default *waveletDeglitcher*) and the BriGAdE method (Smith et al. in prep.) to remove the temperature drift and bring all bolometers to the same level (instead of the default *temperatureDriftCorrection* and the residual, median baseline subtraction). Reduced SPIRE maps have pixel sizes of 6″, 8″ and 12″ at 250, 350 and 500 μm, respectively. The FWHM of the SPIRE beams are 18.2″, 24.5″ and 36.0″ at 250, 350 and 500 μm, respectively. SPIRE images are converted from MJy/beam to Jy/pixel units assuming beam areas of 423, 751 and 1587 $''^2$ at 250, 350 and 500 μm, respectively. Since the calibration in the standard pipeline is optimized for point sources, we apply correction factors (0.9828, 0.9834 and 0.9710 at 250, 350 and 500 μm) to convert the K4 colour correction factors from point source to extended source calibration (SPIRE Observer's Manual, 2011). Additionally, multiplicative colour correction factors (0.9924, 0.9991 and 1.0249 at 250, 350 and 500 μm) were applied and a correction factor of 1.0067 was used to update the fluxes in the 350 μm image to the latest v8 calibration product (SPIRE Observer's Manual, 2011). SPIRE images were also background subtracted, in a similar way as for the PACS images.

Noise calculations

To determine the uncertainty on the PACS and SPIRE photometry data, we need to take into account three independent noise measurements. Aside from the most important uncertainty factor due to the calibration, the random background noise and the map making uncertainty contribute to the flux uncertainty as well. For the calibration uncertainty, values of 3, 3, and 5 % were considered for the PACS 70, 100 and 160 μm data, respectively (Müller, Okumura & Klaas, 2011; PACS Observer's Manual, 2011). All SPIRE wavebands were assumed to have a calibration uncertainty of 7 % (Swinyard et al. 2010, SPIRE Observer's Manual 2011). An estimate for the background noise is derived by taking 100 random apertures in the field around the galaxy (i.e. the same apertures used to determine the background), calculating the mean pixel value within each aperture as well the average mean over all apertures and, finally, computing the standard deviation of the mean pixel values in those individual apertures. Map making uncertainties are derived from the error map, which is produced during the data reduction procedure. Specific uncertainties in map making are determined from this error map. The total uncertainty on the flux value in a pixel is calculated as the square root of the sum of the three squared error contributions. Calibrations and background uncertainties are summarized in Table 4.1.

4.3.2 Structure of the ISM in NGC 205

Figure 4.1 displays the Herschel maps for NGC 205 in the PACS 70, 100, 160 μm and SPIRE 250, 350 and 500 μm wavebands. In all bands, we are able to distinguish three dominant emission regions (north, central and south), which were first identified using MIPS data by Marleau et al. (2006). A substantial amount of dust also resides in between those three distinctive emission regions. Towards the southeast of NGC 205 there is also an indication for a tentative detection of a colder dust component in the SPIRE maps (see the red, dashed ellipse in Figure 4.1). The detection is below the 3σ level, but it coincides with an optical tidal tail reported in Saviane, Monaco & Hallas

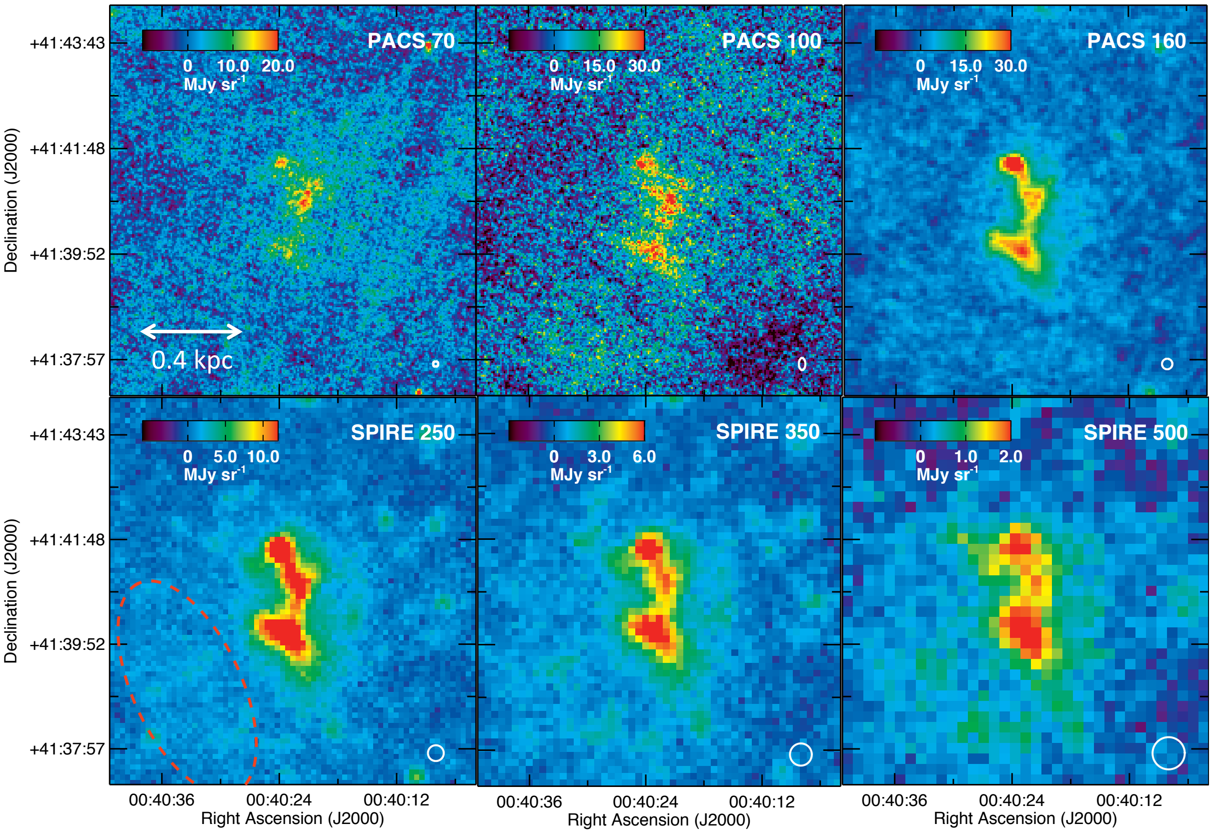

Figure 4.1: An overview of the Herschel maps. From left to right: PACS 70, 100, 160 μm (first row) and SPIRE 250, 350, 500 μm (second row). The displayed maps cover an area of 8.0 arcmin × 6.5 arcmin, with north up and east to the left. Besides the PACS 70 μm (VNGS) and PACS 100 μm (HELGA) maps, all images in the other bands were produced using both VNGS and HELGA observations. The FWHM of the PSF is indicated as a white circle in the lower right corner of each image. The red dashed line indicates the area where there is an indication for a tentative detection of a colder dust component.

(2010). However, we cannot rule out the possibility that the faint blob corresponds to foreground Galactic cirrus emission similar to the emission identified in the surroundings of M81 (Sollima et al., 2010; Davies et al., 2010b) or to emission originating from one or multiple background sources.

When comparing the HI, H_2 and dust distribution in NGC 205 (see Figure 4.2), we find a remarkable correspondence between the peaks in HI and H_2 (as derived from the CO(3-2) observations, see Section 4.4.1) column density and dust emission. This seems to imply that the dust component in NGC 205 is well mixed with the atomic and molecular gas at the observed spatial scales of ~ 100 pc for SPIRE. While a significant part of the atomic gas resides in the area south of the galaxy's center (see Figure 4.2), current CO observations only cover most of the northern part of the galaxy (Johnson & Gottesman 1983; Young & Lo 1997; Welch, Sage & Mitchell 1998; JCMT CO(3-2) map from this work) and a minor part in the south of NGC 205 (Young & Lo, 1996). This lack

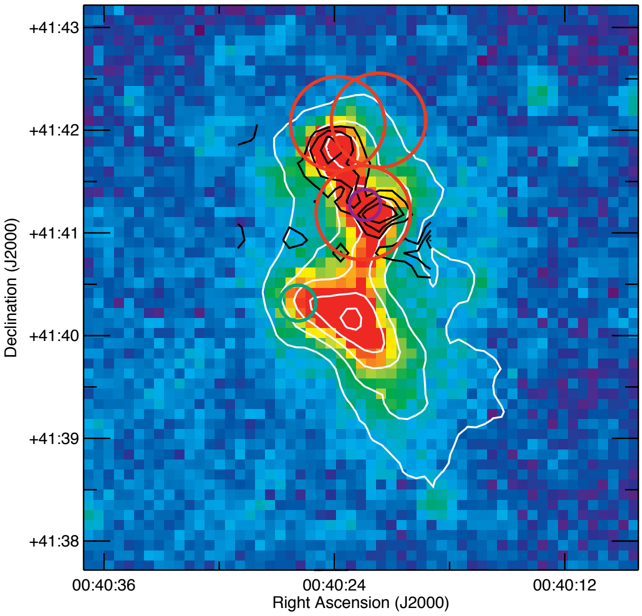

Figure 4.2: HI column density contours (white, solid line; the HI map for NGC 205 obtained from VLA observations, Young & Lo 1997, was kindly provided to us by Lisa Young), H_2 column density contours (black, solid line, derived from the JCMT CO(3-2) map), CO(1-0) pointings (red circles: Welch, Sage & Mitchell 1998, green circle: Young & Lo 1996) and the JCMT 1.1 mm 18″ beam (purple circle, Fich & Hodge 1991) overlaid on the SPIRE 250 μm image. The HI contours range from 2 $\times$ 10^{19} to 3.5 $\times$ 10^{20} cm^{-2} in intervals of 6.6 $\times$ 10^{19} cm^{-2}, while the CO(3-2) contours represent a H_2 column density range $2.6 \times 10^{20} \leqslant N_{H_2} \leqslant 1.9 \times 10^{21}$ cm^{-2} increased in steps of 3.3 $\times$ 10^{20} cm^{-2}.

of data makes it difficult to draw conclusions about the correlation of the molecular gas component with the dust or HI gas in the southern area of NGC 205. At least for the northern part of NGC 205, it seems that also the molecular gas component correlates well with the HI gas and dust.

4.3.3 Consistency of Herschel fluxes with previous observations

Global fluxes in all wavebands were determined from summing over all pixels in the background subtracted image with $> 3\sigma$ detection in the SPIRE 250 μm image. Those global fluxes and the corresponding noise measurements (calibration uncertainty and random background noise) in each waveband are summarized in Table 4.1. Flux measurements have been updated to the last PACS and SPIRE calibration products, converted to the extended source calibration and colour corrected for each filter.

When comparing our fluxes at PACS 70 μm (2.2 $\pm$ 0.2 Jy) and PACS 160 μm (4.0 $\pm$ 0.3 Jy) to the MIPS fluxes at those overlapping wavelengths reported in Marleau et al. (2006) (MIPS 70 μm: 1.4 $\pm$ 0.3 Jy; MIPS 160 μm: 8.8 $\pm$ 4.7 Jy), a large discrepancy between PACS and MIPS fluxes is found. In view of this large difference, we determined

Wavelength	F_ν	σ_{back}	σ_{cal}
μm	(mJy)	(μJy/$''^2$)	(%)
MIPS 24	98 ± 15		15^1
PACS 70	2204 ± 179	0.5	3
PACS 100	3565 ± 515	1.2	3
PACS 160	3912 ± 159	2.2	5
SPIRE 250	2623 ± 29	1.8	7
SPIRE 350	1302 ± 15	1.6	7
SPIRE 500	539 ± 9	2.3	7

Table 4.1: Global fluxes (F_ν) and contributions from the random background noise (σ_{back}) and the calibration uncertainty (σ_{cal}) are provided for every waveband. All tabulated fluxes have been multiplied by extended source calibration and filter colour correction factors.

[1] The 15% uncertainty on the MIPS 24 μm flux includes the uncertainties arising from calibration and background subtraction.

MIPS fluxes (MIPS 70 μm: 1.3 ± 0.3 Jy; MIPS 160 μm: 4.6 ± 0.9 Jy) from reprocessed archival MIPS data[2] by summing over the same pixels (uncertainty values only refer to calibration uncertainties). To determine the corresponding PACS fluxes, the Herschel maps at 70 and 160 μm wavelengths were convolved with the appropriate kernels to match the elongated wings of the MIPS PSFs. The customized kernels were created following the procedure in Bendo et al. (2012) (see also Gordon et al. 2008). Summing the flux values for the same pixels, we find the corresponding flux measurements for PACS 70 μm (2.3 ± 0.2 Jy) and PACS 160 μm (3.8 ± 0.3 Jy). Upon comparison of the fluxes, we find a relatively good agreement between the PACS measurement and the flux determined from the archival MIPS image at 160 μm. The PACS 70 μm flux is sufficiently higher, which might either be a calibration issue or a dissimilarity in the background determination. We argue that the deviation from the MIPS 160 μm measurement reported in Marleau et al. (2006) is either due to a flux calibration issue or an overestimated aperture correction. Indeed, the flux calibration for MIPS (Gordon et al., 2007; Stansberry et al., 2007) was only finalized after the analysis in Marleau et al. (2006).

A similar comparison at 100 μm is possible between PACS and IRAS fluxes. Rice et al. (1988) report a total flux density of 3.78 ± 0.57 Jy for NGC 205, which agrees well with the flux density 3.6 ± 0.5 Jy determined from Herschel observations.

---

[2] We obtained raw MIPS data for NGC 205 from the Spitzer archive, which were reprocessed according to the procedure outlined in Bendo, Galliano & Madden (2012b).

4.3.4 Dust masses

For the SED fitting procedure and, thus, dust mass determination, we apply the DustEm code (Compiègne et al., 2011), which predicts the emission of dust grains given the strength of the interstellar radiation field (ISRF) and a certain composition of grain types, with a specific size distribution, optical and thermal dust properties. DustEm derives the local dust emissivity from computing explicitly the temperature distribution for every grain type of particular size and composition. For the analysis in this thesis, we adopt two different dust compositions (Draine & Li 2007 and Compiègne et al. 2011), each containing polycyclic aromatic hydrocarbons (PAHs) and amorphous silicate grains complemented with either graphite or amorphous carbon dust particles, respectively. The dust composition from Draine & Li (2007) corresponds to the typical dust mixture found in our own Galaxy. The amorphous carbonaceous grains are in the form of hydrogenated amorphous carbon, better known as a-C:H or HAC (Compiègne et al., 2011). The spectral shape of the ISRF is assumed to be the same as determined in the solar neighborhood (Mathis, Mezger & Panagia, 1983) (MMP83). Although the shape and hardness of the ISRF in low-metallicity dwarf galaxies might differ from the Galactic ISRF (Madden et al., 2006), altering the spectral shape of the ISRF will in particular influence the radiation of transiently heated PAHs and very small grains but has been shown to only affect the total dust mass estimate by a factor of $< 10\%$ (Galametz et al., 2009). Moreover, based on the number and spectral type of young massive stars in NGC 205, Young & Lo (1996) found an UV field corresponding well to the ISRF in the solar neighborhood. Under these assumptions, we have only 2 free parameters: the dust mass $M_{\rm d}$ and the intensity of the ISRF $X_{\rm ISRF}$ relative to the Galactic ISRF.

During the SED fitting procedure, we explore a parameter grid in $X_{\rm ISRF}$ and dust mass by increasing them stepwise by a factor of 1.05. In order to facilitate the least-square fitting procedure, we construct a pre-calculated library of dust models in DustEm, each with a different scaling of the ISRF and dust mass. The model SED at those wavelengths is convolved with the response function of the filter-band passes, to include the appropriate colour correction (pixel values were not colour corrected in this case). Finally, the model with the best fitting parameters is determined from a least-square fitting routine. To estimate the uncertainties on the best fitting parameters, we perform a bootstrapping procedure. Hereto, the same fitting routine is applied on a dataset of 100 flux densities, randomly determined from a Gaussian distribution for which the maximum value and width are chosen to correspond to the observed fluxes and uncertainty values. The 1σ uncertainties on our best fitting model parameters correspond to the 16 and 84 percentiles of this Gaussian distribution.

Since the primary goal of this analysis is quantifying the total dust content in NGC 205,

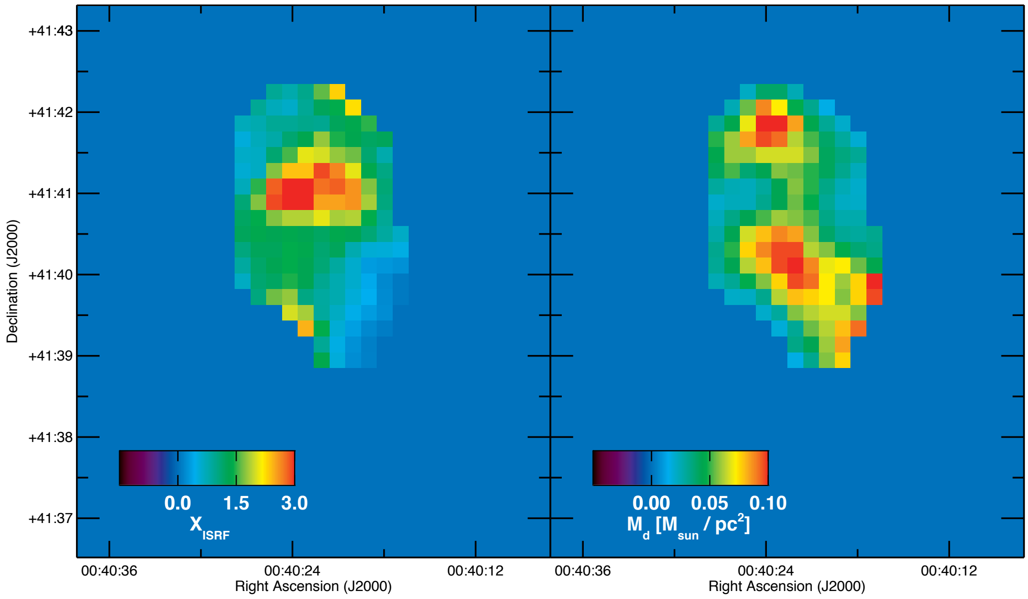

Figure 4.3: The $X_{\rm ISRF}$ (left panel) and dust mass (right panel) obtained from a multi-component DustEm SED fitting procedure for every pixel with at least 3 detections above the 3σ level across the 24 μm to 500 μm wavelength range.

we restrict our SED fitting procedure to the wavelength range from 24 to 500 μm. The spectral shape throughout this wavelength range is determined from the flux measurements in the six available Herschel wavebands (PACS 70, 100, 160 μm and SPIRE 250, 350, 500 μm) and the MIPS 24 μm flux. Prior to SED fitting, all images (Herschel+ancillary MIPS data) were convolved with the appropriate kernels, according to the procedure in Bendo et al. (2012), to match the resolution of the 500 μm images. All images were also rebinned to the pixel scale (12"/pixel) of the 500 μm image.

In a pixel-by-pixel analysis, dust masses and ISRF scaling factors are computed from a SED fitting procedure to every pixel with fluxes in at least three different bands above the 3σ level to constrain the spectral shape of the energy distribution. In this way, we obtain 155 pixels with a sufficient signal to noise level and avoid contribution from noisy pixels (in particular at 100 μm) to the SED fitting procedure, which might bias our estimate of the total dust mass. The uncertainty on the flux values in every pixel are calculated following the procedure outlined in Section 4.3.1.

Figure 4.3 shows the maps with the best fitting ISRF scaling factors (left) and dust column densities (right), determined from SED fitting with the silicate+amorphous carbon dust composition (Compiègne et al., 2011). From those maps, we clearly notice that the dust in the center of NGC 205 has a higher temperature, while most of the dust mass resides in the northern and southern regions of NGC 205, corresponding to peaks in the HI+H_2 and HI column density, respectively. For the three distinctive dust emission regions in NGC 205 the northern and southern areas are brighter because of the large amounts of dust residing in these areas, while the dust grains in the central region emit more prominently because they are exposed to a stronger ISRF. Also outside these three emission regions, a substantial amount of dust is found to be present in the galaxy.

The total dust mass in NGC 205 is determined by adding the dust masses in all pixels, resulting in $M_{\mathrm{d}} \sim 1.8 \times 10^4$ $\mathrm{M}_\odot$. An estimate for the average strength of the ISRF is calculated as the median of the values for X_{ISRF} in all pixels. This median value of X_{ISRF} $\sim$ 1.13 is translated into a large grain dust temperature $T_d \sim 17.8$ K by averaging over all mean temperatures for grains with sizes between 4×10^{-3} and 2 μm for this specific strength of the ISRF. When repeating the SED fitting procedure with a silicate+graphite dust composition (Draine & Li, 2007), we find values for the dust mass ($M_{\mathrm{d}} \sim 1.1 \times 10^4$ $\mathrm{M}_\odot$) and the median value of the scaling factor $X_{\mathrm{ISRF}} \sim 3.12$ (or $T_d \sim 21.2$ K) consistent with the results obtained for a silicate+amorphous carbon dust composition within the uncertainties of the SED fitting procedure. The fitting results for both dust compositions are summarized in Table 4.2. To check whether our results are hampered by the resolution in the SPIRE 500 μm waveband ($\sim$ 36″), we perform the same pixel-by-pixel SED fitting procedure at a resolution of the SPIRE 350 μm waveband ($\sim$ 24.5″). Whereas SED fitting on higher resolution data have shown to probe a more massive dust reservoir in the Large and Small Magellanic Clouds (Galliano et al., 2011), we find best fitting values for the average scaling factor $X_{\mathrm{ISRF}} \sim 0.61^{+0.31}_{-0.31}$ and a total dust mass $M_d \sim 0.9^{+0.5}_{-0.5} \times 10^4$ $\mathrm{M}_\odot$. Since the dust mass is somewhat lower than the results obtained from the SED fit with the 500 μm measurement, we conclude that a gain in resolution does not better trace the dust content in NGC 205. On the contrary, including the 500 μm data in the SED fit results in a more massive dust component at a colder temperature in the outer regions of NGC 205.

A SED fitting procedure for the global fluxes was performed as well, giving similar results as for the pixel-by-pixel dust masses and X_{ISRF} factors (see Table 4.2). Figure 4.4 displays the best fitting DustEm model for the silicate+amorphous carbon dust composition overlaid with the global Herschel fluxes and other data from the literature.

4.3.5 Cold dust component?

The dust masses obtained from our Herschel observations ($M_{\mathrm{d}} \sim$ 1.1-1.8 $\times 10^4$ $\mathrm{M}_\odot$) are comparable to the dust masses derived from the MIPS observations ($M_{\mathrm{d}} \sim 3 \times 10^4$ $\mathrm{M}_\odot$) within the uncertainties of the observations and fitting procedure, but more than one order of magnitude lower than the predicted dust mass ($M_{\mathrm{d}} \sim 5 \times 10^5$ $\mathrm{M}_\odot$) at a temperature of $\sim$ 12 K based on mm+Spitzer observations (Marleau et al., 2006). Since the strength of the ISRF and therefore the heating of the dust grains is variable

Silicate/Am. Carbon	X_{ISRF}	T_d [K]	M_{d} [M$_\odot$]
Pixel-by-pixel	$1.13^{+0.07}_{-0.07}$	$17.8^{+0.2}_{-0.1}$	$1.8^{+0.1}_{-0.1} \times 10^4$
Global	$2.74^{+0.42}_{-0.58}$	$20.7^{+0.5}_{-0.8}$	$1.1^{+0.1}_{-0.1} \times 10^4$
Silicate/graphite	X_{ISRF}	T_d [K]	M_{d} [M$_\odot$]
Pixel-by-pixel	$3.12^{+0.19}_{-0.19}$	$21.2^{+0.2}_{-0.3}$	$1.1^{+0.1}_{-0.1} \times 10^4$
Global	$3.74^{+0.10}_{-1.37}$	$21.8^{+0.1}_{-1.6}$	$1.0^{+0.3}_{-0.1} \times 10^4$

Table 4.2: Overview of the parameters (scaling factor for the ISRF, X_{ISRF}, and dust mass, M_{d}) for the best fitting DustEm model, either with a silicate+amorphous carbon or silicate+graphite dust composition, determined from a pixel-by-pixel or global SED fit. The temperature estimate is obtained by taking the average over all mean temperatures for dust particles with sizes between 4×10^{-3} and 2 μm.

throughout the plane of the galaxy (see Figure 4.3, left panel), we calculate an upper limit for the dust mass at a dust temperature of $T_d \sim 12$ K by scaling the SED until fitting the upper limit of the 500 μm flux measurement ($F_\nu \sim 612$ mJy). We derive an upper mass limit $M_d < 4.9 \times 10^4$ M$_\odot$ for the cold dust reservoir ($T_d \sim 12$ K). Therefore, our Herschel observations do not seem to support the presence of a massive cold dust component, implying that the millimeter flux is unlikely to originate from a cold dust reservoir.

With an upper limit of 0.06 mJy at 21 cm (Lucero & Young, 2007) and the absence of emission lines characteristic for LINER or Seyfert galaxies (Martins et al., 2012), the JCMT 1.1 mm flux measured by Fich & Hodge (1991) is unlikely to be caused by synchrotron emission from either supernova remnants or an AGN-like nucleus. Also the contribution from CO(2-1) line emission seems unable to account for the high mm measurement. Indeed, based on the JCMT CO(2-1) line intensity (0.43 K km/s) for the inner region (Welch, Sage & Mitchell, 1998), we derive a flux density of 0.724 Jy at 1.3 mm. Relying on the narrow CO(2-1) line width (13 km/s or 10 MHz) and the bandwidth of the IRAM UKT14 receiver (74 GHz), a contribution from CO(2-1) line emission to the 1.1 mm continuum observations is found to be negligible. This implies that other explanations (calibration issues, background source, bad weather conditions) need to be invoked to explain the high 1.1 mm flux in the center of NGC 205.

Also Herschel observations at 500 μm do not show any indication for excess emission at submm or mm wavelengths, reminiscent of the submm excess observed in many star-forming dwarf galaxies and blue compact dwarfs (Galliano et al., 2003; Dumke, Krause & Wielebinski, 2004; Galametz et al., 2009, 2010, 2011; Grossi et al., 2010; O'Halloran et al., 2010). In some cases, the observed excess even extends up to millimeter and centimetre wavelengths, such as observed in the Large (LMC) and Small Magellanic Clouds (SMC) (Israel et al., 2010; Bot et al., 2010a; Meixner et al.,

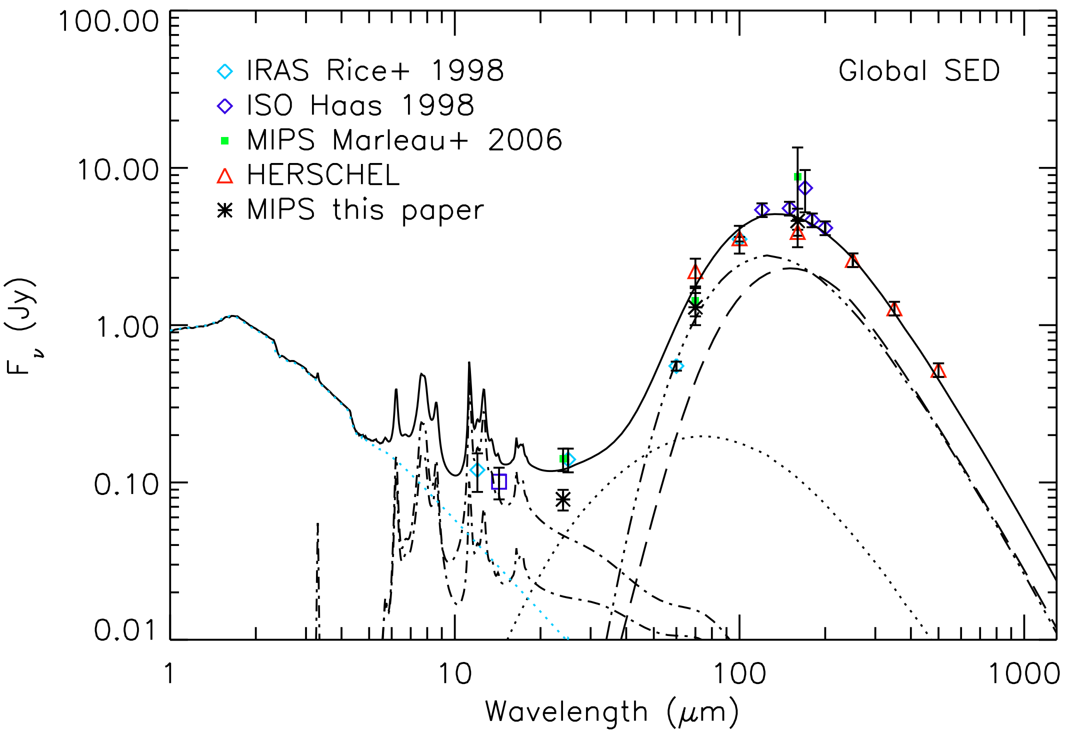

Figure 4.4: The SED for the best fitting DustEm model ($X_{\rm ISRF}$ = 2.74 or $T_d \sim 20.7$ K, $M_{\rm d} \sim 1.1 \times 10^4$ $M_\odot$) with an silicate+amorphous carbon dust composition (black, solid line), overlaid with the measured MIPS 24, PACS 70, 100, 160 μm and SPIRE 250, 350 and 500 μm flux densities. Also the other flux densities from the literature are indicated. The dotted-dashed, dotted, triple dotted-dashed, dashed lines correspond to the PaH dust mixtures, small and large amorphous carbon and silicate dust grains, respectively. Since the SED fitting procedure with the silicate+graphite dust composition gave very similar results and uncertainties, the plot with this SED model is not explicitly shown here. Also a stellar component for NGC 205, parametrized as a Maraston (1998, 2005) Single Stellar Population with an age of 13 Gyr and a metallicity of Z = 0.002 (Bertola et al., 1995) and modelled as a Sersic profile of index n = 1 and effective radius 130″ (De Rijcke et al., 2006), was included on the SED fit, to allow a comparison of our SED model to observations at NIR/MIR wavelengths (blue dotted line).

2010; Planck Collaboration et al., 2011). Several reasons have been invoked to account for this excess emission in the submm/mm wavebands. Either large amounts of very cold dust (e.g. Galliano et al. 2003; Galametz et al. 2009; O'Halloran et al. 2010), dust grains with optical properties diverging from the typical Galactic dust characteristics (e.g. Lisenfeld et al. 2002; Meny et al. 2007) or spinning dust grains (e.g. Bot et al. 2010a; Planck Collaboration et al. 2011) are thought to be responsible for the excess emission. The fact that our SED model can account for the observed 500 μm emission in NGC 205 is interesting, because it is in contrast with the submillimeter excess observed in several other low metallicity dwarf galaxies. This might be an indication for different ISM properties and star-forming conditions in this early-type dwarf galaxy, compared to the typical star-forming dwarfs revealing an excess submm emission. However, an excess in wavebands long wards of 500 μm (see also Galametz et al. 2011) cannot be ruled out based on the currently available dataset for NGC 205.

New gas mass measurements for NGC 205 were also obtained from James Clerk Maxwell Telescope (JCMT) CO(3-2) observations and Herschel [CII] 158 μm and [OI] 63 μm line spectroscopy mapping.

4.4.1 JCMT CO(3-2)

The JCMT observations of the ^{12}CO (3-2) transition (rest frequency 345.79 GHz) were obtained with the HARP-B instrument (Buckle et al., 2009) as part of project M10AC07 (PI: Tara Parkin) over eight nights in May, June and September of 2010, with a telescope beam size of 14.5 arcsec. We obtained a single map in jiggle-chop mode with a footprint of 2 arcmin × 2 arcmin on the sky, and a total integration time of 1350 sec for each of the 16 jiggle positions. The observations were carried out using beam-switching with a chop throw of 150 arcsec from the centre of NGC 205. We used the Auto-Correlation Spectrometer Imaging System (ACSIS) as our backend receiver, and it was set to a bandwidth of 1 GHz with 2048 channels, resulting in a resolution of 0.43 km s^{-1}. The data were then reduced using the Starlink[3] software package (Currie et al., 2008), maintained by the Joint Astronomy Centre. For a full description of our data reduction and map making methods see Warren et al. (2010) and Parkin et al. (2012).

In view of the limited coverage of previous CO(1-0) and CO(2-1) observations with only few pointings across the galaxy, we were able to derive a molecular gas mass estimate for NGC 205 from a CO(3-2) map covering a larger part of the galaxy, however still only probing the H$_2$ gas in the northern region of the galaxy (see Figure 4.2). For all pixels with detections $> 3\sigma$, the integrated CO(3-2) line intensity is converted to a H$_2$ column density according to the formula:

$$N_{\mathrm{H}_2} = \frac{X_{\mathrm{CO}} I_{\mathrm{CO(3\text{-}2)}}}{\eta_{\mathrm{mb}} \left(\frac{I_{\mathrm{CO(3\text{-}2)}}}{I_{\mathrm{CO(1\text{-}0)}}} \right)} \tag{4.1}$$

where $I_{\mathrm{CO(3\text{-}2)}}$ is the total integrated line intensity expressed in units of K km s^{-1}. The scaling factor to convert an antenna temperature $T_A^{\star}$ into a main beam temperature T_{mb} at the JCMT is η_{mb} = 0.6. We assume a value of $\sim$ 0.3 for the CO(3-2)-to-CO(1-0) line intensity ratio corresponding to the typical ratios found in the diffuse ISM of other nearby galaxies (Wilson et al., 2009). Since we derive a line ratio of $\sim$ 0.34 for the central pointing reported in Welch, Sage & Mitchell (1998), we argue that this ratio serves as a good approximation for the entire CO(3-2) emitting region. The same X_{CO}

---

[3] The STARLINK package is available for download at http://starlink.jach.hawaii.edu.

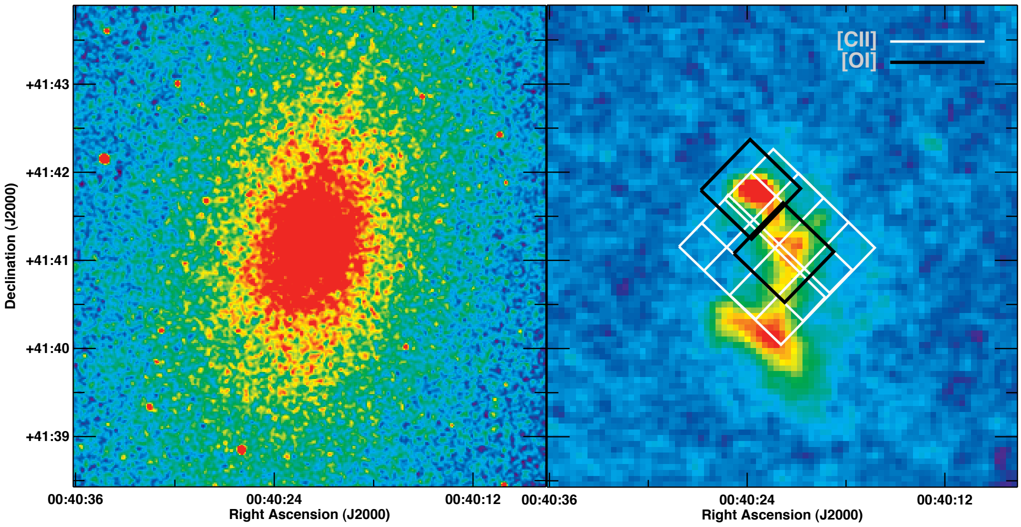

Figure 4.5: Left panel: *K* band image of NGC 205. Right panel: PACS 160 μm image overlaid with the AORs for the [OI] (black, solid lineboxes) and [CII] (raster with white, solid lines) PACS line spectroscopy observations. The [OI] line was observed in the north of NGC 205, where the CO(1-0) emission peaks in the north, and in the central region of NGC 205. The [CII] observations cover both areas.

conversion factor (6.6×10^{20} cm^{-2} (K km s^{-1})$^{-1}$) as introduced in Section 4.2 is applied here. The total molecular gas mass is derived from the column density following the equation:

$$M_{\mathrm{H_2}} = A N_{\mathrm{H_2}} m_{\mathrm{H_2}} \tag{4.2}$$

where A represents the surface of the CO(3-2) emitting region and $m_{\mathrm{H_2}}$ is the mass of a molecular hydrogen atom. Inserting the correct values in equation 4.2 results in an estimate for the total molecular gas mass $M_{\mathrm{H_2}} \sim 1.3 \times 10^5$ M$_{\odot}$. Considering that this value is a factor of $\sim$ 5 lower than the $M_{\mathrm{H_2}} \sim 6.9 \times 10^5$ M$_{\odot}$ inferred from CO(1-0) detections, we argue that most of the H$_2$ in NGC 205 resides in regions of colder temperature ($T \leqslant T_{\mathrm{crit,CO(3\text{-}2)}} \sim 33$ K) and/or lower density ($n \leqslant n_{\mathrm{crit,CO(3\text{-}2)}} \sim 2 \times 10^4$ cm^{-3}).

4.4.2 PACS spectroscopy: [CII], [OI], [OIII]

PACS spectroscopy maps, [CII] 157.74 μm and [OI] 63 μm, were observed on the 14th of February 2011 (ObsID 1342214374, 1342214375, 1342214376). The [CII] observations cover the northern and the central area of NGC 205 (see Figure 4.5), while two smaller [OI] maps are centered on the CO peak in the north and on the centre of NGC 205 (see Figure 4.5). The PACS (Poglitsch et al., 2010) spectroscopic observations of NGC205 were done in the chop/nod mode, and cover an area of 95″ × 95″ (3 × 3 pointings) and 47″ × 47″ (1 pointing) for the [CII] (157.74 μm) and both [OI] (63 μm) maps, res-

Line	Rest wavelength	σ
	μm	(10^{-6} erg s^{-1} cm^{-2} sr^{-1})
[CII]	157.74	1.28
[OI] (center)	63.18	5.50
[OI] (north)	63.18	7.06

Table 4.3: The 1σ noise levels for the PACS spectroscopy observations.

pectively. We used the largest chop throw of 6 arcmin to ensure we were not chopping onto extended source emission. The maps were processed from Level 0 to Level 2 using the standard pipeline in HIPE (version 7.0.0), with version (FM, 32) of the calibration files. Once the data are processed to Level2, we used the PACSman program[4] (Lebouteiller et al., subm.) to perform line fits to the unbinned spectral data in each spatial pixel using a least-squares fitting routine, and to create integrated flux density maps of the results. For [CII], the flux map mosaic was created by projecting the individual rasters onto an oversampled grid. More details can be found in Lebouteiller et al. (subm.). The noise level in PACS spectroscopy observations is determined from the uncertainty in the integrated intensity map, calculated from the formula:

$$\Delta I = \left[\Delta v \sigma \sqrt{N_{line}}\right] \sqrt{1 + \frac{N_{line}}{N_{base}}} \tag{4.3}$$

where Δv corresponds to the channel width in km s^{-1}, σ is the uncertainty in K and N_{line} and N_{base} represent the total number of channels covering the spectral line and the channels used for the baseline fitting, respectively. A 1σ uncertainty value is estimated from taking the mean over 15 random apertures in this uncertainty map. The 1σ noise levels for the [CII] and [OI] line emission are reported in Table 4.3.

Relying on the low metal abundance of the ISM in the inner regions of NGC 205, there might be a significant fraction of molecular gas in NGC 205 which remains undetected by current CO observations, since CO is often a poor diagnostic of the H_2 content in low abundance environments exposed to hard radiation fields. Based on the high values for the $L_{[CII]}$-to-L_{CO} ratio found in several low metallicity dwarf galaxies (e.g. Madden 2000; Cormier et al. 2010), [CII] is often claimed to be a better tracer for the molecular gas in such environments. Also the [OI] fine-structure line, which is considered an important coolant of the neutral gas together with [CII], can be used as an alternative probe for the molecular gas in a low metallicity ISM (e.g. Tielens & Hollenbach 1985). Although both [CII] and [OI] are considered good tracers of molecular

---

[4] PACSman is available for download at http://www.myravian.fr/Homepage/Softwares.html.

Aperture	RA (°)	DEC (°)	a (″)	b (″)
1	10.095534	41.673843	21.20	13.76
2	10.090351	41.687053	33.84	23.45
3	10.098251	41.69641	13.39	9.65

Aperture	F_ν [10^{-14} erg s^{-1} cm^{-2}]	M_{H_2} [$\mathrm{M}_\odot$]
1	1.06 ± 0.25	1.26×10^3
2	9.91 ± 0.52	11.83×10^3
3	3.06 ± 0.56	2.27×10^3

Table 4.4: [CII] line measurements (bottom) within the elliptical apertures (top), shown as overlays on the [CII] map in Figure 4.6.

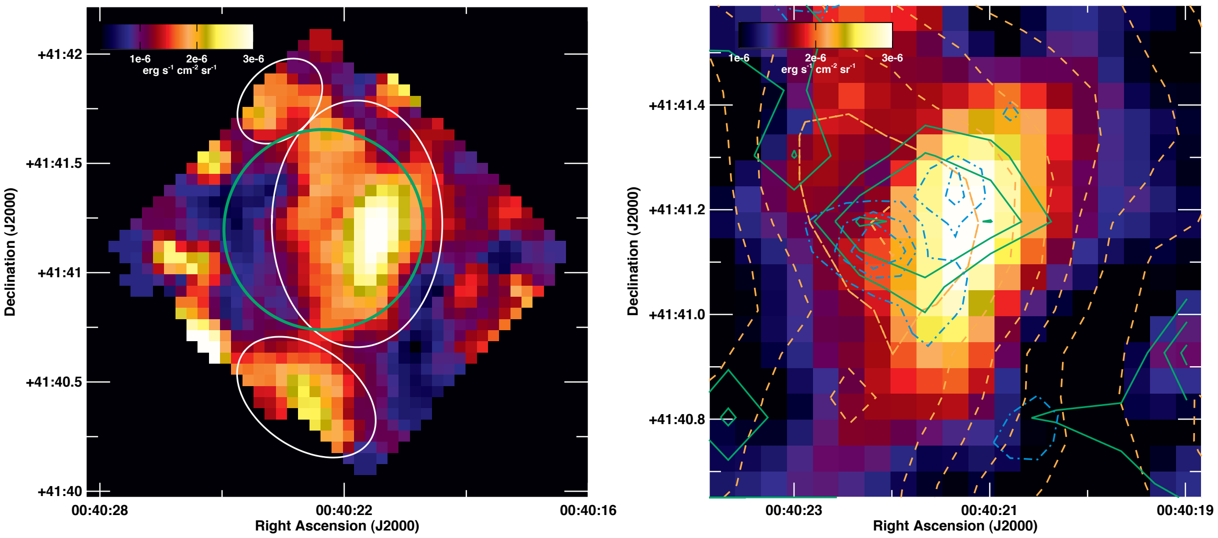

Figure 4.6: Left: PACS [CII] map of NGC 205. The elliptical apertures for photometry are indicated as white circles. The CO(1-0) pointing reported in Welch, Sage & Mitchell (1998) covering the center of NGC 205 as well as the [CII] intensity peak is colour-coded in green. Right: Zoom on the central bright region in the [CII] map, overlaid with contours of MIPS 24 μm surface brightnesses (blue, dashed-dotted curves) and HI and CO(3-2) column densities (yellow, dashed and green, solid lines, respectively). The HI contours range from 2×10^{19} cm^{-2} to 2.6×10^{20} cm^{-2} in intervals of 4×10^{19} cm^{-2}, while the CO(3-2) contours represent a H_2 column density range $1.83 \times 10^{20} \leqslant N_{\mathrm{H}_2} \leqslant 1.28 \times 10^{21}$ cm^{-2} increased in steps of 2.75×10^{20} cm^{-2}. The contours representing the MIPS 24 μm surface brightnesses range from 0.68 to 2 MJy/sr, stepwise increased by 0.33 MJy/sr.

gas in a metal-poor ISM, the interpretation of their line fluxes is hampered by a lack of knowledge about the exact origin of the line emission from within a galaxy. [CII] emission is thought to arise either from the ionized (HII regions) or the neutral (PDRs) media, while [OI] emission originates mainly from the neutral ISM. In those neutral PDRs, the [CII] line provides cooling for gas clouds with a moderate density ($n_{\mathrm{H}_2} < 10^4$ cm^{-3}), while the [OI] line cools the higher density regions.

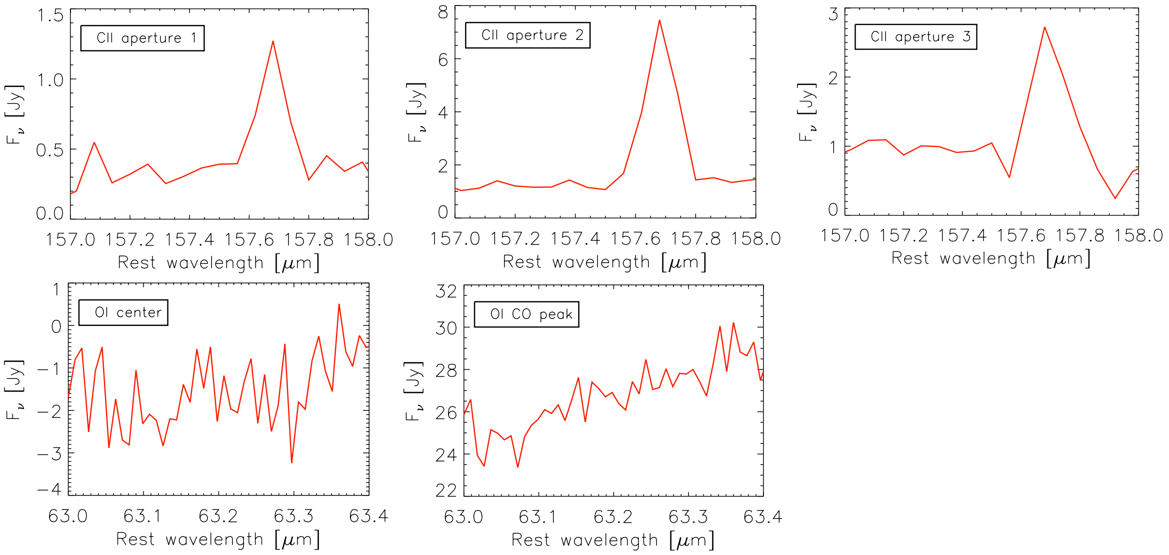

Figure 4.7: PACS spectral line plots. First row shows the [CII] line emission summed over the three individual apertures shown in Figure 4.6 and described in Table 4.4, respectively. The last row shows the non-detection of the [OI] line, with the emission added up within the observed regions covering the center and the CO peak in NGC 205, respectively.

From our PACS spectroscopy observations, we detected [CII] line emission in the center of NGC 205 (see Figure 4.6, left panel) while the [OI] line was not detected in either of the two covered regions in NGC 205 (see Figure 4.7). The faint [CII] emission in NGC 205 originates mainly from the nuclear region, with the peak intensity residing from a dust cloud west of the nucleus. From the gas and dust contours in Figure 4.6 (right panel) it becomes evident that the brightest [CII] emission region is located at the boundary of the most massive HI and molecular clouds in the center of NGC 205. The spatial correlation with the CO reservoir in the center of NGC 205 and the surrounding star formation regions (see contours of hot dust emission from MIPS 24 μm data in Figure 4.6, right panel) suggests that the [CII] emission in NGC 205 originates from photo-dissociation regions in the outer layers of molecular cloud structures. Although the [CII] emission in galaxies might have a significant contribution from ionized media, the unavailability of ionized gas tracers (e.g. [NII], [OIII]) impede a direct quantification of the [CII] emission from ionized regions. The non-detection of Hα line emission (Young & Lo, 1997) seems to point towards a low fraction of ionized gas in the ISM of NGC 205.

To determine the intensity of the [CII] line emission in NGC 205, we performed aperture photometry within ellipses matching the shape of prominent [CII] emission regions in NGC 205 (see Figure 4.6, left panel). The spectral line emission within each emission region is shown in Figure 4.7 (first three panels). The fluxes within those three apertures are summarized in Table 4.4. From equation 1 in Madden et al. (1993), we can derive the column density of atomic hydrogen, when adopting a C^+ abundance per hydrogen atom of $X_{C^+} = 1.4 \times 10^{-4}$ (Savage & Sembach, 1996) and $n_{\rm crit} \sim 2.7 \times 10^3$ cm^{-3}. When assuming $X_{\rm ISRF} \sim$ (or thus G_0) 3 for the strength of the ISRF field (see Section 4.3.4) and an average density $n_{\rm H} \sim 10^4$ cm^{-3}, we estimate a surface density temperature of T $\sim$ 40 K from the PDR models in Kaufman et al. (1999). Inserting those values in equation (1.) from Madden et al. (1993), we obtain average column densities for the three apertures within the range 2.2 $\times$ 10^{19} cm^{-2} $\leqslant N_{\rm H} \leqslant$ 3.7 $\times$ 10^{19} cm^{-2}. Summing over all three apertures, the total atomic gas mass for the [CII] emitting regions in NGC 205 is derived to be $M_{\rm g} \sim 1.5 \times 10^4$ $M_{\odot}$. Since this value is negligible compared to the total gas mass $M_g \sim 6.9 \times 10^6$ $M_{\odot}$ derived from CO(1-0) observations (see Section 4.2), we conclude that the molecular gas reservoir is probably well-traced by the CO lines in the low metallicity ISM of NGC 205. This argument is furthermore supported by the relatively low $L_{\rm [CII]}$-to-$L_{\rm CO(1\text{-}0)}$ line intensity ratio $\sim$ 1850 within the central CO(1-0) pointing from Welch, Sage & Mitchell (1998) (see green aperture overlaid on Figure 4.6). This line intensity ratio is substantially lower than the values observed in star-forming dwarf galaxies ranging from 4,000 to 80,000 (Madden, 2000; Cormier et al., 2010).

Based on PDR models for values $X_{\rm ISRF} \sim 3$ and $n_{\rm H} \sim 10^4$ cm^{-3} in the center of NGC 205, we would expect [CII] line intensities of a few 10^{-6} erg cm^{-2} s^{-1} sr^{-1} and $L_{\rm [OI]}$-to-$L_{\rm [CII]}$ line intensity ratios close to 0.5 (see Figure 3 and 4 from Kaufman et al. 1999). With a peak [CII] line intensity of 3 $\times$ 10^{-6} erg cm^{-2} s^{-1} sr^{-1} and an upper limit of $L_{\rm [OI]}$-to-$L_{\rm [CII]} < 1.75$, the observed [CII] line emission in the center of NGC 205 is in agreement with PDR models.

The lack of any bright [CII] emission from other regions in NGC 205 might be an indication for the strength of the radiation field being insufficient to photo-dissociate CO. This argument is supported by the pixel-by-pixel analysis in Section 4.3.4, which indicates the stronger radiation field in the brightest [CII] region compared to the rest of the galaxy (see Figure 4.3, left panel). Alternatively, a large reservoir of photo-dissociated CO molecules might be present in the outer layers of gas clouds, where a deficiency of ionizing photons might impede the formation of C^+ atoms. A lack of ionizing photons is also supported by the non-detection of Hα in this galaxy (Young & Lo, 1997). According to this latter scenario, we would expect the majority of dissociated carbon to be locked in [CI] rather than C^+.

From our Herschel observations of the dust continuum and far-infrared fine-structure lines [CII] and [OI] and JCMT CO(3-2) data, we are able to revisit the missing ISM mass problem in NGC 205.

We estimate an atomic gas mass of 1.5 $\times$ 10^4 $M_\odot$ associated with the [CII] emitting PDRs in NGC 205. From the CO(3-2) emitting regions in the northern part of NGC 205, we could derive a molecular gas mass of $M_{H_2} \sim 1.3 \times 10^5$ $M_\odot$. In comparison with the $M_{H_2} \sim 6.9 \times 10^5$ $M_\odot$ obtained from pointed CO(1-0) observations (Welch, Sage & Mitchell, 1998) covering the main CO(1-0) emission regions in the north of the galaxy, our measurements indicate a low fraction of dense molecular gas in the diffuse ISM of NGC 205, where star formation is currently only occurring spontaneously in localized dense clouds. Including HI observations (4.0 $\times$ 10^5 $M_\odot$) and scaling the sum of the molecular and atomic hydrogen mass by a factor $\sim$ 1.4 to include heavier elements, we obtain a total gas mass of $M_g \sim$ 0.7-1.5 $\times$ 10^6 $M_\odot$ from CO(3-2) or CO(1-0) observations, respectively.

Alternatively, we probed the ISM content through the galaxy's dust continuum emission. This approach avoids introducing uncertainty factors arising from the X_{CO} conversion factor, but additional errors on the gas mass estimates result from the SED fitting procedure to calculate the dust mass and, even more importantly, the assumption on the value for the gas-to-dust ratio. Since it has been shown that the gas-to-dust ratio in metal-poor galaxies deviates from the Galactic ratio ($\sim$ 160, Zubko, Dwek & Arendt 2004), a gas-to-dust fraction of $\sim$ 400 (Galliano, Dwek & Chanial, 2008) is considered more realistic for the central ISM in NGC 205 in view of the recent star formation episode occurring in those inner regions. This value is obtained from an extrapolation of the dust evolution model in Galliano, Dwek & Chanial (2008), when assuming little or no dust destruction and a first-order trend of the gas-to-dust ratio with metallicity (Z $\sim$ 0.3 $Z_\odot$). Relying on this gas-to-dust ratio of $\sim$ 400, the total dust mass detected from our Herschel observations corresponds to a gas mass $M_g \sim$ 4-7 $\times$ 10^6 $M_\odot$.

Upon comparison with the theoretical gas content in the range [1.3 $\times$ 10^7 $M_\odot$, 4.8 $\times$ 10^8 $M_\odot$] (see Section 4.1), gas mass estimates from either dust continuum (4-7 $\times$ 10^6 $M_\odot$) or HI+CO(1-0)+[CII] (1.5 $\times$ 10^6 $M_\odot$) observations both confirm the missing ISM mass problem in NGC 205. The lower ISM mass inferred from direct gas observations (1.5 $\times$ 10^6 $M_\odot$) in comparison with the indirect gas estimates from dust continuum observations (4-7 $\times$ 10^6 $M_\odot$) most likely results from the poor coverage of molecular gas tracers in NGC 205 and/or the uncertainty on the assumed gas-to-dust fraction (i.e. a gas-to-dust fraction closer to the Galactic value would bring the ISM masses inferred from HI+CO(1-0)+[CII] and dust continuum observations in better agreement). With the JCMT CO(3-2) and previous CO(1-0) and CO(2-1) observations mainly covering the northern part of the galaxy, the lack of knowledge about the molecular gas content for a large southern region in NGC 205, where the HI emission dominates, prevents us from determining the entire molecular gas content. If we assume a similar molecular-to-atomic gas mass ratio for the southern part of NGC 205 as observed in the northern part, the gas component in NGC 205 could be twice as massive than measured by current CO observations. The observed peak in HI (4×10^{20} cm^{-2} or 3.2 M$_{\odot}$ pc^{-2}) and dust (0.1 M$_{\odot}$ pc^{-2}) column density would imply a HI-to-dust ratio of $\sim$ 32 in the south of NGC 205. However, a more realistic gas-to-dust ratio would require a large molecular gas reservoir residing in those southern areas. This argumentation is also confirmed by the H_2 column densities of 1.8 and 2.4×10^{20} cm^{-2} measured from two JCMT CO(2-1) pointings near the southern peak in HI, when assuming a CO(2-1)-to-CO(1-0) line ratio of $\sim 0.9 \pm 0.2$ as found by Young & Lo (1996) in a spatially resolved molecular cloud.

In addition to this unexplored molecular gas reservoir in the southern part of the galaxy, a substantial fraction of the gas component might remain undetected by current observations, either because a fraction of the gas is locked in hot X-ray or ionized gas haloes (similar to the heated gas returned by evolved stars in giant massive ellipticals) and/or the present molecular gas is traced neither by CO nor [CII] molecules. Alternatively, we could invoke an internal/environmental mechanism solely removing the gas from NGC 205 and leaving the dust unharmed to explain the higher gas masses inferred from dust continuum observations. In view of the good correlation found for the gas and dust component, there is however no reason to assume a higher inertia for the dust and thus to imply that gas particles are more easily transported out of the gravitationally bound regions in NGC 205.

In the next paragraphs, we discuss possible explanations for the inconsistency between the observed ISM content (either from HI+CO+[CII] or dust continuum observations) in NGC 205 and theoretical predictions, such as non-standard conditions for the SFE or initial mass function (IMF) or environmental processes able to remove part of the ISM during the last episode of star formation in NGC 205.

4.6.1 Non-standard conditions

Non-standard conditions such as a top-heavy IMF (more massive stars are produced, requiring less input gas mass) or a higher star formation efficiency (> 10 % of the gas is converted into stars) could be invoked to explain the missing ISM in NGC 205. Harmonizing the observed ISM content with the theoretical predictions would require an IMF deviating significantly from the general assumptions and/or an increase in the SFE from 10% to at least 65%. Although such a top-heavy IMF or increased SFE was thought to be present in some ULIRGS or starbursts (e.g. M82, Knapp et al. 1980), the non-standard conditions in those galaxies are owing to the presence of high density gas, introducing a different mode of star formation (Daddi et al., 2010). With a SFR $\sim 7.0 \times 10^{-4}$ M$_{\odot}$ yr^{-1} (Monaco et al., 2009) during the last starburst episode, NGC 205 does not mimic the typical star formation activity (> 10 M$_{\odot}$ yr^{-1}) in those starburst galaxies. Also under less extreme circumstances, local variations in the SFE (Boquien et al., 2011a) and perturbations at the upper mass end of the IMF (Meurer, 2011) have been claimed. However, the latter IMF variations have been questioned on its turn invoking poor extinction corrections and a variable SFR in those galaxies (Boselli et al., 2009a; Weisz et al., 2012). Relying on recent results from Martín-Manjón et al. (2012) and Boylan-Kolchin, Bullock & Kaplinghat (2012), finding no evidence for extreme star formation efficiencies in star-forming dwarf galaxies and therefore rather supporting a moderate SFE of 10-20% or less, we argue that non-standard conditions (top-heavy IMF and/or increased SFE) are not likely to occur in NGC 205. This result implies that we should rather invoke efficient mechanisms of gas removal to explain the low observed gas content in NGC 205.

4.6.2 Gas removal

Supernova feedback

Feedback from supernovae (Dekel & Silk, 1986; Babul & Rees, 1992; De Young & Heckman, 1994) or potentially an AGN are capable of removing a significant amount of gas from NGC 205. Relying on the absence of any LINER or Seyfert diagnostics (Ho, Filippenko & Sargent, 1995), we argue that the effect of AGN feedback in NGC 205 is currently negligible. Based on the 3σ upper limit of 3.8×10^{4} M$_{\odot}$ for the mass of the SMBH in NGC 205 from studies of the stellar kinematics based on deep HST images (Valluri et al., 2005), we believe the role of an AGN was also limited throughout the recent history of NGC 205. On the contrary, supernova feedback and/or stellar winds could be responsible for expelling gas from the central regions, during the last episode of star formation. Examining the effectiveness of SN II feedback during the last episode of star formation, Welch, Sage & Mitchell (1998) confirm that supernova winds or blasts were capable of removing a significant amount of gas from the central regions of NGC 205. Indeed, applying the dwarf galaxy model for $M_{galaxy} \sim 10^9$ $M_\odot$ from De Young & Heckman (1994), a minimum energy of $\sim 10^{55}$ f_{gas} ergs would be required to expel most of the gas from the inner regions. Following the burst mass $\sim 7 \times 10^5$ $M_\odot$ reported in Wilcots et al. (1990), the gas fraction is found to be $f_{gas} \sim 0.007$, when assuming a 10% star formation efficiency. This would require an energy of at least 7×10^{52} ergs to remove gas. This level is easily achieved with the energy $\sim 6 \times 10^{54}$ ergs released by the SNe II associated with the last burst (Welch, Sage & Mitchell, 1998). Keeping in mind the clumpy gas distribution and the offset of the local HI column density peaks from the locations of young stars (Young & Lo, 1997) in addition to those theoretical arguments, we argue that both supernova feedback and/or stellar winds have likely disturbed the ISM of NGC 205. Energy feedback from supernovae has furthermore been proven to have an important share in the formation of dwarf spheroidal systems (Kormendy et al., 2009).

Despite theoretical arguments supporting a history of violent supernova explosions, a previous attempt to detect supernova remnants in NGC 205 failed ($F_\nu < 0.06$ mJy, Lucero & Young 2007). Relying on the low radio continuum detection rate for low surface brightness dwarfs (Hoeppe et al., 1994; Lucero & Young, 2007), it might not be surprising that the detection of supernova remnants at 20 cm was unsuccessful. The majority of the 20 cm emission is thought to arise from synchrotron emission originating from electrons accelerated in the expanding shells of Type II and Type Ib supernova remnants. Due to the increased cosmic ray diffusion timescales (Klein et al., 1992; Murphy et al., 2006) (i.e. electrons are escaping more easily from the ISM) for galaxies with a low star formation activity (SFR $\leqslant 0.2$ $M_\odot$ yr^{-1}), those objects become radio quiet in short timescales. Although violent supernova explosions might have occurred in the past, the associated radio emission is likely smoothed out in the low potential well of NGC 205. Also in other wavelength domains the detection of any supernova remnants will be challenging. While the star formation is known to be active up to at least 60 Myr ago, a typical age $\sim$ 10 Myr for a SNII progenitor and a SNR lifetime $\sim$ 25000 years implies that it is difficult to detect any remaining evidence of supernova remnants in NGC 205.

Environmental interactions

Galaxy harassment (Moore et al., 1996), starvation (Larson, Tinsley & Caldwell, 1980) and viscous stripping (Nulsen, 1982) are important transformation processes for galaxies in clusters, whereas tidal stirring (Mayer et al., 2001) and galaxy threshing (Bekki, Couch & Drinkwater, 2001) are considered responsible for the formation of dwarf spheroidals and ultra-compact dwarfs in the low density environment of groups. Although photometrically classified as dwarf elliptical galaxy (de Vaucouleurs, 1991), the formation processes for NGC 205 seem more closely related to the dwarf spheroidal galaxy population (transformed from late-type galaxies through internal and environmental processes) rather than to merger remnants, thought to be the main driver for the formation of genuine ellipticals (Kormendy et al., 2009). Therefore, a combination of ram pressure and tidal stripping has more likely influenced the formation of NGC 205 since those processes are capable of transforming gas-rich dwarf galaxies into dwarfs with a blue central core when passing through the halo of a galaxy of the same size as the Milky Way (Mayer et al., 2006). Tidal or gravitational interactions are also considered to be the main formation mechanism for spheroidal and lens-shaped galaxies in groups (Kormendy et al., 2009; Bekki & Couch, 2011; Smith et al., 2012). In a similar fashion, ram pressure stripping is found to form dwarf elliptical galaxies with blue nuclei in the Virgo cluster (Boselli et al., 2008a).

Several observations are indicative for the tidal influence of M31 on its companion NGC 205: a twist in the elliptical isophotes (Hodge, 1973; Choi, Guhathakurta & Johnston, 2002), a stellar arc of blue metal-poor red giant branch stars northwest of M31 (Ibata et al., 2001; McConnachie et al., 2004), a tidal debris of C stars to the west of NGC 205 (Demers, Battinelli & Letarte, 2003), a stripped HI cloud 25 arcmin southwest of NGC 205 which overlaps in velocity with the galaxy (Thilker et al., 2004), peculiar HI morphology and kinematics (Young & Lo, 1997), stars moving in the opposite direction with respect to the rotation of the main stellar body (Geha et al., 2006; De Rijcke et al., 2006) and an optical tidal tail extending at least 17 arcmin southwards from the galaxy's center (Saviane, Monaco & Hallas, 2010). This latter stellar tail coincides with the tentative dust tail detected in our SPIRE data (see Section 4.3.2) and, thus, might be an indication for the removal of dust from NGC 205 as a result from the tidal influence of M31. Besides the tidal features characterizing NGC 205, M31 is also affected by the tidal influence exerted by NGC 205. While the origin of two off-centre spiral rings is probably attributable to a head-on collision with M32 (Block et al., 2006), the warped structure in the outer HI disk of M31 (Sato & Sawa, 1986) and a distortion of the spiral structure in the disk (Gordon et al., 2006) are likely caused to some extent by a two-body interaction between M31 and NGC 205.

Although those observations confirm the tidal influence of M31 on the outer regions of NGC 205, it does not provide an explanation for the removal of gas from the inner regions, where the last episode of star formation took place and we would expect to find the left-over gas reservoir. Hydrodynamical simulations suggest that the gaseous component might be disrupted and partly removed even within the tidal radius (4 arcmin, Geha et al. 2006) without any indications for stellar bridges and tails at these radii (Icke, 1985), but whether it is the case for NGC 205 is difficult to inquire due to the uncertainties regarding its orbit around M31 (Howley et al., 2008). However, in combination with supernova feedback expelling the gas from the inner regions, tidal interactions might strip the expelled gas from the outer regions.

Whether or not responsible for the removal of gas from the inner regions, a tidal encounter with a companion closer than 100-200 kpc is able to trigger SF through shocks in the disk of a typical dwarf galaxy when moving on a coplanar prograde orbit (Brosch, Almoznino & Heller, 2004). With a line-of-sight distance between the Andromeda galaxy and NGC 205 of $\sim$ 39 kpc (McConnachie et al., 2005) and the likely prograde trajectory of NGC 205 toward its parent galaxy, M31 (Geha et al., 2006; Howley et al., 2008), tidal interactions might have given the initial start for the last episode of star formation. Furthermore, the most recent episodes of star formation during the last gigayear seem correlated with the orbit about M31 (Davidge, 2003), which provide additional evidence for the tidal triggering of star formation in NGC 205.

4.7 Other dwarf galaxies with missing ISM problem

Two other dwarf companions of M31, NGC 185 and NGC 147, are thought to have a star formation history comparable to NGC 205 based on their nearly identical optical appearances (Holmberg diameters, B - V colours, average surface brightnesses), mass-to-light ratios $(M/L)_B \sim 4\ \mathrm{M}_\odot/\mathrm{L}_{\odot,B}$ (De Rijcke et al., 2006) and specific frequencies of C stars (Davidge, 2005), implying similar fractions of gas and dust which have been turned into stars in the past. Interestingly, both objects also feature a missing ISM mass problem (Sage, Welch & Mitchell, 1998).

In correspondence to the missing ISM mass problem in NGC 205, tidal interactions and supernova feedback are also believed to have influenced the ISM content in NGC 185 and NGC 147. The tidal influence of M31 (D = 785 ± 25 kpc, McConnachie et al. 2005) is considered negligible at distances of D = 616 ± 26 and 675 ± 27 kpc (McConnachie et al., 2005) for NGC 185 and NGC 147, respectively, compared to NGC 205 (D = 824 ± 27 kpc, McConnachie et al. 2005). However, both galaxies are thought to form a gravitationally bound pair (van den Bergh, 1998) and might have tidally interacted in the past. Aside from the possible occurrence of tidal interactions, indications for supernova remnants are found in NGC 185 (Gallagher, Hunter & Mould, 1984; Young & Lo, 1997; Lucero & Young, 2007) and the current ISM content in this galaxy ($\sim 7.3 \times 10^5\ \mathrm{M}_\odot$) resembles the estimated mass returned to the ISM by planetary nebulae ($\sim 8.4 \times 10^5\ \mathrm{M}_\odot$, Sage, Welch & Mitchell 1998). However, the lack of ISM in NGC 147 remains a puzzling feature in this evolutionary framework.

Soon, we will be able to revise also the missing ISM mass problem in those two galaxies, based on Herschel dust continuum observations for both galaxies and PACS spectroscopy mapping ([CII], [OI]) for NGC 185.

5

Sombrero Galaxy (M104, NGC 4594)

5.1 Worth knowing about Sombrero

The Sombrero galaxy is an early-type spiral galaxy (Sa) with a very symmetric dust lane and dominant bulge, which are the main characteristics to which the galaxy owes its peculiar name (see Figure 5.1). At a distance of only 9.2 Mpc (which is the average of measurements from Ford et al. 1996 and Ajhar et al. 1997), it is one of the most nearby early-type spirals. The Sombrero galaxy has been studied in detail, with a particular focus on its supermassive black hole (SMBH) (Kormendy et al., 1996), rich globular cluster population (e.g., Spitler et al. 2008; Cockcroft et al. 2009; Harris et al. 2010; Burkert & Tremaine 2010), stellar population (e.g., Burkhead 1996; Ford et al. 1996; Mould & Spitler 2010) and discrete X-ray sources (e.g., Li, Wang & Hameed 2007; Li et al. 2010). Its proximity implies that also the distribution and characteristics of dust can be examined in much detail. Its inclination of $\sim 84^\circ$ combines the advantages of edge-on spirals with an insight of the inner regions. This allows to put strong constraints on the distribution of stars and dust in the disk. While IRAS observations had to settle for a global SED study in the infrared/submm wavebands due to its limited angular resolving power (Rice et al., 1988; Schmitt et al., 1997), Bendo et al. (2006) could separate the emission from different components contributing to the dust emission at infrared wavelengths. From their image modelling procedure on the highest resolution Spitzer/MIPS (Multiband Imaging Photometer for Spitzer) data (24 and 70 μm), they could separate the emission from the nucleus, the bulge, the inner disk and the dust ring contributing to the different infrared wavebands. In the submillimeter band, Vlahakis et al. (2008) could disentangle the AGN from the dust ring component in the LABOCA (Large APEX Bolometer Camera) 870 μm and MAMBO-2 (Max Planck Millimetre-wave Bolometer Array) 1.2 mm images. This wealth of available FIR observations (IRAS: Rice et al. 1988; MIPS: Bendo et al. 2006; LABOCA & MAMBO: Vlahakis et al. 2008) and the very regular and symmetric shape of the dust lane in M104 permit a spatially resolved analysis of the dust energy balance in this nearby galaxy. In the past, the Sombrero dust ring has been probed in many dust related studies. Matsumura & Seki (1989) derived a radial distribution of the dust in the disk from observations of the polarization along the major axis. Knapen et al. (1991) were the first to study the extinction law in M104. They found a good agreement with the Galactic extinction law, except for the B and V band, which required the assumption of embedded stars in the dust lane or additional foreground light. Emsellem (1995) used high resolution HRCAM (High Resolution Camera) B, V , R_C and I_C data to construct a model for both the stellar and dust component in the Sombrero ring. From discrepancies between his model and observed extinction profiles, he concluded that scattering is an important extinction process and neglecting its effect in highly-inclined dust disks may cause a

Figure 5.1: Hubble Space Telescope (HST) image of the Sombrero galaxy (Christian et al., 2003).

substantial underestimation of the true dust content in such a galaxy.

In our analysis, we will extend the analysis in Emsellem (1995) to a full radiative transfer study, including absorption, scattering and thermal dust re-emission. Continuing on the image modeling at infrared wavelengths from Bendo et al. (2006), this multi-wavelength analysis aims to model the characteristics and distribution of dust in M104 accounting for both the extinction and dust emission properties. We use the SKIRT radiative transfer code to construct a 3D model for the stellar and dust component in the Sombrero galaxy. Subsequently, we compare the FIR/submm emission predicted by our radiative transfer model to the observed FIR/submm images and fluxes, allowing an unprecedented analysis of the dust energy balance in the Sombrero galaxy.

5.2.1 Optical data

The optical data which will be used to constrain the 3D radiative transfer model include the stellar SED, images and minor axis extinction profiles in both the V and R_C band. The stellar emission in the SED is constrained by the GALEX FUV and NUV, optical $BVRI$, 2MASS JHK and IRAC (Infrared Array Camera) 3.6 and 4.5 μm fluxes, which were taken from the Dale et al. (2007) broadband spectral atlas (see Table 5.1 for an overview). IRAC 5.8 and 8.0 μm measurements are also available, but were not used in the fitting procedure since the emission at those wavelengths is not only stellar in origin. Also the GALEX FUV and NUV data were omitted from the fitting procedure, since they critically depend on the amount of extinction and, therefore, the specific amount of young stars in a galaxy (see Section 5.3.2 later on). The minor-axis extinction curves in the V and R_C band are taken from Emsellem (1995). Only the minor axis extinction profiles in the V and R_C band were used in the fitting procedure, because only in those wavebands the signal-to-noise was sufficient in the entire dust lane along the minor axis. The V band images were obtained from the archive of the Spitzer Infrared Nearby Galaxies Survey (Kennicutt et al., 2003). GALEX FUV and NUV images were retrieved from the NASA/IPAC Extragalactic Database (NED).

5.2.2 Infrared+submm data

The infrared dataset from observations that will be used to compare with predictions from our radiative transfer model is composed of the dust SED and the MIPS images at 24, 70 and 160 μm. The dust SED is constrained by the total fluxes obtained from IRAC 5.8 and 8 μm (Dale et al., 2007), IRAS (Rice et al., 1988), MIPS (Bendo et al., 2006), *Herschel* PACS and SPIRE (Dale et al., 2012) and LABOCA/MAMBO (Vlahakis et al., 2008) observations (see Table 5.1 for an overview). The Spitzer 24 and 160 μm images could be retrieved from the Spitzer Local Volume Legacy survey (Dale et al., 2009).

Filter	λ (μm)	F_ν (Jy)	ref[1]
FUV	0.15	0.0056 ± 0.0008	1
NUV	0.28	0.0177 ± 0.0025	1
B	0.45	2.25 ± 0.23	1
V	0.55	2.76 ± 0.28	1
R	0.66	3.41 ± 0.34	1
I	0.81	4.30 ± 0.43	1
J	1.25	8.06 ± 0.81	1
H	1.65	9.19 ± 0.927	1
K	2.17	7.57 ± 0.76	1
IRAC 3.6	3.6	3.94 ± 0.53	1
IRAC 4.5	4.5	2.31 ± 0.32	1
IRAC 5.8	5.8	1.75 ± 0.22	1
IRAC 8.0	8.0	1.30 ± 0.16	1
IRAS 12	12	0.74 ± 0.19	2
MIPS 24	24	0.65 ± 0.07	3
IRAS 25	25	0.50 ± 0.13	2
IRAS 60	60	4.26 ± 1.07	2
MIPS 70	70	6.7 ± 1.3	3
PACS 70	70	7.87 ± 0.49	4
IRAS 100	100	22.86 ± 5.72	2
PACS 100	100	23.0 ± 1.3	4
MIPS 160	160	35.1 ± 7.0	3
PACS 160	160	38.9 ± 2.0	4
SPIRE 250	250	25.6 ± 1.8	4
SPIRE 350	350	12.1 ± 0.9	4
SPIRE 500	500	5.56 ± 0.41	4
LABOCA 870	870	0.924 ± 0.092	5
MAMBO 1200	1200	0.442 ± 0.044	5

Table 5.1: Overview of photometry measurements for the Sombrero galaxy.

[1] References: (1) Dale et al. (2007); (2) Rice et al. (1988); (3) Bendo et al. (2006); (4) Dale et al. (2012); (5) Vlahakis et al. (2008)

i	σ_i(pc)	q_i	L_i ($L_{\odot,V}$)
1	8.028	0.037	7.385×10^6
2	18.375	0.562	1.702×10^7
3	43.842	0.641	7.572×10^7
4	92.545	0.672	2.904×10^8
5	109.270	0.059	8.126×10^7
6	203.153	0.150	2.348×10^7
7	206.899	0.619	7.726×10^8
8	463.795	0.820	1.832×10^9
9	1074.592	0.784	2.995×10^9
10	1659.834	0.045	1.152×10^9
11	2553.127	0.620	7.775×10^9
12	3701.042	0.090	5.937×10^9
13	4610.926	0.778	8.981×10^9
14	9630.969	0.953	1.032×10^{10}
15	30659.820	1.000	1.656×10^{10}

Table 5.2: *V* band MGE–components

5.3 Dust energy balance study

5.3.1 Model I: standard model

Stellar component

A model for the emission at optical wavelengths in M104 needs to account for the contribution from the bulge, disk, nucleus and the halo. Considering that only minor departures from axial symmetry have been perceived along the disk and in the central region due to dust patches, resembling dust lanes in a stellar bar (Emsellem & Ferruit, 2000), we assume an axisymmetric geometry for the stellar component in the Sombrero galaxy. We adopt the 15 Multi-Gaussian Expansion (MGE) components, both in the *V* and R_C band, reported in Emsellem (1995). Only the global intensity of the stellar component is scaled linearly until our models achieve the best fit with the stellar SED using a χ^2 minimization procedure. The intensities of the individual Multi-Gaussian Expansion components are summarized in Table 5.2 and 5.3 for the *V* and R_C band, respectively.

The intrinsic SED of the stars is parametrized by a Maraston (1998, 2005) single stellar population with an age of 10 Gyr and a close to solar metallicity Z = 0.016, based on the chemo-evolutionary analysis in Vazdekis et al. (1997). This value for the metallicity

i	σ_i(pc)	q_i	L_i ($L_{\odot,V}$)
1	6.690	0.716	9.597×10^6
2	17.885	0.371	1.928×10^7
3	42.595	0.612	7.831×10^7
4	93.262	0.649	3.084×10^8
5	106.509	0.037	7.904×10^7
6	203.205	0.612	7.550×10^8
7	203.294	0.135	2.468×10^8
8	446.997	0.827	1.776×10^9
9	1054.516	0.756	2.961×10^9
10	1765.644	0.027	1.363×10^9
11	2553.219	0.620	7.877×10^9
12	3720.000	0.090	5.578×10^9
13	4611.100	0.778	9.102×10^9
14	9631.31	0.953	1.054×10^{10}
15	30660.924	1.000	1.603×10^{10}

Table 5.3: R_C band MGE–components

is somewhat higher than the estimate [Fe/H] $\sim$ -0.5 from Mould & Spitler (2010), who determined the modal metallicity value for a field 6.8 effective radii from the center of M104. Considering that this field is mainly populated by halo stars and, therefore, constitutes mainly of old metal-poor objects, we consider the metallicity estimate from Mould & Spitler (2010) within the same order of magnitude of the nearly solar metallicity (Z $\sim$ 0.016) adopted in this work. Besides the main stellar body of the Sombrero galaxy, we also added a nuclear source to the model. At optical wavelengths, the nucleus of M104 was modelled as a point source in our radiative transfer model. Also at IR/submm wavelengths, a significant portion of the emission arises from the nucleus. Especially the origin for the high 850 μm compared to the 160 μm flux in the nucleus remains an unsettled issue (Bendo et al., 2006; Vlahakis et al., 2008). In order to account for this peculiar emission from the nucleus at submm wavelengths, we also include the nucleus of the Sombrero galaxy as a point source emitting brightly in the IR. The shape of the SED was obtained through an interpolation between the fluxes from the nucleus at IR/submm wavelengths (Bendo et al., 2006; Vlahakis et al., 2008).

Dust component

A dust model will need a representative parametrization of the dust distribution in both the ring and inner disk of M104. Similar to the stellar component, the very regular and symmetric dust lane in the Sombrero galaxy justifies our choice of an axisymmetric dust geometry for the dust ring. Detailed analyses of the extinction profiles along the vertical axis showed that the dust in the dust lane is distributed in a ring with three peaks, which average out to a double ring structure along vertical profiles further from the galactic center (Knapen et al., 1991; Emsellem, 1995). Therefore, we model the dust ring as a linear combination of 4 Gaussian functions:

$$\rho_{\rm d}(R,z) = \sum_{i=1}^{4} \rho_{0,i} \, \exp\left[-\frac{(R-R_i)^2}{2\sigma_i^2}\right], \quad -\frac{h_z}{2} \leqslant z \leqslant \frac{h_z}{2}. \tag{5.1}$$

For each Gaussian component, the radial distribution is Gaussian, while the density in the vertical direction is assumed to be constant. This constant density is justified by the small extent of the dust lane in vertical direction ($h_z \sim 20$ pc) (Emsellem, 1995). Three of the Gaussians are used to fit the peaks in the minor axis extinction profile, the fourth is used to describe the broader, ring-wide distribution of dust. The spatial distribution of each individual Gaussian component is determined by three parameters: the radial distance R_i at which the maximum value of the Gaussian function is situated, the width σ_i of the Gaussian function and the central mass density $\rho_{0,i}$. From the extinction curves, one can already determine fairly accurate estimates of the radial distance of the density peaks. Therefore, the only unknowns which are allowed to vary in our fitting procedure are the width σ_i and central density $\rho_{0,i}$ of each Gaussian component. Although the bulk of the dust content in the Sombrero galaxy is distributed in the symmetric ring, the inner disk also contains an amount of dust and young stars. In correspondence to the model from Bendo et al. (2006), we represent the inner dust disk as an exponential disk with a radial scale length of 2000 pc. The scale height is confined to 20 pc, following the height of the dust ring. The dust content of the inner disk was determined from a modified blackbody fit to the MIPS 70 and 160 μm fluxes and was set to 4.07×10^5 $\mathrm{M}_\odot$. Throughout the ring and inner disk of the Sombrero galaxy, we assume a single dust mixture, consisting of different dust particles with a particular grain size distribution. The abundances, extinction and emissivity of the dust mixture are taken from the Draine & Li (2007) model, which accurately reproduces the optical properties of the dust in our own Galaxy.

When optimizing the spatial distribution of dust in the Sombrero ring to fit the minor axis extinction profiles in the V and R_C band, we find the parameters (R_i, σ_i, $\rho_{0,i}$) that correspond to the best fitting model. Table 5.4 summarizes those parameters for our standard model (first part of table). Instead of the central mass density $\rho_{0,i}$, Table 5.4 states the relative mass contribution M_i/M_d, from which $\rho_{0,i}$ can be derived knowing that $M_d = 7.5 \times 10^6$ $\mathrm{M}_\odot$ is the dust mass in the ring. Knowing that $M_d = 4.1 \times 10^5$ $\mathrm{M}_\odot$ of dust resides in the inner disk, the total dust content in our standard model

Standard model			
$M_{\mathrm{d,ring}} = 7.5 \times 10^6$ $\mathrm{M}_\odot$			
Gaussian component	R_i	σ_i	M_i/M_d
1	6100	480	0.30
2	7900	250	0.18
3	8750	180	0.27
4	6850	1500	0.25

Model with embedded SF			
$M_{\mathrm{d,ring}} = 7.8 \times 10^6$ $\mathrm{M}_\odot$			
Gaussian component	R_i	σ_i	M_i/M_d
1	6100	480	0.33
2	7900	250	0.18
3	8750	180	0.26
4	6850	1500	0.23

Table 5.4: The parameters of the 4 Gaussian components

amounts to $M_d = 7.9 \times 10^6$ $\mathrm{M}_\odot$. Figures 5.2 and 5.3 show the ability of this basic model to reproduce optical data of the Sombrero galaxy. In the upper panel of Figure 5.2, the observed SED fluxes (see Table 5.1) are overlaid on the SED model. The middle and bottom rows represent the minor axis extinction profiles in the V and R_C band. Figure 5.3 displays the images in the V, MIPS 24 μm and MIPS 160 μm wavebands, where the left and right panels correspond to the observed data and model images, respectively.

Comparison to FIR/submm data

When comparing the FIR/submm emission predicted from radiative transfer calculations to the observed quantities, we find a large discrepancy between the radiative transfer model and FIR/submm observations. Our standard model underestimates the true FIR/submm SED emission by a factor of ~ 3 (see Figure 5.2), similar to what has been found in energy balance studies of edge-on spirals (Popescu et al., 2000; Misiriotis et al., 2001; Popescu &Tuffs, 2002; Alton et al., 2004; Dasyra et al., 2005; Baes et al., 2010). This lack of IR emission is also obvious if we look at the 24 and 160 μm SKIRT model images (see Figure 5.3, two bottom rows). Our model furthermore is inconsistent with the UV emission observed in the Sombrero galaxy (see Figure 5.2 and Figure 5.3, top row). Although this standard model could reproduce the optical data, modifications to this model are necessary to eliminate the remaining discrepancy in the IR emission and balance the dust energy budget.

5.3.2 Model II: model with embedded star formation

Relying on the large inconsistency between model and observations for the standard model, we require a substantial modification of this basic model to account for the discrepancies in dust emission. A possible explanation for the energy balance problem in the Sombrero galaxy is the presence of young stars, either in relatively unobscured HII regions or embedded in heavily obscured dust clouds. The former young stars will be capable of reproducing the UV emission originating from M104. The latter embedded sources will provide a significant boost to the thermal dust heating, while their locally absorbed radiation only has a minor contribution to the global extinction of starlight. The presence of an additional component of young stars in the dust lane was already claimed by Knapen et al. (1991) to explain the inconsistencies between his modelled and observed B and V band extinction profiles. Here, we investigate whether an additional component of young stars in our model can account for the missing dust emission. To obtain a self-consistent model for the Sombrero galaxy, we not only require fitting the direct UV emission from young stars and the thermal emission at FIR/submm wavelengths, but also the optical SED, V and R_C band images and extinction profiles still need to be reproduced. Considering that young stars supply additional dust heating, the amount of dust will need reconsideration in order to still account for the observed extinction profiles. In response to an additional component of young stars, the extinction profile in the V band might decrease (depending on the amount of young stars). Although the emission from young stars will augment the number of absorption events taken place, the total amount of emitted V band photons grows even more, causing a drop in the relative amount of extinction. Nevertheless we expect the changes to be small in the V band and almost negligible in the R_C band, since the bulk of emission from these young stars peaks at shorter wavelengths (UV).

Young stellar component

To reproduce the emission from a warm dust component at mid-infrared wavelengths, we supplement the standard model from Section 5.3.1 with heavily embedded young star clusters of ages < 10 Myr. Based on the MIPS 24 μm image (see Figure 5.6, third row) and major-axis profile (see Figure 5.5, bottom panel), we distribute this young stellar component in the inner part of the dust ring and the inner disk. Also Vlahakis et al. (2008) concluded that the dominant heating sources for the dust ring are located on the inside of the ring, based on the more extended dust ring at 870 μm and 1.2 mm compared to the emission in the wavelength range from 5.7 to 70 μm. Therefore, we insert $\sim 75\%$ of this young stellar population in the first component of the dust ring (located closest to the nucleus). The remaining 25% resides in the second density peak of the dust ring. This distribution more or less corresponds to the ratio of the dust masses in the first and second Gaussian component describing the dust lane in the Sombrero galaxy. For the distribution of star-forming regions in M104 in the inner disk, we assume the same model describing the spatial distribution of dust in the disk. The SED of this young stellar population is parametrized with an emission spectrum generated from the one-dimensional evolution models of HII regions around massive clusters of young stars presented in Groves et al. (2008). For the specific parameters constraining those models, we refer to Section 6.3.2, which provides a more thorough discussion on the model assumptions.

To reproduce the UV emission observed in the Sombrero galaxy, we need to supplement our model furthermore with young stars of ages between 10 and 100 Myr old, of which the non-ionizing radiation typically dominates the UV emission spectrum in galaxies (Calzetti et al., 2005). Representative emission spectra for this young stellar component are obtained from the Starburst99 library (Leitherer et al., 1999), for an instantaneous burst with a metallicity similar to the old stellar population in the Sombrero galaxy, a burst mass M_{cl} = 10^6 $M_\odot$ and a Kroupa (2002) broken power-law IMF. The latter assumption on the IMF is consistent with the stellar emission spectra used to compute the SED of stellar clusters younger than 10 Myr in Groves et al. (2008). From the GALEX NUV image (see Figure 5.6, first row) and the corresponding major-axis profile (see Figure 5.5, top panel), we can constrain the position of less obscured star-forming regions in the Sombrero galaxy. The relatively unobscured young stellar component seems to reside mainly in the bulge and disk component also harboring the old stellar population in the Sombrero galaxy, with also a smaller fraction of young stars located in the inner regions of the dust lane.

The best fitting model obtained from a least-square fitting procedure to the SED fluxes and images at UV and mid-infrared wavelengths complements the standard model with a young stellar component (< 10 Myr) of modest SF activity in the inner disk (SFR $\sim$ 0.03 $M_\odot$ yr^{-1}) and in the inner part of the dust ring (SFR $\sim$ 0.09 $M_\odot$ yr^{-1}). An average star formation rate $\sim$ 0.25 $M_\odot$ yr^{-1} was found for the population of young stars with ages ranging from 10 to 100 Myr, with the bulge being the host of majority of these young stars (SFR $\sim$ 0.15 $M_\odot$ yr^{-1}) and the dust ring harboring the remainder of 10 to 100 Myr aged stars (SFR $\sim$ 0.1 $M_\odot$ yr^{-1}). The dust mass in the dust ring was a little increased ($M_d = 7.8 \times 10^6$ $M_\odot$) to maintain the resemblance between the modelled and observed V band extinction curve due to the emission of young (10-100 Myr) stars, while the dust mass in the inner disk did not require an additional dust mass. The relative distribution of dust in the different components of the ring needed some fine-tuning due to the presence of a young stellar component (see Table 5.4, second part). Furthermore, we need to account for the dust mass related to the evolution models of HII regions described in Groves et al. (2008), which is estimated to be $M_d = 2.1 \times 10^6$ $M_\odot$, which sums up to a total dust mass of $M_d = 1.0 \times 10^7$ $M_\odot$ in our radiative

SFR tracer(s)	SFR relation	SFR [$M_\odot$ yr^{-1}]
FUV	Salim et al. (2007)	0.04
24μm	Rieke et al. (2009)	0.07
FUV+24μm	Zhu et al. (2008) (ext. corr.) Kennicutt et al. (2009) (SFR rel.)	0.15
FUV+TIR	Cortese et al. (2008) (ext. corr.) Kennicutt et al. (2009) (SFR rel.)	0.19
Hα+8μm	Kennicutt et al. (2009)	0.14
Hα+24μm	Kennicutt et al. (2009)	0.07
Hα+TIR	Kennicutt et al. (2009)	0.16
Hα+1.4GHz	Kennicutt et al. (2009)	0.26 (total) 0.06 (disk)

Table 5.5: Star formation rates in M104: predictions from different SFR tracers.

transfer model. Considering that the Sombrero ring contains the majority of dust mass, it is rather surprising that about half of the recent star formation activity occurred in the inner regions (bulge+inner disk), close to the nucleus. On the other hand, a recent image decomposition analysis based on IRAC data supports a more disk-like bulge structure, distinct from the prominent stellar halo in M104 (Gadotti, Baes & Falony, 2010). In view of this scenario, the presence of a young stellar population in the plane of the disk-like bulge already seems more plausible.

Comparison to FIR/submm data

This model with embedded SF is able to fit the UV as well as 24 and 70 μm observations (see top panel in Figure 5.4 and first and third row in Figure 5.6). The young stars also provide a heating source for very small grains and PAH molecules. Indeed, the typical peaks characteristic for PAH emission show up in mid-infrared wavebands in the model SED (see Figure 5.4). This result is consistent with the low-resolution IRS (Infrared Spectrograph) spectrum taken from the ring in M104, which shows the most prominent PAH feature in the 11.3 μm band, consistent with star formation activity in the ring (Bendo et al., 2006). The total star formation activity (SFR $\sim$ 0.37 $M_\odot$ yr^{-1}) in our model agrees reasonable well with the SFR estimate obtained from Hα and radio observations of the Sombrero galaxy in Kennicutt et al. (2009) and is of the same order of magnitude as other SFR estimates based on a suite of other diagnostics (see Table 5.5). Table 5.5 summarizes the predictions for the SFR from different diagnostics and also mentions the reference to the applied SFR relation. All values of the SFR were adjusted to the Kroupa (2002) IMF. This correspondence with different SFR tracers makes us confident that the star formation activity in our model was not overestimated. On the contrary, we argue that the level of star formation accounted for in our model was maximized, since any additional star formation activity would imply that our radiative transfer model no longer fits the observed UV and mid-infrared emission from the Sombrero galaxy. While this model with star formation can account for the dust emission at infrared wavelengths short wards of 100 μm, the SED and MIPS 160 μm image at the bottom row in Figure 5.6 clearly show that the IR emission at longer wavelengths ($>$ 100 μm) is still significantly underestimated.

5.3.3 Model III: model with embedded star formation + clumpy dust component

Relying on the agreement of our model with the SFR calibrations and UV, 24 and 70 μm observations, we argue that an additional component of heavily extinguished star formation will not bring a solution to the remaining discrepancy. Rather than embedded localized sources, it seems that either an additional dust component, not associated to star-forming regions, or dust grains with a higher emissivity at FIR/submm wavelengths, compared to Galactic values, need to be invoked to explain the discrepancy in the energy budget at longer wavelengths ($>$ 100 μm). The former assumption of a dust component distributed in clumps throughout the dust ring is a reasonable assumption. Emsellem (1995) already inferred a clumpy dust structure from his absorption A_V^{eff} map in the southern part of M104 (see Figure 4 in his paper). Also, high resolution optical HST data (Christian et al., 2003) of the Sombrero galaxy hint at a clumpy dust structure.

To achieve an estimate of the total amount of dust residing in dense clumps, we calculate the dust mass required to explain the dust energy balance problem in M104. Therefore, we subtract the emission from the model with embedded star formation from the observed fluxes at wavelengths $>$ 100 μm. By fitting a single-component modified blackbody to the residual fluxes, we obtain a dust mass of $M_d = 1.8 \times 10^7$ M$_\odot$ at a temperature of $T_d = 17.2$ K. Making the assumption of an additional dust component distributed in quiescent compact clumps throughout the dust lane of the Sombrero galaxy, the model can account for the IR emission, also at wavelengths longer than 100 μm (see Figure 5.7). Bianchi (2008) already showed that only a dust distribution for which half of the dust is distributed in clumps can explain the energy balance in NGC 891. In the Sombrero galaxy, the total amount of dust residing in clumps is estimated to exceed the amount of diffusely distributed dust and account for about two-thirds of the total dust content (M_d = 2.8 $\times$ 10^7 M$_\odot$). The dust mass in our model is a bit higher than previous estimates of the dust content in M104, when scaled to the same distance (9.2 Mpc). Emsellem (1995) and Bendo et al. (2006) inferred a dust mass (M$_d$

$= 7.9 \times 10^6$ $M_\odot$) comparable to the dust content in our standard model. When taking into account observations at longer wavelengths, a total dust content of 1.3×10^7 $M_\odot$ and 1.5×10^7 $M_\odot$ with dust temperatures $T_d = 22$ K and 18.4 K was found in Krause, Wielebinski & Dumke (2006) and Vlahakis et al. (2008) from radio and submm/mm observations, respectively. Recent Herschel observations have estimated a dust mass of $M_d \sim 8.1 \times 10^6$ $M_\odot$ at a temperature of $T_d = 22$ K (Skibba et al., 2011). The small dissimilarity with the higher dust content in our self-consistent Sombrero dust model is largely due to the lower dust temperature for the majority of the dust grains in our model ($T_d = 17.2$ K).

While the standard model constrained by optical data still underestimates the FIR and submm emission by a factor of $\sim$ 3-4, a model with embedded star formation (SFR ~ 0.37 M$_\odot$ yr^{-1}) and an additional dust component, distributed in quiescent compact clumps throughout the dust ring and accounting for two-thirds of the total dust content ($M_d \sim 2.8 \times 10^7$ M$_\odot$), can explain the discrepancy in the energy balance for M104. Although a clumpy dust structure is a reasonable assumption, we are not capable of completely ruling out the possibility that part of the discrepancy might be caused by a dust component composed of grains with a higher emissivity in the submm wave bands, compared to Galactic properties.

In late-type galaxies the discrepancy in the energy balance between model and IR observations mainly arises at shorter IR wavelengths (NGC 891: Bianchi 2008 ; UGC 4754: Baes et al. 2010), where the warm dust component dominates the IR emission spectrum, and, hence, the presence of embedded star-forming clouds seems to be the most likely explanation for the dust energy balance problem in those objects. In case of the Sombrero galaxy, an early-type spiral (Sa), the majority of compact clumps are not associated to localized sources and, therefore, have not been triggered to for stars (yet). These compact clumps are optically thick to the diffuse UV and optical radiation field and, therefore, will not have a substantial influence on the observed extinction profile, because most of the diffuse UV/optical radiation from young stellar objects is locally absorbed. Since these quiescent clumps are not associated to any source in a star-forming region, we could consider them as dust clouds for which the conditions are not appropriate to initiate star formation. Because these clouds might still start forming stars, we expect the density of dust in these clumps to be very high. Therefore, these compact structures could contain a substantial amount of dust in addition to the diffuse dust component, which is distributed more smoothly among the dust lane. Given the low star formation activity in the Sombrero galaxy (SFR ~ 0.26 M$_\odot$ yr^{-1}) compared to late-type galaxies such as NGC 891 (SFR ~ 3 M$_\odot$ yr^{-1} , Popescu et al. 2000; Bianchi 2008) and NGC 4565 (SFR ~ 1.8 M$_\odot$ yr^{-1}, see Section 6), it is not surprising that M104 overall would contain more quiescent dust clumps, with no associated embedded sources.

This might be a first indication for a difference in the dust distribution for spiral galaxies along the Hubble sequence. While early-type spirals tend to have the majority of dust distributed in quiescent clumps throughout a ring-like structure, most of the dust in late-type spiral galaxies resides in an exponential disk and is associated to embedded localized sources.

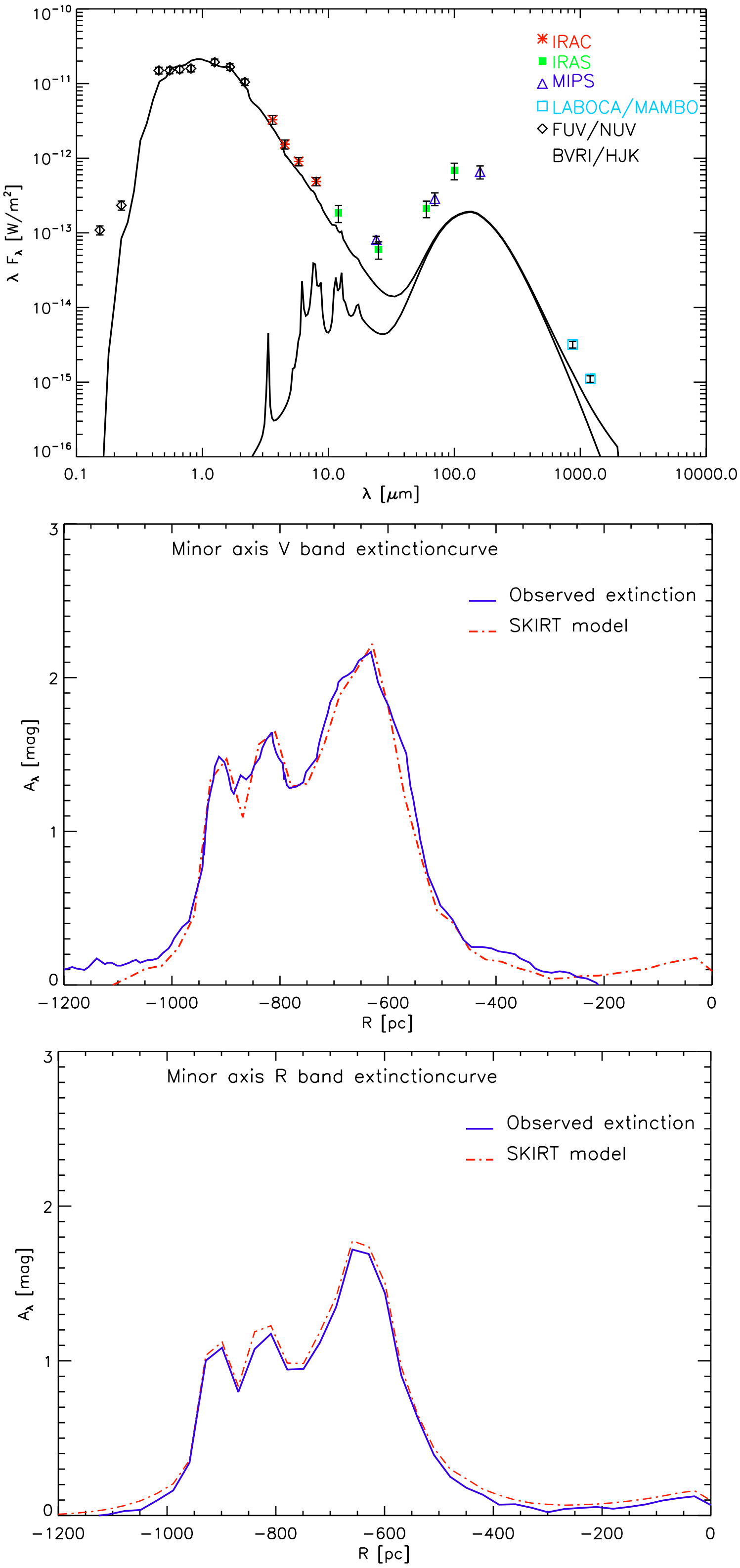

Figure 5.2: The modelled SED and the minor-axis extinction profiles bands for the standard model. The top panel represents the total SED as obtained with the SKIRT model (solid black line) overlaid with the observed fluxes (see Table 5.1). The contribution of the dust to the SED is also shown. The central and bottom panels show the minor-axis extinction profile in the V and R_C, where the solid blue and dashed red lines represent the observed and modelled extinction profiles, respectively.

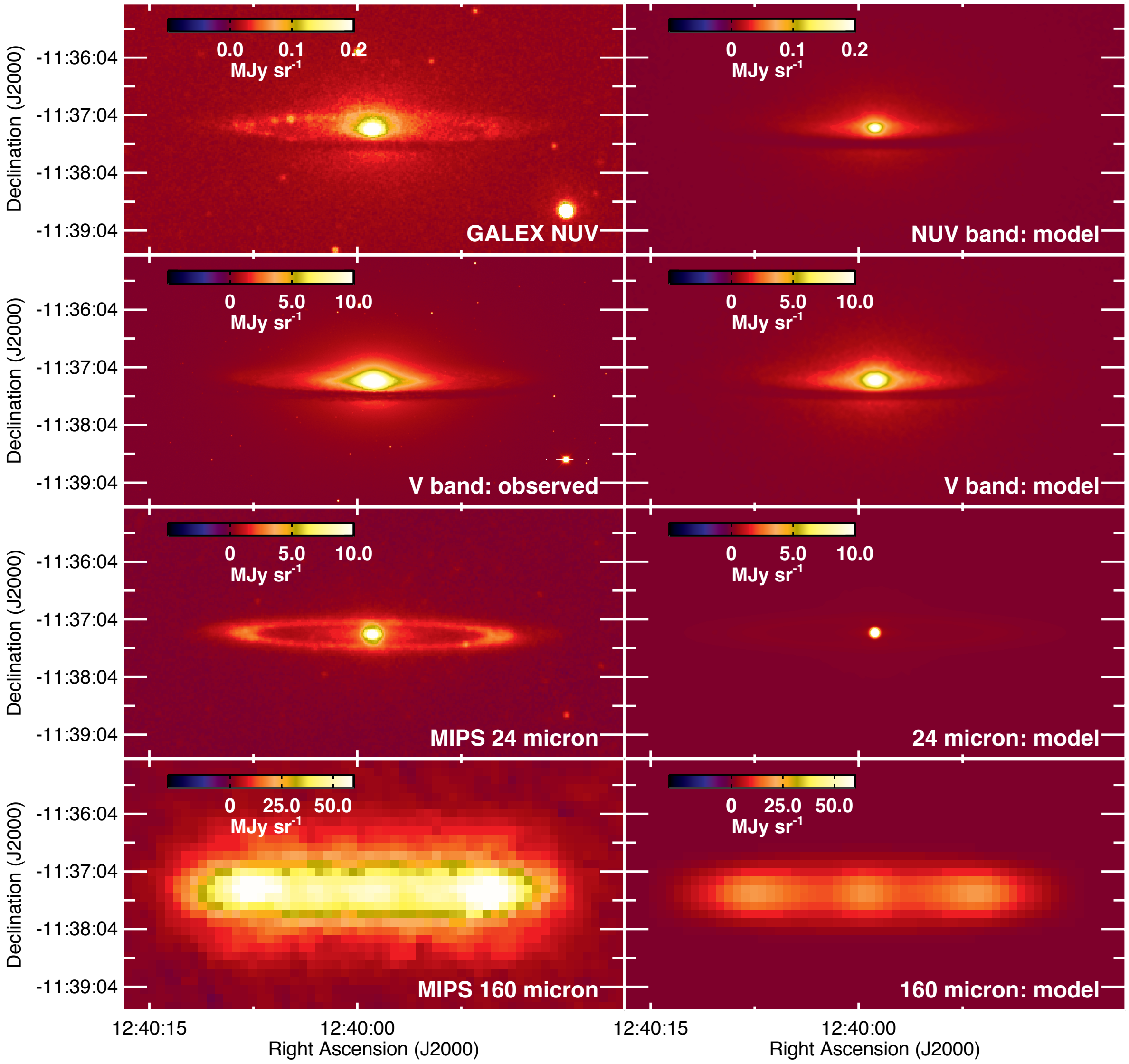

Figure 5.3: A comparison of the observed and modelled images for the Sombrero galaxy for the standard model. From top to bottom, the different rows represent NUV, V, 24 μm and 160 μm images. Images in a specific band are scaled accordingly for both observed and modelled data, allowing an immediate visual comparative inspection.

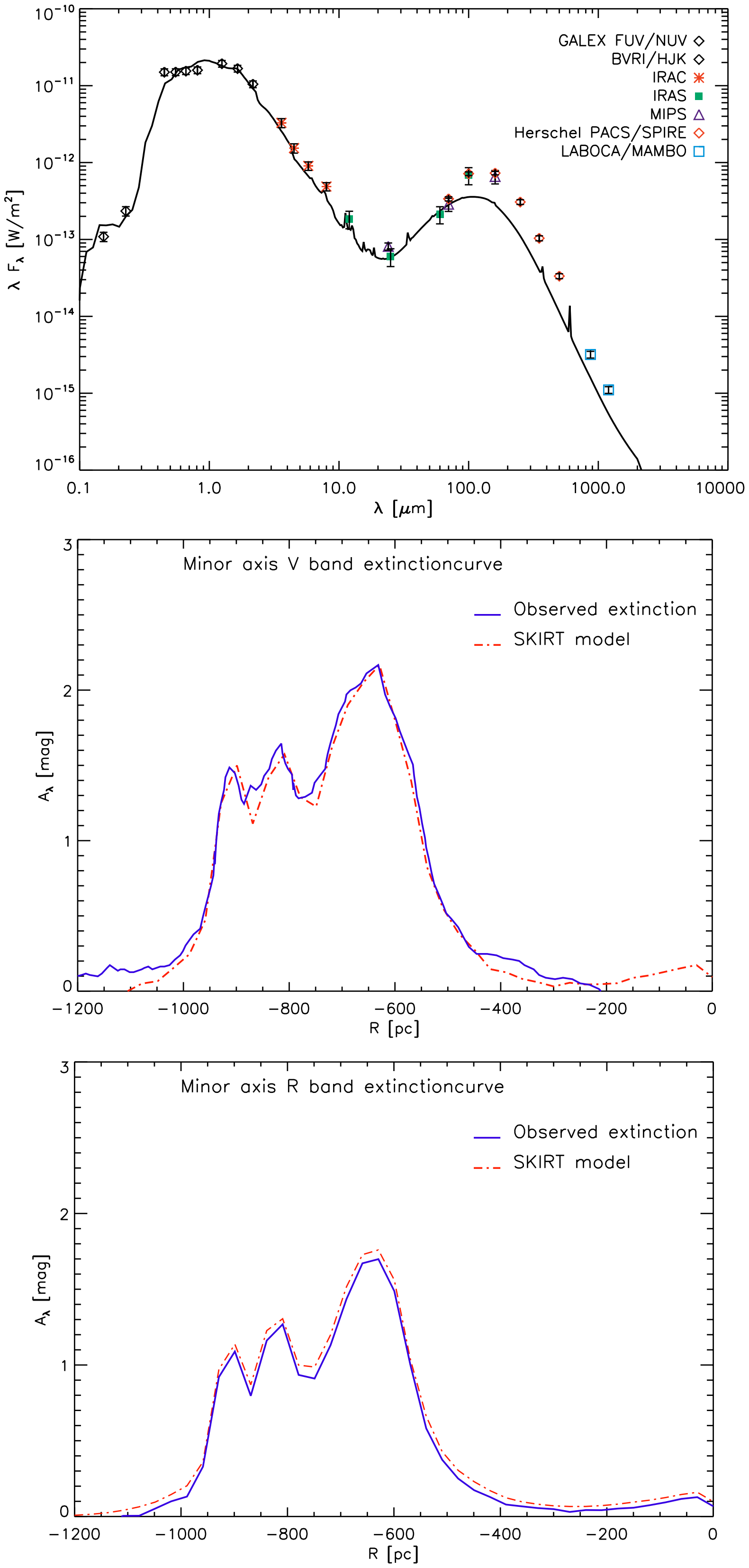

Figure 5.4: Same as Figure 5.2, but for the model with embedded star formation.

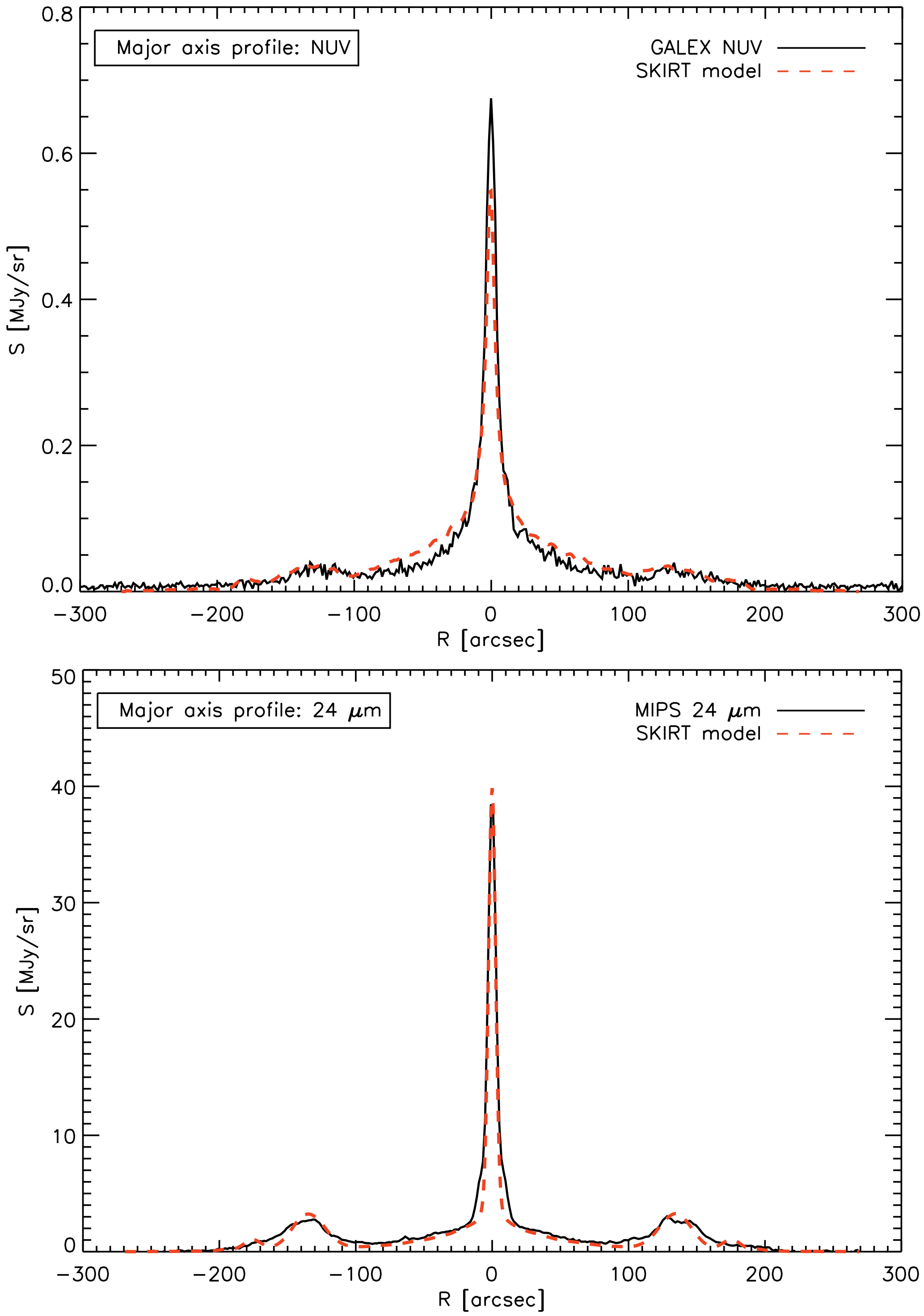

Figure 5.5: Model 2: observed and modelled NUV and 24 μm major axis profiles for M104.

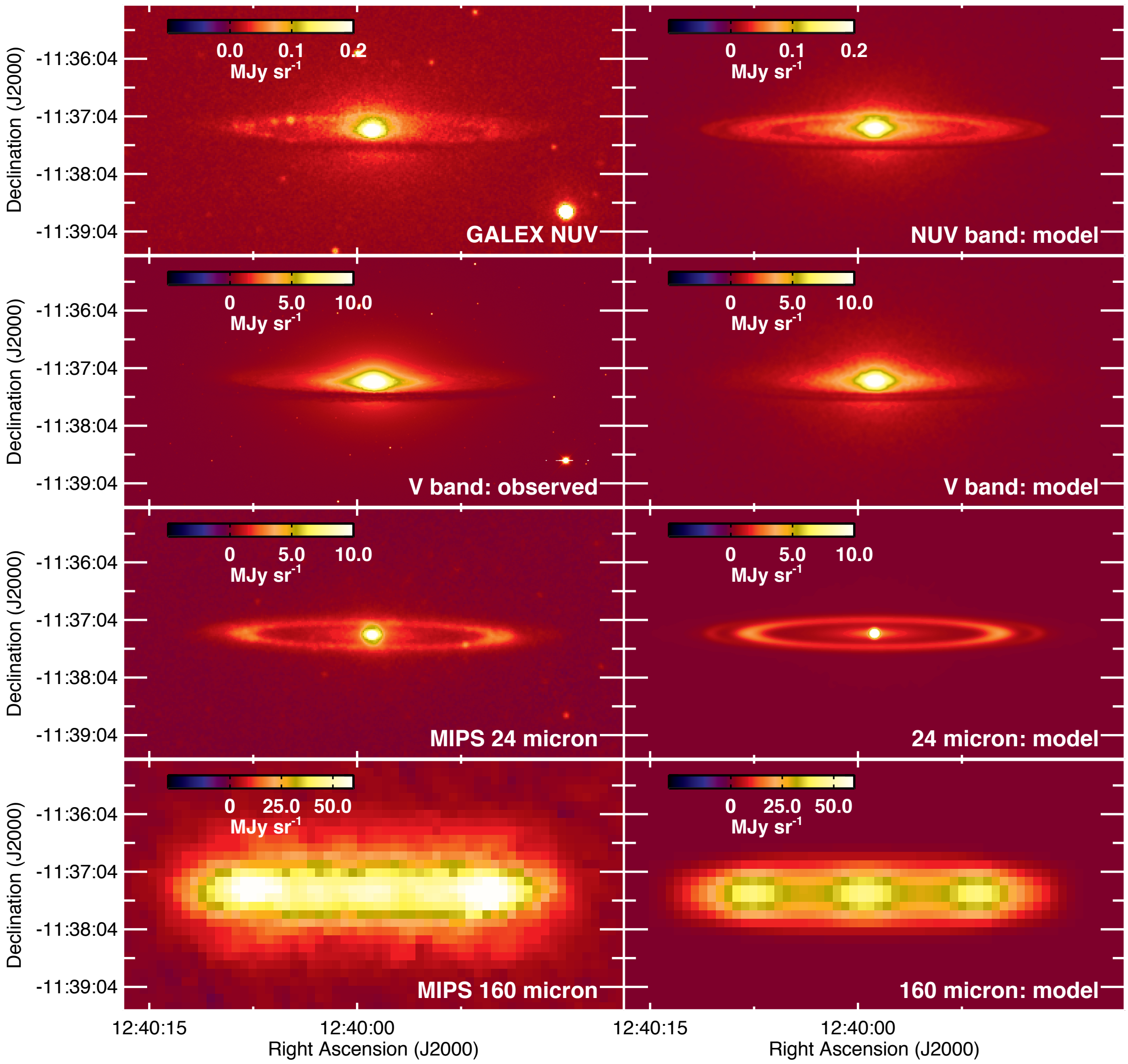

Figure 5.6: Same as Figure 5.3, but for the model with embedded star formation. Also the scaling of the image graphics was adopted from Figure 5.3.

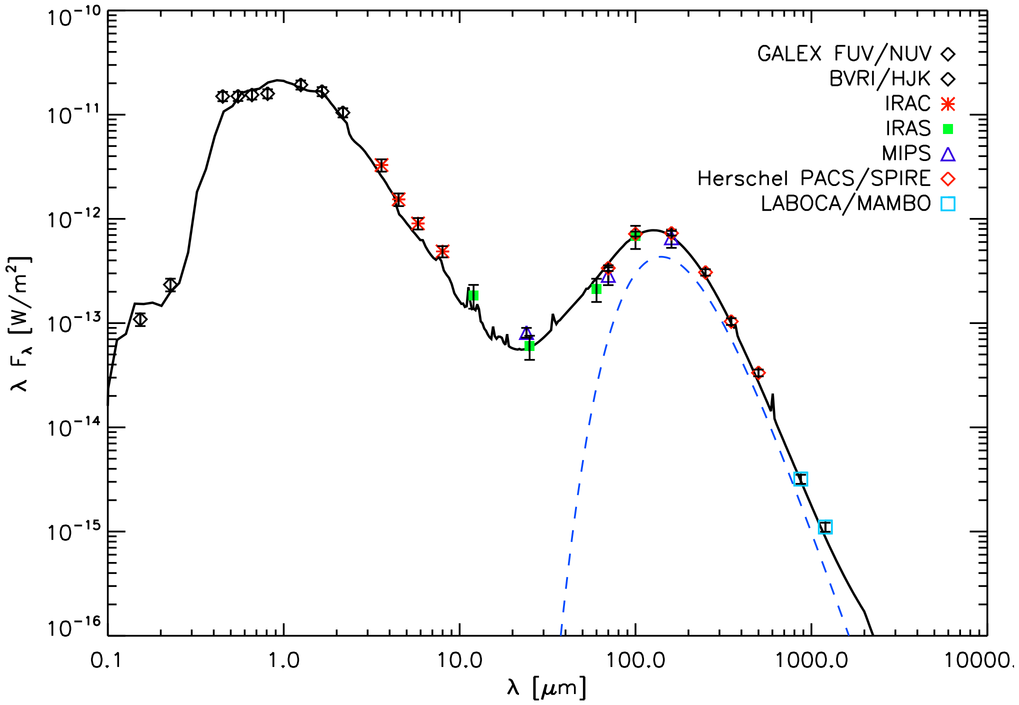

Figure 5.7: Spectral energy distribution (SED) for the Sombrero with a young stellar component, supplemented with a dust component $M_\mathrm{d} = 1.8 \times 10^7$ $\mathrm{M}_\odot$ distributed in clumps. The solid line represents the modelled SED. The modified black-body, modelling the additional dust component in compact clumps, is shown by the blue dashed-dotted line. The symbols correspond to observations in the optical and infrared spectrum.

6

Needle Galaxy (NGC4565)

At a distance of about 16.9 Mpc, the Needle Galaxy (NGC 4565) is one of the most nearby edge-on spiral galaxies covering an angular scale of $\sim$ 15 arcmin on the sky. Distance measurements for NGC 4565 range from 9 to 22 Mpc depending on the applied technique. We adopt a value of $D \sim 16.9$ Mpc throughout this work, which is the average of the most recent distance measurements from I band surface brightness fluctuations as reported in Tonry et al. (2001) and Jensen et al. (2003). NGC 4565 is a Sb spiral, classified as a Seyfert galaxy (Ho et al., 1997b) and located in the Coma I cloud. Recently its classification as an active galactic nucleus has been confirmed in the mid-infrared with the detection of the [Ne V] lines with *Spitzer* (Laine et al., 2010), which are among the strongest indicators of AGNs (see e.g. Tommasin et al. 2010). The stellar geometry in NGC 4565 has been studied extensively at optical and NIR wavelengths (van der Kruit, 1979; Hamabe et al., 1980; van der Kruit & Searle, 1981; Jensen & Thuan, 1982; Dettmar & Wielebinski, 1986; Rice et al., 1996; Naeslund & Joersaeter, 1997; Wu et al., 2002; Seth, Dalcanton & de Jong, 2005; Mosenkov, Sotnikova & Reshetnikov, 2010; Kormendy & Barentine, 2010). In optical data, the boxy shape of the bulge immediately catches the eye. Based on a radial intensity profile diverging from the typical $I \propto r^{-2}$ distribution found in classical bulges, the bulge in NGC 4565 is considered a pseudo-bulge, resulting from a bar in the inner region of NGC 4565 viewed edge-on (Combes & Sanders, 1981). Also the kinematics in NGC 4565 (i.e. a constant rotation from the center to a radius of $\sim$ 30 arcsec) resembles the cylindrical rotation observed in galaxies with known bars and/or boxy bulges (Kormendy & Illingworth, 1982; Jarvis, 1990; Shaw, Wilkinson & Carter, 1993; Bettoni & Galletta, 1994; Fisher, Illingworth & Franx, 1994; D'Onofrio et al., 1999; Falcón-Barroso et al., 2004; Howard et al., 2008). Furthermore, the velocity dips in the otherwise circular solid body rotation in NGC 4565 at radial distances of ± 2.5 arcmin are indicative for streaming motions at those positions, likely resulting from the presence of a central bar (Neininger et al., 1996; Kormendy & Barentine, 2010). Similar velocity profiles have been observed as a response to the central bar in our own Galaxy (Binney et al., 1991) and in NGC 891 and NGC 5907 (Garcia-Burillo & Guelin, 1995; Garcia-Burillo, Guelin & Neininger, 1997). Deep optical observations from the edge-on spiral NGC 4565 were used to probe a possible luminous counterpart of dark matter in the halo of the galaxy, accounting for the missing mass in galaxies flattening the rotation curve at large galactocentric radii (e.g. Jensen & Thuan 1982). Such a massive spherical luminous component dominating at outer radii was however never found to be present in NGC 4565.

From studies of the absorption layer in NGC 4565, Ohta & Kodaira (1995) claim a dust distribution in a ring-like structure and an inner cut-off radius along the major axis

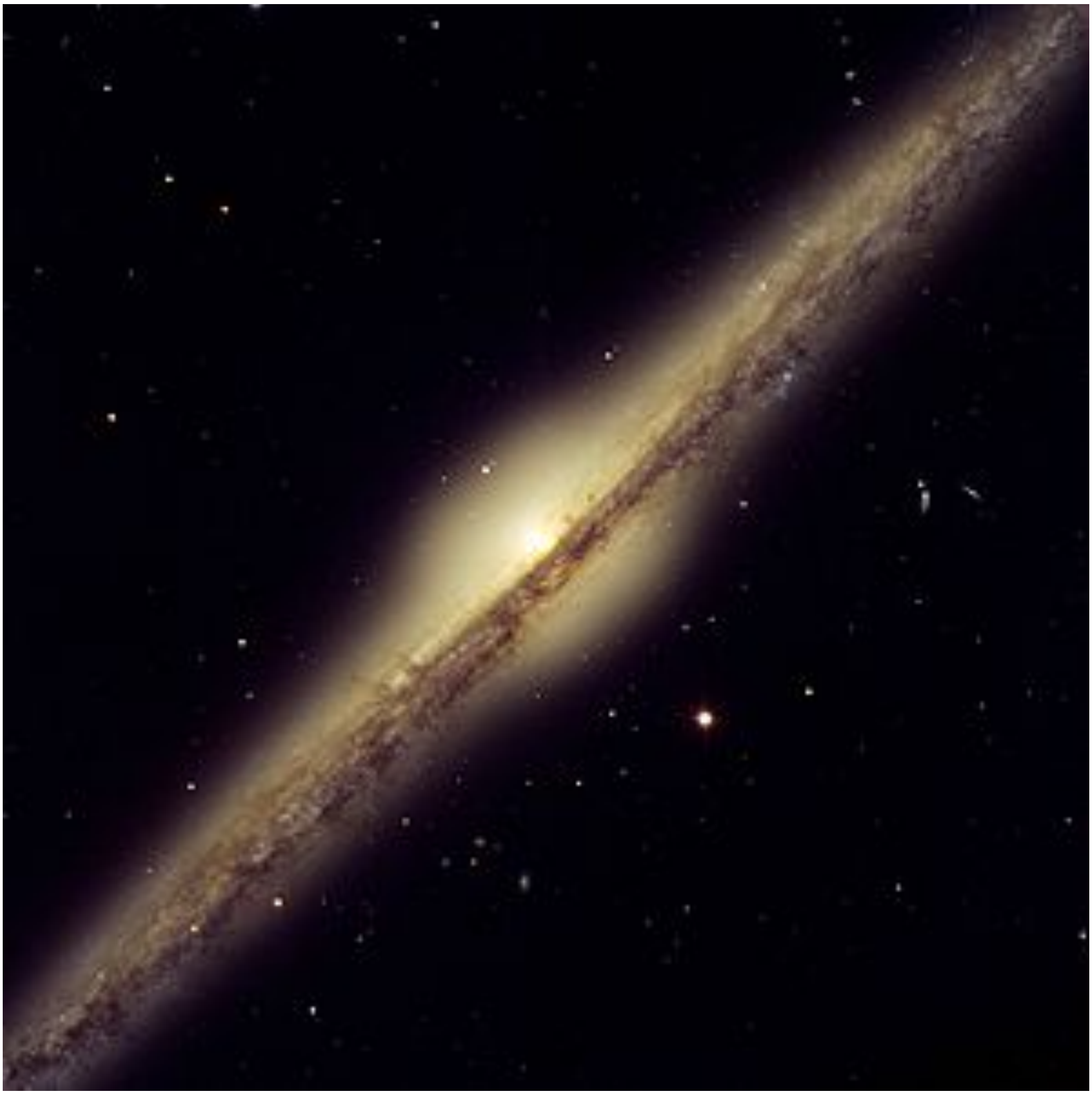

Figure 6.1: Optical image (ESO, FORS) of the Needle galaxy.

at $\sim$ 130 arcsec. At radii smaller than the cut-off radius dust obscuration effects seem to be absent, either due to a deficiency of dust or the distribution of a central dust component preventing the identification of dust attenuation from optical data (Ohta & Kodaira, 1995). Studies of residual J and K band images obtained after fitting the stellar component and subtracting those models from the near-infrared images in Rice et al. (1996) result in estimates for the dust scale length $\sim$ 66 arcsec and scale height $\sim$ 5 arcsec in NGC 4565, which corresponds to about 60 and 50% of the stellar disk in the K band.

In addition to these optical/NIR studies of the dust component, the properties and geometry of the dust in NGC 4565 have been analyzed as well from infrared and submillimeter observations (Wainscoat, de Jong & Wesselius, 1987; Engargiola & Harper, 1992; Rice et al., 1996; Neininger et al., 1996; Alton et al., 2004; Kormendy & Barentine, 2010; Laine et al., 2010). In the mid-infrared IRAC 8μm waveband, Kormendy & Barentine (2010) and Laine et al. (2010) identify a ring of prominent polycyclic aromatic hydrocarbon emission from dust at the same position as the molecular gas ring at radii of $\sim$ 80-100 arcsec (Sofue & Nakai, 1994; Neininger et al., 1996). The first far-infrared study on dust emission in NGC 4565 based on IRAS data calculate a total infrared luminosity $L_{\mathrm{FIR}} \sim 3 \times 10^9$ L$_\odot$ (Wainscoat, de Jong & Wesselius, 1987), which compares well to the dust emission from our Galaxy. The dust emission in NGC 4565 however is more extended compared to the dust distribution in our Galaxy (Wainscoat, de Jong & Wesselius, 1987). Based on estimates of the infrared excess, Wainscoat, de Jong & Wesselius (1987) argue that only one quarter of the dust reservoir in NGC 4565 is heated by embedded stars in molecular clouds with the remainder of the dust heating power provided by the diffuse interstellar radiation field.

Observations at FIR wavelengths (100, 160, 200 μm) with the Kuiper Airborne Observatory (Engargiola & Harper, 1992) find a two-component dust model with a cold dust reservoir ($T_d \sim 20$ K) distributed in an exponential disk and a warmer dust component ($T_d \sim 30$ K) spatially coinciding with a bisymmetric spiral pattern in NGC 4565. In spatial correlation with the more extended ring of HI gas, Neininger et al. (1996) also found a colder dust component ($\sim$ 15 K) in the outskirts of the galaxy. A second dust reservoir ($T_d \sim 18$ K) was found in the center of NGC 4565 and in the molecular gas ring at radii of $\sim$ 80-100 arcsec. The central concentration of both dust and molecular gas (Neininger et al., 1996) contradicts the suggested absence of dust in the centre of the galaxy (Ohta & Kodaira, 1995).

Alton et al. (2004) constrain the amount of dust in NGC 4565 from a complementary study of the attenuation properties of dust in the optical and the thermal dust re-emission at 1.2 mm. From optical constraints, they construct a radiative transfer model for the stars and dust in NGC 4565. Upon comparison of the visual optical depth in their radiative transfer model with thermal continuum radiation in the 1.2 mm waveband, Alton et al. (2004) infer a dust emissivity at 1.2 mm which is 1.5 times higher than the benchmark, semi-empirical model from Draine & Lee (1984) used in the radiative transfer simulation. From their combined study on the dust emissivity in NGC 4565 and two other nearby spirals, they argue that coagulation of well-ordered dust crystalline grains into amorphous particles in high-density environments can influence the emissivity of dust at submm/mm wavelengths.

The first submillimeter observations of NGC 4565 were obtained during the first test flight of the 2 m Balloon-borne Large Aperture Submillimeter Telescope (BLAST) in 2005 (Wiebe et al., 2009), covering the galaxy in the same wavebands (250, 350, 500 μm) as offered by the SPIRE instrument onboard the *Herschel* Space Observatory. Although the resolution in their final images was degraded by the large point-spread functions (PSF) ($\sim$ 186-189 arcsec, Truch et al. 2008), Wiebe et al. (2009) could estimate the scale length of the dust lane $h_R \sim 150$ arcsec from the beam-convolved image at 250 μm, which is about twice the value obtained from optical studies (Rice et al., 1996). A modified black-body fit to the BLAST fluxes and additional constraints from ISO (170 μm, Stickel et al. 2004) and IRAS (12, 25, 60, 100 μm, Sanders et al. 2003) observations predict a dust reservoir of mass $M_d \sim 3 \times 10^8$ $M_\odot$ (scaled to a distance of 16.9 Mpc) at a temperature $T_d \sim 16$ K for an emissivity index $\beta = 2$ and a Draine & Li (2007) dust grain composition (Wiebe et al., 2009).

6.2.1 Herschel data (250-500 micron)

NGC 4565 was observed on the 31st of December 2009 (ObsID 0×50002cd8) as part of the *Herschel* Reference Survey (HRS, Boselli et al. 2010a), a *Herschel* Guaranteed Time Key Program observing 323 galaxies in the nearby Universe spanning a wide range in morphological type and environment. Dust continuum maps were obtained in all SPIRE wavebands (centered at 250, 350 and 500 μm), covering the galaxy in three cross-linked scans (nominal and orthogonal) at medium scan speed (30 arcsec/s). The final maps cover a square area of 30 arcmin, corresponding to an extent of at least 1.5 times the optical isophotal diameter D_{25} in NGC 4565.

The SPIRE data were processed up to Level-1 in the *Herschel* Interactive Processing Environment (HIPE, version 4.0.1367, Ott 2010) with the standard script adapted from the official pipeline (POF5 pipeline.py, dated 8 Jun 2010) as provided by the SPIRE Instrument Control Centre (ICC). Instead of the ICC default settings for deglitching, we used the waveletDeglitcher, which was adjusted to mask the sample following a glitch. The waveletDeglitcher algorithm was applied a second time after the flux calibration, since this was shown to significantly improve the removal of remaining glitches for the version of the code at that time (currently it is only run once). Instead of the pipeline default temperature drift correction and median baseline subtraction, we applied a custom method (BriGAdE; Smith et al. in prep.) to remove the temperature drift and bring all bolometers to the same level. Final SPIRE maps (see Figure 6.2, last three bottom panels) were created with the naive mapper in HIPE with pixel sizes of 6″, 8″, and 12″ at 250, 350, and 500 μm, respectively. The FWHM of the SPIRE beams have sizes of 18.2″, 24.5″, and 36.0″[1] at 250, 350, and 500 μm (for map sizes of 6, 8 and 12 arcsec), respectively. To update our flux densities to the latest v8 calibration product, the 350 μm images are multiplied by a factor of 1.0067 (SPIRE Observer's Manual, 2011). Since the calibration in the standard data reduction pipeline was optimized for point sources, correction factors (0.9828, 0.9834 and 0.9710 at 250, 350 and 500 μm) are applied to convert the K4 colour correction factors from point source to extended source calibration (SPIRE Observer's Manual, 2011). Appropriate colour correction factors were determined from a single component modified blackbody fit to the Rayleigh-Jeans tail of dust emission (constrained by fluxes from MIPS 160 μm and all SPIRE wavebands) for values $\beta = 1.0$, 1.5 and 2.0 (i.e. the range of spectral indices derived for the HRS sample galaxies, Boselli et al. 2012). With the best fit obtained for values $\beta = 2$ and $T_{\rm d} = 17$ K,

---

[1] Retrieved from document available at http://herschel.esac.esa.int/twiki/pub/Public/SpireCalibrationWeb/beam_release_note_v1-1.pdf

Filter	λ (μm)	F_ν (Jy)	Ref[1]
FUV	0.15	0.008 ± 0.001	1
NUV	0.23	0.015 ± 0.002	1
SDSS u	0.36	0.07 ± 0.01	2
SDSS g	0.47	0.33 ± 0.03	1
SDSS r	0.62	0.70 ± 0.07	1
SDSS i	0.75	1.08 ± 0.10	1
SDSS z	0.89	1.45 ± 0.14	2
2MASS J	1.25	2.18 ± 0.03	3
2MASS H	1.65	3.05 ± 2.51	3
2MASS K	2.20	2.51 ± 0.04	3
WISE 1	3.4	1.54 ± 0.04	4
IRAC 3.6	3.6	1.39 ± 0.14	5
IRAC 4.5	4.5	0.91 ± 0.09	5
WISE 2	4.6	0.90 ± 0.03	4
IRAC 5.8	5.8	1.17 ± 0.14	5
IRAC 8.0	8.0	1.85 ± 0.19	5
WISE 3	12.1	2.20 ± 0.05	4
IRAS 12	12	1.53 ± 0.23	6
WISE 4	22.2	1.60 ± 0.16	4
MIPS 24	24	1.65 ± 0.07	6
IRAS 25	25	1.70 ± 0.26	6
IRAS 60	60	9.83 ± 1.47	6
MIPS 70	70	19.3 ± 1.9	6
IRAS 100	100	47.23 ± 7.08	6
KUIPER 100	100	52.00 ± 10.40	8
MIPS 160	160	86 ± 10	7
KUIPER 160	160	62.00 ± 12.40	8
KUIPER 200	200	55.00 ± 11.00	8
SPIRE 250	250	63.24 ± 1.18	9
SPIRE 350	350	31.35 ± 0.69	9
SPIRE 500	500	13.14 ± 0.29	9
IRAM 1200	1200	1.00 ± 0.10	10

Table 6.1: Panchromatic overview of flux densities used in the dust energy balance study of NGC 4565

[1] References: (1) Cortese et al. 2012b; (2) Cortese (priv. comm.); (3) Jarrett et al. 2003; (4) this work, see Section 6.2.3; (5) Ciesla et al. (in prep.); (6) Rice et al. 1988; (7) Bendo, Galliano & Madden 2012b; (8) Engargiola & Harper 1992; (9) Ciesla et al. 2012; (10) Neininger et al. 1996

we apply colour correction factors of 1.019, 1.009 and 1.021 to the 250, 350 and 500 μm images (SPIRE Observer's Manual, 2011), respectively, to correct for the shape of the response function in every filter. An uncertainty in the calibration of 7% was assumed (Swinyard et al., 2010; SPIRE Observer's Manual, 2011).

From aperture photometry within an elliptical aperture (20 arcmin × 2.7 arcmin) flux densities of 62.06, 31.07 and 12.87 Jy for NGC 4565 were obtained at 250, 350 and 500 μm, respectively (Ciesla et al., 2012). Since those fluxes were corrected for extended source calibration, we only need to correct those values with appropriate colour corrections factors (1.019, 1.009, 1.021). This results in final flux densities of 63.24, 31.35 and 13.14 Jy at 250, 350 and 500 μm, respectively. The large ancillary dataset of far-infrared/submillimeter observations allows us to compare those SPIRE fluxes to flux measurements from other space or airborne missions in overlapping wavebands. Wiebe et al. (2009) report fluxes obtained with BLAST at 250 μm (37.2 $\pm$ 4.5 Jy), 350 μm (21.0 $\pm$ 2.1 Jy) and 500 μm (9.8 $\pm$ 0.9 Jy), which are 40, 32 and 24 % lower with respect to SPIRE flux measurements (see Table 6.1). BLAST observations of NGC 4565 covered an area of $\sim$ 0.4 deg^2 centered on the galaxy, sufficient to detect the dust emission from NGC 4565 in those wavebands. Considering that BLAST fluxes for NGC 4565 were measured from data taken during the first BLAST test flight in 2005, the images were degraded by the large point-spread function of BLAST05 ($\sim$ 186-189 arcsec, Truch et al. 2008). Prior to aperture photometry, the images were deconvolved following the method outlined in Chapin et al. (2008). Either this beam deconvolution might be the cause of the lower BLAST fluxes compared to SPIRE measurements. Alternatively, calibration issues might be responsible for the small off-set between BLAST and SPIRE. Also Planck measurements (Planck Collaboration et al., 2011) at 350 μm (24.35 $\pm$ 1.43 Jy) and 550 μm (8.12 $\pm$ 0.48 Jy) are about 20% below our SPIRE measurements. The lower Planck values can easily be explained from the radius applied for aperture photometry on point sources in their first release catalog (Planck Collaboration et al., 2011). Indeed, an aperture with radius fixed to the FWHM of Planck at 350 μm ($\sim$ 4.23 arcmin) does not cover the entire galaxy's emission in that waveband (see the upper right panel of Figure 10 in Ciesla et al. 2012). Performing aperture photometry within the Planck radius at 350 μm on the SPIRE images results in a flux density $S_{\nu} \sim 25.5 \pm 0.9$ Jy (Ciesla et al., 2012), which is in close agreement with the reported Planck value (Planck Collaboration et al., 2011).

Figure 6.2 (last three bottom panels) shows the *Herschel* maps for NGC 4565 in the SPIRE 250, 350 and 500 μm wavebands. Weak warping signatures at the edges of the dust disk can be identified in all *Herschel* dust maps, with the warp on the northwestern side of the galaxy's disk being more pronounced. These warp features were earlier identified in NGC 4565 from optical data (e.g. van der Kruit 1979; Jensen & Thuan

1982; Naeslund & Joersaeter 1997), HI (Sancisi, 1976; Ruben, 1991) and dust continuum (Neininger et al., 1996) observations and are most likely the relicts of a tidal interaction with its neighboring galaxy NGC 4562 (Jensen & Thuan, 1982).

Aside from the warps on the edges of the galaxy, three peaks in the dust emission can be identified in the SPIRE 250 and 350 μm images (see Figure 6.2, second and third bottom panels). The two brightest emission peaks originate from a narrow ring structure centered around 80-100 arcsec, coinciding with a ring of molecular gas in NGC 4565 (Sofue & Nakai, 1994; Neininger et al., 1996). In the center of NGC 4565 the emission peak corresponds to a central concentration of dust, which was already identified from 1.2 mm observations (Neininger et al., 1996). Due to the growing size of the SPIRE beam towards longer wavelengths, the three peaks are more difficult to distinguish in the SPIRE 500 μm image (see Figure 6.2, fourth bottom panel), only showing a small increase in emission at the edges of the narrow dust ring.

Figure 6.3 compares the distribution of dust in the SPIRE 250 μm image with the gas distribution from integrated HI and CO line intensities (Neininger et al., 1996), the total gas column density and dust emission profiles along the major-axis from 24 μm and 1.2 mm dust continuum observations, smoothed to a common resolution of 20″. Based on these major axis profiles, we can identify a depression in the HI profile from the center up to the 80″ radius and a more or less constant column density profile in the outskirts of the galaxy from that radius onwards. The CO profile in NGC 4565 indicates the presence of a large molecular gas reservoir in the inner regions, distributed in a central disk and narrow ring with peak density around 80 arcsec, where also the inner depression in HI density ends. The SPIRE 250 μm dust emission profile along the major axis correlates well with the molecular gas density profile (see also Wainscoat, de Jong & Wesselius 1987, Rice et al. 1996, Kormendy & Barentine 2010 and Laine et al. 2010) as well as the column density of the combined HI and H_2 gaseous components. The latter column density profile seems dominated by the peaks in the molecular gas component, rather than the smooth HI distribution across the plane of the galaxy. In contrast to the CO profile reported in Neininger et al. (1996), the CO observations from Sofue & Nakai (1994) identified a more asymmetric CO distribution with the majority of the molecular gas reservoir residing on the northwest side of the galaxy. The dust emission from the colder dust reservoir in the SPIRE 250 μm waveband however does not show a tendency for asymmetry.

6.2.2 Spitzer data (3.6-160 micron)

NGC 4565 was observed with the IRAC and MIPS instruments onboard the *Spitzer* Space Observatory as part of the programs *Brown Dwarf Galaxy Haloes* (PI: Giovanni

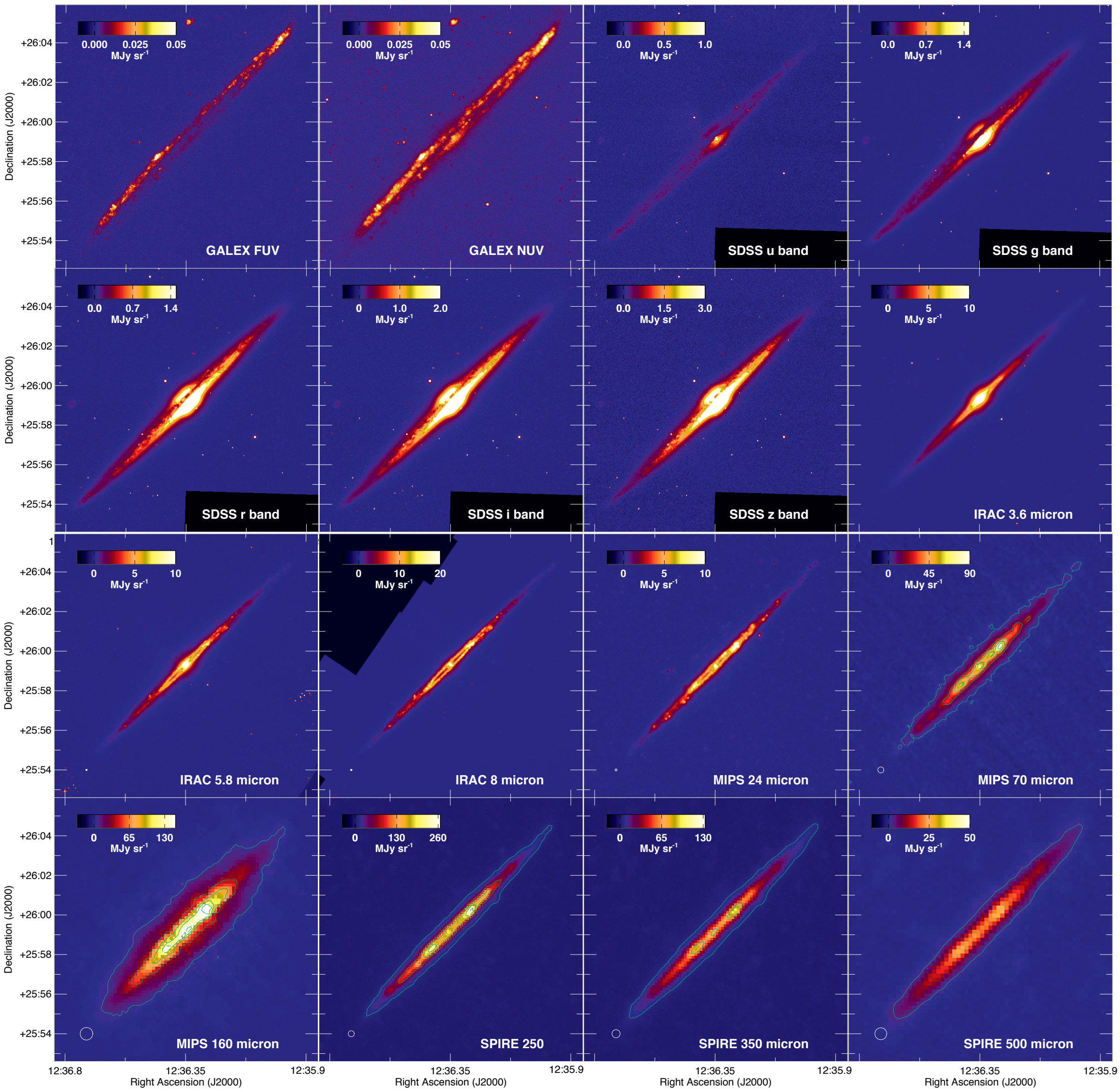

Figure 6.2: The stellar and dust emission from NGC 4565 as observed from GALEX *FUV* and *NUV*, SDSS *ugriz*, *Spitzer* IRAC 3.6, 5.8 and 8.0 μm, *Spitzer* MIPS 24, 70 and 160 μm and *Herschel* SPIRE 250, 350 and 500 μm images. The IRAC 4.5 μm map is not explicitly shown here because of the great resemblance with the IRAC 3.6 μm image. The beam sizes of all instruments in the infrared/submillimeter wavebands have been indicated as white circles in the bottom left corner of the corresponding panels.

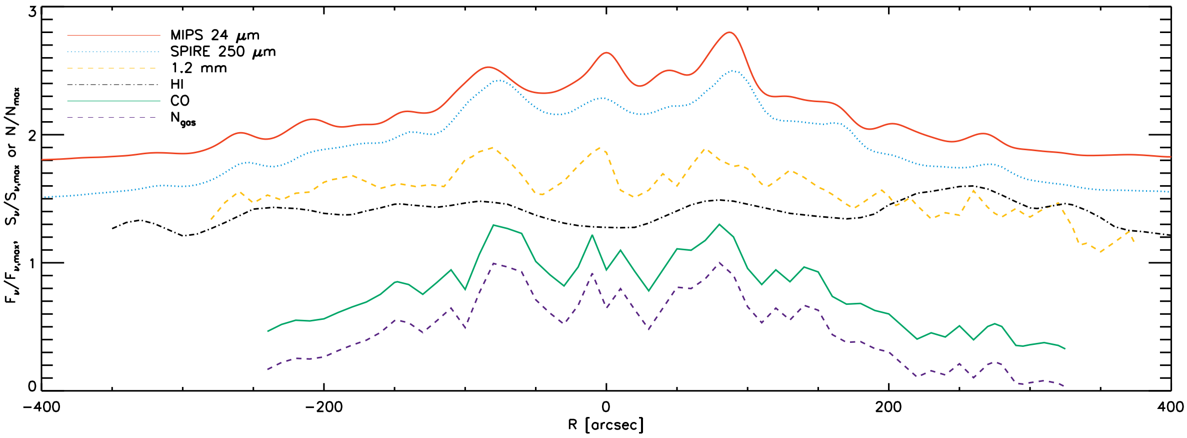

Figure 6.3: Major-axis profiles of the dust emission in MIPS 24 μm (red solid curve), SPIRE 250 μm (cyan dotted curve), IRAM 1.2 mm (yellow dashed curve) wavebands, the gas distribution from the HI (black dashed-dotted curve) and CO (green solid curve) temperature brightnesses and the column density of gas combining the atomic and molecular components in NGC 4565 (blue dashed curve). The HI column density could be obtained directly from the HI temperature brightness (N_{HI} = 1.822 × 10^{18} $\int T_b(\nu)\mathrm{d}\nu$). For the calculation of the H_2 column density from the CO temperature brightness ($N_{H_2} = X_{CO} \int T_b(\nu)\mathrm{d}\nu$), we assumed a factor X_{CO} representative for the H_2-to-CO fraction in our own Galaxy ($X_{CO} \sim 2.3 \times 10^{20}$ cm^{-2} (K km s^{-1})$^{-1}$, Strong et al. 1988). All data were smoothed to a resolution of 20 arcsec. For ease of reference, all profiles were normalized by their maximum value. Those normalized profiles were then given an offset in the vertical direction to facilitate a mutual comparison.

Fazio; AOR key: 3627776) and *The formation of dust lanes in nearby, edge-on disk galaxies* (PI: Roelof S. de Jong; AOR key 14481408), respectively. IRAC (3.6, 4.5, 5.8, 8.0 μm) and MIPS (24, 70, 160 μm) data were retrieved from the *Spitzer* archive and reduced following the procedure outlined in Ciesla et al.(in prep.) and Bendo, Galliano & Madden (2012b). Although *Spitzer* IRAC data of NGC 4565 were already used in the analyses of Kormendy & Barentine (2010) and Laine et al. (2010), the maps presented in this work were processed independently. Final IRAC images have pixel sizes of 0.6 arcsec, whereas MIPS images were processed to final maps with pixel sizes of 1.5″, 4.5″ and 9.0″ at 24, 70 and 160 μm, respectively. The IRAC beam has an almost uniform size in all wavebands (mean FWHM ∼ 1.7″, 1.7″, 1.9″ and 2.0″ at 3.6, 4.5, 5.8 and 8 μm, Fazio et al. 2004). The FWHM of the MIPS beam varies from 6″ at 24 μm, 18″ at 70 μm to 38″ at 160 μm (Engelbracht et al., 2007; Gordon et al., 2007; Stansberry et al., 2007).

To determine flux densities for NGC 4565 from the processed IRAC images, stars in the surrounding field were masked to obtain realistic estimates for the background emission (Ciesla et al. in prep.). Once the images were background subtracted, flux measurements were derived within elliptical aperture matching the shape of the galaxy and encompassing all emission (see Table 6.1 and Ciesla et al. in prep.). Similarly, the identification and removal of fore- and background emission from MIPS data required some efforts before fluxes could be determined from the background subtracted MIPS images (Bendo, Galliano & Madden 2012b, see Table 6.1). Uncertainties for IRAC and MIPS photometry measurements include uncertainties owing to the calibration, background noise and map making. For IRAC, the calibration is assumed to be accurate within 1.8, 1.9, 2.0 and 2.1 % in IRAC 3.6, 4.8, 5.8 and 8.0 μm wavebands (Reach et al., 2005). For MIPS, calibration uncertainties of 4, 10 and 12 % were reported for the 24, 70 and 160 μm wavebands (Engelbracht et al., 2007; Gordon et al., 2007; Stansberry et al., 2007).

MIPS fluxes at 24 and 70 μm compare reasonably well with IRAS observations of NGC 4565 at 25 and 60 μm (see Table 6.1). The longer wavelength MIPS observations at 160 μm are furthermore consistent within 30% with data from the Kuiper Airborne Observatory (KAO) in the same waveband (see Table 6.1).

Figure 6.2 (last panel on the second row) shows the stellar emission in the IRAC 3.6 μm image. Dust emission from IRAC (5.8 and 8 μm) and MIPS observations are presented in Figure 6.2 (third row and first panel on fourth row). The emission in the IRAC 3.6 and 4.5 μm wavebands is dominated by the stellar emission from the bulge in NGC 4565. The stellar emission from the bulge is also discernible in the IRAC 5.8 μm image. At 5.8 and 8 μm, emission from polycyclic aromatic hydrocarbons (PAHs) and very small grains (VSGs) distributed in a ring centered at 80-100″ dominates. The presence of a hot dust component heated predominantly by star formation is also clearly detected in the MIPS 24 μm image. Besides this ring of hot dust, the central region of NGC 4565 is also a prominent emission source in the IRAC 5.8, 8 μm and MIPS 24 μm wavebands. This central dust concentration in NGC 4565 is most likely heated by the AGN, since the inner 80″ region of NGC 4565 seems to lack any star formation activity (see Section 6.2.4). Owing to the coarser resolution at 70 and 160 μm, the dust emission features are not as easily identified compared to shorter wavelength data. To better contrast the structures in the far-infrared dust emission, we overlaid the contours of dust emission on those far-infrared MIPS data. The contours show three peaks in the far-infrared dust emission of NGC 4565, similar to the peaks identified from the *Herschel* data, with prominent emission from a ring at 80-100″ and a central dust concentration. Also the dust warps are manifested on the edges of the dust disk, in particular on the northwestern side, in both IRAC (5.8, 8 μm) and all MIPS wavebands.

In a similar way as for the SPIRE observations at 250 μm, the resolution in the MIPS 24 μm map was degraded to 20″, allowing an immediate comparison with the distribution of atomic and molecular gas along the major axis of NGC 4565 (see Figure 6.3). With the shape of the PSF in the MIPS 24 μm filter deviating from a Gaussian distribution, appropriate kernels were constructed following the procedure outlined in Bendo et al. (2012) to degrade the resolution in the MIPS 24 μm image. With the

24 μm emission tracing the warm dust component in NGC 4565, we find a spatial correspondence with the dust heated by young stellar objects in NGC 4565 and the molecular gas reservoir, which provides the birth material for this star formation. The resemblance between the MIPS 24 μm, SPIRE 250 μm and IRAM 1.2 mm dust profiles suggests that the cold and warm dust component are well mixed in the interstellar medium of NGC 4565. However, the asymmetry in CO observations from Sofue & Nakai (1994) does become evident in the dust emission profiles of the warmer dust component. This asymmetry is most likely the consequence of spiral arm structures in the plane of the galaxy. Similar asymmetric absorption features could also be identified in optical images (Hamabe et al., 1980; Rice et al., 1996) and were assigned to a spiral arm structure at position angle $\sim 135°$.

6.2.3 Other infrared/(sub)millimeter data

To refine the sampling of the spectral energy distribution, we include photometric data, other than obtained by *Herschel* and *Spitzer*, ranging from the infrared to millimeter wavelength domain. At near- and mid-infrared wavelengths, we complement our dataset of observations with flux measurements from the Wide-field Infrared Survey Explorer (WISE, Wright et al. 2010). Images belonging to the WISE all-sky survey at 3.4, 4.6, 12.1 and 22.2 μm were retrieved from the NASA/IPAC Infrared Science Archive. To measure fluxes from those images, all stars and background sources were masked in the field of the galaxy. Since the galaxy is located at the edge of the map, a determination of the background level from an annulus around the galaxy was made impossible. A background value was determined from averaging the flux over 100 apertures taken randomly within a 30 arcmin field in this masked image. The size of the apertures was adapted to the FWHM of the PSF in every waveband with a diameter of 4 × FWHM. The FHWM in the different WISE bands varies from 6.1″, 6.4″, 6.5″ at 3.4, 4.6, 12.1 μm up to 12″ in the longest 22.2 μm waveband (Wright et al., 2010). The mean background value was subtracted from the masked image. From this masked and background-subtracted image, we determined fluxes in all wavebands from aperture photometry. With the stellar bulge being a prominent emission feature at near-infrared wavelengths and the mid-infrared images having a dominant contribution from PAHs and very small grains in the star-forming disk of NGC 4565, the size of the aperture was adjusted to fit the size of the galaxy emitting in each waveband. Fluxes of the stellar emission from WISE at 3.4 and 4.6 μm are consistent with IRAC flux measurements at 3.6 and 4.5 μm (see Table 6.1). Also the WISE emission in the longer wavelength bands corresponds well with measurements by IRAS and MIPS at similar wavelengths (see Table 6.1).

IRAS flux measurements at 12, 25, 60 and 100 μm were adopted from the Catalog of IRAS observations of large optical galaxies (Rice et al., 1988). Also the Kuiper Space Airborne Observatory observed NGC 4565 (Engargiola & Harper, 1992) in wavebands centered at 100, 160 and 200 μm (see Table 6.1). ISO observations at 170 μm (32.5 ± 4.9 Jy, Stickel et al. 2004) were not considered here due to aperture effects (see also Wiebe et al. 2009). With *Akari* measurements at 65, 90, 140 and 160 μm (1.17 ± 0.12 Jy, 3.99 ± 0.22 Jy, 11.85 ± 1.07 Jy and 12.58 ± 2.39 Jy, respectively) being up to one order of magnitude lower in comparison to results from other airborne and space telescope facilities (IRAS, ISO, MIPS, KAO) in overlapping wavebands, we decided not to take into account *Akari* flux measurements for the analysis in this work.

At millimeter wavelengths, IRAM observations at 1.2 mm constrain the emission from cold dust in those wavebands. Alton et al. (2004) reported a flux density of 55 mJy when integrating along the major axis profile of the 1.2 mm emission for a 20″ beam. Based on the extent of the dust distribution along the minor axis in the SPIRE 250 μm, we estimate a total flux density of 99 mJy at 1.2 mm for NGC 4565 (see Table 6.1).

6.2.4 GALEX and optical data (0.15-0.89 micron)

GALEX *FUV*/*NUV* and optical SDSS *ugriz* data for NGC 4565 were recovered from the GALEX and SDSS archives and reduced following the instructions outlined in Cortese et al. (2012b). Final maps were reduced to obtain pixel sizes of 1.5″ and 0.4″ for GALEX and SDSS observations, respectively. GALEX *FUV* and *NUV* channels are characterized by a FHWM of 4.2″ and 5.3″, respectively (Morrissey et al., 2007), whereas the shape of the PSF in SDSS maps depends on the seeing during sky exposures. GALEX images for NGC 4565 were obtained in a single run of 1693 s exposure time, with SDSS images covered in 54 s of observing time. The first two panels on the top row of Figure 6.2 show the GALEX *FUV* and *NUV* images, respectively. Both GALEX images clearly show the low level of star formation activity in the inner most regions in NGC 4565. This lack of direct UV emission from young stars in the inner 80″ region in NGC 4565 was already identified by Engargiola & Harper (1992) and Ohta & Kodaira (1995), relating this deficiency in star formation to a bar structure in the central regions.

Figure 6.2 presents the SDSS *u*, *g*, *r*, *i* and *z* band images in the last two top panels and first three panels on the second row. The main emission features in the optical SDSS images are the stellar disk and bulge. At shorter optical wavelengths (in particular *u* band), a large fraction of the stellar light is extinguished along the line-of-sight by the prominent dust lane. Towards longer wavelengths, the dust obscuration diminishes and also the boxy shape of the bulge becomes more evident. This boxy shaped bulge is thought to result from a bar in the inner region of NGC 4565 viewed edge-on (Combes & Sanders, 1981) and is therefore considered to be a pseudo-bulge. A genuine bulge component is also present in NGC 4565, but its spatial extent and intensity is inferior to the dominant emission from the pseudo-bulge (Kormendy & Barentine, 2010).

Both from GALEX and SDSS images, the warping structures on the southeastern and northwestern sides of the galaxy's disk can be discerned. Especially at UV wavelengths, the warps are prominent emission features, indicative for the ongoing star formation in these tidally disrupted parts of the interstellar medium (ISM) in NGC 4565. Flux densities for the stellar emission in UV/optical wavebands were adopted from Cortese et al. (2012b) for GALEX FUV/NUV and SDSS gri bands (see Table 6.1). Fluxes for the remaining SDSS bands (u, z) were obtained in an homogeneous way from aperture photometry similar to the procedure for the other SDSS bands.

6.3.1 Model I: standard model

A first model accounting for the observed properties of stars and dust in NGC 4565 based on optical data is obtained from the FitSKIRT fitting algorithm. FitSKIRT was applied to determine the best fitting model parameters using our SDSS g band image (see Figure 6.2, last top panel) as a reference image. We choose the g-band image for the fitting procedure, since the emission in this waveband is dominated by the old stellar population. At shorter wavelengths, the contribution from young stars increases rapidly. The g band image is also optimal to perceive the attenuation effects of dust, which diminishes at longer wavelengths. Prior to the FitSKIRT fitting algorithm, the stellar warps on both ends of the galactic disk were masked in this image.

The input model for the stellar component consists of three components. The first component is an exponential disk with scale length h_R and height h_z to fit the disk component

$$\rho(R,z) = \rho_0 \exp\left(-\frac{R}{h_R}\right) \exp\left(-\frac{|z|}{h_z}\right). \tag{6.1}$$

The second component is a flattened Sersic geometry for the outer bulge component. It is modelled as

$$\rho(r) = \rho_0 \, \mathcal{S}_n\left(\frac{m}{r_{\text{eff}}}\right), \tag{6.2}$$

where $m = \sqrt{R^2 + \frac{z^2}{q^2}}$ is the spheroidal radius and $\mathcal{S}_n(s)$ represents the dimensionless 3D spatial density of a model that deprojects to a projected surface brightness profile

$$I(r_p) = I_0 \exp\left[-b_n \left(\frac{r_p}{r_{\text{eff}}}\right)^{1/n}\right]. \tag{6.3}$$

Finally, the third component consists of an inner bulge described as a Sersic function (same as Equation 6.2 but with $m = \sqrt{R^2 + z^2}$) with a Sersic index $n \sim 1.4$ and a scale length $r_{\text{eff}} \sim 1.3''$, similar to the values reported in Kormendy & Barentine (2010). The luminosity of the inner bulge was scaled to a fixed value $L_{\text{V}} \sim 3.6 \times 10^4$ $\text{L}_{\text{V},\odot}$, optimized to reproduce the g band minor-axis profile (see Figure 6.4, last bottom panel).

For the spectral energy distribution (SED) of the stars, we assume a Maraston (1998, 2005) single stellar population (SSP) parametrization. The age and metallicity of the SSP in the disk and bulge are fixed to 8 Gyr old and a solar metallicity ($Z = 0.02$), as obtained from diagnostic plots of several Lick indices (see Figures 5 and 6 in Proctor, Sansom & Reid 2000). The age of the SSP is assumed to be the same in the stellar disk and bulge, since the boxy bulge is considered to be a pseudo bulge. The intensity of the stellar components is set by its V band luminosity (L_{V}).

Earlier studies of the dust geometry in NGC 4565 have suggested a ring-like structure for a large fraction of the dust (Engargiola & Harper, 1992; Ohta & Kodaira, 1995; Neininger et al., 1996; Kormendy & Barentine, 2010; Laine et al., 2010). Therefore, our dust model is composed of an exponential disk with a density distribution as represented in Eq. 6.1 and a ring with a Gaussian distribution in radial direction and an exponential vertical profile

$$\rho(R,z) = \rho_0 \exp\left[-\frac{(R-R_0)^2}{2\sigma^2}\right] \exp\left(-\frac{|z|}{h_z}\right), \tag{6.4}$$

where R, w and h_z describe the radius of the ring, the radial dispersion and the vertical scale height. The content of the dust reservoir in NGC 4565 is scaled by the dust mass in each of the dust components. The dust population is assumed to be uniform across the entire galaxy, consisting of a composition of dust particles with a fixed grain size distribution. The abundances, extinction and emissivity of the dust mixture are taken from the Draine & Li (2007) model for the dust in our own Galaxy.

With the different model components for the stars and dust in NGC 4565 and furthermore assuming a variable inclination for the galaxy, the degrees of freedom in the fitting procedure amount to 15 parameters. Our model does not account for the continuum emission from the AGN in the center of NGC 4565, since the low [Ne III] 15.55 μm-to-[Ne II] 12.81 μm ratio ($\sim$ 1, Laine et al. 2010) suggest that the AGN continua are weak in this galaxy (Deo et al., 2007). Table 6.2 gives an overview of the best fitting parameters obtained from the FitSKIRT algorithm. Since a sufficient number of photon packages were used to obtain this best fitting model, we assume an uncertainty of about 20% for all derived parameters (see also De Geyter et al. in prep.).

Exploring the compatibility of this model with optical data, we compare the observed g band image (see Figure 6.4, top row) and the major- and minor-axis g band profiles for several galactocentric radii (see Figure 6.4, bottom row) with the modelling results. The resemblance between modelled and observed images, major- and minor-axis profiles suggests that our radiative transfer model is representative for the observed stellar emission and optical properties of dust in NGC 4565. For the inclination, we find a best fitting value of $\sim 87.25^\circ$, which is in agreement with earlier reported results. Indeed, H I observations of the gaseous disk in the past have constrained the inclination $> 84^\circ$ (Ruben, 1991), with more recent H I observations reporting an inclination angle of 87.5° (Zschaechner et al. in prep.). From a similar radiative transfer study, Alton et al. (2004) estimated an inclination of 88°.

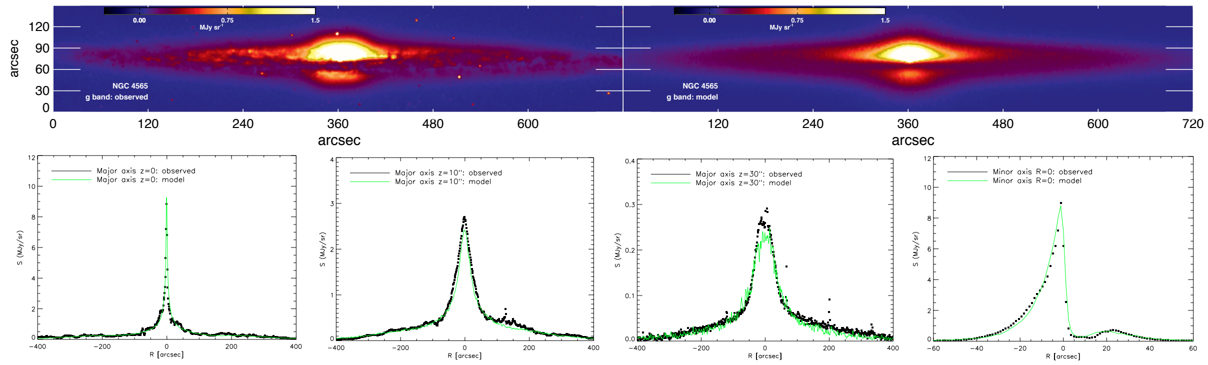

Figure 6.4: Model 1: the observed (left) and modelled (right) g band image for NGC 4565 on the top row. The bottom row shows from left to right the major axis g band profiles at distances z=0, 10 and 30″ from the center of NGC 4565, respectively. The most right panel represents the minor axis profiles at R=0. The observed profiles are indicated in black, with the modelled emission colour-coded in green.

From the stellar distribution in this radiative transfer model, we infer a bulge-to-disk ratio of B-to-D $\sim$ 0.47 in the V band. The model indicates a total dust mass of $M_d \sim 1.0 \times 10^8$ M$_{\odot}$ of which about 60 % resides in an exponential disk, with the remaining 40 % distributed in a broad ring structure. The scale size of the exponential dust disk ($h_R \sim$ 223 ″, $h_z \sim$ 2.5″) agrees well with the results obtained from a similar radiative transfer modelling procedure in Alton et al. (2004) ($h_R \sim$ 200″, $h_z \sim$ 4.3″). The diffuse dust component in Alton et al. (2004) has a face-on optical depth $\tau_V^f \sim 0.63$, which corresponds to $M_d \sim 9.7 \times 10^7$ M$_{\odot}$, when assuming the same extinction cross-section for the Draine & Li (2007) dust composition applied in our dust model.

Figure 6.5 represents the spectral energy distribution as modelled by our radiative transfer code SKIRT (solid, black line). Available flux measurements were overlaid on this SED model to describe the observed spectral energy distribution. An overview of flux measurements for NGC 4565 is given in Table 6.1. Less accurate flux measurements were considered non-relevant for this analysis and were omitted from this plot (see Section 6.2). Although our model shows great resemblance with the g band image and major- and minor-axis profiles, the spectral energy distribution in Figure 6.5 shows that our model fails to reproduce the emission from NGC 4565 in the UV and MIR/FIR wavelength domains. The higher observed UV and MIR emission from NGC 4565 indicates the presence of a young stellar population in this galaxy, which is not yet accounted for by our model.

6.3.2 Model II: standard model with star formation

In an attempt to reproduce the ultraviolet and infrared emission observed from NGC 4565, we add a star formation component to the model constructed in Section 6.3.1. Rather

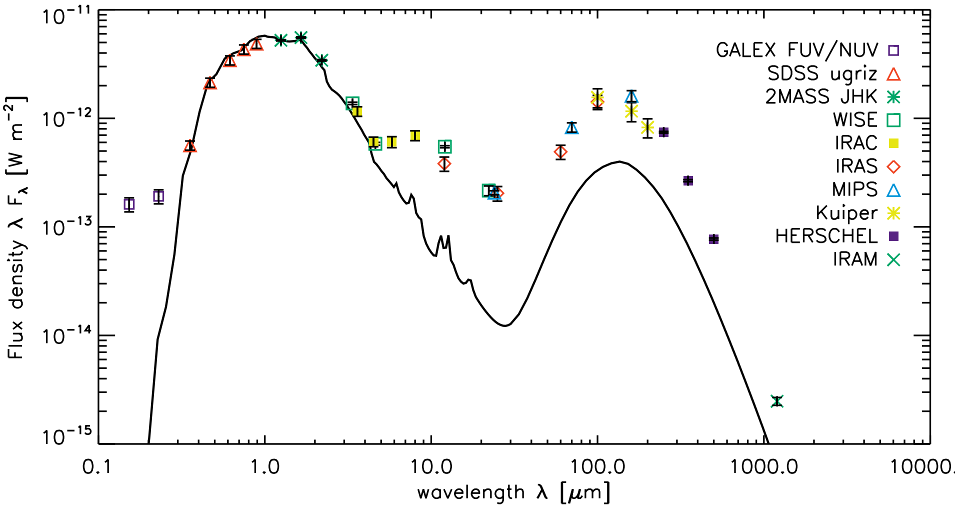

Figure 6.5: Model 1: the modelled SED as obtained with the SKIRT model (solid black line) overlaid with the observed fluxes (see Table 6.1).

than using an empirical star formation template (e.g. MacLachlan et al. 2011), we adopt starburst templates from the library of pan-spectral SED models for the emission from young star clusters with ages $<$ 10 Myr presented in Groves et al. (2008). The SED templates in Groves et al. (2008) were generated from a one-dimensional dynamical evolution model of HII regions around massive clusters of young stars, the stellar spectral synthesis code Starburst 99 (Leitherer et al., 1999) and the nebular modelling code MAPPINGS III (Groves, 2004). The Starburst99 templates used in these models correspond to an instantaneous burst with a Kroupa (2002) broken power-law IMF. The main parameters controlling the shape of the emission spectrum from these young stellar clusters are the metallicity (Z) of the gas, mean cluster mass ($M_{\rm cl}$), age and compactness (C) of the stellar clusters, the pressure of the surrounding ISM (P_0) and the cloud covering fraction ($f_{\rm PDR}$). The metallicity is chosen similar to the metallicity of the old stellar population in NGC 4565 ($Z \sim 1$ Z$_\odot$). To eliminate the age parameter, we use age-averaged templates obtained from averaging spectra over 21 cluster ages, ranging from 0.01 to 10 Myr in steps of 0.5 Myr. For the mean cluster mass and ISM pressure, we assume fixed values $M_{\rm cl} \sim 10^5$ M$_\odot$ and $P_0/k \sim 10^6$ cm^{-3} K. Those approximations are justified since more massive star clusters can be simply thought of as the superposition of several individual clusters. A variation in the ISM pressure furthermore mainly affects the nebular emission lines rather than altering the shape of the emission spectrum (Groves et al., 2008). For the cloud covering fraction $f_{\rm PDR}$, we will assume a value of f_{PDR} = 1 to describe the emission from heavily obscured star-forming regions in NGC 4565. The choices for $M_{\rm cl}$ and P_0/k leave us to explore the effect of the compactness parameter C on the shape of the SED for values of log C ranging between 4.5 and 6.5. With the compactness parameter controlling the position of the far-infrared emission bump by shifting it in peak wavelength without significantly altering the width of the emission curve, the parameter C is closely related to the dust temperature (Groves et al., 2008). Although the emission at 24 μm might still be dominated by hot dust emission predominantly heated by young stars of ages < 10 Myr, the contribution of diffuse dust emission is non-negligible at far-infrared and sub-millimeter wavelengths. Therefore, it is difficult to constrain the shape of the emission spectrum from hot dust grains and thus to determine the appropriate value of $\log C$ in the models. With values of 6.5 for $\log C$ describing extremely compact star-forming regions, which are characteristic for the high pressure ISM and/or massive young clusters in starburst galaxies, we assume a more moderate compactness factor of $\log C = 5.5$. A value of $\log C = 5.5$ is furthermore consistent with the dust temperature $T_d = 30$ K found for the warm dust component heated predominantly by stellar emission originating from star-forming regions (Engargiola & Harper, 1992).

Emission spectra for the young stellar population with ages between 10 and 100 Myr are taken from the Starburst99 library (Leitherer et al., 1999). The Starburst99 templates were constructed for an instantaneous burst with a solar metallicity, a burst mass $M_{cl} = 10^6$ $M_\odot$ and a Kroupa (2002) broken power-law IMF, which is consistent with the stellar emission spectra used to compute the SED of stellar clusters younger than 10 Myr in Groves et al. (2008). With the young stellar clusters < 10 Myr emitting predominantly in mid-infrared wavebands, the non-ionizing radiation of the evolved stellar population up to ages 50-100 Myr will dominate the UV emission spectrum (Calzetti et al., 2005).

Although most details on the exact location of star-forming complexes within the disk vanish along the line of sight, we try to recover the average geometry of unobscured and dust-enshrouded star-forming regions from the emission profiles along the major axis of NGC 4565 in the GALEX *NUV* and MIPS 24 μm wavebands (see Figure 6.6, top and bottom panel, respectively). By allocating a certain distribution to the star-forming regions, the proper amount of attenuation due to the foreground screen of diffuse dust is applied on every specific location within the galaxy. Indeed, due to the high inclination angle the different star-forming regions in NGC 4565 will experience wide ranges in obscuration depending on whether they are located on the near- or far end of the galaxy's disk with respect to the line-of-sight. From the major axis *NUV* emission profile, we derive a ring-like geometry for the unobscured star formation component, modelled as a ring (see Equation 6.4) with central radius $R \sim 290''$ and width $\sigma \sim 72''$. The scale height of the ring of young stars is assumed to be identical to the scale height of the stellar disk populated with the old stellar population ($h_z \sim 8.2''$). From the MIPS 24 μm image, it becomes immediately evident that a component of obscured star formation resides in a narrow ring coinciding with the CO molecular ring centered at 80-100″ (Sofue & Nakai, 1994; Neininger et al., 1996). The parameters for the ring (see Equation 6.4) of embedded star formation are chosen similar to the molecular CO ring with central radius at $R \sim 90''$, width $\sigma \sim 3.4''$ and scale height $h_z \sim 1.5''$. Aside from this concentration of embedded localized sources distributed in a ring, a more extended component of obscured star formation seems also present in NGC 4565. To reproduce the more extended 24 μm emission in the major axis profile, obscured star-forming complexes are distributed in the ring harboring the unobscured star formation component and the dust ring containing $\sim$ 40% of the diffuse dust component in NGC 4565. From the 24 μm major axis profile (see Figure 6.6, bottom panel), the presence of a central dust disk becomes evident. This central dust concentration is modelled as an exponential disk with radial and vertical scale lengths of 5″ and 1″, respectively. The distribution of this central dust reservoir ($M_d \sim 3 \times 10^4$ M$_\odot$) is truncated at a radius of 20″.

When fitting the UV and 24 μm emission of NGC 4565, we require an average star formation rate in the outer regions of the disk in NGC 4565 of 3.1 M$_\odot$ yr^{-1} for the 10 to 100 Myr old stellar population. The heavily obscured star-forming regions of ages $<$ 10 Myr seem to reproduce the observed 24 μm emission when assuming an average star formation rate of 2.0 M$_\odot$ yr^{-1} over the past 10 Myr. The dust-enshrouded star-forming clumps in the narrow ring produce young stars at a rate of SFR $\sim$ 0.6 $M_\odot$ yr^{-1}, with a somewhat higher productivity for the dense clouds distributed in the ring of unobscured star formation (SFR $\sim$ 0.7 $M_\odot$ yr^{-1}) and the diffuse dust ring (SFR $\sim$ 0.7 $M_\odot$ yr^{-1}). This obscured star formation rate inferred from the models is perfectly consistent with the SFR $\sim$ 2.0 M$_\odot$ yr^{-1} calculated in Wu & Cao (2006) from the far-infrared luminosity $L_{\rm FIR}$ in NGC 4565, corrected for the contribution from an old stellar population (Satyapal et al., 2005). Also monochromatic SFR tracers such as the 24 μm emission result in similar estimates for the SFR $\sim$ 2.0 M$_\odot$ yr^{-1} (Rieke et al., 2009). We argue furthermore that the star formation rate of stars between 10 and 100 Myr in our model (SFR $\sim$ 3.1 M$_\odot$ yr^{-1}) is in close agreement with the SFR $\sim$ 2.7 M$_\odot$ yr^{-1} calculated from the FUV luminosity $L_{\rm FUV}$ for NGC 4565 and relying on the SFR calibration in Salim et al. (2007).

Accounting for all young stellar objects in our model, we derive an average star formation rate of 5.1 M$_\odot$ yr^{-1} over the past 100 Myr. The small decrease in the star formation activity during the recent 10 Myr is in agreement with a delayed exponential law describing the star formation history in other late-type spiral galaxies (Boselli et al., 2001; Gavazzi et al., 2002). The total star formation activity in our model (SFR $\sim$ 5.1 M$_\odot$ yr^{-1}) is furthermore consistent with the total star formation rates derived from a combination of unobscured and obscured star formation tracers (e.g. SFR$_{\rm FUV+24\mu m} \sim$ 3.2 M$_\odot$ yr^{-1}, Zhu et al. 2008; SFR$_{\rm FUV+TIR} \sim$ 3.9 M$_\odot$ yr^{-1}, Buat et al. 2005).

This model with both unobscured and obscured star formation is able to account for the young stellar emission at UV/mid-IR wavelengths (see images on the first and third row of Figure 6.7, respectively) and remains in agreement with the optical constraints (see images on the second row and plots on the last row of Figure 6.7) upon reducing the luminosity of the old stellar population in the disk by a small factor to correct for the emission from those young stars in optical wavebands (L_{V} = 4.6 × 10^7 $\mathrm{L}_{\odot,\mathrm{V}}$). The total dust mass associated to the young stellar clusters ($<$ 10 Myr) in our models is M_d $\sim$ 3.1 × 10^7 $\mathrm{M}_{\odot}$, which increases the total dust mass in NGC 4565 to M_d $\sim$ 1.3 × 10^8 $\mathrm{M}_{\odot}$. The geometry for the embedded, localized sources in NGC 4565 is able to account for the 24 μm emission in NGC 4565 as observed from the major axis profile (see Figure 6.6, bottom panel) or the MIPS 24 μm image (see images on the first row of Figure 6.7). The geometry for the less obscured young stars with ages $>$ 10 Myr is capable of reproducing the emission profile along the major axis (see Figure 6.6, top panel) as well as the emission originating from the entire galaxy at NUV wavelengths (see Figure 6.7, third row). The peak at $R \sim 420''$ in the NUV major axis profile belongs to the residual star formation in the warp structure on the northwestern side of the galaxy's disk and is not taken into account in our model. The stellar clusters do have a more clumpy distribution throughout the disk than was accounted for by our model.

More critical is the inconsistency in the FIR/submm, where our radiative transfer model continues to underestimate the observed emission spectrum for NGC 4565 (see Figure 6.8). Even though the model accounts for the dust heating provided by star formation, the modelled dust emission underestimates the observed far-infrared and submillimeter emission by a factor of $\sim$ 3-4, in correspondence to dust energy balance studies for other nearby edge-on spirals.

6.3.3 Model III: standard model with star formation and clumpy dust component

Although in agreement with the observed properties of stars and dust at optical wavelengths and the young stellar emission in UV and MIR wavebands, the model from section 6.3.2 underestimates the observed dust emission in the far-infrared and (sub-) millimeter wavelength regime. Whereas the dust emissivity of dust grains could influence the shape of the SED at some wavelengths (Alton et al., 2004), the inconsistency in the integrated dust energy balance can not be solely caused by a grain population with dust emissivities diverging from Galactic values at longer wavelengths. Although we can not exclude a possible variation in dust emissivity at submm/mm wavelengths (diverging from the assumed emissivity in the Draine & Li 2007 dust model), we argue that this discrepancy is likely due to a clumpy morphology of the dust in NGC 4565 un-

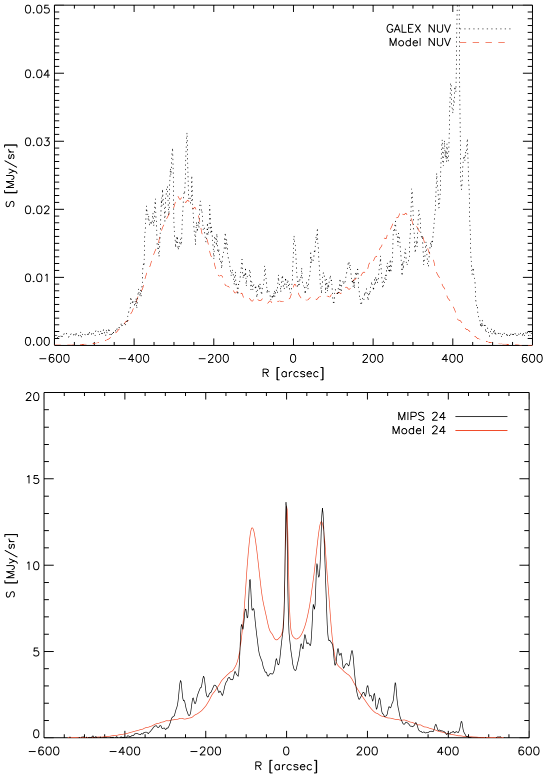

Figure 6.6: Model 2: *NUV* (top) and MIPS 24 μm (bottom) major axis profiles. The observed profiles are indicated in black, with the modelled emission colour-coded in red.

resolved in the currently available dataset of far-infrared/submillimeter observations for. Due to the high density in those clumps, they hardly contribute to the attenuation of stellar light and can therefore not be distinguished from optical observations.

Due to the edge-on inclination of NGC 4565 and the current limitations in resolving power of infrared instrumentation, we are not capable of constraining the exact location and size of those dust clumps and rather have to content with information on the average mass and temperature of this clumpy dust reservoir. Those dust clumps either correspond to quiescent clouds where star formation has not (yet) been initialized. On the other hand, this extra dust reservoir might reside in the outer shells of star-forming complexes where the heating by the young embedded objects becomes negligible due to the high optical depth of the dust shells in the immediate vicinity of the stellar source.

To estimate the amount of dust residing in clumps, we fit the DustEm dust model with a Draine & Li (2007) grain composition to the residual fluxes after subtracting the dust emission in our model from the observed flux densities (IRAC 5.8, 8.0 μm, WISE 12.1 μm, IRAS 12 and 100 μm, Kuiper 100 and 160 μm, MIPS 160 μm, SPIRE 250, 350, 500 μm, IRAM 1.2 mm). Figure 6.8 shows the resulting SED (black, solid curve) when supplementing our model with a dust reservoir of $\sim 1.6 \times 10^8$ $M_\odot$ at a tempera-

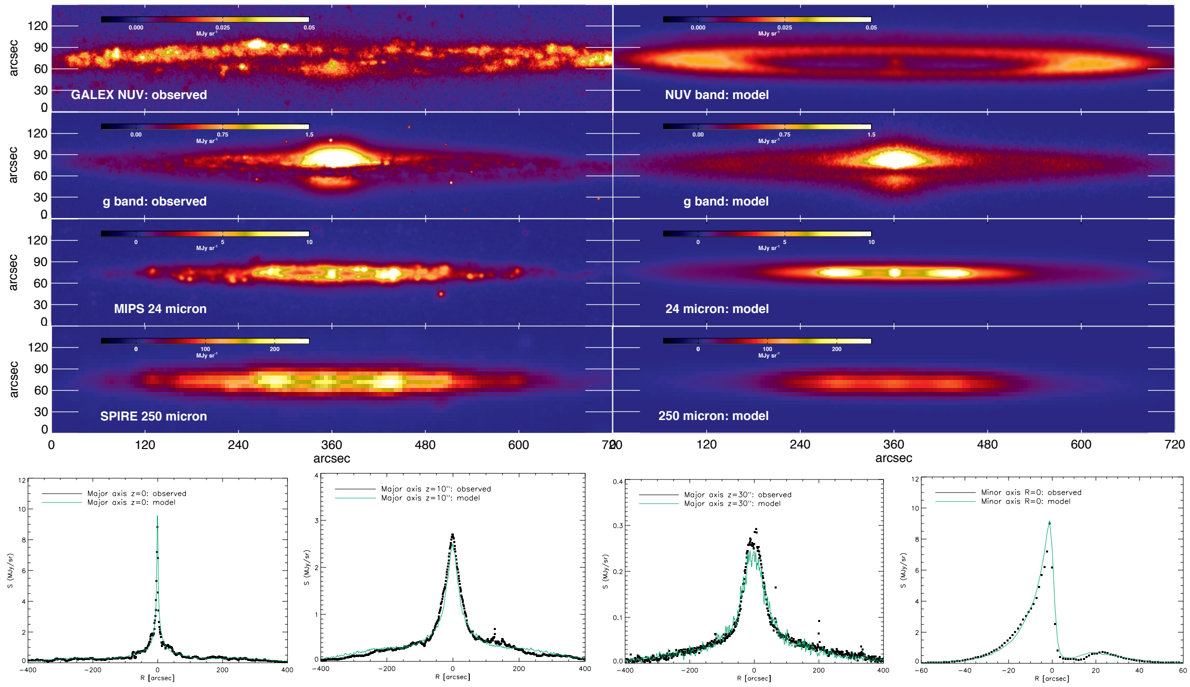

Figure 6.7: Model 2 with on the top row: the observed (left) and modelled (right) *NUV* band (top row), *g* band (second row), 24 μm (third row) and 250 μm image (fourth row). The bottom row represents from left to right the major axis *g* band profiles at distances z=0″, 10″ and 30″ from the center of NGC 4565, respectively. The most right panel represents the minor axis profiles at R=0. The observed profiles are indicated in black, with the modelled emission colour-coded in green.

ture of $T_d \sim 16$ K (green, dotted curve). The average temperature $T_d \sim 16$ K obtained for the residual dust reservoir is consistent with the temperature of the diffuse dust in the disk of NGC 4565 ($T_d \sim$ 14-18 K) and the average colour temperatures derived in other nearby spiral galaxies at wavelengths longwards of 160 μm (e.g. M81, M83 and NGC 2403, Bendo et al. 2012). At mid-IR wavelengths, this additional dust reservoir is capable of explaining the PAH emission in NGC 4565. Also at FIR/submm wavelengths, a massive cold dust component seems adequate to explain the emission in those wavebands. At 60 and 70 μm, our radiative transfer model however overestimates the observed fluxes. This inconsistency could be an indication for the star-forming complexes in NGC 4565 to be more compact than currently accounted for by our model. Due to the high inclination angle of NGC 4565, a direct identification of heavily obscured star-forming complexes within the disk of the galaxy and their individual size distribution and compactness is impeded.

With these additional cold dust clumps, the total dust mass in NGC 4565 amounts to $M_d \sim 2.9 \times 10^8\ M_\odot$ of which one-third has a diffuse distribution throughout the disk and the remaining two-thirds resides in clumps. From those dense dust clouds, the majority ($\sim$ 83%) is not heated by UV-emitting sources while the remainder ($\sim$ 17%)

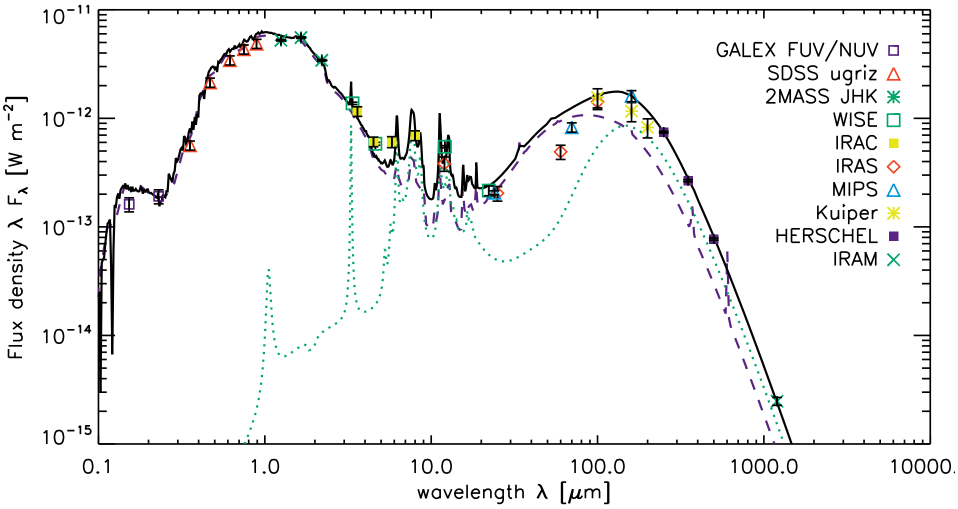

Figure 6.8: Model 2: the modelled SED as obtained with the SKIRT model (dashed purple line) overlaid with the observed fluxes (see Table 6.1). Model 2 corresponds to model 1 supplemented with young star clusters (< 100 Myr). To estimate the dust mass residing in quiescent dust clumps in NGC 4565, we fit the DustEm dust model with a Draine & Li (2007) grain composition (green, dotted line) to the residual fluxes for NGC 4565 in the far-infrared and submillimeter wavebands. The model with star formation and an additional dust reservoir distributed in clumps can explain the multi-wavelength observations for NGC 4565 (see black, solid curve).

host embedded star-forming complexes. The total dust mass $M_d \sim 2.9 \times 10^8$ M$_\odot$ in our model is consistent with the dust reservoir accounted for by BLAST observations (Wiebe et al., 2009), but $\sim$ 10 times higher than the dust content reported in Engargiola & Harper (1992) (2.7×10^7 M$_\odot$) based on IRAS observations up to 100 μm. This confirms the need for longer wavelength observations to trace the entire dust reservoir in a galaxy (e.g. Bendo et al. 2010; Gordon et al. 2010; Bendo et al. 2012).

Geometry	i [°]	87.25
Stellar disk	h_R [″]	102
	h_z [″]	8.2
	L_V [$\mathrm{L}_{\odot,\mathrm{V}}$]^1	4.9×10^{10}
Outer bulge	n	2.12
	r_eff [″]	20.2
	q	0.744
	L_V [$\mathrm{L}_{\odot,\mathrm{V}}$]	2.0×10^{10}
Dust disk	h_R [″]	223
	h_z [″]	2.5
	M_d [$\mathrm{M}_\odot$]	6.3×10^7
Dust ring	R [″]	146
	h_z [″]	4.3
	σ [″]	41.2
	M_d [$\mathrm{M}_\odot$]	4.0×10^7

Table 6.2: Best fitting model parameters for the stellar (exponential disk + outer bulge) and dust components (exponential disk + ring) in NGC 4565 as obtained from FitSKIRT.

[1] The luminosity of the stellar disk is later adjusted to L_V = 4.6 × 10^{10} $\mathrm{L}_{\odot,\mathrm{V}}$ to correct for the emission from young stars in the *V* band when supplementing our model with star formation.

6.4 Comparison to other dust energy balance studies

The solution to the dust energy budget problem for NGC 4565 accounting for a sizable fraction of the dust (∼ 70%) distributed in compact clumps is in agreement with other energy balance studies of edge-on objects (e.g. Bianchi 2008; Baes et al. 2010; Popescu et al. 2011; De Looze et al. 2012a; Holwerda et al. 2012, etc.).

From the HI mass $M_\mathrm{HI} \sim 1.8 \times 10^{10}$ $\mathrm{M}_\odot$ (Zschaechner et al. in prep.) and the CO observations ($M_{\mathrm{H}_2} \sim 2.9 \times 10^9$ $\mathrm{M}_\odot$) presented in Neininger et al. (1996), we derive a total gas mass of $\sim 2.9 \times 10^{10}$ $\mathrm{M}_\odot$ for NGC 4565 when applying a correction factor of ∼ 1.4 to correct for heavier elements. Based on the total dust mass in our radiative transfer model ($M_d \sim 2.9 \times 10^8$ $\mathrm{M}_\odot$), we estimate an average gas-to-dust ratio of ∼ 100 in NGC 4565, which is in fair agreement with the gas-to-dust fraction found in other late-type spirals (e.g. ∼ 120 in our own Galaxy, Zubko, Dwek & Arendt 2004) and the dust-to-HI mass fraction derived for Sb galaxies with normal HI components (as opposed to HI deficient objects) in the HRS sample of galaxies (Cortese et al., 2012a).

Investigating the dust heating in NGC 4565, we find that about 57% of the far-infrared luminosity is attributed to the absorption of stellar light from the old stellar population, with the heating for the remaining 43% provided by the young stellar population. In this calculation, we assume that the high-density dust clumps distributed throughout the diffuse ISM in NGC 4565 are merely heated by the old stellar population, since the temperature of the dust ($T_d \sim 16$ K) in those dense dust cores does not suggest any link to localized embedded sources and is more closely related to the average temperature of the diffuse dust in the disk of the galaxy ($T_d \sim$ 14-18 K). Those heating fractions are in agreement with similar studies of dust heating mechanisms in other nearby galaxies, where the old stellar population also accounts for an important fraction of the far-infrared radiation (e.g. Bianchi 2008; Bendo et al. 2010; Boquien et al. 2011b; Popescu et al. 2011; Bendo et al. 2012). Similar results were obtained from accurate modelling of the absorption of stellar light as well as careful investigations of UV observations (Buat & Xu, 1996; Charlot & Fall, 2000; Witt & Gordon, 2000; Cortese et al., 2008). Also Engargiola & Harper (1992) report a similar dust heating efficiency of 54 and 46% for the young and old stellar population in NGC 4565, respectively.

Although the fraction of dust heated by the young stellar population in NGC 4565 is less than 50%, the contribution of hot dust emission from star-forming complexes is about 85 and 80 % in the 24 and 70 μm wavebands, after which it decreases quickly to less than half at 100 μm, 25% at 160 μm, about 10-15% in all SPIRE wavebands and below 10% at 1.2 mm. Those values are consistent with the decreasing contribution of star-forming regions for increasing wavelength in M81, M83 and NGC 2403 (Bendo et al., 2012), with a relative contribution of the young stellar population to the total dust heating of more than 50% shortwards of 250 μm and dropping below 30% in the SPIRE wavebands.

This self-consistent analysis of the dust heating mechanisms in NGC 4565 based on a realistic radiative transfer model confirms earlier studies reporting on a non-negligible fraction of the dust heating in spiral galaxies powered by the more evolved stellar population. With the young stellar population being responsible for less than half of the total infrared dust emission originating from NGC 4565, we believe caution is needed when using the total infrared emission in galaxies to trace the star-forming activity. Although a tight correlation was found between the star formation and the total infrared dust emission for large samples of nearby spiral galaxies (Devereux & Young, 1990; Devereux, Jacoby & Ciardullo, 1995; Buat & Xu, 1996; Kennicutt et al., 2009), this relation might be the result of an indirect link between the star-forming activity and the total-infrared emission in galaxies, tracing the surface density of gas in the interstellar medium. In the latter case, the SFR-L_{FIR} correlation is governed by the Schmidt law (Schmidt, 1959; Kennicutt, 1998), relating the surface density of gas and star formation in galaxies, rather than the dust heating provided by star-forming regions.

7

Conclusions and future work

The main goal of this PhD thesis was to quantify a number of characteristics of the interstellar medium in nearby galaxies, ranging from their star formation rate to the properties of their dust component.

In chapter 2, we present an analysis of the [CII] luminosity in a sample of galaxies of normal star formation activity (SFR $\sim$ 0.03-127 $M_{\odot}$ yr^{-1}). We find a good one-to-one correlation between the [CII] luminosity and the SFR in these galaxies, and managed to calibrate the SFR as a function of $L_{[\mathrm{CII}]}$. This SFR relation allows to quantify the star formation activity in galaxies for which other SFR tracers are unavailable or less reliable. The extension of this SFR relation towards objects characterized by more extreme star formation conditions and systems in the early Universe however will need to be investigated in the future. With the booming number of [CII] line measurements from galaxies since the launch of the Herschel telescope, an update on this SFR calibration will be possible for a large sample of galaxies with broad ranges in SFR and [CII] luminosity. In the near future, we plan to extend our work to galaxies from the Very Nearby Galaxies Survey, for which spatially resolved [CII] maps have been taken. This increase in resolution will enable us to pin down and constrain the origin of [CII] emission from galaxies and of the tight correlation between $L_{[CII]}$ and SFR (shared photo-excitation processes or an indirect correlation through the Schmidt law).

A second topic under analysis in this PhD thesis involves the dust content in early-type dwarf galaxies, both in group and cluster environments. Whereas some Local Group dwarf elliptical galaxies in groups had previously been shown to contain a significant amount of dust, no dust emission had been detected in early-type dwarf galaxies residing in clusters before the launch of Herschel. In chapter 3, we present new Herschel observations of the central part of the Virgo Cluster, obtained during the science demonstration phase of the Herschel Virgo Cluster Survey (HeViCS). These observations allowed us to detect large reservoirs of dust in two cluster dwarf elliptical galaxies. This is the first detection of the FIR/submm emission from dust in cluster early-type dwarf galaxies. After completion of the observations of the Herschel Virgo Cluster Survey and the Herschel Reference Survey, we identified 12 additional early-type dwarf galaxies in the Virgo cluster at FIR wavelengths. All these galaxies have properties in between star-forming late-type galaxies and quiescent elliptical galaxies, and can hence be considered transition-type objects. In the near future, we plan to analyze the spectrophotometric properties of these galaxies in more detail and explore how these characteristics change under the influence of several gravitational and/or environmental processes in order to verify the transformation mechanism at work.

Besides probing the dust reservoir in Virgo early-type dwarf galaxies, part of my PhD thesis discusses new Herschel and JCMT observations of the dust and gas components in NGC 205. NGC 205 is the most nearby dwarf elliptical galaxy and is a satellite of the Andromeda Galaxy in the Local Group. Interesting about this galaxy is the large discrepancy between its observed ISM mass and theoretical predictions for its current gas reservoir . In chapter 4, we revise the missing ISM mass problem in NGC 205 based on direct gas observations from JCMT CO(3-2), Herschel [CII] and [OI] line emission. Alternatively, we also probed its ISM content through Herschel dust continuum observations. Both new gas and dust measurements confirm the ISM deficiency in this object, which we believe is attributable to the removal of a significant amount of gas and dust from the galaxy in the past due to efficient supernova feedback and/or tidal interactions with the Andromeda galaxy. In the future, we will extend our study in two different ways. On the one hand, we have been awarded observing time at the Nobeyama 45m telescope, the JCMT and the Very Large Array to observe NGC 205 in the CO(1-0) line, at 850 μm, and in the radio continuum. From these observations, we hope to refine the total ISM content and the importance of past supernova feedback in NGC 205. On the other hand, we have been awarded observing time with Herschel to measure the ISM content in NGC 185 and NGC 147, the other dwarf elliptical companions of the Andromeda galaxy characterized by a similar deficiency in ISM mass. From the comparison of the specific ISM physics and environmental conditions for those three objects, we hope to identify the reason for their missing ISM mass problem.

A last part of this research thesis was attributed to the study of the dust component in nearby edge-on spiral galaxies through a detailed analysis of their dust energy balance. Similar studies in the past have shown that the amount of stellar light that is absorbed by dust at UV/optical wavelengths does not correspond to the thermal re-emission of dust in infrared and submillimeter wavebands. Dust energy balance studies of the nearby Sombrero Galaxy (chapter 5) and the Needle Galaxy (chapter 6) are in agreement with previously obtained results (i.e. the dust emission in our model underestimates the observed thermal re-emission of dust by a factor of 3-4). After accounting for the presence of young stars in both galaxies, a clumpy dust morphology seems to provide the best answer to the dust energy balance problem. A distribution of a sizable fraction of dust in high-density dust clouds provides an extra source of FIR/submm emission, but has a negligible contribution to the global extinction. A larger sample of galaxies is needed to confirm this hypothesis. Our group is currently analyzing in a systematic way a large sample of dust-lane galaxies, ranging from early-type galaxies (in the frame of the FRIEDL project) to late-type galaxies (as part of the HEROES and NHEMESES projects). For all these galaxies, we have obtained Herschel PACS and SPIRE data, and we are currently building up a large multi-wavelength data set to support these FIR/submm data. In the near future, we also aim to extend dust energy balance studies to face-on galaxies. Although the radiative transfer modelling of face-on galaxies involves complex geometries and a careful characterization of the extinction properties of dust, the possibility of the direct identification of unobscured and dust-enshrouded star formation regions and clumpy structures will be rewarding and provide valuable information to identify the true cause for the discrepancy in the dust energy budget of edge-on spirals.

8

Nederlandse samenvatting

Inleiding

Als je weet dat onze eigen Melkweg reeds uit meer dan 200 miljard sterren zoals onze eigen Zon bestaat, is het moeilijk te geloven dat het heelal nog eens miljarden soortgelijke sterrenstelsels herbergt. Een dergelijk sterrenstelsel is een systeem van sterren, gas en stof dat door gravitatiekrachten bij elkaar gehouden wordt. Met het menselijke oog kunnen we enkel de straling van sterren waarnemen, terwijl de andere componenten in een sterrenstelsel hun straling uitzenden op andere golflengten. Om de werking en evolutie van een sterrenstelsel ten volle te doorgronden is het noodzakelijk de emissie van alle componenten nauwkeurig te registreren. De specifieke aard van de straling en de doorlatendheid van de atmosfeer voor deze emissie (figuur 8.1) maken waarnemingen met aangepaste instrumentatie, zowel van op aarde als vanuit de ruimte, een onontbeerlijke must.

De meest energetische gebeurtenissen in een sterrenstelsel zijn waarneembaar op de kortste golflengten. Bij explosies van sterren op het einde van hun levensloop of bij de creatie van een zwart gat kunnen we hoog-energetische gamma en X-straling (figuur 8.2, linksboven). UV straling wordt dan weer uitgezonden door de jongste, massieve sterren in het heelal, terwijl de iets oudere sterren op optische golflengten stralen, waar ze dus ook waarneembaar zijn met het menselijke oog. De koudere materialen in het heelal zenden minder energetische straling uit en zijn daarom ook slechts zichtbaar op langere golflengten. Zo zal stof met een temperatuur variërend van 10 K tot 100 K een bron van infraroodstraling zijn (figuur 8.2, rechtsboven). Er zijn echter ook andere emissiemechanismen die ons in staat stellen om de inhoud van het heelal te bepalen. Koud interstellair gas is bijvoorbeeld waarneembaar als lijnstraling op welbepaalde golflengten in het infrarode, millimeter en radio golflengtegebied (figuur 8.2, linksonder). Op radio golflengten kunnen we naast gas ook synchrotronstraling zien, afkomstig van geladen deeltjes die versneld worden tot bijna de lichtsnelheid in een magnetisch veld van een supermassief zwart gat of een uitdeinende ring van materiaal na een supernova uitbarsting (figuur 8.2, rechtsonder).

Van op aarde kan typisch enkel de optische, nabije-infrarode straling en een deel van de radiogolven worden waargenomen (zie Figuur 8.1). De rest van de straling wordt tegengehouden door de beschermende laag van atmosfeer rond onze planeet. Om ook de andere lichtgolven op te kunnen vangen worden telescopen op grote hoogte gebouwd, om aan het merendeel van de atmosferische invloed te ontsnappen, en op plaatsen waar de luchtlagen minder beïnvloed worden door atmosferische storingen. Voor bepaalde golflengten brengt dit echter geen alternatief en worden ruimtemissies gelanceerd die een telescoop in een baan rond de aarde of de zon brengen. In het golflengtedomein van de UV straling tot de kortste infrarode straling is de Hubble

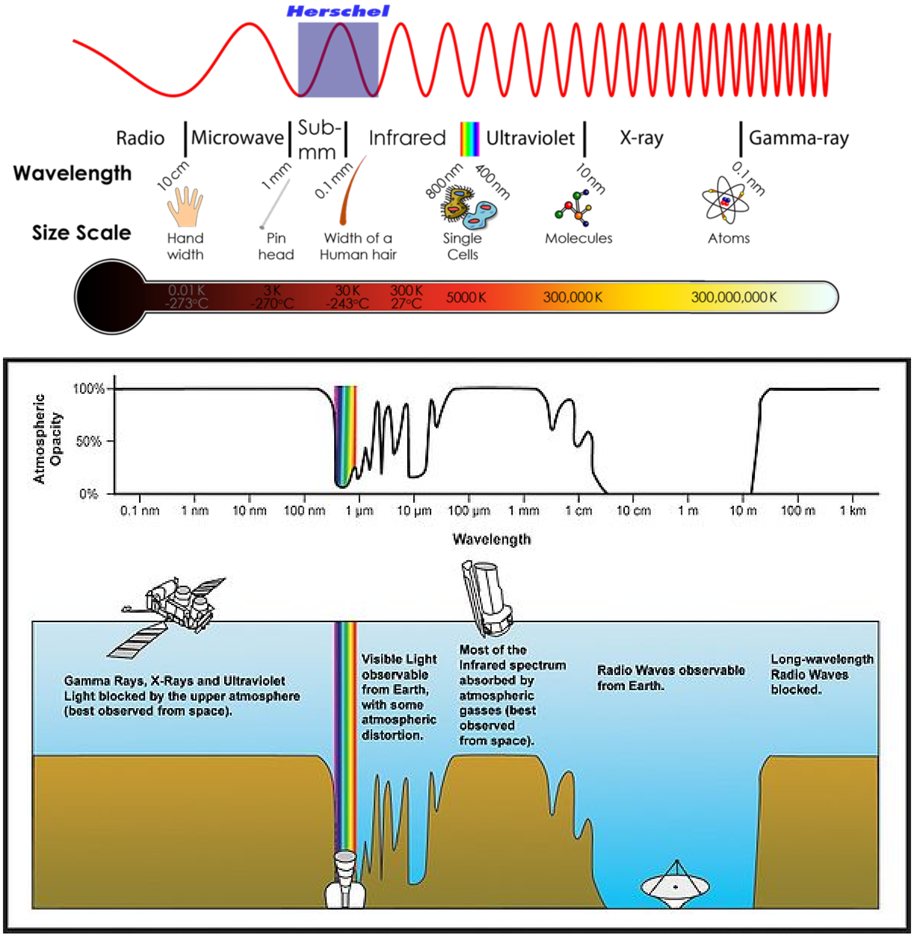

Figure 8.1: Het bovenste paneel toont het elektromagnetisch spectrum waarbij de typische grootte van de lichtgolven en de temperatuur van stralende objecten worden aangeduid voor verschillende golflengten. Het onderste paneel (waar radiogolven nu rechts staan en gammastraling links) toont de transparantie van de atmosfeer voor straling op verschillende golflengten. Dit diagram geeft duidelijk aan dat enkel de optische straling, de nabije-infrarode emissie en een groot deel van het radio gebied doorheen de atmosfeer het aardoppervlak kunnen bereiken. Door de steeds veranderende condities in de atmosfeer is het echter ook op kortere golflengten beter om waarnemingen vanuit de ruimte te doen om aan de turbulentie van de atmosfeer te ontsnappen.

Space Telescope de belangrijkste ruimtemissie, die de sterrenkundige wereld heeft verrijkt met wonderbaarlijke beelden van de meest spectaculaire fenomenen (zie Figuur 8.3). Met de recente lancering van de Herschel Space Telescope (op 14 mei 2009) kan ook de emissie van het universum op ver-infrarood en submillimeter golflengten in kaart gebracht worden.

Aangezien dit doctoraatsonderzoek voornamelijk de eigenschappen van het koude materiaal in sterrenstelsels bestudeert, werd ook veelvuldig gebruik gemaakt van beelden die recentelijk door de Herschel satelliet gemaakt werden.

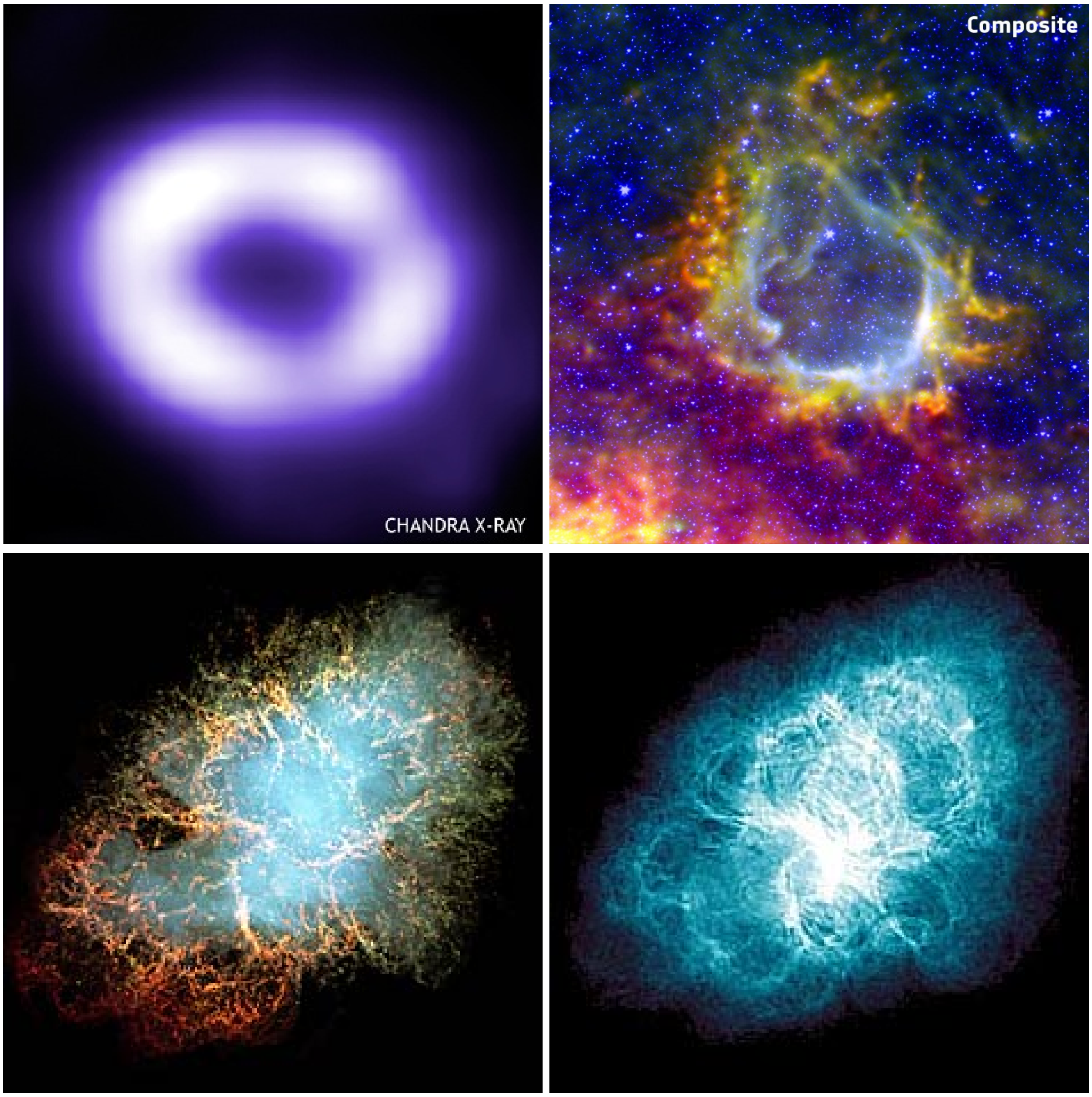

Figure 8.2: Linksboven: X-straling geassocieerd met de supernova explosie SN 1987A in beeld gebracht door Chandra. Rechtsboven: een ring van stof rond een actief stervormingsgebied, RCW 120, in onze eigen Melkweg. Het koudere stof zoals waargenomen met de Herschel telescoop is aangegeven in gele en rode kleuren en omgeeft een ring van warmer stof (witte kleur) dat werd gedetecteerd door de Spitzer satelliet. Linksonder: gas (blauw: warmer, rood: kouder) waargenomen in de Krabnevel na een supernova explosie. Rechtsonder: de radiostraling in de Krabnevel, die de structuur van het uitdeinende materiaal na de supernova explosie weergeeft.

Dit doctoraatsonderzoek heeft zich voornamelijk toegelegd op het bestuderen van de stofeigenschappen in melkwegstelsels in het nabije universum. Hoewel stof typisch maar een fractie uitmaakt van het medium dat zich tussen de sterren bevindt en het merendeel van de massa in gas zit, hebben stofdeeltjes een niet verwaarloosbare in-

Figure 8.3: Orion nevel (links) en Carina nevel (rechts), i.e. actieve stervormingsgebieden omhuld door gas en stof waar zich momenteel duizenden sterren aan het vormen zijn, onder de loep genomen door de Hubble Space Telescope.

vloed op een aantal fundamentele fysische processen in een melkwegstelsel. Stof is in de eerste plaats een belangrijke katalysator bij de vorming van moleculair waterstof, wat op zijn beurt het geboortemateriaal voor nieuwe sterren levert. Anderzijds heeft stof een onrechtstreekse invloed op de afkoeling en opwarming van dit gas, zodat het mee bepaalt of interstellair gas kan samentrekken en uiteindelijk nieuwe sterren kan vormen. Het is bovendien ook belangrijk om de verdeling en eigenschappen van het stof in een melkwegstelsel goed te begrijpen, aangezien een groot deel van de straling uitgezonden door sterren wordt geabsorbeerd door stofkorrels, die op hun beurt de straling opnieuw uitzenden op langere golflengten vanwege hun lagere temperatuur. Voornamelijk de geboorteplaatsen van jonge sterren zijn verhuld in een dichte wolk van stof, waardoor we enkel onrechtstreeks informatie over stervorming kunnen vergaren door het gereproduceerde licht van stof te analyseren.

In de volgende subsecties worden de specifieke vragen en resultaten besproken die in deze scriptie worden behandeld.

De emissie van geïoniseerd koolstof en stervorming

Interstellair stof speelt een belangrijke rol in de opwarming en afkoeling van gas in een sterrenstelsel. Om interstellair gas af te koelen zodat het kan samentrekken en sterren vormen, zenden zogenaamde koelingsatomen of -moleculen een deel van hun inwendige energie uit onder de vorm van lijnstraling. De helderste emissielijn in ster-

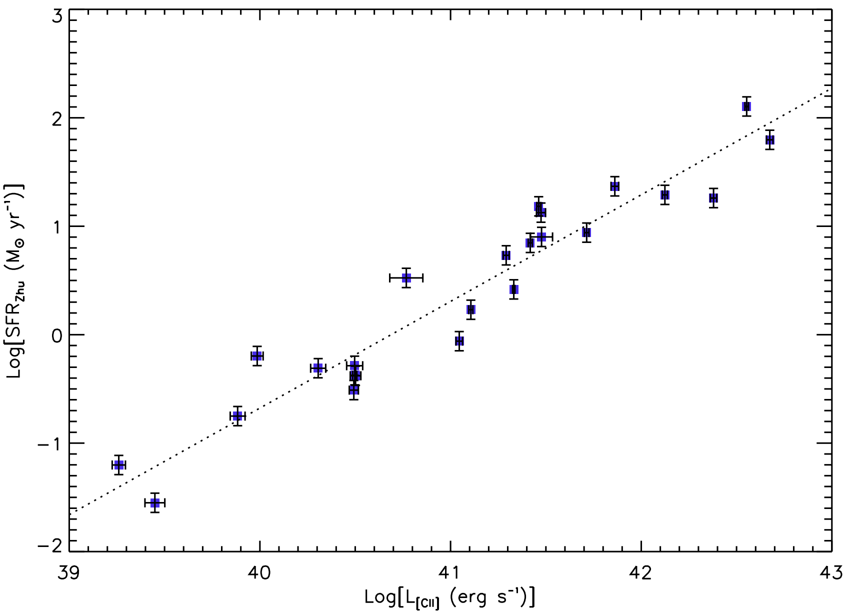

Figure 8.4: De correlatie tussen de lichtkracht uitgezonden in de koelingslijn van geïoniseerd koolstof en de recente stervormingsgraad van melkwegstelsels (bepaald uit hun UV en infrarode lichtkracht).

renstelsels met een actieve stervorming is de [CII] 157 μm lijn van geïoniseerd koolstof. Aangezien deze koeling typisch veel efficiënter gebeurt in gebieden van actieve stervorming, lijkt het op het eerste zicht logisch dat een direct verband zou bestaan tussen de emissie van de [CII] koelingslijn en de stervormingsgraad in een sterrenstelsel. Dit verband is echter geen perfecte 1-1 relatie aangezien de emissie van deze koelingslijn niet enkel afkomstig is van stervormingsgebieden in een sterrenstelsel. Bovendien hangt de graad van koeling ook af van de specifieke condities van het gas (bv. dichtheid, temperatuur, metalliciteit van het gas).

In Hoofdstuk 2 gaan we na in hoeverre de intensiteit van de [CII] koelingslijn kan gebruikt worden om de stervormingsactiviteit in een melkwegstelsel te peilen. Een dergelijk onmiddellijk verband zou immers van groot belang kunnen zijn om de stervormingsgraad in melkwegstelsels op hoge roodverschuiving in te schatten, waar deze heldere lijn een alternatief kan bieden om de stervormingsacitviteit te analyseren. Ondanks de dubbelzinnigheid over de juiste oorsprong van de lijnemissie in een sterrenstelsel en een koelingsefficiëntie die beïnvloed kan worden door de gascondities, vinden we een duidelijk rechtlijnig verband tussen de stervormingsgraad in een sterrenstelsel en deze welbepaalde lijnemissie (figuur 8.4). De sterrenstelsels die we gebruikten om deze relatie te testen zijn gekenmerkt door een normale stervormingsgraad. Of deze relatie al dan niet kan uitgebreid worden naar sterrenstelsels met meer extreme stervormingsgraden of juist een heel lage sterproductiviteit moet nog onder-

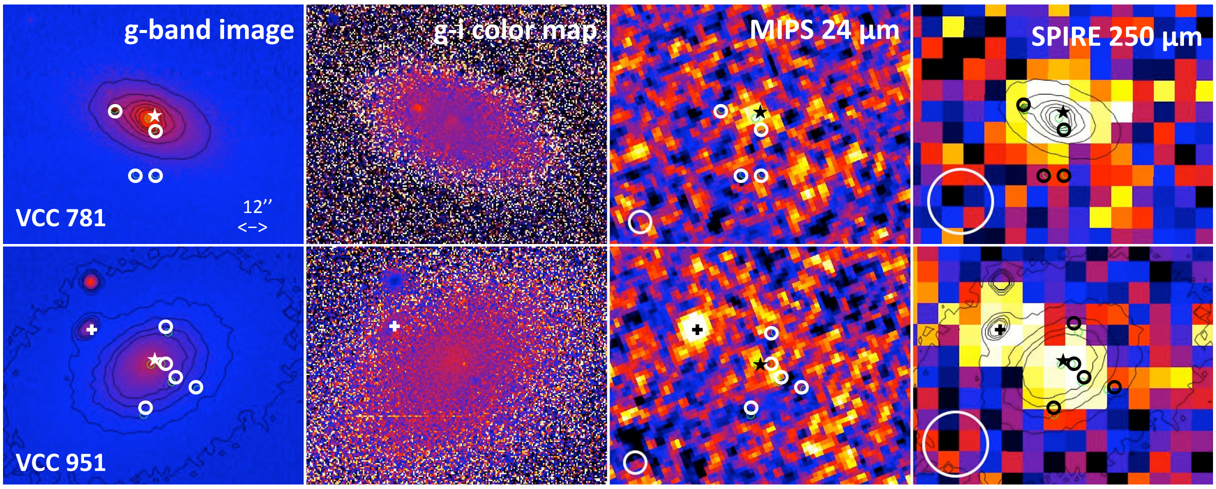

Figure 8.5: De detectie van de emissie door interstellair stof in twee elliptische dwerggalaxieën in de Virgo Cluster (VCC 781 en VCC 951). De meest rechtse panelen tonen de Herschel waarnemingen op 250 μm, die enkel te wijten kunnen zijn aan interstellair stof.

zocht worden eens een grotere collectie van sterrenstelsels met waarnemingen van deze specifieke lijnemissie voorhanden is (zoals nu met Herschel het geval is). Ook de bruikbaarheid van deze relatie om de stervormingsactiviteit in sterrenstelsels op hoge roodverschuiving in te schatten zal in de toekomst moeten geanalyseerd worden, aangezien de specifieke stervormingscondities in deze verafgelegen stelsels mogelijkerwijs niet corresponderen met de omstandigheden waarin sterren gevormd worden in ons huidig universum.

Emissie door stof in elliptische dwergstelsels

Een tweede onderdeel van deze doctoraatsthesis handelt over interstellair stof in elliptische dwergstelsels. Dit zijn de kleinste melkwegstelsels met een lagere massa en helderheid dan gewone sterrenstelsels, en ze komen veelvuldig voor in het universum, voornamelijk in clusters van melkwegstelsels. Elliptische dwerggalaxieën worden vaak aanschouwd als de laatste fase in de evolutie van een dwergmelkwegstelsel, wanneer het zijn volledige gasreservoir heeft opgebruikt voor de vorming van sterren en nog maar weinig bewijsmateriaal van zijn ooit woelige stervormingsgeschiedenis vertoont. Recent werden echter toch sporen van recente stervorming, substructuur en de aanwezigheid van interstellair gas teruggevonden in deze elliptische dwergstelsels, wat er op zou wijzen dat niet alle elliptische melkwegstelsels de overblijfselen zijn van een melkwegstelsel dat reeds lang geleden zijn gasreservoir uitputte bij de vorming van sterren. Als er inderdaad elliptische dwergstelsels zijn die momenteel nog steeds sterren vormen of slechts recentelijk hun stervormingsactiviteit hebben stopgezet, dan verwachten we ook een niet verwaarloosbare hoeveelheid stof in deze stelsels.

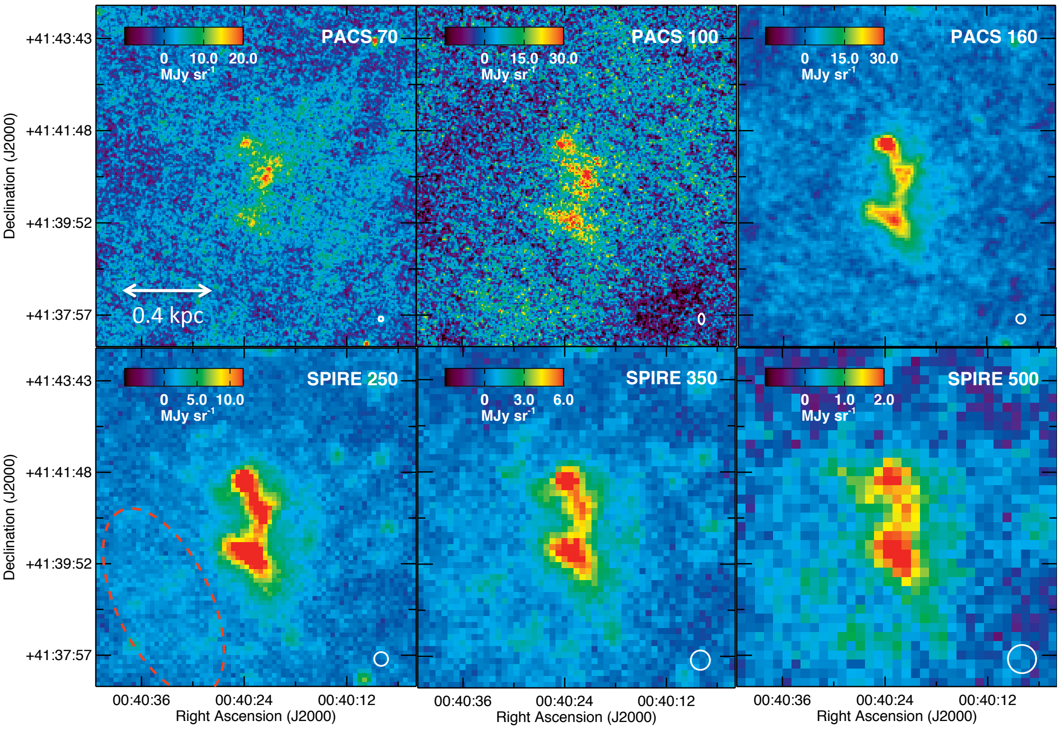

Figure 8.6: Waargenomen Herschel beelden van het elliptische dwergstelsel NGC 205. De verschillende beelden tonen waarnemingen genomen met het PACS instrument op 70, 100 en 160 μm (bovenste rij) en met het SPIRE instrument op 250, 350 en 500 μm (onderste rij).

Aan de hand van Herschel waarnemingen die het stof in de meest nabijgelegen cluster van sterrenstelsels, de Virgo Cluster, in kaart brengt, kunnen we de stofinhoud van dergelijke stelsels in een cluster analyseren. Reeds in de eerste set van Herschel test waarnemingen van het centrale deel van de Virgo cluster werd een grote hoeveelheid stof waargenomen in twee elliptische dwergstelsels (figuur 8.5). Uit de volledige data set van Herschel waarnemingen van de Virgo cluster kon de stofinhoud worden geanalyseerd in een verzameling van bijna 886 elliptische sterrenstelsels van lage massa. In onze studie hebben we vooral aandacht geschonken aan objecten die transitie eigenschappen vertonen karakteristiek voor een overgang van stervormende spiraalstelsels naar elliptische stelsels met weinig of geen stervorming. Uit een verzameling van 81 sterrenstelsels van deze soort, konden we voor 14 objecten de aanwezigheid van aanzienlijke hoeveelheden interstellair stof (10^{5-6} zonsmassa's) detecteren. Welk gravitationeel of omgevingsgerelateerd proces in een cluster de overgang bewerkstelligt tussen deze twee verschillende types van sterrenstelsels moet nog bepaald worden.

Gas en stof in het nabije dwergstelsel NGC 205

Het derde deel van mijn onderzoek sluit dicht aan bij het voorgaande, maar bestudeert nu in detail het interstellaire medium van een elliptisch dwergstelsel dat zich in de Lokale Groep (de groep van melkwegstelsels waartoe ook de Melkweg behoort) bevindt. Een groep van melkwegstelsels bestaat typisch uit een beperkt aantal grotere sterrenstelsels omgeven door een aantal kleinere satellietstelsels, terwijl een cluster van sterrenstelsels tot duizenden melkwegstelsels kan omvatten. De meest nabijgelegen elliptische dwergstelsels in de Lokale Groep zijn satellietstelsels van het Andromeda melkwegstelsel. Elk van deze dwergstelsels heeft te kampen met een tekort aan stof en gas. Wanneer we waarnemingen van de meest jonge sterren in deze stelsels analyseren, kunnen we de hoeveelheid sterren bepalen die geproduceerd werd tijdens de laatste stervormingsperiode en daaruit ook de hoeveelheid gas die nog zou moeten overblijven (stervorming is nooit 100% efficiënt). Als we directe waarnemingen van het gas vergelijken met het voorspelde reservoir aan gas, blijkt er veel te weinig gas aanwezig te zijn in deze elliptische dwergstelsels.

Tijdens mijn doctoraatsonderzoek analyseer ik de stofinhoud van het elliptisch dwergstelsel NGC 205 aan de hand van Herschel waarnemingen (figuur 8.6). Waarnemingen van de stofinhoud geven op een onrechtstreekse manier inzicht in de gasinhoud van een sterrenstelsel, wanneer we een realistische gas-stof verhouding in sterrenstelsels met een bepaalde metaalfractie in acht nemen. Anderzijds bestuderen we ook nieuwe directe waarnemingen van de gasinhoud in dit stelsel (Herschel, JCMT) aan de hand van de emissielijnen van verschillende moleculen en atomen, namelijk CO(3-2), [CII] en [OI]. Zowel de Herschel als de JCMT waarnemingen bevestigen het tekort aan gas en stof in NGC 205 vergeleken met de theoretische voorspellingen voor de huidige gasmassa. Om de reden voor deze ongelijkheid te achterhalen analyseren we verschillende mogelijkheden. We konden concluderen dat het verschil tussen de waarnemingen en voorspellingen te groot is om verklaard te kunnen worden door foute veronderstellingen in de theoretische modellen. Inderdaad, om waarnemingen en voorspellingen te verzoenen zou een onrealistische stervormingsefficiëntie van om en bij de 65% of de onnatuurlijke vorming van uitsluitend heel massieve sterren ingeroepen moeten worden. Als alternatieve verklaringen worden de terugkoppelende kracht van supernova explosies en/of omgevingsfactoren naar voor gebracht die een deel van de gas- en stofinhoud van het elliptische sterrenstelsel wegblazen.

De energiebalans van het stof in spiraalstelsels op hun kant

Een laatste aspect van dit onderzoek analyseert de eigenschappen van het interstellair stof in twee sterrenstelsels in het nabije universum die van op aarde onder een

Figure 8.7: Optische beelden van de twee spiraalgalaxieën op hun kant die worden bestudeerd in deze thesis: de Sombrero Galaxie M104 (links) en de Naaldgalaxie NGC 4565 (rechts).

hellingsgraad van om en bij de 90 graden gezien worden. Om de stofcomponent in deze sterrenstelsels op een zelf-consistente manier te bestuderen maken we gebruik van een code om de interactie van sterlicht met het aanwezige materiaal (gas, stof) in een sterrenstelsel te simuleren. In een eerste stap analyseren we het stof aan de hand van zijn absorptie efficiëntie in het optische golflengtegebied. Op basis van optische waarnemingen kunnen we de hoeveelheid sterlicht die werd weggenomen langsheen de gezichtslijn omzetten in een stofdichtheid met een welbepaalde verdeling. In een tweede stap laten we de stralingsoverdrachtcode de stofemissie berekenen en vergelijken we deze voorspelling met de waargenomen stofemissie in sterrenstelsels. In normale omstandigheden verwachten we dat dezelfde hoeveelheid energie die geabsorbeerd wordt door stofkorrels opnieuw zal worden uitgezonden als thermische straling. Een aantal recente studies suggereren echter een probleem: melkwegstelsels op hun kant zenden ongeveer drie keer zoveel straling uit in het verre infrarood als kan worden verwacht op basis van de hoeveelheid sterlicht die wordt geabsorbeerd.

Om de oorzaak voor deze onevenwichtige balans te achterhalen, hebben we een gelijkaardige, tweeledige studie van de stofcomponent uitgevoerd voor twee spiraalvormige melkwegstelsels in het nabije universum. We hebben hiervoor twee nabijgelegen spiraalstelsels op hun kant geselecteerd: de Sombrero Galaxie M104 en de Naaldgalaxie NGC 4565 (figuur 8.7). Voor beide stelsels beschikken we over een unieke dataset, bestaande uit waarnemingen van UV tot submillimeter golflengten. Onze gedetailleerde studie, gepresenteerd in de Hoofdstukken 5 en 6, bevestigt de eerder waargenomen trend dat ongeveer 3 keer meer licht wordt uitgezonden door stof dan er sterlicht werd geabsorbeerd door deze stofkorrels. Voor deze beide spiraalstelsels vermoeden we dat een klonterige distributie van het stof in deze melkwegstelsels waarschijnlijk de oorzaak is van de onevenwichtige balans tussen het geabsorbeerde sterlicht en de heruitgezonden stofemissie. De verdeling van stof in deze klonters van hoge dichtheid zorgt er immers voor dat deze samengeperste stofwolken nauwelijks invloed hebben op de absorptie van sterlicht en enkel bijdragen tot de stofemissie in een sterrenstelsel.

Bibliography

Ajhar, E. A., Lauer, T. R., Tonry, J. L., et al., 1997, AJ, 114, 626
Calibration of the Surface Brightness Fluctution Method for use with the Hubble Space Telescope.

Alonso-Herrero, A., Rieke, G. H., Rieke, M. J. et al., 2006, ApJ, 650, 835
Near-Infrared and Star-forming Properties of Local Luminous Infrared Galaxies.

Alton, P. B., Xilouris, E. M., Bianchi, S. et al., 2000, A&A, 356, 795
Dust properties of external galaxies; NGC 891 revisited.

Alton, P. B., Xilouris, E. M., Misiriotis, A. et al., 2004, A&A, 425, 109
The emissivity of dust grains in spiral galaxies.

Auld, R., Minchin, R. F., Davies, J. I. et al., 2004, MNRAS, 371, 1617
The Arecibo Galaxy Environment Survey: precursor observations of the NGC 628 group.

Auld, R., Smith, M. W. L., Bendo, G. et al., 2012, MNRAS, 420, 1882
Herschel observations of Cen A: stellar heating of two extragalactic dust clouds.

Baade, W., 1951, Publications of Michigan Observatory, 10, 7
Galaxies - Present Day Problems.

Baan, W. A. & Klöckner, H.-R., 2006, A&A, 449, 559
Radio properties of FIR-megamaser nuclei.

Babul, A. & Rees, M. J, 1992, MNRAS, 255, 346
On dwarf elliptical galaxies and the faint blue counts.

Baes, M. & Dejonghe, H, 2001, MNRAS, 326, 722
Radiative transfer in disc galaxies - I. A comparison of four methods to solve the transfer equation in plane-parallel geometry.

Baes, M. & Dejonghe, H, 2001, MNRAS, 326, 733
Radiative transfer in disc galaxies - II. The influence of scattering and geometry on the attenuation curve.

Baes, M. & Dejonghe, H, 2001, MNRAS, 335, 441
Kinematics of elliptical galaxies with a diffuse dust component - III. A Monte Carlo approach to include the effects of scattering.

Baes, M., Davies, J. I., Dejonghe, H. et al. 2003, MNRAS, 343, 1081
Radiative transfer in disc galaxies - III. The observed kinematics of dusty disc galaxies.

Baes, M., Dejonghe, H. & Davies, J. I., 2005, American Institute of Physics Conference Series, 27
Efficient radiative transfer modelling with SKIRT.

Baes, M., Stamatellos, D., Davies, J. I. et al. 2005, NewA, 10, 523
Radiative equilibrium in Monte Carlo radiative transfer using frequency distribution adjustment.

Baes, M., Fritz, J., Gadotti D. A. et al. 2010, A&A, 518, L39
Herschel-ATLAS: The dust energy balance in the edge-on spiral galaxy UGC 4754.

Baes, M., Clemens, M., Xilouris E. M. et al. 2010, A&A, 518, L53
The Herschel Virgo Cluster Survey . VI. The far-infrared view of M 87.

Baes, M., Verstappen, J., De Looze I. et al. 2011, ApJS, 196, 22
Efficient Three-dimensional NLTE Dust Radiative Transfer with SKIRT.

Bajaja, E., Dettmar, R.-J. & Hummel, E. et al. 2011, A&A, 202, 35
The large-scale radio continuum structure of the Sombrero galaxy (NGC 4594).

Bakes, E. L. O. & Tielens, A. G. G. M. 1994, ApJ, 427, 822
The photoelectric heating mechanism for very small graphitic grains and polycyclic aromatic hydrocarbons.

Bakes, E. L. O. & Tielens, A. G. G. M. 1994, ApJ, 499, 258
The Effects of Polycyclic Aromatic Hydrocarbons on the Chemistry of Photodissociation Regions.

Barazza, F. D., Binggeli, B. & Jerjen, H. 2002, A&A, 391, 823
More evidence for hidden spiral and bar features in bright early-type dwarf galaxies.

Bauschlicher, Jr., C. W., Peeters, E. & Allamandola, L. J., 2009, ApJ, 697, 311
The Infrared Spectra of Very Large Irregular Polycyclic Aromatic Hydrocarbons (PAHs): Observational Probes of Astronomical PAH Geometry, Size, and Charge.

Bavouzet, N., Dole, H. & Le Floc'h, E., 2008, A&A, 479, 83
Estimating the total infrared luminosity of galaxies up to z $\sim$ 2 from mid- and far-infrared observations.

Bekki, K., Couch, W. J. & Drinkwater, M. J., 2001, ApJL, 552, L105
Galaxy Threshing and the Formation of Ultracompact Dwarf Galaxies.

Bekki, K. & Couch, W. J., 2011, MNRAS, 415, 1783
Transformation from spirals into S0s with bulge growth in groups of galaxies.

Bendo, G. J., Buckalew, B. A. & Dale, D. A. et al., 2006, ApJ, 645, 134
Spitzer and JCMT Observations of the Active Galactic Nucleus in the Sombrero Galaxy (NGC 4594).

Bendo, G. J., Wilson, C. D. & Pohlen, M. et al., 2006, A&A, 518, L65
The Herschel Space Observatory view of dust in M81.

Bendo, G. J., Boselli, A. & Dariush, A. et al., 2012, MNRAS, 419, 1833
Investigations of dust heating in M81, M83 and NGC 2403 with the Herschel Space Observatory.

Bendo, G. J., Galliano, F. & Madden, S. C., 2012, MNRAS, in press
MIPS 24-160 micron photometry for the Herschel-SPIRE Local Galaxies Guaranteed Time Programs.

Bennett, C. L., Fixsen, D. J. & Hinshaw, G., 1994, ApJ, 434, 587
Morphology of the interstellar cooling lines detected by COBE.

Bergvall, N., Masegosa, J. & Östlin, G., 2000, A&A, 359, 41
LWS spectroscopy of the luminous blue compact galaxy Haro 11.

Bertin, E. & Arnouts, S., 1996, A&AS, 117, 393
SExtractor: Software for source extraction.

Bertola, F., Bressan, A., Burstein, D. et al. 1995, ApJ, 438, 680
Hubble Space Telescope far-ultraviolet imaging of M31, M32, and NGC 205.

Bettoni, D. & Galletta, G.,1994, A&A, 281, 1
Study of NGC 4442: A link between bars and boxy bulges.

Bianchi, S. 2007, A&A, 471, 765
The dust distribution in edge-on galaxies. Radiative transfer fits of V and K′-band images.

Bianchi, S. 2008, A&A, 490, 461
Dust extinction and emission in a clumpy galactic disk. An application of the radiative transfer code TRADING.

Bica, E., Alloin, D. & Schmidt, A. A., 1990, A&A, 228, 23
Star formation history and chemical enrichment in the nuclear regions of M31 and its dwarf companions M32 and NGC205.

Binggeli, B., Sandage, A. & Tammann, G. A., 1985, AJ, 90, 1681
Studies of the Virgo Cluster. II - A catalog of 2096 galaxies in the Virgo Cluster area.

Binney, J., Gerhard, O. E., Stark, A. A. et al. 1991, MNRAS, 252, 210
Understanding the kinematics of Galactic centre gas.

Black, J. H. 1994, Astronomical Society of the Pacific Conference Series, 58, 355
Energy Budgets of Diffuse Clouds.

Block, D. L. Bournaud, F., Combes, F. et al. 2006, Nature, 443, 832
An almost head-on collision as the origin of two off-centre rings in the Andromeda galaxy.

Böhringer, H., Briel, U. G., Schwarz, R. A. et al. 1994, Nature, 368, 828
The structure of the Virgo cluster of galaxies from Rosat X-ray images.

Bolatto, A. D., Leroy, A. K., Rosolowsky, E. et al. 2008, ApJ, 686, 948
The Resolved Properties of Extragalactic Giant Molecular Clouds.

Boquien, M., Bendo, G., Calzetti, D. et al. 2010, ApJ, 713, 626
Total Infrared Luminosity Estimation of Resolved and Unresolved Galaxies.

Boquien, M., Lisenfeld, U., Duc, P.-A. et al. 2011, A&A, 533, A19
Studying the spatially resolved Schmidt-Kennicutt law in interacting galaxies: the case of Arp 158.

Boquien, M., Calzetti, D., Combes, F. et al. 2011, AJ, 142, 111
Dust Heating Sources in Galaxies: The Case of M33 (HERM33ES).

Boquien, M., Buat, V., Boselli, A. et al. 2011, A&A, 539, A145
The IRX-β relation on subgalactic scales in star-forming galaxies of the Herschel Reference Survey.

Boselli, A., Gavazzi, G., Donas, J. et al., 2001, AJ, 121, 753
1.65 Micron (H Band) Surface Photometry of Galaxies. VI. The History of Star Formation in Normal Late-Type Galaxies.

Boselli, A., Lequeux, J., Gavazzi, G. et al., 2002, A&A, 384, 33
Molecular gas in normal late-type galaxies.

Boselli, A., Gavazzi, G., Lequeux, J. et al., 2002, A&A, 385, 454
[CII] at 158 μm as a star formation tracer in late-type galaxies.

Boselli, A., Lequeux, J. & Gavazzi, G., 2004, A&A, 428, 409
Mid-IR emission of galaxies in the Virgo cluster and in the Coma supercluster. IV. The nature of the dust heating sources.

Boselli, A., Boissier, S., Cortese, L. et al. 2008, ApJ, 674, 742
The Origin of Dwarf Ellipticals in the Virgo Cluster.

Boselli, A., Boissier, S., Cortese, L. et al. 2008, A&A, 489, 1015
The origin of the $< \mu_e >$*-*M_B *and Kormendy relations in dwarf elliptical galaxies.*

Boselli, A., Boissier, S., Cortese, L. et al. 2009, ApJ, 706, 1527
High-mass Star Formation in Normal Late-type Galaxies: Observational Constraints to the Initial Mass Function.

Boselli, A. & Gavazzi, G. 2009, A&A, 508, 201
The HI properties of galaxies in the Coma I cloud revisited.

Boselli, A., Eales, S., Cortese, L. et al. 2010, PASP, 122, 261
The Herschel Reference Survey.

Boselli, A., Ciesla, L., Buat, V. et al. 2010, A&A, 518, L61
FIR colours and SEDs of nearby galaxies observed with Herschel.

Boselli, A., Boissier, S., Heinis, S. et al. 2011, A&A, 528, A107
The GALEX Ultraviolet Virgo Cluster Survey (GUViCS). I. The UV luminosity function of the central 12 sq. deg.

Boselli, A., Ciesla, L., Cortese, L. et al. 2012, A&A, 540, A54
FIR colours of nearby late-type galaxies in the Herschel Reference Survey.

Bot, C., Ysard, N., Paradis, D. et al. 2010, A&A, 523, A20
Submillimeter to centimeter excess emission from the Magellanic Clouds. II. On the nature of the excess.

Bot, C., Rubio, M., Boulanger, F. et al. 2010, A&A, 524, A52
LABOCA observations of giant molecular clouds in the southwest region of the Small Magellanic Cloud.

Bouchard, A., Jerjen, H., Da Costa, G. S. et al. 2005, AJ, 130, 2058
Detection of Neutral Hydrogen in Early-Type Dwarf Galaxies of the Sculptor Group.

Boylan-Kolchin, M., Bullock, J. S. & Kaplinghat, M., 2012, MNRAS, in press
The Milky Way's bright satellites as an apparent failure of LCDM.

Brauher, J. R., Dale, D. A. & Helou, G. 2012, ApJS, 178, 280
A Compendium of Far-Infrared Line and Continuum Emission for 227 Galaxies Observed by the Infrared Space Observatory.

Brosch, N., Almoznino, E. & Heller, A. B. 2004, MNRAS, 349, 357
Are interactions the primary triggers of star formation in dwarf galaxies?

Bruzual, A. G., Magris, G. & Calvet, N. 1988, ApJ, 333, 673
A model for the effects of dust on the spectra of disk galaxies. I - General treatment.

Buat, V. 1992, A&A, 264, 444
Global recent star formation in normal galaxies from a multi-wavelength study - Comparison with their gas content.

Buat, V. & Xu, C., 1996, A&A, 306, 61
Star formation and dust extinction in disk galaxies. Comparison between the UV non-ionizing and the FIR emissions.

Buat, V., Iglesias-Páramo, J., Seibert, M. et al. 2005, ApJL, 619, L51
Dust Attenuation in the Nearby Universe: A Comparison between Galaxies Selected in the Ultraviolet and in the Far-Infrared.

Buat, V., Giovannoli, E., Burgarella, D. et al. 2010, MNRAS, 409, L1
Measures of star formation rates from infrared (Herschel) and UV (GALEX) emissions of galaxies in the HerMES fields.

Buckle, J. V., Hills, R. E. & Smith, H. et al. 2009, MNRAS, 399, 1026
HARP/ACSIS: a submillimetre spectral imaging system on the James Clerk Maxwell Telescope.

Burke, J. R. & Hollenbach, D. J, 1983, ApJ, 265, 223
The gas-grain interaction in the interstellar medium - Thermal accommodation and trapping.

Burkert, A. & Tremaine, S., 2010, ApJ, 720, 516
A Correlation Between Central Supermassive Black Holes and the Globular Cluster Systems of Early-type Galaxies.

Burkhead, M. S., 1996, AJ, 91, 777
A photometric study of M104.

Burton, M. G., Hollenbach, D. J. & Tielens, A. G. G. M., 1990, ApJ, 365, 620
Line emission from clumpy photodissociation regions.

Buyle, P., De Rijcke, S., Michielsen, D. et al. 2005, MNRAS, 360, 853
The HI content of Fornax dwarf elliptical galaxies: FCC032 and FCC336.

Calzetti, D., Kennicutt, Jr., H. C., Bianchi, L. et al., 2005, ApJ, 633, 871
Star Formation in NGC 5194 (M51a): The Panchromatic View from GALEX to Spitzer.

Calzetti, D., Kennicutt, R. C., Engelbracht C. W. et al., 2007, ApJ, 666, 870
The Calibration of Mid-Infrared Star Formation Rate Indicators.

Calzetti, D., Wu, S.-Y. & Hong, S. et al., 2010, ApJ, 714, 1256
The Calibration of Monochromatic Far-Infrared Star Formation Rate Indicators.

Cardelli, J. A., Clayton, G. C. & Mathis, J. S., 1989, ApJ, 345, 245
The relationship between infrared, optical, and ultraviolet extinction.

Carral, P., Hollenbach, D. J., Lord, S. D. et al., 1994, ApJ, 423, 223
The interstellar medium in the starburst regions of NGC 253 and NGC 3256.

Chabrier, G., 2003, PASP, 115, 763
Galactic Stellar and Substellar Initial Mass Function.

Chapin, E. L., Ade, P. A. R., Bock, J. J., et al. 2008, ApJ, 681, 428
The Balloon-borne Large Aperture Submillimeter Telescope (BLAST) 2005: A 4 deg^2 *Galactic Plane Survey in Vulpecula (l = 59°).*

Charlot, S. & Fall, S. M., 2000, ApJ, 539, 718
A Simple Model for the Absorption of Starlight by Dust in Galaxies.

Choi, P. I., Guhathakurta, P. & Johnston, K. V. 2002, AJ, 124, 310
Tidal Interaction of M32 and NGC 205 with M31: Surface Photometry and Numerical Simulations.

Christian, C. A., Bond, H. E., Frattare, L. M. et al. 2003, Bulletin of the American Astronomical Society, 35, 116
Spectacular Image of the Sombrero Galaxy: Hubble Heritage Celebrates their Fifth Year Anniversary.

Ciesla, L., Boselli, A., Smith, M W. L. et al., 2012, A&A, in press
Submillimetre Photometry of 323 Nearby Galaxies from the Herschel Reference Survey.

Clemens, M. S., Jones, A. P., Bressan, A. et al., 2010, A&A, 518, L50
The Herschel Virgo Cluster Survey. III. A constraint on dust grain lifetime in early-type galaxies.

Clements, E. D., 1983, MNRAS, 204, 811
Optical positions of Seyfert galaxies. - II.

Cockcroft, R., Harris, W. E., Wehner, E. M. H. et al., 2009, AJ, 138, 758
Further Definition of the Mass-Metallicity Relation in Globular Cluster Systems Around Brightest Cluster Galaxies.

Colbert, J. W., Malkan, M. A., Clegg, P. E. et al., 1999, ApJ, 511, 721
ISO LWS Spectroscopy of M82: A Unified Evolutionary Model.

Combes, F. & Sanders, R. H., 1981, A&A, 164, 173
Formation and properties of persisting stellar bars.

Compiègne, M., Verstraete, L., Jones, A. et al., 2011, A&A, 525, A103
The global dust SED: tracing the nature and evolution of dust with DustEM.

Conselice, C. J., O'Neil, K., Gallagher, J. S. et al., 2003, ApJ, 591, 167
Galaxy Populations and Evolution in Clusters. IV. Deep HI Observations of Dwarf Elliptical Galaxies in the Virgo Cluster.

Contursi, A., Kaufman, M. J. & Helou, G. et al., 2002, AJ, 124, 751
ISO LWS Observations of the Two Nearby Spiral Galaxies NGC 6946 and NGC 1313.

Cormier, D., Madden, S. C., Hony, S. et al., 2010, A&A, 518, L57
The effects of star formation on the low-metallicity ISM: NGC 4214 mapped with Herschel/PACS spectroscopy.

Cortese, L., Gavazzi, G., Boselli, A. et al., 2004, A&A, 416, 119
An extragalactic HII region in the Virgo cluster.

Cortese, L., Boselli, A., Franzetti, P. et al., 2008, MNRAS, 386, 1157
Ultraviolet dust attenuation in star-forming galaxies - II. Calibrating the A(UV) versus L_{TIR}/L_{UV} *relation.*

Cortese, L., Davies, J. I., Pohlen, M. et al., 2010, A&A, 518, L49
The Herschel Virgo Cluster Survey . II. Truncated dust disks in HI-deficient spirals.

Cortese, L., Bendo G. J., Boselli, A. et al., 2010, A&A, 518, L63
Herschel-SPIRE observations of the disturbed galaxy NGC 4438.

Cortese, L., Ciesla, L., Boselli, A. et al., 2012, A&A, 540, A52
The dust scaling relations of the Herschel Reference Survey.

Cortese, L., Boissier, S., Boselli, A. et al., 2012, A&A, submitted
The GALEX view of the Herschel Reference Survey: Ultraviolet structural properties of nearby galaxies.

Crawford, M. K., Genzel, R., Townes, C. H. et al., 1985, ApJ, 291, 755
Far-infrared spectroscopy of galaxies - The 158 micron C(+) line and the energy balance of molecular clouds.

Crocker, D. A., Baugus, P. D. & Buta, R., 1996, ApJS, 105, 353
The Distribution and Properties of HII Regions in Early-to-Intermediate Hubble Type Ringed Galaxies.

Currie, M. J., Draper, P. W., Berry, D. S. et al., 2008, Astronomical Society of the Pacific Conference Series, 394, 650
Starlink Software Developments.

Daddi, E., Elbaz, D. & Walter, F. et al., 2010, ApJL, 714, L118
Different Star Formation Laws for Disks Versus Starbursts at Low and High Redshifts.

Dale, D. A. & Helou, G., 2002, ApJ, 576, 159
The Infrared Spectral Energy Distribution of Normal Star-forming Galaxies: Calibration at Far-Infrared and Submillimeter Wavelengths.

Dale, D. A., Gil de Paz, A., Gordon, K. D. et al., 2007, ApJ, 655, 863
An Ultraviolet-to-Radio Broadband Spectral Atlas of Nearby Galaxies.

Dale, D. A., Cohen, S. A., Johnson, L. C. et al., 2009, ApJ, 703, 517
The Spitzer Local Volume Legacy: Survey Description and Infrared Photometry.

Dale, D. A., Aniano, G., Engelbracht, C. W., et al. 2012, ApJ, 745, 95
Herschel Far-infrared and Submillimeter Photometry for the KINGFISH Sample of nearby Galaxies.

Dalgarno, A. & McCray, R. A., 1972, ARA&A, 10, 375
Heating and Ionization of HI Regions.

Dasyra, K. M., Xilouris, E. M., Misiriotis, A. et al. 2005, A&A, 437, 447
Is the Galactic submillimeter dust emissivity underestimated?

Davidge, T. J. 2003, ApJ, 597, 289
The Asymptotic Giant Branch of NGC 205: The Characteristics of Carbon Stars and M Giants Identified from JHK′ Images.

Davidge, T. J. 2005, AJ, 130, 2087
The Evolved Stellar Content of NGC 147, NGC 185, and NGC 205.

Davies, J. I., Baes, M., Bendo, G. J. et al., 2010, A&A, 518, L48
The Herschel Virgo Cluster Survey. I. Luminosity function.

Davies, J. I., Wilson, C. D., Auld, R. . et al., 2010, MNRAS, 409, 102
On the origin of M81 group extended dust emission.

Davies, J. I., Bianchi, S., Cortese, L. et al., 2012, MNRAS, 419, 3505
The Herschel Virgo Cluster Survey - VIII. The Bright Galaxy Sample.

Decarli, R., Gavazzi, G., Arosio, I. et al., 2007, MNRAS, 381, 136
The census of nuclear activity of late-type galaxies in the Virgo cluster.

de Graauw, T., Helmich, F. P., Phillips, T. G. et al., 2010, A&A, 518, L6
The Herschel-Heterodyne Instrument for the Far-Infrared (HIFI).

Dekel, A. & Silk, J., 1986, ApJ, 303, 39
The origin of dwarf galaxies, cold dark matter, and biased galaxy formation.

De Looze, I., Baes, M., Zibetti, S. et al. 2010, A&A, 518, L54
The Herschel Virgo Cluster Survey . VII. Dust in cluster dwarf elliptical galaxies.

De Looze, I., Baes, M., Bendo, G. J. et al. 2011, MNRAS, 416, 2712
The reliability of [C II] as an indicator of the star formation rate.

De Looze, I., Baes, M., Fritz, J. et al. 2012, MNRAS, 419, 895
Panchromatic radiative transfer modelling of stars and dust in the Sombrero galaxy.

De Looze, I., Baes, M., Parkin, T. J. et al. 2012, MNRAS, in press
Herschel and JCMT observations of the early-type dwarf galaxy NGC 205.

Demers, S., Battinelli, P. & Letarte, B., 2003, AJ, 125, 3037
Carbon Star Survey in the Local Group. VI. The Dwarf Spheroidal Galaxy NGC 205.

Deo, R. P., Crenshaw, D. M., Kraemer, S. B., et al. 2007, ApJ, 671, 124
Spitzer IRS Observations of Seyfert 1.8 and 1.9 Galaxies: A Comparison with Seyfert 1 and Seyfert 2.

De Rijcke, S., Dejonghe, H., Zeilinger, W. W. et al. 2003, A&A, 400, 119
Embedded disks in Fornax dwarf elliptical galaxies.

De Rijcke, S., Dejonghe, H., Zeilinger, W. W. et al. 2004, A&A, 426, 53
Dwarf elliptical galaxies with kinematically decoupled cores.

De Rijcke, S., Prugniel, P., Simien, F. et al. 2006, MNRAS, 369, 1321
The internal dynamics of the Local Group dwarf elliptical galaxies NGC 147, 185 and 205.

Desert, F.-X., Boulanger, F. & Puget, J. L., 1990, A&A, 237, 215
Interstellar dust models for extinction and emission.

Dettmar, R.-J. & Wielebinski, R., 1986, A&A, 167, L21
The minor axis profiles of galaxies with box- and peanut-shaped bulges.

de Vaucouleurs, G., de Vaucouleurs, A., Corwin, Jr., H. G. et al., 1991, Springer, New York, NY (USA), 1991, 2091 p., ISBN 0-387-97552-7
Third Reference Catalogue of Bright Galaxies. Volume I: Explanations and references. Volume II: Data for galaxies between 0^h and 12^h. Volume III: Data for galaxies between 12^h and 24^h.

Devereux, N. A. & Young, J. S., 1990, ApJL, 350, L25
The origin of the far-infrared luminosity from spiral galaxies.

Devereux, N. A., Jacoby, G. & Ciardullo, R., 1995, AJ, 110, 1115
Hα and Far-Infrared Emission Within the Early Type Spiral Galaxy M81.

Devost, D., Roy, J.-R. & Drissen, L. 1997, ApJ, 482, 765
The Ionized Gas in the Aftermath of a Starburst: The Case of NGC 1569.

De Young, D. S. & Heckman, T. M. 1994, ApJ, 431, 598
The effect of central starbursts on the interstellar medium of dwarf galaxies.

di Bartolomeo, A., Barbaro, G. & Perinotto, M., 1995, MNRAS, 277, 1279
Internal extinction in spiral disc galaxies.

di Serego Alighieri, S., Gavazzi, G., Giovanardi, C. et al., 2007, A&A, 474, 851
The HI content of early-type galaxies from the ALFALFA survey. I. Catalogued HI sources in the Virgo cluster.

D'Onofrio, M., Capaccioli, M., Merluzzi, P. et al., 1999, A&AS, 134, 437
Structure and kinematics of the peculiar galaxy NGC 128.

Draine, B. T. 1978, ApJS, 36, 595
Photoelectric heating of interstellar gas.

Draine, B. T. & Lee, H. M.,1984, ApJ, 285, 89
Optical properties of interstellar graphite and silicate grains.

Draine, B. T. & Li, A.,2001, ApJ, 551, 807
Infrared Emission from Interstellar Dust. I. Stochastic Heating of Small Grains.

Draine, B. T. & Li, A.,2007, ApJ, 657, 810
Infrared Emission from Interstellar Dust. IV. The Silicate-Graphite-PAH Model in the Post-Spitzer Era.

Draine, B. T., 2011, Princeton University Press, 2011. ISBN: 978-0-691-12214-4
Physics of the Interstellar and Intergalactic Medium.

Dumke, M., Krause, M. & Wielebinski, R., 2004, A&A, 414, 475
Cold dust in a selected sample of nearby galaxies. I. The interacting galaxy NGC 4631.

Eales, S. A., Dunne, L., Clements, D. et al., 2010, PASP, 122, 499
The Herschel ATLAS.

Eales, S. A., Smith, M. W. L., Wilson, C. D. et al. 2010, A&A, 518, L62
Mapping the interstellar medium in galaxies with Herschel/SPIRE.

Emsellem, E.,1995, A&A, 303, 673
The Sombrero galaxy. I. Modelling the dust content.

Emsellem, E. & Ferruit, P., 2000, A&A, 357, 111
The Sombrero galaxy. III. Ionised gas and dust in the central 200 pc: a nuclear bar?

Engargiola, G. & Harper, D. A., 1992, ApJ, 394, 104
The structure of NGC 4565 at 100, 160, and 200 microns - Continuum dust emission in a quiescent SB galaxy.

Engelbracht, C. W., Blaylock, M., Su, K. Y. L. et al., 2007, PASP, 119, 994
Absolute Calibration and Characterization of the Multiband Imaging Photometer for Spitzer. I. The Stellar Calibrator Sample and the 24 µm Calibration.

Faber, S. M. & Gallagher, J. S., 1976, ApJ, 204, 365
HI in early-type galaxies. II - Mass loss and galactic winds.

Fadda, D., Biviano, A. & Edwards, L. O. V., 2010, AAS, 42, #215, 436.13
Spitzer Images of the Virgo Cluster.

Falcón-Barroso, J., Peletier, R. F., Emsellem, E. et al., 2004, MNRAS, 350, 35
Formation and evolution of S0 galaxies: a SAURON case study of NGC 7332.

Fazio, G. G., Hora, J. L., Allen, L. E., et al. 2004, ApJS, 154, 10
The Infrared Array Camera (IRAC) for the Spitzer Space Telescope.

Ferrarese, L., Côté, P., Jordán, A. et al., 2006, ApJS, 164, 334
The ACS Virgo Cluster Survey. VI. Isophotal Analysis and the Structure of Early-Type Galaxies.

Fich, M. & Hodge, P., 1991, ApJ, 374, L17
Continuum emission at 1 millimeter from the elliptical galaxy NGC 205.

Field, G. B., Goldsmith, D. W. & Habing, H. J.,1969, ApJL, 155, L149
Cosmic-Ray Heating of the Interstellar Gas.

Fioc, M. & Rocca-Volmerange, B.,1997, A&A, 326, 950
PEGASE: a UV to NIR spectral evolution model of galaxies. Application to the calibration of bright galaxy counts.

Fisher, D., Illingworth, G. & Franx, M.,1994, AJ, 107, 160
The dynamics and structure of the S0 galaxy NGC 7332.

Flannery, B. P., Roberge, W. & Rybicki, G. B.,1980, ApJ, 236, 598
The penetration of diffuse ultraviolet radiation into interstellar clouds.

Ford, H. C., Hui, X., Ciardullo, R. et al.,1996, ApJ, 458, 455
The Stellar Halo of M104. I. A Survey for Planetary Nebulae and the Planetary Nebula Luminosity Function Distance.

Forgan, D., 2009, Lectures, Institute for Astronomy, Royal Observatory, Edinburgh
An introduction to Monte Carlo radiative transfer.

Foyle, K., Wilson, C. D., Mentuch, E. et al., 2012, MNRAS, 421, 2917
The dust and gas properties of M83.

Fritz, J., Poggianti, B. M., Bettoni, D. et al., 2007, A&A, 470, 137
A spectrophotometric model applied to cluster galaxies: the WINGS dataset.

Gadotti, D. A., Baes, M. & Falony, S., 2010, MNRAS, 403, 2053
Radiative transfer in disc galaxies - IV. The effects of dust attenuation on bulge and disc structural parameters.

Galametz, M., Madden, S., Galliano, F. et al., 2009, A&A, 508, 645
Probing the dust properties of galaxies up to submillimetre wavelengths. I. The spectral energy distribution of dwarf galaxies using LABOCA.

Galametz, M., Madden, S., Galliano, F. et al., 2010, A&A, 518, 55
Herschel photometric observations of the nearby low metallicity irregular galaxy NGC 6822.

Galametz, M., Madden, S., Galliano, F. et al., 2011, A&A, 532, 56
Probing the dust properties of galaxies up to submillimetre wavelengths. II. Dust-to-gas mass ratio trends with metallicity and the submm excess in dwarf galaxies.

Gallagher, III, J. S., Hunter, D. A. & Mould, J., 1984, ApJ, 281, 63
A probable supernova remnant in the dwarf elliptical galaxy NGC 185.

Galliano, F., Madden, S. C., Jones, A. P. et al., 2003, A&A, 407, 159
ISM properties in low-metallicity environments. II. The dust spectral energy distribution of NGC 1569.

Galliano, F., Madden, S. C., Jones, A. P. et al., 2005, A&A, 434, 867
ISM properties in low-metallicity environments. III. The spectral energy distributions of II Zw 40, He 2-10 and NGC 1140.

Galliano, F., Dwek, E. & Chanial, P., 2008, ApJ, 672, 214
Stellar Evolutionary Effects on the Abundances of Polycyclic Aromatic Hydrocarbons and Supernova-Condensed Dust in Galaxies.

Galliano, F., Hony, S. & Bernard, J.-P. et al., 2011, A&A, 536, 88

Non-standard grain properties, dark gas reservoir, and extended submillimeter excess, probed by Herschel in the Large Magellanic Cloud.

Gao, Y., Wang, Q. D., Appleton, P. N. et al., 2003, ApJ, 596, 171
Nonnuclear Hyper/Ultraluminous X-Ray Sources in the Starbursting Cartwheel Ring Galaxy.

Garcia-Burillo, S. & Guelin, M., 1995, A&A, 299, 657
The distorted kinematics of molecular gas in the center of NGC 891.

Garcia-Burillo, S., Guelin, M. & Neininger, N., 1997, A&A, 319, 450
A high-resolution ^{12}*CO(1-0) study of the nucleus of NGC 5907. Observations and modelling.*

Gavazzi, G., Boselli, A., Scodeggio, M. et al., 1999, MNRAS, 304, 595
The 3D structure of the Virgo cluster from H-band Fundamental Plane and Tully-Fisher distance determinations.

Gavazzi, G., Bonfanti, C., Sanvito, G. et al., 2002, ApJ, 576, 135
Spectrophotometry of Galaxies in the Virgo Cluster. I. The Star Formation History.

Gavazzi, G., Boselli, A., Donati, A. et al., 2003, A&A, 400, 451
Introducing GOLDMine: A new galaxy database on the WEB.

Geha, M., Guhathakurta, P. & van der Marel, R. P., 2003, AJ, 126, 1794
Internal Dynamics, Structure, and Formation of Dwarf Elliptical Galaxies. II. Rotating versus Nonrotating Dwarfs.

Geha, M., Guhathakurta, P., Rich, R. M. et al., 2006, AJ, 131, 332
Local Group Dwarf Elliptical Galaxies. I. Mapping the Dynamics of NGC 205 Beyond the Tidal Radius.

Genzel, R. & Cesarsky, C. J., 2000, ARA&A, 38, 761
Extragalactic Results from the Infrared Space Observatory.

Giovanelli, R., Haynes, M. P., Kent, B. R. et al. 2005, AJ, 130, 2613
The Arecibo Legacy Fast ALFA Survey. II. Results of Precursor Observations.

Giovanelli, R., Haynes, M. P., Kent, B. R. et al. 2007, AJ, 133, 2569
The Arecibo Legacy Fast ALFA Survey. III. HI Source Catalog of the Northern Virgo Cluster Region.

Gomez, H. L., Baes, M. & Cortese, L. et al., 2010, A&A, 518, L45
The dust morphology of the elliptical Galaxy M 86 with SPIRE.

Gordon, K. D., Misselt, K. A., Witt, A. N. et al., 2001, ApJ, 551, 269
The DIRTY Model. I. Monte Carlo Radiative Transfer through Dust.

Gordon, K. D., Rieke, G. H., Engelbracht, C. W. et al., 2005, PASP, 117, 503
Reduction Algorithms for the Multiband Imaging Photometer for Spitzer.

Gordon, K. D., Bailin, J., Engelbracht, C. W. et al., 2006, ApJ, 638, 87
Spitzer MIPS Infrared Imaging of M31: Further Evidence for a Spiral-Ring Composite Structure.

Gordon, K. D., Engelbracht, C. W., Fadda, D. et al., 2007, PASP, 119, 1019
Absolute Calibration and Characterization of the Multiband Imaging Photometer for Spitzer. II. 70 μm Imaging.

Gordon, K. D., Engelbracht, C. W., Rieke, G. H. et al., 2008, ApJ, 682, 336
The Behavior of the Aromatic Features in M101 HII Regions: Evidence for Dust Processing.

Gordon, K. D., Galliano, F., Hony, S. et al., 2010, A&A, 518, 89
Determining dust temperatures and masses in the Herschel era: The importance of observations longward of 200 micron.

Graciá-Carpio, J., Sturm, E., Hailey-Dunsheath, S. et al., 2011, ApJ, 728, L7
Far-infrared Line Deficits in Galaxies with Extreme L_{FIR}/M_{H_2} *Ratios.*

Graham, A. W. & Guzmán, R., 2003, AJ, 125, 2936
HST Photometry of Dwarf Elliptical Galaxies in Coma, and an Explanation for the Alleged Structural Dichotomy between Dwarf and Bright Elliptical Galaxies.

Graham, A. W., Erwin, P., Trujillo, I. et al., 2003, AJ, 125, 2951
A New Empirical Model for the Structural Analysis of Early-Type Galaxies, and A Critical Review of the Nuker Model.

Griffin, M. J., Abergel, A., Abreu, A. et al., 2010, A&A, 518, L3
The Herschel-SPIRE instrument and its in-flight performance.

Grossi, M., Hunt, L. K., Madden, S. et al., 2010, A&A, 518, L52
The Herschel Virgo Cluster Survey. V. Star-forming dwarf galaxies - dust in metal-poor environments.

Groves, 2004, PhD thesis
Dust in Photoionized Nebulae.

Groves, B., Dopita, M. A., Sutherland, R. S. et al., 2008, ApJS, 176, 438
Modeling the Pan-Spectral Energy Distribution of Starburst Galaxies. IV. The Controlling Parameters of the Starburst SED.

Gry, C., Swinyard, B., Harwood, A. et al., 2003, Series edited by T.G. Mueller, J.A.D.L. Blommaert, and P. Garcia-Lario. ESA SP-1262, ISBN No. 92-9092-968-5, ISSN No. 0379-6566. European Space Agency, 2003
The ISO Handbook, Volume III - LWS - The Long Wavelength Spectrometer.

Guelin, M., Zylka, R., Mezger, P. G. et al., 1993, A&A, 279, L37
1.3 MM emission in the disk of NGC 891: Evidence of cold dust.

Guelin, M., Zylka, R., Mezger, P. G. et al., 1995, A&A, 298, L29
Cold dust emission from spiral arms of M 51.

Gunn, J. E. & Gott, III, J. R., 1972, ApJ, 176, 1
On the Infall of Matter Into Clusters of Galaxies and Some Effects on Their Evolution.

Haas, M., 1998, A&A, 337, L1
Very cold dust in the peculiar dwarf elliptical galaxy NGC 205.

Habing, H. J., 1968, Bull. Astron. Inst. Netherlands, 19, 421
The interstellar radiation density between 912 A and 2400 A.

Hailey-Dunsheath, S., Nikola, T., Stacey, G. J. et al., 2010, ApJ, 714, L162
Detection of the 158 μm [C II] Transition at z = 1.3: Evidence for a Galaxy-wide Starburst.

Hamabe, M., Kodaira, K., Okamura, S. et al., 1980, PASJ, 32, 197
Surface Photometry of Edge-On Galaxies - Part Two - NGC4565.

Harris, W. E., Spitler, L. R., Forbes, D. A. et al., 2010, MNRAS, 401, 1965
Diamonds on the Hat: globular clusters in the Sombrero galaxy (M104).

Haynes, M. P., Giovanelli, R., Martin, A. M. et al., 2011, AJ, 142, 170
The Arecibo Legacy Fast ALFA Survey: The α.40 HI Source Catalog, Its Characteristics and Their Impact on the Derivation of the HI Mass Function.

Heiles, C., 1994, ApJ, 436, 720
On the origin of the diffuse C(+) 158 micron line emission.

Helou, G., Soifer, B. T. & Rowan-Robinson, M., 1985, ApJ, 298, L7
Thermal infrared and nonthermal radio - Remarkable correlation in disks of galaxies.

Helou, G., 2000, Infrared Space Astronomy, Today and Tomorrow, 337
Course 8: Normal Galaxies in the Infrared.

Hildebrand, R. H., 1983, QJRAS, 24, 267
The Determination of Cloud Masses and Dust Characteristics from Submillimetre Thermal Emission.

Hinz, J. L., Rieke, M. J., Rieke, G. H. et al., 2007, ApJ, 663, 895
Spitzer Observations of Low-Luminosity Isolated and Low Surface Brightness Galaxies.

Ho, L. C., Filippenko, A. V. & Sargent, W. L., 1995, ApJS, 98, 477
A search for 'dwarf' Seyfert nuclei. 2: an optical spectral atlas of the nuclei of nearby galaxies.

Ho, L. C., Filippenko, A. V. & Sargent, W. L., 1997, ApJS, 112, 315
A Search for "Dwarf" Seyfert Nuclei. III. Spectroscopic Parameters and Properties of the Host Galaxies.

Ho, L. C., Filippenko, A. V. & Sargent, W. L. et al., 1997, ApJS, 112, 391
A Search for "Dwarf" Seyfert Nuclei. IV. Nuclei with Broad H alpha Emission.

Hodge, P. W., 1973, ApJ, 182, 671
The Structure and Content of NGC 205.

Hodge, P. W. & Kennicutt, Jr., R. C., 1983, AJ, 88, 296
An atlas of HII regions in 125 galaxies.

Hoeppe, G., Brinks, E., Klein, U. et al., 1994, AJ, 108, 446
Radio continuum and far-infrared observations of low surface brightness galaxies.

Hollenbach, D. & Salpeter, E. E., 1971, ApJ, 163, 155
Surface Recombination of Hydrogen Molecules.

Hollenbach, D., Werner, M. W. & Salpeter, E. E., 1971, ApJ, 163, 165
Molecular Hydrogen in HI Regions.

Hollenbach, D., Takahashi, T. & Tielens, A. G. G. M., 1991, ApJ, 377, 192
Low-density photodissociation regions.

Hollenbach, D. & Tielens, A. G. G. M., 1999, Reviews of Modern Physics, 71, 173
Photodissociation regions in the interstellar medium of galaxies.

Holwerda, B. W., Bianchi, S., Böker, T. et al., 2012, A&A, in press
Herschel/SPIRE Observations of the Dusty Disk of NGC 4244.

Howard, C. D., Rich, R. M., Reitzel, D. B. et al., 2008, ApJ, 688, 1060
The Bulge Radial Velocity Assay (BRAVA). I. Sample Selection and a Rotation Curve.

Howley, K. M., Geha, M., Guhathakurta, P. et al., 2008, ApJ, 683, 722
Darwin Tames an Andromeda Dwarf: Unraveling the Orbit of NGC 205 Using a Genetic Algorithm.

Ibata, R., Irwin, M., Lewis, G. et al., 2001, Nature, 412, 49
A giant stream of metal-rich stars in the halo of the galaxy M31.

Icke, V., 1985, A&A, 144, 115
Distant encounters between disk galaxies and the origin of S0 spirals.

Iono, D., Yun, M. S., Elvis, M. et al., 2006, ApJL, 645, L97
A Detection of [C II] Line Emission in the z = 4.7 QSO BR 1202-0725.

Israel, F. P., 1988, A&A, 194, 24
A detailed study of the post-starburst galaxy NGC 1569. I - Global parameters and starburst properties.

Israel, F. P., Maloney, P. R., Geis, N. et al., 1996, ApJ, 465, 738
C+ Emission from the Magellanic Clouds. I. The Bright HII Region Complexes N159 and N160.

Israel, F. P., Wall, W. F., Raban, D. et al., 2010, A&A, 519, A67
Submillimeter to centimeter excess emission from the Magellanic Clouds. I. Global spectral energy distribution.

Ivison, R. J., Swinbank, A. M., Swinyard, B. et al., 2010, A&A, 518, L35
Herschel and SCUBA-2 imaging and spectroscopy of a bright, lensed submillimetre galaxy at z = 2.3.

James, A., Dunne, L., Eales, S. et al., 2002, MNRAS, 335, 753
SCUBA observations of galaxies with metallicity measurements: a new method for determining the relation between submillimetre luminosity and dust mass.

Jarrett, T. H., Chester, T., Cutri, R. et al., 2003, AJ, 125, 525
The 2MASS Large Galaxy Atlas.

Jarvis, B., 1990, Dynamics and Interactions of Galaxies, 416
The NGC 128 group of galaxies.

Jensen, E. B. & Thuan, T. X., 1982, ApJS, 50, 421
Stellar populations in the edge-on spiral galaxy NGC 4565. I - Surface brightness and color distributions.

Jensen, J. B., Tonry, J. L., Barris, B. J, et al., 2003, ApJ, 583, 712
Measuring Distances and Probing the Unresolved Stellar Populations of Galaxies Using Infrared Surface Brightness Fluctuations.

Jerjen, H., Kalnajs, A. & Binggeli, B., 2000, A&A, 358, 845
IC3328: A "dwarf elliptical galaxy" with spiral structure.

Johnson, D. W. & Gottesman, S. T., 1983, ApJ, 275, 549
VLA observations of the neutral hydrogen content of NGC 185 and 205.

Johnson, B. D., Schiminovich, D., Seibert, M. et al., 2007, ApJ, 173, 392
Ultraviolet through Infrared Spectral Energy Distributions from 1000 SDSS Galaxies: Dust Attenuation.

Jonsson, P., 2006, MNRAS, 372, 2
SUNRISE: polychromatic dust radiative transfer in arbitrary geometries.

Jonsson, P., Groves, B. A. & Cox, T. J., 2010, MNRAS, 403, 17
High-resolution panchromatic spectral models of galaxies including photoionization and dust.

Kaufman, M. J., Wolfire, M. G., Hollenbach, D. J. et al., 1999, ApJ, 527, 795
Far-Infrared and Submillimeter Emission from Galactic and Extragalactic Photodissociation Regions.

Kennicutt, Jr., R. C. & Kent, S. M., 1983, AJ, 88, 1094
A survey of H-alpha emission in normal galaxies.

Kennicutt, Jr., R. C., 1998, ApJ, 498, 541
The Global Schmidt Law in Star-forming Galaxies.

Kennicutt, Jr., R. C., 1998, ARA&A, 36, 189
Star Formation in Galaxies Along the Hubble Sequence.

Kennicutt, Jr., R. C., Armus, L., Bendo, G. J. et al., 2003, PASP, 115, 928
SINGS: The SIRTF Nearby Galaxies Survey.

Kennicutt, Jr., R. C., Lee, J. C., Funes, José G., S. J. et al., 2008, ApJS, 178, 247
An Hα Imaging Survey of Galaxies in the Local 11 Mpc Volume.

Kennicutt, Jr., R. C., Hao, C.-N., Calzetti, D. et al., 2009, ApJ, 703, 1672
Dust-corrected Star Formation Rates of Galaxies. I. Combinations of Hα and Infrared Tracers.

Kessler, M. F., Steinz, J. A., Anderegg, M. E. et al., 1996, A&A, 315, L27
The Infrared Space Observatory (ISO) mission.

Kessler, M. F., Mueller, T. G., Leech, K. et al., 2003, Series edited by T.G. Mueller, J.A.D.L. Blommaert, and P. Garcia-Lario. ESA SP-1262, ISBN No. 92-9092-968-5, ISSN No. 0379-6566. European Space Agency, 2003
The ISO Handbook, Volume I - Mission & Satellite Overview.

Klein, U., Giovanardi, C., Altschuler, D. R. et al., 1992, A&A, 255, 49
A sensitive radio continuum survey of low surface brightness dwarf galaxies.

Knapen, J. H., Hes, R., Beckman, J. E. et al., 1991, A&A, 241, 42
Dust extinction in NGC 4594, the Sombrero galaxy.

Knapp, G. R., Leighton, R. B., Wannier, P. G. et al., 1980, ApJ, 240, 60
Detection of the CO J = 2-1 line in M82 and IC 342.

Koleva, M., De Rijcke, S., Prugniel, P. et al., 2009, MNRAS, 396, 2133
Formation and evolution of dwarf elliptical galaxies - II. Spatially resolved star formation histories.

Kong, X., Charlot, S., Brinchmann, J. et al., 2004, MNRAS, 349, 769
Star formation history and dust content of galaxies drawn from ultraviolet surveys.

Kormendy, J. & Bruzual A., G., 1978, ApJL, 223, L63
The minor-axis brightness profile of the spiral galaxy NGC 4565 and the problem of massive halos.

Kormendy, J. & Illingworth, G., 1982, ApJ, 256, 460
Rotation of the bulge components of disk galaxies.

Kormendy, J., Bender, R., Ajhar, E. A. et al., 1996, ApJL, 473, L91
Hubble Space Telescope Spectroscopic Evidence for a $1 \times 10^9\ M_\odot$ *Black Hole in NGC 4594.*

Kormendy, J., Fisher, D. B., Cornell, M. E. et al., 2009, ApJS, 182, 216
Structure and Formation of Elliptical and Spheroidal Galaxies.

Kormendy, J. & Barentine, J. C., 2010, ApJL, 715, L176
Detection of a Pseudobulge Hidden Inside the "Box-shaped Bulge" of NGC 4565.

Krause, M., Wielebinski, R. & Dumke, M., 2006, A&A, 448, 133
Radio polarization and sub-millimeter observations of the Sombrero galaxy (NGC 4594). Large-scale magnetic field configuration and dust emission.

Kroupa, P., 2001, MNRAS, 322, 231
On the variation of the initial mass function.

Kroupa, P., 2002, Science, 295, 82
The Initial Mass Function of Stars: Evidence for Uniformity in Variable Systems.

Kroupa, P. & Weidner, C., 2003, ApJ, 598, 1076
Galactic-Field Initial Mass Functions of Massive Stars.

Kulkarni, S. R. & Heiles, C., 1987, Astrophysics and Space Science Library, Interstellar Processes, vol. 134, 87
The atomic component.

Kwok, S. 2007, University Science Books, 2007
Physics and Chemistry of the Interstellar Medium.

Kylafis, N. D. & Bahcall, J. N. 1987, ApJ, 317, 637
Dust distribution in spiral galaxies.

Laine, S., Appleton, P. N., Gottesman, S. T. et al., 2000, AJ, 140, 753
Warm Molecular Hydrogen Emission in Normal Edge-on Galaxies NGC 4565 and NGC 5907.

Larson, R. B., Tinsley, B. M. & Caldwell, C. N., 1980, ApJ, 237, 692
The evolution of disk galaxies and the origin of S0 galaxies.

Leech, K. J., Völk, H. J., Heinrichsen, I. et al., 1999, MNRAS, 310, 317
[CII] 158 μm observations of a sample of late-type galaxies from the Virgo cluster.

Leitherer, C., Schaerer, D., Goldader, J. D et al., 1999, ApJS, 123, 3
Starburst99: Synthesis Models for Galaxies with Active Star Formation.

Lepp, S. & Dalgarno, A., 1996, A&A, 306, L21
X-ray-induced chemistry of interstellar clouds.

Lequeux, J., Le Bourlot, J., Pineau des Forets, G. et al., 1994, A&A, 292, 371
Results of the ESO-SEST Key Program: CO in the Magellanic Clouds. 4: Physical properties of molecular clouds in the Small Magellanic Cloud.

Leroy, A., Bolatto, A. D., Simon, J. D. et al., 2005, ApJ, 625, 763
The Molecular Interstellar Medium of Dwarf Galaxies on Kiloparsec Scales: A New Survey for CO in Northern, IRAS-detected Dwarf Galaxies.

Leroy, A., Bolatto, A. D., Stanimirovic, S. et al., 2005, ApJ, 658, 1027
The Spitzer Survey of the Small Magellanic Cloud: Far-Infrared Emission and Cold Gas in the Small Magellanic Cloud.

Leroy, A. K., Walter, F., Brinks, E. et al., 2008, AJ, 136, 2782
The Star Formation Efficiency in Nearby Galaxies: Measuring Where Gas Forms Stars Effectively.

Li, Z., Wang, Q. D. & Hameed, S., 2007, MNRAS, 376, 960
Chandra and XMM-Newton detection of large-scale diffuse X-ray emission from the Sombrero galaxy.

Li, Z., Spitler, L. R., Jones, C. et al., 2010, ApJ, 721, 1368
X-ray Emission from the Sombrero Galaxy: Discrete Sources.

Lisenfeld, U., Israel, F. P., Stil, J. M. et al., 2002, A&A, 382, 860
(Sub)millimetre emission from NGC 1569: An abundance of very small grains.

Lisker, T., Grebel, E. K. & Binggeli, B., 2006, AJ, 132, 497
Virgo Cluster Early-Type Dwarf Galaxies with the Sloan Digital Sky Survey. I. On the Possible Disk Nature of Bright Early-Type Dwarfs.

Lisker, T., Glatt, K., Westera, P. et al., 2006, AJ, 132, 2432
Virgo Cluster Early-Type Dwarf Galaxies with the Sloan Digital Sky Survey. II. Early-Type Dwarfs with Central Star Formation.

Lord, S. D., Hollenbach, D. J., Haas, M. R. et al., 1996, ApJ, 465, 703
Interstellar Properties of a Dual Nuclear Starburst: Far-Infrared Spectroscopy of M82.

Lu, N. Y., Bendo, G. J. & VNGS Team, 2011, American Astronomical Society Meeting Abstracts #218, 330.04
A Herschel SPIRE Study of M81: Separating Cold and Warm PAH Emissions.

Lucero, D. M. & Young, L. M. 2007, AJ, 134, 2148
Radio Continuum and Star Formation in CO-rich Early-Type Galaxies.

Luhman, M. L., Satyapal, S., Fischer, J. et al. 1998, ApJ, 504, L11
Infrared Space Observatory Measurements of a [C II] 158 Micron Line Deficit in Ultraluminous Infrared Galaxies.

Luhman, M. L., Satyapal, S., Fischer, J. et al. 2003, ApJ, 594, 758
The [CII] 158 Micron Line Deficit in Ultraluminous Infrared Galaxies Revisited.

MacLachlan, J. M., Matthews, L. D., Wood, K. et al., 2011, ApJ, 741, 6
The Stability of Low Surface Brightness Disks Based on Multi-wavelength Modeling.

Madden, S. C., Geis, N., Genzel, R. et al., 1993, ApJ, 407, 579
158 micron forbidden CII mapping of NGC 6946 - Probing the atomic medium.

Madden, S. C., Poglitsch, A., Geis, N. et al., 1997, ApJ, 483, 200
[CII] 158 Micron Observations of IC 10: Evidence for Hidden Molecular Hydrogen in Irregular Galaxies.

Madden, S. C., 2000, Nature, 44, 249
Effects of massive star formation on the ISM of dwarf galaxies.

Madden, S. C., Galliano, F., Jones, A. P. et al., 2006, A&A, 446, 877
ISM properties in low-metallicity environments.

Magrini, L., Bianchi, S., Corbelli, E. et al., 2011, A&A, 535, A13

The Herschel Virgo Cluster Survey. IX. Dust-to-gas mass ratio and metallicity gradients in four Virgo spiral galaxies.

Maiolino, R., Cox, P., Caselli, P. et al., 2005, A&A, 440, L51
First detection of [CII] 158 μm at high redshift: vigorous star formation in the early universe.

Maiolino, R., Caselli, P., Nagao, T. et al., 2009, A&A, 500, L1
Strong [CII] emission at high redshift.

Malhotra, S., Helou, G., Stacey, G. et al., 1997, ApJ, 491, L27
Infrared Space Observatory Measurements of [CII] Line Variations in Galaxies.

Malhotra, S., Hollenbach, D., Helou, G. et al., 2000, ApJ, 543, 634
Probing the Interstellar Medium in Early-Type Galaxies withInfrared Space Observatory Observations.

Malhotra, S., Kaufman, M. J., Hollenbach, D. et al., 2001, ApJ, 561, 766
Far-Infrared Spectroscopy of Normal Galaxies: Physical Conditions in the Interstellar Medium.

Maloney, P. R., Hollenbach, D. J. & Tielens, A. G. G. M., 1996, ApJ, 466, 561
X-Ray-irradiated Molecular Gas. I. Physical Processes and General Results.

Maraston, C., 1998, MNRAS, 300, 872
Evolutionary synthesis of stellar populations: a modular tool.

Maraston, C., 2005, MNRAS, 362, 799
Evolutionary population synthesis: models, analysis of the ingredients and application to high-z galaxies.

Marleau, F. R., Noriega-Crespo, A., Misselt, K. A. et al., 2006, ApJ, 646, 929
Mapping and Mass Measurement of the Cold Dust in NGC 205 with Spitzer.

Marleau, F. R., Noriega-Crespo, A., Misselt, K. A. et al., 2010, ApJ, 713, 992
Dust Abundance and Properties in the Nearby Dwarf Galaxies NGC 147 and NGC 185.

Martin, P. G. & Mandy, M. E. 1995, ApJL, 455, L89
Analytic Temperature Dependences for a Complete Set of Rate Coefficients for Collisional Excitation and Dissociation of H_2 *Molecules by H Atoms.*

Martin, P. G., Schwarz, D. H. & Mandy, M. E. 1995, ApJ, 461, 265
Master Equation Studies of the Collisional Excitation and Dissociation of H_2 *Molecules by H Atoms.*

Martín-Manjón, M. L., Mollá, M., Díaz, A. I. et al. 2012, MNRAS, 420, 1294
Evolution of star-forming dwarf galaxies: characterizing the star formation scenarios.

Martins, L. P., Lanfranchi, G., Gonçalves, D. R. et al. 2012, MNRAS, 419, 3159
The ionization mechanism of NGC 185: how to fake a Seyfert galaxy?

Mathis, J. S., Rumpl, W. & Nordsieck, K. H., 1977, ApJ, 217, 425
The size distribution of interstellar grains.

Mathis, J. S., Mezger, P. G. & Panagia, N., 1983, A&A, 128, 212
Interstellar radiation field and dust temperatures in the diffuse interstellar matter and in giant molecular clouds.

Matsumura, M. & Seki, M., 1989, A&A, 209, 8
Dust grains in M 104 - an interpretation of the optical polarization in an external galaxy.

Mayer, L., Governato, F., Colpi, M. et al., 2001, ApJ, 559, 754
The Metamorphosis of Tidally Stirred Dwarf Galaxies.

Mayer, L., Mastropietro, C., Wadsley, J. et al., 2006, MNRAS, 369, 1021
Simultaneous ram pressure and tidal stripping; how dwarf spheroidals lost their gas.

McConnachie, A. W., Irwin, M. J., Lewis, G. F. et al., 2004, MNRAS, 351, L94
The tidal trail of NGC 205?

McConnachie, A. W., Irwin, M. J., Ferguson, A. M. N. et al., 2005, MNRAS, 356, 979
Distances and metallicities for 17 Local Group galaxies.

McKee, C. F. & Ostriker, J. P., 1977, ApJ, 218, 148
A theory of the interstellar medium - Three components regulated by supernova explosions in an inhomogeneous substrate.

Mei, S., Blakeslee, J. P. & Côté, P. et al., 2007, ApJ, 655, 144
The ACS Virgo Cluster Survey. XIII. SBF Distance Catalog and the Three-dimensional Structure of the Virgo Cluster.

Meixner, M., Galliano, F., Hony, S. et al., 2010, A&A, 518, L71
HERschel Inventory of The Agents of Galaxy Evolution (HERITAGE): The Large Magellanic Cloud dust.

Meny, C., Gromov, V., Boudet, N. et al., 2007, A&A, 468, 171
Far-infrared to millimeter astrophysical dust emission. I. A model based on physical properties of amorphous solids.

Meurer, G. R., Heckman, T. M., Leitherer, C. et al., 1995, AJ, 110, 2665
Starbursts and Star Clusters in the Ultraviolet.

Meurer, G. R., Heckman, T. M., Calzetti, D., 1999, ApJ, 521, 64

Dust Absorption and the Ultraviolet Luminosity Density at z $\sim$ 3 as Calibrated by Local Starburst Galaxies.

Meurer, G. R., 2011, Astronomical Society of the Pacific Conference Series, Vol. 440, 189
Upper End IMF Variations Deduced from HI-Selected Galaxies.

Michielsen, D., De Rijcke, S. & Dejonghe, H., 2004, Astronomische Nachrichten Supplement, Vol. 325, 122
N-body/SPH Study of the Evolution of Dwarf Galaxies in a Cluster Environment.

Misiriotis, A., Popescu, C. C., Tuffs, R.H. et al., 2001, A&A, 372, 775
Modeling the spectral energy distribution of galaxies. II. Disk opacity and star formation in 5 edge-on spirals.

Misiriotis, A. & Bianchi, S., 2002, A&A, 384, 866
The influence of clumping on surface brightness fits of edge-on spiral galaxies.

Monaco, L., Saviane, I., Perina, S. et al., 2009, A&A, 502, L9
The young stellar population at the center of NGC 205.

Moore, B., Katz, N., Lake, G. et al., 1996, Nature, 379, 613
Galaxy harassment and the evolution of clusters of galaxies.

Morrissey, P., Conrow, T., Barlow, T. A. et al., 2007, ApJS, 173, 682
The Calibration and Data Products of GALEX.

Mosenkov, A. V., Sotnikova, N. Y. & Reshetnikov, V. P., 2010, MNRAS, 401, 559
2MASS photometry of edge-on spiral galaxies - I. Sample and general results.

Mould, J., Kristian, J. & Da Costa, G. S., 1984, ApJ, 278, 575
Stellar populations in local group dwarf elliptical galaxies. II - NGC 205.

Mould, J. & Spitler, L., 2010, ApJ, 722, 721
The Stellar Population and Metallicity Distribution of the Sombrero Galaxy.

Müller, T., Okumura, K. & Klaas, U., 2011, PACS ICC manual
PACS Photometer - Point-Source Flux Calibration, PICC-ME-TN-038, available from the ESA Herschel Science Centre.

Muñoz-Mateos, J. C., Gil de Paz, A. & Boissier, S. et al., 2009, ApJ, 701, 1965
Radial Distribution of Stars, Gas, and Dust in Sings Galaxies. II. Derived Dust Properties.

Murakami, H., Baba, H., Barthel, P. et al., 2007, PASJ, 59, 369
The Infrared Astronomical Mission AKARI.

Murphy, E. J., Helou, G., Braun, R. et al., 2006, ApJL, 651, L111
The Effect of Star Formation on the Far-Infrared-Radio Correlation within Galaxies.

Naeslund, M. & Joersaeter, S., 1997, A&A, 325, 915
Surface photometry of the edge-on spiral NGC 4565. I. V-band data and the extended optical warp.

Nagamine, K., Wolfe, A. M. & Hernquist, L., 2006, ApJ, 647, 60
Detectability of [C II] 158 μm Emission from High-Redshift Galaxies: Predictions for ALMA and SPICA.

Nakagawa, T., Yui, Y. Y., Doi, Y. et al., 2006, ApJS, 115, 259
Far-Infrared [CII] Line Survey Observations of the Galactic Plane.

Neininger, N., Guelin, M., Garcia-Burillo, S. et al., 2006, A&A, 310, 725
Cold dust and molecular line emission in NGC4565.

Negishi, T., Onaka, T., Chan, K.-W. et al., 2001, A&A, 375, 566
Global physical conditions of the interstellar medium in nearby galaxies.

Neugebauer, G., Habing, H. J., van Duinen, R. et al., 1984, ApJL, 278, L1
The Infrared Astronomical Satellite (IRAS) mission.

Nulsen, P. E. J., 1982, MNRAS, 198, 1007
Transport processes and the stripping of cluster galaxies.

Oberst, T. E., Parshley, S. C., Stacey, G. J. et al., 2006, ApJ, 652, L125
Detection of the 205 μm [N II] Line from the Carina Nebula.

O'Halloran, B., Galametz, M., Madden, S. C. et al., 2010, A&A, 518, L58
Herschel photometric observations of the low metallicity dwarf galaxy NGC 1705.

Ohta, K. & Kodaira, K., 1995, PASJ, 47, 17
Absorption-layer analyses of early-type edge-on galaxies: NGC 4217, NGC 4565, and NGC 4594.

Ott, S., Astronomical Society of the Pacific Conference Series, Vol. 434, 139
The Herschel Data Processing System – HIPE and Pipelines – Up and Running Since the Start of the Mission.

PACS Observer's Manual, 2011, HERSCHEL-HSC-DOC-0832, available from the ESA Herschel Science Centre

Pak, S., Jaffe, D. T., van Dishoeck, E. F. et al., 1998, ApJ, 498, 735
Molecular Cloud Structure in the Magellanic Clouds: Effect of Metallicity.

Panuzzo, P., Rangwala, N., Rykala, A. et al., 2010, A&A, 518, L37
Probing the molecular interstellar medium of M82 with Herschel-SPIRE spectroscopy.

Papadopoulos, P. P., Isaak, K. & van der Werf, P., 2010, ApJ, 711, 757
CO J = 6-5 in Arp 220: Strong Effects of Dust on High-J CO Lines.

Parkin, T. J., Wilson, C. D., Foyle, K. et al., 2012, MNRAS, in press
The gas-to-dust mass ratio of Centaurus A as seen by Herschel.

Pedraz, S., Gorgas, J., Cardiel, N. et al., 2002, MNRAS, 332, L59
Evidence of fast rotation in dwarf elliptical galaxies.

Pérez-González, P. G., Kennicutt, Jr., R. C., Gordon, K. D. et al., 2006, ApJ, 648, 987
Ultraviolet through Far-Infrared Spatially Resolved Analysis of the Recent Star Formation in M81 (NGC 3031).

Pierini, D., Leech, K. J., Tuffs, R. J. et al., 1999, MNRAS, 303, L29
[CII] emission and star formation in late-type galaxies.

Pierini, D., Lequeux, J., Boselli, A. et al., 2001, A&A, 373, 827
Gas cooling within the diffuse ISM of late-type galaxies.

Pierini, D., Leech, K. J. & Völk, H. J., 2003, A&A, 397, 871
[C II] emission and star formation in late-type galaxies. II. A model.

Pilbratt, G. L., Riedinger, J. R., Passvogel, T. et al., 2003, A&A, 518, L1
Herschel Space Observatory. An ESA facility for far-infrared and submillimetre astronomy.

Pineda, J. L., Velusamy, T., Langer, W. D. et al., 2010, A&A, 521, L19
A sample of [C II] clouds tracing dense clouds in weak FUV fields observed by Herschel.

Pinte, C., Ménard, F., Duchêne, G. et al., 2006, A&A, 459, 797
Monte Carlo radiative transfer in protoplanetary disks.

Planck Collaboration et al., 2011, A&A, 536, A7
Planck early results. VII. The Early Release Compact Source Catalogue.

Planck Collaboration et al., 2011, A&A, 536, A17
Planck early results. XVII. Origin of the submillimetre excess dust emission in the Magellanic Clouds.

Poglitsch, A., Waelkens, C., Geis, N. et al., 2010, A&A, 518, L2
The Photodetector Array Camera and Spectrometer (PACS) on the Herschel Space Observatory.

Pohlen, M., Cortese, L., Smith, M. W. L. et al., 2010, A&A, 518, L72

Radial distribution of gas and dust in spiral galaxies . The case of M 99 (NGC 4254) and M 100 (NGC 4321).

Popescu, C. C., Misiriotis, A., Kylafis, N. D. et al., 2000, A&A, 362, 138
Modelling the spectral energy distribution of galaxies. I. Radiation fields and grain heating in the edge-on spiral NGC 891.

Popescu, C. C. & Tuffs, R. J. 2002, MNRAS, 335, L41
The percentage of stellar light re-radiated by dust in late-type Virgo Cluster galaxies.

Popescu, C. C., Tuffs, R. J., Dopita, M. A. et al. 2011, A&A, 527, A109
Modelling the spectral energy distribution of galaxies. V. The dust and PAH emission SEDs of disk galaxies.

Proctor, R. N., Sansom, A. E. & Reid, I. N. 2000, MNRAS, 311, 37
Constraining the star formation histories of spiral bulges.

Rangwala, N., Maloney, P. R., Glenn, J. et al. 2011, ApJ, 743, 94
Observations of Arp 220 Using Herschel-SPIRE: An Unprecedented View of the Molecular Gas in an Extreme Star Formation Environment.

Reach, W. T., Megeath, S. T. & Cohen, M. et al., 2005, PASP, 117, 978
Absolute Calibration of the Infrared Array Camera on the Spitzer Space Telescope.

Relaño, M., Lisenfeld, U., Pérez-González, P. G. et al., 2007, ApJ, 667, L141
On the Metallicity Dependence of the 24 μm Luminosity as a Star Formation Tracer.

Rice, W., Lonsdale, C. J., Soifer, B. T. et al., 1988, ApJS, 68, 91
A catalog of IRAS observations of large optical galaxies.

Rice, W., Merrill, K. M., Gatley, I. et al., 1996, AJ, 112, 114
Near-Infrared Structure of the Edge-on Spiral NGC 4565.

Richer, M. G. & McCall, M. L., 2008, ApJ, 684, 1190
Bright Planetary Nebulae and their Progenitors in Galaxies Without Star Formation.

Rieke, G. H., Young, E. T., Engelbracht, C. W. et al., 2004, ApJS, 154, 25
The Multiband Imaging Photometer for Spitzer (MIPS).

Rieke, G. H., Alonso-Herrero, A., Weiner, B. J. et al., 2009, ApJ, 692, 556
Determining Star Formation Rates for Infrared Galaxies.

Risaliti, G., 2004, Memorie della Societa Astronomica Italiana Supplementi, Vol. 5, 217
The starburst-AGN connection in ULIRGs.

Roberge, W. G., 1983, ApJ, 275, 292

The spherical harmonics solution for the radiation field in plane-parallel clouds with embedded sources.

Roediger, E. & Hensler, G., 2005, A&A, 433, 875
Ram pressure stripping of disk galaxies. From high to low density environments.

Röllig, M., Ossenkopf, V., Jeyakumar, S. et al. 2006, A&A, 451, 917
[CII] 158 μm emission and metallicity in photon dominated regions.

Roussel, H., Wilson, C. D., Vigroux, L. et al. 2010, A&A, 518, L66
SPIRE imaging of M 82: Cool dust in the wind and tidal streams.

Ruben, G., 1991, Ap&SS, 177, 465
Cosmic rotation and the inertial system.

Sage, L. J., Welch, G. A. & Mitchell, G. F., 1998, ApJ, 507, 726
The Missing Interstellar Medium of NGC 147 and M32.

Salama, F., 1999, Solid Interstellar Matter: The ISO Revolution, 65
Polycyclic Aromatic Hydrocarbons in the Interstellar Medium: A Review.

Salim, S., Rich, R. M., Charlot, S. et al., 2007, ApJS, 173, 267
UV Star Formation Rates in the Local Universe.

Salim, S., Dickinson, M., Michael Rich, R. et al., 2009, ApJ, 700, 161
Mid-IR Luminosities and UV/Optical Star Formation Rates at $z < 1.4$.

Salpeter, E. E., 1955, ApJ, 121, 161
The Luminosity Function and Stellar Evolution.

Sancisi, R., 1976, A&A, 53, 159
Warped HI Disks in Galaxies.

Sandage, A. & Tammann, G. A., 1975, ApJ, 196, 313
Steps toward the Hubble constant. V - The Hubble constant from nearby galaxies and the regularity of the local velocity field.

Sanders, D. B., Mazzarella, J. M., Kim, D.-C. et al., 2003, AJ, 126, 1607
The IRAS Revised Bright Galaxy Sample.

Sato, N. R. & Sawa, T., 1955, PASJ, 38, 63
Neutral hydrogen in M31. VI - The tidal interaction between M31 and NGC 205.

Satyapal, S., Dudik, R. P. & O'Halloran, B. et al., 2005, ApJ, 633, 86
The Link between Star Formation and Accretion in LINERs: A Comparison with Other Active Galactic Nucleus Subclasses.

Sauty, S., Gerin, M. & Casoli, F., 1998, A&A, 339, 19
FIR and C^+ emissions of spiral galaxies disks. The example of NGC 6946.

Sauvage, M., Tuffs, R. J. & Popescu, C. C., 2005, SSR, 119, 313
Normal Nearby Galaxies.

Sauvage, M., Sacchi, N., Bendo, G. J. et al., 2010, A&A, 518, L64
The central region of spiral galaxies as seen by Herschel. M 81, M 99, and M 100.

Savage, B. D. & Sembach, K. R., 1996, ARA&A, 34, 279
Interstellar Abundances from Absorption-Line Observations with the Hubble Space Telescope.

Saviane, I., Monaco, L. & Hallas, T., 2010, IAU Symposium, Vol. 262, 426
Morphological transformation of NGC 205?

Schechtman-Rook, A., Bershady, M. A. & Wood, K., 2012, ApJ, 746, 70
The Three-dimensional Distribution of Dust in NGC 891.

Schindler, S., Binggeli, B. & Böhringer, H., 1999, A&A, 343, 420
Morphology of the Virgo cluster: Gas versus galaxies.

Schlegel, D. J., Finkbeiner, D. P. & Davis, M., 1998, ApJ, 500, 525
Maps of Dust Infrared Emission for Use in Estimation of Reddening and Cosmic Microwave Background Radiation Foregrounds.

Schmidt, M., 1959, ApJ, 129,243
The Rate of Star Formation.

Schmitt, H. R., Kinney, A. L., Calzetti, D. et al., 1997, AJ, 114, 592
The Spectral Energy Distribution of Normal, Starburst, and Active Galaxies.

Semionov, D. & Vansevičius, V., 2005, Baltic Astronomy, Vol. 14, 543
Radiative Transfer Problem in Dusty Galaxies: Galactic Fog Engine.

Seth, A. C., Dalcanton, J. J. & de Jong, R. S., 2005, AJ, 129, 1331
A Study of Edge-On Galaxies with the Hubble Space Telescope Advanced Camera for Surveys. I. Initial Results.

Sharina, M. E., Afanasiev, V. L. & Puzia, T. H., 2006, MNRAS, 372, 1259
Ages, metallicities and [α/Fe] ratios of globular clusters in NGC 147, 185 and 205.

Shaw, M., Wilkinson, A. & Carter, D., 1993, A&A, 268, 511
The stellar dynamics of 'box/peanut' galactic bulges. I - NGC 3079.

Shetty, R., Glover, S. C., Dullemond, C. P. et al., 2011, MNRAS, 412, 1686

Modelling CO emission - I. CO as a column density tracer and the X factor in molecular clouds.

Shibai, H., Okuda, H., Nakagawa, T. et al., 1991, ApJ, 374, 522
Large-scale forbidden C II 158 micron emission from the Galaxy.

Simien, F. & Prugniel, P., 2002, A&A, 384, 371
Kinematical data on early-type galaxies. VI.

Skibba, R. A., Engelbracht, C. W., Dale, D. A. et al., 2011, ApJ, 738, 89
The Emission by Dust and Stars of Nearby Galaxies in the Herschel KINGFISH Survey.

Smith, M. W. L., Vlahakis, C., Baes, M. et al., 2010, A&A, 518, L51
The Herschel Virgo Cluster Survey. IV. Resolved dust analysis of spiral galaxies.

Smith, M. W. L., Gomez, H. L., Eales, S. A. et al., 2012, ApJ, 748, 123
The Herschel Reference Survey: Dust in Early-type Galaxies and across the Hubble Sequence.

Sofue, Y. & Nakai, N. 1994, PASJ, 46, 147
CO observations of edge-on galaxies. 4. NGC 4565: Radial variation of the H2-to-H I ratio.

Sollima, A., Gil de Paz, A., Martinez-Delgado, D. et al., 2010, A&A, 516, A83
A multi-wavelength analysis of M 81: insight on the nature of Arp's loop.

SPIRE Observer's Manual, 2011, HERSCHEL-HSC-DOC-0798, available from the ESA Herschel Science Centre

Spitler, L. R., Forbes, D. A., Strader, J. et al., 2008, MNRAS, 385, 361
The connection between globular cluster systems and their host galaxy and environment: a case study of the isolated elliptical NGC 821.

Stacey, G. J., Viscuso, P. J., Fuller, C. E. et al., 1985, ApJ, 289, 803
The 157-micron forbidden CII luminosity of the Galaxy. II - The presence of knot-like features in the forbidden CII emission.

Stacey, G. J., Geis, N., Genzel, R. et al., 1991, ApJ, 373, 423
The 158 micron CII line - A measure of global star formation activity in galaxies.

Stacey, G. J., Jaffe, D. T., Geis, N. et al., 1993, ApJ, 404, 219
158 micron forbidden CII mapping of the Orion molecular cloud.

Stacey, G. J., Hailey-Dunsheath, S., Ferkinhoff, C. et al., 2010, ApJ, 724, 957
A 158 μm [CII] Line Survey of Galaxies at z $\sim$ 1-2: An Indicator of Star Formation in the Early Universe.

Stalevski, M., Fritz, J., Baes, M. et al., 2012, MNRAS, 420, 2756
3D radiative transfer modelling of the dusty tori around active galactic nuclei as a clumpy two-phase medium.

Stansberry, J. A., Gordon, K. D., Bhattacharya, B. et al., 2007, PASP, 119, 1038
Absolute Calibration and Characterization of the Multiband Imaging Photometer for Spitzer. III. An Asteroid-based Calibration of MIPS at 160 μm.

Stark, A. A., 1997, ApJ, 481, 587
Potential Measurement of the Luminosity Function of 158 Micron [CII] at High Redshifts: A Test of Galaxy Formation Models.

Stasińska, G., 1990, A&AS, 83, 501
A grid of model HII regions for extragalactic studies.

Steinacker, J., Henning, T., Bacmann, A. et al., 2003, A&A, 401, 405
3D continuum radiative transfer in complex dust configurations around stellar objects and active galactic nuclei. I. Computational methods and capabilities.

Stepnik, B., Abergel, A., Bernard, J.-P. et al., 2003, A&A, 398, 551
Evolution of dust properties in an interstellar filament.

Sternberg, A. & Dalgarno, A., 1989, ApJ, 338, 197
The infrared response of molecular hydrogen gas to ultraviolet radiation - High-density regions.

Stickel, M., Lemke, D., Klaas, U. et al., 2004, A&A, 422, 39
The ISOPHOT 170 μm Serendipity Survey II. The catalog of optically identified galaxies.

Strong, A. W., Bloemen, J. B. G. M., Dame, T. M. et al., 1988, A&A, 207, 1
The radial distribution of galactic gamma rays. IV - The whole galaxy.

Swinyard, B. M., Ade, P., Baluteau, J.-P. et al., 2010, A&A, 518, L4
In-flight calibration of the Herschel-SPIRE instrument.

Tielens, A. G. G. M. & Hollenbach, D., 1985, ApJ, 291, 722
Photodissociation regions. I - Basic model. II - A model for the Orion photodissociation region.

Tielens, A. G. G. M., 2005, ISBN 0521826349. Cambridge, UK: Cambridge University Press, 2005
The Physics and Chemistry of the Interstellar Medium.

Thilker, D. A., Braun, R., Walterbos, R. A. M. et al., 2004, ApJ, 601, L39

On the Continuing Formation of the Andromeda Galaxy: Detection of HI Clouds in the M31 Halo.

Thomas, D., Brimioulle, F., Bender, R. et al., 2006, A&A, 445, L19
A counter-rotating core in the dwarf elliptical galaxy VCC 510.

Toloba, E., Boselli, A., Gorgas, J. et al., 2009, ApJ, 707, L17
Kinematic Properties as Probes of the Evolution of Dwarf Galaxies in the Virgo Cluster.

Tommasin, S., Spinoglio, L., Malkan, M. A. et al., 2010, ApJ, 709, 1257
Spitzer-IRS High-Resolution Spectroscopy of the 12 μm Seyfert Galaxies. II. Results for the Complete Data Set.

Tonry, J. L., Dressler, A., Blakeslee, J. P. et al., 2001, ApJ, 546, 681
The SBF Survey of Galaxy Distances. IV. SBF Magnitudes, Colors, and Distances.

Treffers, R. & Cohen, M., 1974, ApJ, 188, 545
High-resolution spectra of cool stars in the 10- and 20-micron regions.

Truch, M. D. P., Ade, P. A. R., Bock, J. J. et al., 2008, ApJ, 681, 415
The Balloon-borne Large Aperture Submillimeter Telescope (BLAST) 2005: Calibration and Targeted Sources.

Tuffs, R. J., Popescu, C. C., Völk, H. J. et al., 2004, A&A, 419, 821
Modelling the spectral energy distribution of galaxies. III. Attenuation of stellar light in spiral galaxies.

Tully, R. B., 1988, Cambridge and New York, Cambridge University Press, 1988, 221 p
Nearby galaxies catalog.

Tully, R. B., Rizzi, L., Shaya, E. J. et al., 2009, AJ, 138, 323
The Extragalactic Distance Database.

Valcke, S., De Rijcke, S. & Dejonghe, H. 2008,MNRAS, 389, 1111
Simulations of the formation and evolution of isolated dwarf galaxies.

Valluri, M., Ferrarese, L., Merritt, D. et al., 2005, ApJ, 628, 137
The Low End of the Supermassive Black Hole Mass Function: Constraining the Mass of a Nuclear Black Hole in NGC 205 via Stellar Kinematics.

van den Bergh, S., 1998, AJ, 116, 1688
The Binary Galaxies NGC 147 and NGC 185.

van der Kruit, P. C., 1979, A&AS, 38, 15
Optical surface photometry of eight spiral galaxies studied in Westerbork.

van der Kruit, P. C. & Searle, L. 1981, A&A, 95, 105
Surface photometry of edge-on spiral galaxies. I - A model for the three-dimensional distribution of light in galactic disks.

van Zee, L., Skillman, E. D. & Haynes, M. P. 2004, AJ, 128, 121
Rotationally Supported Virgo Cluster Dwarf Elliptical Galaxies: Stripped Dwarf Irregular Galaxies?

Vazdekis, A., Peletier, R. F., Beckman, J. E. et al., 1997, ApJS, 111, 203
A New Chemo-evolutionary Population Synthesis Model for Early-Type Galaxies. II. Observations and Results.

Veilleux, S., Kim, D.-C., Sanders, D. B. et al., 1995, ApJS, 98, 171
Optical Spectroscopy of Luminous Infrared Galaxies. II. Analysis of the Nuclear and Long-Slit Data.

Verma, A., Charmandaris, V., Klaas, U. et al., 2005, SSR, 119, 355
Obscured Activity: AGN, Quasars, Starbursts and ULIGs Observed by the Infrared Space Observatory.

Veron-Cetty, M.-P. & Veron, P., 1986, A&AS, 66, 335
Study of a complete sample of galaxies. II - Spectroscopy of the nuclei.

Veron-Cetty, M.-P. & Veron, P., 2010, A&A, 518, A10
A catalogue of quasars and active nuclei: 13th edition.

Verstraete, L., Leger, A., D'Hendecourt, L. et al., 1990, A&A, 237, 436
Ionization cross-section measurements for two PAH molecules - Implications for the heating of diffuse interstellar gas.

Vidal, E. & Baes, M., 2007, Baltic Astronomy, Vol. 16, 101
Dust Radiative Transfer Simulations in the Inhomogeneous Circumstellar Medium.

Vlahakis, C., Baes, M., Bendo, G. et al., 2008, A&A, 485, L25
LABOCA and MAMBO-2 imaging of the dust ring of the Sombrero galaxy (NGC 4594).

Wagg, J., Carilli, C. L., Wilner, D. J. et al., 2010, A&A, 519, L1
[CII] line emission in BRI 1335-0417 at z = 4.4.

Wainscoat, R. J., de Jong, T. & Wesselius, P. R., 1987, A&A, 181, 225
IRAS observations of three edge-on galaxies.

Walcher, J., Groves, B., Budavári, T. et al., 2011, Ap&SS, 331, 1
Fitting the integrated spectral energy distributions of galaxies.

Warren, B. E., Wilson, C. D., Israel, F. P. et al., 2010, ApJ, 714, 571
The James Clerk Maxwell Telescope Nearby Galaxies Legacy Survey. II. Warm Molecular Gas and Star Formation in Three Field Spiral Galaxies.

Watson, W. D., 1972, ApJ, 176, 103
Heating of Interstellar HI Clouds by Ultraviolet Photoelectron Emission from Grains.

Weingartner, J. C. & Draine, B. T., 2001, ApJ, 548, 296
Dust Grain-Size Distributions and Extinction in the Milky Way, Large Magellanic Cloud, and Small Magellanic Cloud.

Weisz, D. R., Johnson, B. D., Johnson, L. C. et al., 2012, ApJ, 744, 44
Modeling the Effects of Star Formation Histories on Hα and Ultraviolet Fluxes in nearby Dwarf Galaxies.

Welch, G. A., Sage, L. J. & Mitchell, G. F., 1998, ApJ, 499, 209
The Puzzling Features of the Interstellar Medium in NGC 205.

Werner, M. W., Roellig, T. L., Low, F. J. et al., 2004, ApJS, 154, 1
The Spitzer Space Telescope Mission.

Wiebe, D. V., Ade, P. A. R., Bock, J. J. et al., 2009, ApJ, 707, 1809
BLAST Observations of Resolved Galaxies: Temperature Profiles and the Effect of Active Galactic Nuclei on FIR to Submillimeter Emission.

Wilcots, E. M., Hodge, P., Eskridge, P. B. et al., 1990, ApJ, 364, 87
Ultraviolet observations of NGC 205.

Wilson, C. D., 1995, ApJ, 448, L97
The Metallicity Dependence of the CO-to-H 2 Conversion Factor from Observations of Local Group Galaxies.

Wilson, C. D., Warren, B. E., Israel, F. P. et al., 2009, ApJ, 693, 1736
The James Clerk Maxwell Telescope Nearby Galaxies Legacy Survey. I. Star-Forming Molecular Gas in Virgo Cluster Spiral Galaxies.

Witt, A. N. & Gordon, K. D., 1999, American Astronomical Society Meeting Abstracts #194, Vol. 31, 946
Reddening and Attenuation by Dust in Galaxies with a Clumpy ISM.

Witt, A. N. & Gordon, K. D., 2000, ApJ, 528, 799
Multiple Scattering in Clumpy Media. II. Galactic Environments.

Wolfire, M. G., Hollenbach, D. & Tielens, A. G. G. M., 1989, ApJ, 344, 770
The correlation of CII 158 micron and CO (J = 1 - 0) line emission.

Wolfire, M. G., Hollenbach, D., McKee, C. F. et al., 1995, ApJ, 443, 152
The neutral atomic phases of the interstellar medium.

Wright, E. L., Mather, J. C., Bennett, C. L. et al., 1991, ApJ, 381, 200
Preliminary spectral observations of the Galaxy with a 7 deg beam by the Cosmic Background Explorer (COBE).

Wright, E. L., Eisenhardt, P. R. M. & Mainzer, A. K. et al., 2010, AJ, 140, 1868
The Wide-field Infrared Survey Explorer (WISE): Mission Description and Initial On-orbit Performance.

Wu, H., Burstein, D., Deng, Z. et al., 2002, AJ, 123, 1364
Intermediate-Band Surface Photometry of the Edge-on Galaxy NGC 4565.

Wu, H., Cao, C., Hao, C.-N. et al., 2005, ApJL, 632, L79
PAH and Mid-Infrared Luminosities as Measures of Star Formation Rate in Spitzer First Look Survey Galaxies.

Wu, Q. & Cao, X., 2006, PASP, 118, 1098
The Relation between Star Formation Rate and Accretion Rate in LINERs.

Xilouris, E. M., Kylafis, N. D., Papamastorakis, J. et al., 1997, A&A, 325, 135
The distribution of stars and dust in spiral galaxies: the edge-on spiral UGC 2048.

Xilouris, E. M., Alton, P. B., Davies, J. I.. et al., 1998, A&A, 331, 894
Optical and NIR modelling of NGC 891.

Xilouris, E. M., Byun, Y. I., Kylafis, N. D. et al., 1999, A&A, 344, 868
Are spiral galaxies optically thin or thick?

Xu, C. & Buat, V., 1995, A&A, 293, L65
Are spiral disks really opaque?

Young, L. M. & Lo, K. Y., 1996, ApJ, 464, L59
Molecular Clouds in the Dwarf Elliptical Galaxy NGC 205.

Young, L. M. & Lo, K. Y., 1997, ApJ, 476, 127
The Neutral Interstellar Medium in Nearby Dwarf Galaxies. II. NGC 185, NGC 205, and NGC 147.

Zhu, Y.-N., Wu, H., Cao, C. et al. 2008, ApJ, 686, 155
Correlations between Mid-Infrared, Far-Infrared, Hα, and FUV Luminosities for Spitzer SWIRE Field Galaxies.

Zubko, V., Dwek, E. & Arendt, R. G., 2004, ApJS, 152, 211

Interstellar Dust Models Consistent with Extinction, Emission, and Abundance Constraints.